Optimal Design of Laminated Composite Beams

Blasques, José Pedro Albergaria Amaral; Stolpe, Mathias; Berggreen, Christian; Branner, Kim

Publication date:
2011

Document Version
Publisher's PDF, also known as Version of record

Optimal Design of Laminated Composite Beams

PhD Thesis

$$(EIv'')''=q-\rho A\ddot{v}$$

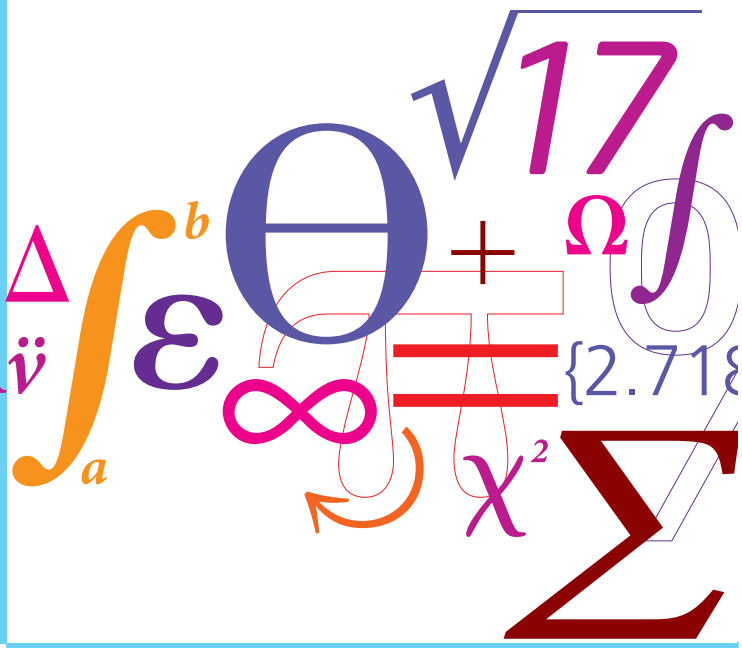

José Pedro Blasques
DCAMM Special Repport No. S134
August 2011

DTU Mechanical Engineering
Department of Mechanical Engineering

Optimal Design of Laminated Composite Beams

José Pedro Blasques

Department of Mechanical Engineering

Technical University of Denmark

To Dad
... everything is fun once you learn it!

Title of Thesis:
Optimal design of laminated composite beams

Ph.D. student:
José Pedro Blasques
Department of Mechanical Engineering
Technical University of Denmark
Address: Nils Koppels Allé, Building 403, DK-2800 Lyngby, Denmark
E-mail: jpbl@mek.dtu.dk

Supervisors:
Associate Professor Mathias Stolpe
Department of Mathematics
Technical University of Denmark
Address: Matematiktorvet, Building 303S, DK-2800 Lyngby, Denmark
E-mail: m.stolpe@mat.dtu.dk

Associate Professor Christian Berggreen
Department of Mechanical Engineering
Technical University of Denmark
Address: Nils Koppels Allé, Building 403, DK-2800 Lyngby, Denmark
E-mail: cbe@mek.dtu.dk

Senior Scientist Kim Branner
Risø National Laboratory for Sustainable Energy
Wind Energy Division
Technical University of Denmark
Address: Frederiksborgvej 399, Building 118, 4000 Roskilde, Denmark
E-mail: kibr@risoe.dtu.dk

Ph.D. Committe:
Senior Scientist Thomas Buhl, Risø - National Laboratory for Sustainable Energy
Professor Pierre Duysinx, University of Liége
Professor Erik Lund, Aalborg University

Preface

This thesis is submitted in partial fulfillment of the requirements for obtaining the degree of Ph.D. at the Technical University of Denmark. The Ph.D. project was funded by the Technical University of Denmark and carried out at the Department of Mechanical Engineering during the period between October 1st 2007 and August 1st 2011. Supervisors on the project were Associate Professor Mathias Stolpe from the Department of Mathematics, Associate Professor Christian Berggreen from the Department of Mechanical Engineering, and Senior Scientist Kim Branner from the Wind Energy Division at the National Laboratory for Sustainable Energy (Risø).

I would first like to thank my supervisors for their invaluable support. I would specially like to thank my main supervisor Mathias Stolpe for all the guidance, endless patience, and friendship. I would also like to thank Senior Scientist Gunjit Bir and everyone at the National Renewable Energy Laboratory (Colorado, USA), and Associate Professor Kurt Maute and the staff at Colorado University at Boulder (Colorado, USA) for making my external research stay so pleasurable. I would like to thank all my colleagues at the Department of Mechanical Engineering for the friendly and academically inspiring working environment. Many thanks to Scientist Boyan Lazarov for his generous support and patience during the development of BECAS. Thanks also to Martin Haugaard for his friendship and endless "ping-pong" of ideas.

Finally, I would like to express my deep gratitude to my family. Mom, Dad (if only you were here), and Chico for their endless support, love and enthusiasm. It would have been impossible without you. Thank you Ingunn for all your love, kind patience every time the code had a bug, and taking such good care of me while I sank deeper into this thesis. Soon it will be three of us.

To everyone, it has been a fantastic ride!

José Pedro Blasques

Kgs. Lyngby, August 2011

Summary

This thesis presents an optimal design framework for the structural design of laminated composite beams. The possibility of improving the static and dynamic performance of laminated composite beam through the use of optimal design techniques motivates the investigation presented here.

A structural model for the analysis of laminated composite beams is proposed. The structural analysis is performed in a beam finite element context. The development of a finite element based tool for the analysis of the cross section stiffness properties is described. The resulting beam finite element formulation is able to account for the effects of material anisotropy and inhomogeneity in the global response of the beam. Beam finite element models allow for a significant reduction in problem size and are therefore an efficient alternative in computationally intensive applications like optimization frameworks. Furthermore, the devised beam model is able account for the different levels of anisotropic elastic couplings which depend on the laminate lay-up.

An optimization model based on multi-material topology optimization techniques is described. The design variables represent the volume fractions of the different candidate materials. Existing material interpolation, penalization, and filtering techniques have been extended to accommodate any number of anisotropic materials. The resulting optimization model is suitable for the simultaneous optimization of cross section topology and laminate properties in the optimal design of laminated composite beams.

The devised framework is applied in the optimal design of laminated composite beams with different cross section geometries and subjected to different load cases. Design criteria such as beam stiffness, weight, magnitude of the natural frequencies of vibration, and the position of the cross section shear and mass center, are considered. The proposed optimal design framework can be applied to tailor the static and dynamic properties of laminated composite structures like wind turbine blades.

Resumé (in Danish)

Denne afhandling beskriver en metodik til optimalt design for det strukturelle design af laminerede kompositbjælker. Forskningen der ligger til grund for denne afhandling, er motiveret af muligheden for at forbedre de statiske og dynamiske egenskaber af laminerede kompositbjælker, ved benyttelse af designoptimeringsmetoder.

I afhandlingen præsenteres en strukturel model til analyse af kompositbjælker. Den strukturelle analyse gør brug af bjælkelementer.Udviklingen af et værktøj til tværsnitsanalyse ved hjælp af finit element metoden beskrives. Værktøjet tjener til at bestemme stivhedsegenskaberne af kompositbjælken på grundlag af tværsnit langs med bjælken. Det resulterende bjælkeelement, og dermed dettes statiske og dynamiske opførsel, tager materialets anisotropi og inhomogenitet i regning. Bjælkeelementer tillader en betydelig reduktion i problemstørrelse i sammenligning med andre, mere beregningsintensive, tilgange til strukturelle optimeringsproblemer. Den udviklede bjælkemodel er ydermere i stand til at beskrive de forskellige niveauer af elastisk kobling, som afhænger af den konkrete lamineringsbeskaffenhed.

Afhandlingen beskriver en optimeringsmodel baseret på multimateriale topologioptimering. Designvariablerne repræsenterer volumenandelene af de forskellige kandidatmaterialer. Kendte teknikker til materialeinterpolation, straf og filtrering er udvidet til at omfatte et arbitrært antal anisotrope materialer. Den resulterende optimeringsmodel er egnet til simultan optimering af tværsnitstopologi og laminategenskaber med henblik på det optimale design af laminerede kompositbjælker.

Den udviklede fremgangsmåde anvendes til bestemmelse af optimale designs af laminerde kompositbjælker med forskellige ydergeometrier under forskellige lastbetingelser. Designkriterier så som stivhed, vægt, egensvingningsfrekvenser og positionen af forskydningsspændingscenter og massemidtpunkt behandles. Den fremsatte optimeringsmetodik kan anvendes til at skræddersy de statiske og dynamiske egenskaber af laminerede kompositbjælker så som vindmøllevinger.

Contents

Introduction

The objective of this thesis is to devise a framework for the structural optimization of laminated composite beams.

The optimal design of laminated composite beam structures entails not only the identification of the optimal cross section topology and shape, but also the determination of the optimal laminate properties. Controlling the properties of the laminate it is possible to generate stiffer, stronger, lighter, and therefore more efficient structural design solutions. This motivated the development of the optimal design framework presented in this thesis. The aim is to employ optimal design techniques to tailor the properties of the laminate and ultimately control the static and dynamic structural response of the beam to meet our demands within the physical limitations.

This thesis presents an optimal design framework combining a structural model specific for the structural analysis of beams, and an optimization model which addresses the particular issues entailed in the optimization of laminated composite structures. Results are presented in which the beam cross section topology and laminate properties are simultaneously optimized. The design criteria include the beam stiffness, its weight, the magnitude of its natural frequencies of vibration, and the position of the cross section shear and mass center.

Summary of the thesis

The thesis is organized as follows. **Part 1** of this thesis provides a brief presentation of the theoretical background for much of the work presented in this thesis. This part is organized as follows:

Chapter 1 describes the structural model. The equations of motion of the beam are derived first. The development of the beam finite element model and cross section analysis tool are presented afterwards. Finally, the numerical implementation and validation are briefly described.

Chapter 2 describes on the optimization model. Two different approaches for the optimal design of laminated composite structures are described. The optimal design problem is formulated and the considered objective functions and constraints are described. The sensitivity expressions are presented and the numerical implementation is briefly discussed.

Chapter 3 presents the main conclusions of this work, examines the main contributions, and suggests topics for future research.

Part 2, includes all the publications associated with this thesis. This part consists of the following chapters, each referring to a different publication:

Paper 1 Maximum stiffness and minimum weight optimization of laminated composite beams using continuous fiber angles.

Paper 2 Multi-material topology optimization of laminated composite beam cross sections.

Paper 3 Multi-material topology optimization of laminated composite beams with eigenfrequency constraints.

Paper 4 BECAS - A cross section analysis tool for anisotropic and inhomogeneous sections of arbitrary geometry.

Paper 5 Hydro-elastic analysis and optimization of a composite marine propeller.

Part I

Background

Chapter 1

Structural analysis of beams

A beam is essentially a solid structural element whose geometry presents a certain degree of slenderness such that its length is relatively larger than the cross section dimensions. When working with beam models it is assumed that the geometry of the solid is represented by the geometry of its cross sections and that the beam is represented by the line that goes through the reference points of this sections. The deformation of the beam is represented by the rigid body translations and rotations of the sections. The three-dimensional problem of the analysis of the beam is separated in two parts. The first part concerns the two-dimensional analysis of the cross section properties while the second regards the one-dimensional analysis of the global response of the beam. This separation allows for a reduction in problem size which makes beam models a suitable alternative for computationally intensive applications like optimal design frameworks.

Some assumptions must be observed when working with beam models. It is assumed that the reference line presents a certain degree of continuity. Moreover, the section geometry, when not constant along the length of the beam is restricted to moderate variations. The same holds for the structural properties. Namely, the material properties and applied loads should also vary smoothly along the length of the beam. As a consequence, the resulting displacements, strains and stresses will also present a smooth variation. These geometrical and structural restrictions do not apply in the cross section face along the width and height directions. The cross section geometry can be arbitrarily defined and the materials with distinct mechanical properties may be distributed inhomogeneously in the cross section.

This chapter describes the structural beam model used in this thesis. The beam model is developed in a finite element context. The cross section stiffness and mass properties are estimated using a finite element cross section analysis tool which is able to correctly estimate the effects of material anisotropy and inhomogeneity.

The chapter is organized as follows. Section 1.1 describes the general three dimensional continuum formulation of the beam and the subsequent derivation of the static and dynamic beam finite element equations. The different approaches

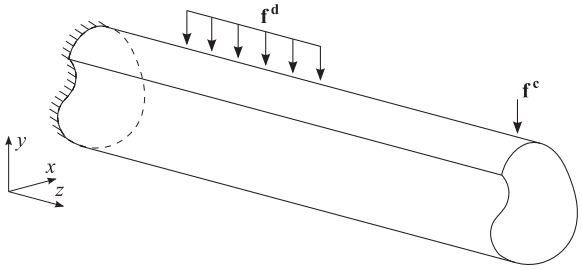

Figure 1.1: General three-dimensional beam.

used in this thesis for the analysis of the cross section stiffness and mass properties are described in Sections 1.2. Finally, the implementation and validation of the beam finite element model and cross section analysis tool is discussed in Section 1.3.

1.1 Beam finite element model

The beam finite element static and dynamic equations are derived in this section. The kinematics of the beam are established first. The static and dynamic equations are derived next based on the principle of virtual work and using standard finite element techniques.

Consider the equilibrium of a three-dimensional beam subjected to the external distributed and concentrated forces $\mathbf{f}^s$ and $\mathbf{f}^c$, respectively (see Figure 1.1). The strains $\boldsymbol{\epsilon}$ and stresses $\boldsymbol{\sigma}$ acting at a point in the beam slice are

$$\boldsymbol{\epsilon} = [\epsilon_{xx}\ \epsilon_{yy}\ 2\epsilon_{xy}\ 2\epsilon_{xz}\ 2\epsilon_{yz}\ \epsilon_{zz}]^T \quad \text{and} \quad \boldsymbol{\sigma} = [\sigma_{xx}\ \sigma_{yy}\ \sigma_{xy}\ \sigma_{xz}\ \sigma_{yz}\ \sigma_{zz}]^T .$$

For linear elastic materials, the stresses and strains are related by the linear constitutive relation

$$\boldsymbol{\sigma} = \mathbf{Q}\boldsymbol{\epsilon} \tag{1.1}$$

where $\mathbf{Q}$ is the 6×6 material constitutive matrix holding the material stiffness properties. The forces $\mathbf{T} = [T_x\ T_y\ T_z]^T$ and moments $\mathbf{M} = [M_x\ M_y\ M_z]^T$ are statically equivalent to the stress components $\mathbf{p} = [\sigma_{xz}\ \sigma_{yz}\ \sigma_{zz}]^T$ acting on the cross section face, and are defined as

$$\mathbf{T} = \int_A \mathbf{p}\ \mathrm{dA}, \quad \mathbf{M} = \int_A \mathbf{n}^T\mathbf{p}\ \mathrm{dA}$$

where A is the cross section area and

$$\mathbf{n} = \begin{bmatrix} 0 & -z & y \\ z & 0 & -x \\ -y & x & 0 \end{bmatrix} \tag{1.2}$$

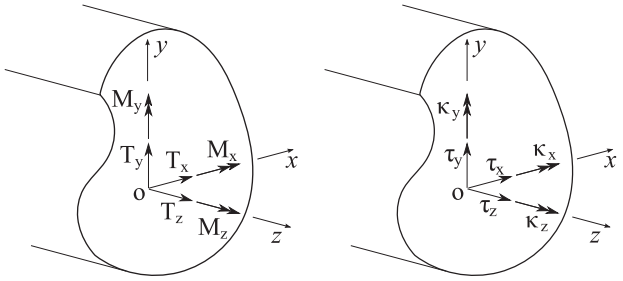

(a) Forces and moments (b) Strains and curvatures

Figure 1.2: Cross section coordinate system, forces and moments (a) and corresponding strains and curvatures (b).

The components of the force vector $\mathbf{T}$ are the transverse forces T_x and T_y and the tension force T_z. The moment vector $\mathbf{M}$ is composed of the bending moment components M_x and M_y, and the torsion moment M_z. The coordinates x and y in the section plane are defined with respect to the cross section reference point O (cf. Figure 1.2(a)). The vector of generalized cross section forces and moments $\boldsymbol{\theta} = \left[\mathbf{T}^T \ \mathbf{M}^T\right]^T$ can be written as

$$\boldsymbol{\theta} = \int_A \mathbf{Z}^T \mathbf{p} \ \mathrm{dA}$$

where the matrix $\mathbf{Z} = \begin{bmatrix}\mathbf{I}_3 & \mathbf{n}^T\end{bmatrix}$, and $\mathbf{I}_3$ is an identity matrix of size 3×3.

In the formulation of structural beam elements, the deformation of the beam is defined by the translations of the cross section reference point $\boldsymbol{\chi} = [\chi_x \ \chi_y \ \chi_z]^T$ and rotations $\boldsymbol{\varphi} = [\varphi_x \ \varphi_y \ \varphi_z]^T$ gathered in vector $\mathbf{r} = \left[\boldsymbol{\chi}^T \ \boldsymbol{\varphi}^T\right]^T$ (cf. Figure 1.3). The cross section strains associated with the displacements $\mathbf{r}$ at a slice dz of the beam are described by the strain-curvature vector $\boldsymbol{\psi} = \left[\boldsymbol{\tau}^T \ \boldsymbol{\kappa}^T\right]^T$ (cf. Figure 1.2(b)). The shear component $\boldsymbol{\tau} = [\tau_x \ \tau_y \ \tau_z]^T$ is composed of the shear strains τ_x and τ_y, and the tension strain τ_z. The components of the vector of curvatures $\boldsymbol{\kappa} = [\kappa_x \ \kappa_y \ \kappa_z]^T$ are the bending curvatures κ_x and κ_y, and the twist rate κ_z. The vector of generalized strains and curvatures $\boldsymbol{\psi}$ is defined in function of the rigid body motions of the cross section, $\mathbf{r}$, as

$$\boldsymbol{\psi} = \widehat{\mathbf{B}}\mathbf{r} \tag{1.3}$$

The strain-displacement operator $\widehat{\mathbf{B}}$ is defined as (cf. Giavotto et al. [6])

$$\widehat{\mathbf{B}} = \left(\mathbf{T}_r + \frac{\partial}{\partial z}\right)$$

where

$$\mathbf{T}_r = \begin{bmatrix} \mathbf{0}_3 & \mathbf{t}_r \\ \mathbf{0}_3 & \mathbf{0}_3 \end{bmatrix}, \quad \mathbf{t}_r = \begin{bmatrix} 0 & -1 & 0 \\ 1 & 0 & 0 \\ 0 & 0 & 0 \end{bmatrix},$$

and $\mathbf{0}_3$ is the 3×3 zero matrix. The resulting strain and curvature components are

$$\tau_x = \frac{\partial \chi_x}{\partial z} - \varphi_y, \quad \tau_y = \frac{\partial \chi_y}{\partial z} + \varphi_x, \quad \tau_z = \frac{\partial \chi_x}{\partial z}$$
$$\kappa_x = \frac{\partial \boldsymbol{\varphi}_x}{\partial z}, \quad \kappa_y = \frac{\partial \boldsymbol{\varphi}_y}{\partial z}, \quad \kappa_z = \frac{\partial \boldsymbol{\varphi}_z}{\partial z}$$

This result can be obtained from static considerations following basic beam theory (see, e.g., Bathe [20]).

For linear elastic beams the cross section generalized strains and curvatures $\boldsymbol{\psi}$ are related to the vector of generalized forces and moments $\boldsymbol{\theta}$ through the following linear constitutive relation

$$\boldsymbol{\theta} = \mathbf{K}_s \boldsymbol{\psi}. \tag{1.4}$$

The matrix $\mathbf{K}_s$ is the 6×6 cross section stiffness matrix. In its most general form (considering, e.g., anisotropic and inhomogeneous sections of arbitrary geometry) $\mathbf{K}_s$ may be fully populated and its 21 stiffness parameters will have to be determined to fully describe the deformation of a slice dz of the beam. The determination of the entries of $\mathbf{K}_s$ is discussed in Section 1.2.

1.1.1 The virtual work equation

The equilibrium equations for a general three dimensional beam can be derived using the principle of virtual displacements. The principle states that "*the equilibrium of the body requires that for any compatible, small virtual displacements (which satisfy the essential boundary conditions) imposed onto the body, the total internal virtual work is equal to the total external virtual work*" (cf. Bathe [20]). Hence, for a linearly elastic beam the equilibrium can be stated as

$$\int_0^L \delta \boldsymbol{\psi}^T \boldsymbol{\theta} \ \mathrm{dz} = \int_0^L \delta \mathbf{r}^T \mathbf{f}^{\mathrm{s}} \ \mathrm{dz} + \delta \mathbf{r}^T \mathbf{f}^{\mathrm{c}} \tag{1.5}$$

where δ is the virtual operator and z is the direction along the beam length. The term on the left-hand side represents the work done by the generalized forces and moments in $\boldsymbol{\theta}$ going through the virtual strains and curvatures in $\delta\boldsymbol{\psi}$. The terms on the right-hand side represent the work done by the distributed and concentrated load $\mathbf{f}^{\mathrm{s}}$ and $\mathbf{f}^{\mathrm{c}}$, respectively, going through the virtual translations and rotations in $\delta\mathbf{r}$.

1.1.2 Finite element discretization

Following the typical finite element approach, we assume that the beam reference line is approximated by an assemblage of discrete beam finite elements interconnected at the end nodes (as schematically described in Figure 1.4). The

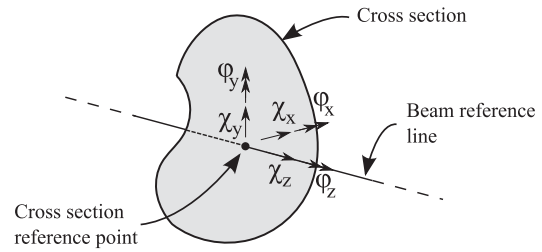

Figure 1.3: Schematic representation of the cross section reference point and beam reference line. Definition of the cross section rigid body motions.

translations and rotations in $\mathbf{r}$ at element b are approximated as

$$\mathbf{r}(z) \approx \widehat{\mathbf{N}}_b(z)\widehat{\mathbf{u}}_b \tag{1.6}$$

where $\widehat{\mathbf{N}}_b(z)$ is the matrix of interpolation functions and $\widehat{\mathbf{u}}$ is the vector of translational and rotational nodal degrees of freedom. The strains at element b can be described in terms of the nodal degrees of freedom in $\widehat{\mathbf{u}}_b$ by inserting (1.6) in (1.3) to obtain

$$\boldsymbol{\psi}_b = \widehat{\mathbf{B}}\widehat{\mathbf{N}}_b\widehat{\mathbf{u}}_b \tag{1.7}$$

1.1.3 Static equilibrium

The beam static equilibrium equations are presented in this section. Inserting the discretized form of the strain-displacement relation in (1.7) into (1.5) and observing the material constitutive relation in (1.4), yields

$$\delta\widehat{\mathbf{u}}^T \left[\sum_{b=1}^{n_b} \int_0^{L_b} \widehat{\mathbf{N}}_b^T \widehat{\mathbf{B}}^T \mathbf{K}_s \widehat{\mathbf{B}}\widehat{\mathbf{N}}_b \, \mathrm{dz}\right] \widehat{\mathbf{u}} = \delta\widehat{\mathbf{u}}^T \left[\sum_{b=1}^{n_b} \int_0^{L_b} \widehat{\mathbf{N}}_b^T \mathbf{f}^s \, \mathrm{dz} + \mathbf{f}^c\right]$$

where L_b is the length of element b and n_b is the total number of beam finite elements. The summation in the expression above refers to the typical assembly procedure from finite element analysis. The nodal degrees of freedom $\widehat{\mathbf{u}}$ are independent of the element considered and have therefore been moved out of the summation signs. Furthermore, note that $\mathbf{f}^c$ is the vector of concentrated loads whose non-zero components are associated with the corresponding degrees of freedom of the displacement vector $\widehat{\mathbf{u}}$. The shape function in $\widehat{\mathbf{N}}$ corresponding to these entries in the displacement vector is defined such that its value is equal to unity at the node and zero elsewhere. Thus, $\widehat{\mathbf{N}}$ can be set to unity in the term corresponding to the concentrated load. The principle of virtual displacement is invoked by imposing that $\delta\widehat{\mathbf{u}}^T = \mathbf{I}$ which corresponds to setting each of the displacement components to unity in turn. The finite element form of the beam

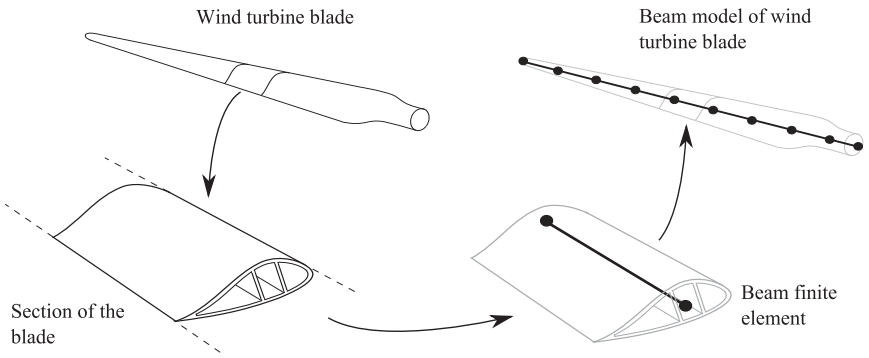

Figure 1.4: Schematic description of the generation of the beam finite element model of a wind turbine blade. The blade reference line is discretized using beam finite elements.

equilibrium equations is finally obtained and written as

$$\sum_{b=1}^{n_b} \int_0^{L_b} \widehat{\mathbf{N}}_b^T \widehat{\mathbf{B}}^T \mathbf{K}_s \widehat{\mathbf{B}} \widehat{\mathbf{N}}_b \, \mathrm{dz} \, \widehat{\mathbf{u}} = \sum_{b=1}^{n_b} \int_0^{L_b} \widehat{\mathbf{N}}_b^T \mathbf{f}^s \, \mathrm{dz} + \mathbf{f}^c \tag{1.8}$$

The beam finite element stiffness matrix $\widehat{\mathbf{K}}_b$ is obtained from the expression above and defined as

$$\widehat{\mathbf{K}}_b = \int_0^{L_b} \widehat{\mathbf{N}}_b^T \widehat{\mathbf{B}}^T \mathbf{K}_s \widehat{\mathbf{B}} \widehat{\mathbf{N}}_b \, \mathrm{dz}$$

The global stiffness matrix of the beam model, $\widehat{\mathbf{K}}$, is obtained following the typical finite element assembly procedures and given by

$$\widehat{\mathbf{K}} = \sum_{b=1}^{n_b} \widehat{\mathbf{K}}_b \tag{1.9}$$

The global load vector $\widehat{\mathbf{f}}$ is defined as

$$\widehat{\mathbf{f}} = \sum_{b=1}^{n_b} \int_0^{L_b} \widehat{\mathbf{N}}_b^T \mathbf{f}^s \, \mathrm{dz} \; + \mathbf{f}^c$$

Thus, the beam equilibrium equations in compact form can be written as

$$\widehat{\mathbf{K}} \widehat{\mathbf{u}} = \widehat{\mathbf{f}} \tag{1.10}$$

The linear system of equations above yields the nodal translations and rotations in $\widehat{\mathbf{u}}$ for a beam subject to the static load $\widehat{\mathbf{f}}$.

This concludes the derivation of the beam finite element equilibrium equations considering static loading. The practical implementation of the beam finite element model entails a suitable choice of the interpolation functions in $\widehat{\mathbf{N}}$ (see Section 1.3) and the determination of the stiffness parameters in $\mathbf{K}_s$ (see Section 1.2).

1.1.4 Dynamic equations

The equations of motion for an undamped system are derived in this section. The aim is to establish the equations for the analysis of the natural frequencies of vibration and associated vibration modes of a given beam finite element assemblage. Hence, the static equilibrium equations in (1.8) are extended to account for inertia effects. The inertia forces can be subtracted from the term associated with the distributed forces $\mathbf{f}^s$ (cf. Bathe [20]). First, assume that the accelerations $\ddot{\widehat{\mathbf{u}}}_b$ are approximated using the same interpolations functions as for the displacements in (1.6) yielding

$$\ddot{\mathbf{r}}(z) \approx \widehat{\mathbf{N}}_b(z)\ddot{\widehat{\mathbf{u}}}_b$$

The $\dot{(\,)}$ notation refers to the time derivative $\partial/\partial t$. Next, (1.8) is re-written to include the inertia forces as

$$\sum_{b=1}^{n_b}\int_0^{L_b}\widehat{\mathbf{N}}_b^T\widehat{\mathbf{B}}^T\mathbf{K}_s\widehat{\mathbf{B}}\widehat{\mathbf{N}}_b\ \mathrm{dz}\ \widehat{\mathbf{u}} = \sum_{b=1}^{n_b}\int_0^{L_b}\widehat{\mathbf{N}}_b^T\left[\mathbf{f}^d - \mathbf{M}_s\widehat{\mathbf{N}}_b\ddot{\widehat{\mathbf{u}}}_b\right]\ \mathrm{dz}\ + \mathbf{f}^c$$

where $\mathbf{M}_s$ is the cross section mass matrix, and $\mathbf{f}^d$ is obtained from the distributed load vector $\mathbf{f}^s$ after subtracting the inertia forces. Rearranging the expression above yields

$$\sum_{b=1}^{n_b}\left[\widehat{\mathbf{M}}_b\ddot{\widehat{\mathbf{u}}} + \widehat{\mathbf{K}}_b\widehat{\mathbf{u}}\right] = \sum_{b=1}^{n_b}\int_0^{L_b}\widehat{\mathbf{N}}_b^T\mathbf{f}^s\ \mathrm{dz}\ + \mathbf{f}^c$$

where

$$\widehat{\mathbf{M}}_b = \int_0^{L_b}\widehat{\mathbf{N}}_b^T\mathbf{M}_s\widehat{\mathbf{N}}_b\ \mathrm{dz}$$

is the consistent form of the beam finite element mass matrix. The mass matrix for the global finite element assemblage is

$$\widehat{\mathbf{M}} = \sum_{b=1}^{\widehat{n}_b}\widehat{\mathbf{M}}_b \tag{1.11}$$

The equations of motion of the beam neglecting damping are given in matrix form as

$$\widehat{\mathbf{M}}\ddot{\widehat{\mathbf{u}}} + \widehat{\mathbf{K}}\widehat{\mathbf{u}} = \widehat{\mathbf{f}}$$

For the analysis of the natural frequencies of vibration and associated modes assuming no damping and null static loads (i.e., free vibrations) the following set of differential equations is obtained

$$\widehat{\mathbf{M}}\ddot{\widehat{\mathbf{u}}} + \widehat{\mathbf{K}}\widehat{\mathbf{u}} = \mathbf{0} \tag{1.12}$$

The set of equations above can be solved assuming solutions of the type

$$\widehat{\mathbf{u}} = \widehat{\mathbf{v}} e^{i\omega t}, \quad \ddot{\widehat{\mathbf{u}}} = -\omega^2 \widehat{\mathbf{v}} e^{i\omega t}. \tag{1.13}$$

Inserting (1.13) in (1.12) and since $e^{i\omega t}$ cannot be zero, gives

$$\left(-\omega^2 \widehat{\mathbf{M}} + \widehat{\mathbf{K}}\right) \widehat{\mathbf{v}} = 0 \tag{1.14}$$

The solution to the structural eigenvalue problem above yields the natural vibration frequencies $\boldsymbol{\omega} = \{\omega_1, ..., \omega_{n_u}\}$ and corresponding vibration modes $\widehat{\mathbf{V}} = \{\widehat{\mathbf{v}}_1, ..., \widehat{\mathbf{v}}_{n_u}\}$ for a given beam finite element assemblage, where n_u is the number of degrees of freedom in $\widehat{\mathbf{u}}$.

This concludes the derivation of the equations leading to the structural eigenvalue problem for a beam finite element assemblage. The determination of the natural vibration frequencies and corresponding modes reduces to the evaluation of the cross section mass matrix $\mathbf{M}_s$ necessary for the computation of the beam finite element mass matrix $\widehat{\mathbf{M}}$. The determination of the parameters in $\mathbf{M}_s$ is described in Section 1.2.3.

1.2 Cross section analysis

Most of the effort in the construction of sufficiently general beam models involves the correct assessment of the cross section properties. Hodges [5] has presented a comprehensive and thorough historical overview of the developments in the beam modeling field. Furthermore, Jung et al. [1] and Volovoi et al. [2] present an assessment of the different cross section analysis formulations and include comparative results which highlight the advantages and limitations of each. Two different approaches have been considered in this thesis for the evaluation of the cross section stiffness matrix $\mathbf{K}_s$:

- The BEam Cross section Analysis Software – BECAS,
- The Variational Asymptotical Beam Sectional analysis tool – VABS.

The theory underlying the development of BECAS is described in Paper 4 and employed within the optimal design framework in Papers 2 and 3. BECAS is described next, in Section 1.2.1. VABS has been used in Paper 1 and a brief description is presented in Section 1.2.2.

1.2.1 BECAS – BEam Cross section Analysis Software

A brief account of the theory underlying the BEam Cross section Analysis Software – BECAS – is presented in this section (see Paper 4 for further details). BECAS is a cross section analysis tool for the determination of the cross section stiffness parameters in $\mathbf{K}_s$. The underlying formulation was originally presented by Giavotto et al. [6]. BECAS is a finite element based tool suitable for the analysis of

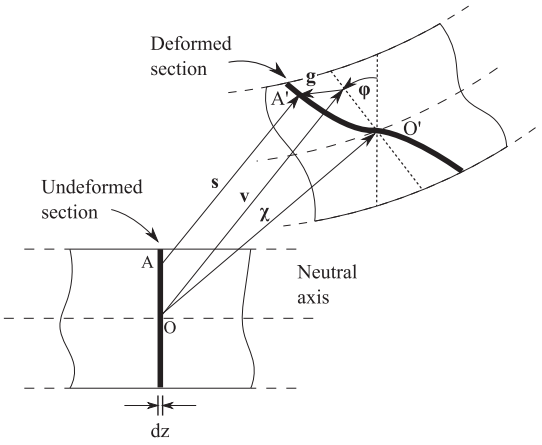

Figure 1.5: Total displacement **s** of a point in the cross section. The displacement is composed of a translation $\boldsymbol{\chi}$, a rotation $\boldsymbol{\varphi}$, and a warping displacement **g**.

laminated composite beam cross sections of arbitrary geometry and can correctly account for the effects stemming from material anisotropy and inhomogeneity.

1.2.1.1 Kinematics

Assume that the displacement $\mathbf{s} = [s_x \; s_y \; s_z]^T$ of a point in the cross section is given by (cf. Figure 1.5)

$$\mathbf{s} = \mathbf{v} + \mathbf{g}$$

The displacement components $\mathbf{v} = [v_x \; v_y \; v_z]^T$ are associated with the rigid body translations and rotations of the cross section. The warping displacements $\mathbf{g} = [g_x \; g_y \; g_z]^T$ are associated with the in- and out-of-plane cross section distortion. Assuming small displacements and rotations,

$$\mathbf{v} = \mathbf{Z}\mathbf{r}$$

where the components of **r** are the translations and rotations of the cross section as defined in Section 1.1. The expression for the total displacement is then given as

$$\mathbf{s} = \mathbf{Z}\mathbf{r} + \mathbf{g} \tag{1.15}$$

Assuming small strains, the strain components at a point in the cross section are defined as

$$\epsilon_{\alpha\beta} = \frac{1}{2}\left(\frac{\partial s_\alpha}{\partial \beta} + \frac{\partial s_\beta}{\partial \alpha}\right), \qquad (\alpha, \beta = x, y, z) \tag{1.16}$$

Inserting (1.15) into the expression above yields

$$\boldsymbol{\epsilon} = \mathbf{SZ}\boldsymbol{\psi} + \mathbf{Bg} + \mathbf{S}\frac{\partial \mathbf{g}}{\partial z}$$

where the terms have been conveniently arranged so that the local strains $\boldsymbol{\epsilon}$ are expressed in function of the generalized strains and curvatures $\boldsymbol{\psi}$. The strain-displacement operators, $\mathbf{B}$ and $\mathbf{S}$, are defined as

$$\mathbf{B} = \begin{bmatrix} \partial/\partial x & 0 & 0 \\ 0 & \partial/\partial y & 0 \\ \partial/\partial y & \partial/\partial x & 0 \\ 0 & 0 & \partial/\partial x \\ 0 & 0 & \partial/\partial y \\ 0 & 0 & 0 \end{bmatrix} \quad , \quad \mathbf{S} = \begin{bmatrix} 0 & 0 & 0 \\ 0 & 0 & 0 \\ 0 & 0 & 0 \\ 1 & 0 & 0 \\ 0 & 1 & 0 \\ 0 & 0 & 1 \end{bmatrix}$$

The strain-displacement operators $\mathbf{B}$ and $\mathbf{S}$ are recognizable from typical solid finite element formulations (see, e.g., Bathe [20]). The difference is in this case the components yielding the partial derivatives along the length direction, $\partial/\partial z$, have been left unsolved. The aim is to determine the stiffness properties of the beam slice first and perform the integration along the length afterwards at the beam finite element level.

1.2.1.2 Finite element formulation

Following the typical finite element procedure, assume that the cross section is discretized using two-dimensional finite elements. The three dimensional warping displacements in $\mathbf{g}$ are determined by interpolation of the nodal values and given by

$$\mathbf{g}(x, y) \approx \mathbf{N}_e(x, y)\mathbf{u}_e \tag{1.17}$$

where $\mathbf{N}_e$ is the matrix of interpolation functions and $\mathbf{u}_e$ are the nodal warping displacements at element e of the cross section mesh. The discretized form of the total displacement is obtained by inserting (1.17) into (1.15) yielding

$$\mathbf{s} = \mathbf{Zr} + \mathbf{Nu} \tag{1.18}$$

Inserting (1.18) into (1.16) yields the finite element form of three dimensional strain field

$$\boldsymbol{\epsilon} = \mathbf{SZ}\boldsymbol{\psi} + \mathbf{BNu} + \mathbf{SN}\frac{\partial \mathbf{u}}{\partial z} \tag{1.19}$$

1.2.1.3 Virtual displacement equations

The principle of virtual displacements is subsequently invoked in the derivation of the finite element form of the cross section equilibrium equations. The internal energy per unit length $\partial W_{int}/\partial z$ is defined as the internal virtual work done by

the stresses $\boldsymbol{\sigma}$ going through the virtual strains $\delta\boldsymbol{\epsilon}$. Hence, observing the material constitutive relation in (1.1) and the finite element form of the strain-displacement relation in (1.19), the following is obtained

$$\frac{\partial W_{int}}{\partial z} = \int_A \delta\boldsymbol{\epsilon}^T \boldsymbol{\sigma} \; \mathrm{dA} = \begin{bmatrix} \delta\mathbf{u} \\ \delta\boldsymbol{\psi} \\ \delta\frac{\partial \mathbf{u}}{\partial z} \end{bmatrix}^T \begin{bmatrix} \mathbf{E} & \mathbf{R} & \mathbf{C} \\ \mathbf{R}^T & \mathbf{A} & \mathbf{L} \\ \mathbf{C}^T & \mathbf{L}^T & \mathbf{M} \end{bmatrix} \begin{bmatrix} \mathbf{u} \\ \boldsymbol{\psi} \\ \frac{\partial \mathbf{u}}{\partial z} \end{bmatrix} \tag{1.20}$$

The finite element matrices presented above are defined as

$$\begin{aligned} \underset{(6\times 6)}{\mathbf{A}} &= \sum_{e=1}^{n_e} \int_A \mathbf{Z}_e^T \mathbf{S}_e^T \mathbf{Q}_e \mathbf{S}_e \mathbf{Z}_e \; \mathrm{dA} & \underset{(n_d\times 6)}{\mathbf{R}} &= \sum_{e=1}^{n_e} \int_A \mathbf{N}_e^T \mathbf{B}_e^T \mathbf{Q}_e \mathbf{S}_e \mathbf{Z}_e \; \mathrm{dA} \\ \underset{(n_d\times n_d)}{\mathbf{E}} &= \sum_{e=1}^{n_e} \int_A \mathbf{N}_e^T \mathbf{B}_e^T \mathbf{Q}_e \mathbf{B}_e \mathbf{N}_e \; \mathrm{dA} & \underset{(n_d\times n_d)}{\mathbf{C}} &= \sum_{e=1}^{n_e} \int_A \mathbf{N}_e^T \mathbf{B}_e^T \mathbf{Q}_e \mathbf{S}_e \mathbf{N}_e \; \mathrm{dA} \\ \underset{(6\times n_d)}{\mathbf{L}} &= \sum_{e=1}^{n_e} \int_A \mathbf{Z}_e^T \mathbf{S}_e^T \mathbf{Q}_e \mathbf{S}_e \mathbf{N}_e \; \mathrm{dA} & \underset{(n_d\times n_d)}{\mathbf{M}} &= \sum_{e=1}^{n_e} \int_A \mathbf{N}_e^T \mathbf{S}_e^T \mathbf{Q}_e \mathbf{S}_e \mathbf{N}_e \; \mathrm{dA} \end{aligned} \tag{1.21}$$

where e is the element number and n_e is the number of finite elements in the cross section mesh. The total number of degrees of freedom associated with the cross section finite element mesh is $n_d = n_n \times 3$ where the number of nodes n_n multiplies the number of degrees of freedom at each node – the three dimensional nodal displacements u_x, u_y and u_z. The sums in (1.21) refer to the typical assembly procedure used in finite element analysis. The geometry of the cross section is defined by the finite element discretization. The material properties are defined at each element by the three-dimensional material constitutive matrix $\mathbf{Q}_e$. The material may be anisotropic and the cross section may be composed of different materials inhomogeneously distributed therein. As will be seen, the design variables of the optimization models described in Chapter 2 act on the material constitutive matrix $\mathbf{Q}_e$.

The total external virtual work per unit length, $\partial W_{ext}/\partial z$, is associated with the work done by the stresses in $\mathbf{p}$ going through the virtual displacements $\delta\mathbf{s}$. Thus, based on the expression in (1.18) for the total displacement of a point, the external virtual work is

$$\frac{\partial W_{ext}}{\partial z} = \int_A \frac{\partial \left(\delta\mathbf{s}^T\mathbf{p}\right)}{\partial z} \; \mathrm{dA} = \begin{bmatrix} \delta\frac{\partial \mathbf{u}^T}{\partial z} \\ \delta\mathbf{u} \\ \delta\boldsymbol{\psi} \end{bmatrix}^T \begin{bmatrix} \mathbf{P} \\ \frac{\partial \mathbf{P}}{\partial z} \\ \boldsymbol{\theta} \end{bmatrix} + \delta\mathbf{r}^T \left(\frac{\partial \boldsymbol{\theta}}{\partial z} - \mathbf{T}_r^T \boldsymbol{\theta} \right) \tag{1.22}$$

where

$$\mathbf{P} = \int_A \mathbf{N}^T \mathbf{p} \; \mathrm{dA}, \quad \frac{\partial \mathbf{P}}{\partial z} = \int_A \mathbf{N}^T \frac{\partial \mathbf{p}}{\partial z} \; \mathrm{dA}$$

The components of vector $\mathbf{P}$ are the nodal stresses acting on the cross section finite element discretization.

At equilibrium the work performed by the internal forces in (1.20) has to balance the work done by the external forces in (1.22). Furthermore, from the

principle of virtual work, the result must be valid for any admissible virtual displacements – $\delta\boldsymbol{\psi}$, $\delta\mathbf{u}$, $\delta\frac{\partial\mathbf{u}^T}{\partial z}$ and $\delta\mathbf{r}$. Hence, the following set of second order linear differential equations is obtained

$$\begin{cases} \mathbf{M}\frac{\partial^2\mathbf{u}}{\partial z^2} + \left(\mathbf{C} - \mathbf{C}^T\right)\frac{\partial\mathbf{u}}{\partial z} + \mathbf{L}\frac{\partial\boldsymbol{\psi}}{\partial z} - \mathbf{E}\mathbf{u} - \mathbf{R}\boldsymbol{\psi} = \mathbf{0} \\ \mathbf{L}^T\frac{\partial\mathbf{u}}{\partial z} + \mathbf{R}^T\mathbf{u} + \mathbf{A}\boldsymbol{\psi} = \boldsymbol{\theta} \\ \frac{\partial\boldsymbol{\theta}}{\partial z} = \mathbf{T}_r^T\boldsymbol{\theta} \end{cases} \tag{1.23}$$

1.2.1.4 Cross section equilibrium equations

The set of second order linear differential equations in (1.23) yields a homogeneous and a particular solution or, *extremity* and *central* solutions, respectively, as originally coined by Giavotto et al. [6]. The homogeneous or *extremity* solutions are obtained for $\boldsymbol{\theta} = \mathbf{0}$ which corresponds to the case where the stresses in the cross section face are null. This solution is associated with the deformation at the ends or extremities of the beam and will not be the subject of further discussion in this thesis. The particular or *central* solution yields the deformation field at the central part of the beam. This solution serves as the basis for the derivation of the cross section stiffness matrix $\mathbf{K}_s$.

Before proceeding with the derivation of the cross section equilibrium equations note that the displacement definition presented in (1.15) is redundant. The six rigid body motions represented in $\mathbf{r}$ can also be replicated by the warping displacements in $\mathbf{u}$. In order to overcome this issue a set of six constraint equations is introduced to remove the rigid body modes from the warping displacements $\mathbf{u}$. The six constraints are

$$\sum_{n=1}^{n_n} u_{x,n} = 0, \quad \sum_{n=1}^{n_n} u_{y,n} = 0, \quad \sum_{n=1}^{n_n} u_{z,n} = 0,$$

$$\sum_{n=1}^{n_n} -z_n u_{y,n} + y_n u_{z,n} = 0, \quad \sum_{n=1}^{n_n} z_n u_{x,n} - x_n u_{z,n} = 0, \quad \sum_{n=1}^{n_n} -y_n u_{x,n} + x_n u_{y,n} = 0,$$

where (x_n, y_n, z_n) and $(u_{x,n}, u_{y,n}, u_{z,n})$ are the position and displacement of node n, respectively. The constraints are imposed on both the displacements $\mathbf{u}$ and corresponding derivatives $\partial\mathbf{u}/\partial z$ and can be written in matrix form as

$$\begin{bmatrix} \mathbf{D}^T & \mathbf{0} \\ \mathbf{0} & \mathbf{D}^T \end{bmatrix} \begin{bmatrix} \mathbf{u} \\ \frac{\partial\mathbf{u}}{\partial z} \end{bmatrix} = \begin{bmatrix} \mathbf{0} \\ \mathbf{0} \end{bmatrix}, \text{ where } \mathbf{D} = \begin{bmatrix} \mathbf{I}_3 & \dots & \mathbf{I}_3 \\ \mathbf{n}_1 & \dots & \mathbf{n}_{n_n} \end{bmatrix}^T \tag{1.24}$$

where $\mathbf{I}_3$ is the 3×3 identity matrix, and $\mathbf{n}_n$ is obtained from replacing the nodal coordinates (x_n, y_n, z_n) of node n in (1.2).

The cross section equilibrium equations are obtained from (1.23) after some manipulation (see Paper 4) and finally given as

$$\mathbf{K}\mathbf{w} = \mathbf{f} \Leftrightarrow \begin{bmatrix} \mathbf{K}_{11} & \mathbf{K}_{12} \\ \mathbf{0} & \mathbf{K}_{11} \end{bmatrix} \begin{bmatrix} \mathbf{w}_1 \\ \mathbf{w}_2 \end{bmatrix} = \begin{bmatrix} \mathbf{f}_1 \\ \mathbf{f}_2 \end{bmatrix} \tag{1.25}$$

where

$$\mathbf{K}_{11} = \begin{bmatrix} \mathbf{E} & \mathbf{R} & \mathbf{D} \\ \mathbf{R}^T & \mathbf{A} & \mathbf{0} \\ \mathbf{D}^T & \mathbf{0} & \mathbf{0} \end{bmatrix}, \; \mathbf{K}_{12} = \begin{bmatrix} (\mathbf{C}^T - \mathbf{C}) & -\mathbf{L} & \mathbf{0} \\ \mathbf{L}^T & \mathbf{0} & \mathbf{0} \\ \mathbf{0} & \mathbf{0} & \mathbf{0} \end{bmatrix} \tag{1.26}$$

and, $\mathbf{w}_1 = \begin{bmatrix} \mathbf{u}^T \; \boldsymbol{\psi}^T \; \boldsymbol{\lambda}_1^T \; \end{bmatrix}^T$, $\mathbf{w}_2 = \begin{bmatrix} \partial\mathbf{u}^T/\partial z \; \partial\boldsymbol{\psi}^T/\partial z \; \boldsymbol{\lambda}_2^T \end{bmatrix}^T$, $\mathbf{f}_1 = \begin{bmatrix} \mathbf{0}^T \; \boldsymbol{\theta}^T \; \mathbf{0}^T \; \end{bmatrix}^T$, and $\mathbf{f}_2 = \begin{bmatrix} \mathbf{0}^T \; (\mathbf{T}_r^T\boldsymbol{\theta})^T \; \mathbf{0}^T \end{bmatrix}^T$. The vectors of Lagrange multipliers $\boldsymbol{\lambda}_1$ and $\boldsymbol{\lambda}_2$, are associated with the constraints (1.24) imposed on $\mathbf{u}$ and $\partial\mathbf{u}/\partial z$, respectively.

The set of linear equations in (1.25) allows for the determination of the generalized strains $\boldsymbol{\psi}$ and warping displacements $\mathbf{u}$ for a cross section subjected to a given set of generalized forces $\boldsymbol{\theta}$. This concludes the derivation of the cross section equilibrium equations. The next step consists of the determination of the cross section stiffness parameters or the entries of matrix $\mathbf{K}_s$.

1.2.1.5 Cross section stiffness matrix

Consider the case where each entry of $\boldsymbol{\theta}$ is set to unity in turn and (1.25) is solved sequentially for each value of $\boldsymbol{\theta}$. This corresponds to replacing $\boldsymbol{\theta}$ in (1.25) by the 6×6 identity matrix $\mathbf{I}_6$ thus yielding

$$\mathbf{KW} = \mathbf{F} \Leftrightarrow \begin{bmatrix} \mathbf{K}_{11} & \mathbf{K}_{12} \\ \mathbf{0} & \mathbf{K}_{11} \end{bmatrix} \begin{bmatrix} \mathbf{W}_1 \\ \mathbf{W}_2 \end{bmatrix} = \begin{bmatrix} \mathbf{F}_1 \\ \mathbf{F}_2 \end{bmatrix} \tag{1.27}$$

where $\mathbf{W}_1 = \begin{bmatrix} \mathbf{U}^T \; \boldsymbol{\Psi}^T \; \boldsymbol{\Lambda}_1^T \; \end{bmatrix}^T$, $\mathbf{W}_2 = \begin{bmatrix} \partial\mathbf{U}^T/\partial z \; \partial\boldsymbol{\Psi}^T/\partial z \; \boldsymbol{\Lambda}_2^T \end{bmatrix}^T$, $\mathbf{F}_1 = \begin{bmatrix} \mathbf{0}^T \; \mathbf{I}_6 \; \mathbf{0}^T \; \end{bmatrix}^T$, and $\mathbf{F}_2 = \begin{bmatrix} \mathbf{0}^T \; \mathbf{T}_r \; \mathbf{0}^T \end{bmatrix}^T$. The resulting solution matrices $\mathbf{U}$, $\partial\mathbf{U}/\partial z$, $\boldsymbol{\Psi}$ and $\partial\boldsymbol{\Psi}/\partial z$ have six columns each corresponding to each of the right-hand sides associated with a different vector $\boldsymbol{\theta}$. The determination of the solutions to (1.25) reduces to the evaluation of the following matrix-vector products

$$\mathbf{u} = \mathbf{U}\boldsymbol{\theta}, \qquad \frac{\partial\mathbf{u}}{\partial z} = \frac{\partial\mathbf{U}}{\partial z}\boldsymbol{\theta}, \qquad \boldsymbol{\psi} = \boldsymbol{\Psi}\boldsymbol{\theta}, \qquad \frac{\partial\boldsymbol{\psi}}{\partial z} = \frac{\partial\boldsymbol{\Psi}}{\partial z}\boldsymbol{\theta} \tag{1.28}$$

Furthermore, it is assumed that the relation between the generalized strains and forces acting on the cross section is linear. In this case the internal energy is equal to the complementary energy. Hence, the following holds

$$\delta\boldsymbol{\theta}^T\mathbf{F}_s\boldsymbol{\theta} = \int_A \delta\boldsymbol{\epsilon}^T\boldsymbol{\sigma} \; \mathrm{dA}$$

where the left-hand term is the complementary form of the internal elastic energy presented in the right-hand term. Inserting the expressions in (1.28) into the internal elastic energy expression in (1.20) and inserting the result into the equation above yields

$$\delta\boldsymbol{\theta}\mathbf{F}_s\boldsymbol{\theta} = \delta\boldsymbol{\theta}^T \begin{bmatrix} \mathbf{W}_1 \\ \mathbf{W}_2 \end{bmatrix}^T \begin{bmatrix} \mathbf{G}_{11} & \mathbf{G}_{12} \\ \mathbf{G}_{12}^T & \mathbf{G}_{22} \end{bmatrix} \begin{bmatrix} \mathbf{W}_1 \\ \mathbf{W}_2 \end{bmatrix} \boldsymbol{\theta} = \delta\boldsymbol{\theta}^T\mathbf{W}^T\mathbf{G}\mathbf{W}\boldsymbol{\theta} \tag{1.29}$$

where

$$\mathbf{G}_{11} = \begin{bmatrix} \mathbf{E} & \mathbf{R} & \mathbf{0} \\ \mathbf{R}^T & \mathbf{A} & \mathbf{0} \\ \mathbf{0} & \mathbf{0} & \mathbf{0} \end{bmatrix}, \mathbf{G}_{12} = \begin{bmatrix} \mathbf{C} & \mathbf{0} & \mathbf{0} \\ \mathbf{L} & \mathbf{0} & \mathbf{0} \\ \mathbf{0} & \mathbf{0} & \mathbf{0} \end{bmatrix}, \mathbf{G}_{22} = \begin{bmatrix} \mathbf{M} & \mathbf{0} & \mathbf{0} \\ \mathbf{0} & \mathbf{0} & \mathbf{0} \\ \mathbf{0} & \mathbf{0} & \mathbf{0} \end{bmatrix}$$

An expression for the cross section compliance matrix $\mathbf{F}_s$ is then readily obtained as

$$\mathbf{F}_s = \mathbf{W}^T \mathbf{G} \mathbf{W} \tag{1.30}$$

In all cases considered in this thesis $\mathbf{F}_s$ is symmetric positive definite and thus the cross section stiffness matrix is determined through $\mathbf{K}_s = \mathbf{F}_s^{-1}$.

This concludes the derivation of the cross section stiffness parameters. In practice, the determination of $\mathbf{K}_s$ entails first the assembly of the matrices in (1.21). The next step concerns the assembly of $\mathbf{K}$ and the solution to the linear system of equations in (1.27). The last step entails the assembly of $\mathbf{G}$ and the determination of $\mathbf{F}_s$ in (1.30).

Note that the result in (1.28) is specially convenient for the analysis of the three-dimensional strains acting on the cross section in cases where the geometry and structural properties of the section remain constant while the forces and moments vary (e.g., codes for the aeroelastic analysis of wind turbine blades). The distribution along the length of the beam of the forces $\mathbf{T}$ and moments $\mathbf{M}$ in $\boldsymbol{\theta}$ can be determined from the global response of the beam finite element model. The strains at a given cross section are then determined by inserting the corresponding $\boldsymbol{\theta}$ in (1.28) and inserting the result into (1.19). In this case, the solution vectors to (1.27) can be determined once and reused each time the strains are evaluated. The alternative is computationally far more expensive as it consists of solving the cross section equilibrium equations in (1.25) for each $\boldsymbol{\theta}$.

1.2.1.6 Shear and tension center positions

The cross section shear center $\mathbf{s}_c = (x_s, y_s)$ is defined as the point at which the application of a transverse force will induce no twist. It is obtained through the evaluation of (cf. Paper 4)

$$\begin{aligned} x_s &= -\frac{F_{s,62} + F_{s,64}(L-z)}{F_{s,66}} \\ y_s &= \frac{F_{s,61} + F_{s,65}(L-z)}{F_{s,66}} \end{aligned} \tag{1.31}$$

where $F_{s,ij}$ is the entry (i,j) of the compliance matrix $\mathbf{F}_s$, and L is the beam length. The tension center $\mathbf{s}_t = (x_t, y_t)$ is defined as the point at which an applied tension load will not induce a bending moment and is determined as (cf. Paper

4)

$$x_t = -\frac{-F_{s,44}F_{s,53} + F_{s,45}F_{s,43}}{F_{s,44}F_{s,55} - F_{s,45}^2}$$
$$y_t = -\frac{F_{s,43}F_{s,55} - F_{s,45}F_{s,53}}{F_{s,44}F_{s,55} - F_{s,45}^2}$$

The analysis of the position of the shear and tension center can give valuable insight into the static and dynamic properties of laminated composite beams. Namely, in the design of wind turbine blades, the relative position of the shear center affects the limit speed for divergence and flutter instabilities (Hansen [28]). The formulation presented in this thesis for the determination of $\mathbf{F}_s$ allows for the accurate evaluation of the position of this reference point.

1.2.2 VABS – Variational Asymptotical Beam Sectional analysis

The Variational Asymptotical Beam Sectional (VABS) analysis tool allows for the determination of the cross section stiffness and mass matrix, $\mathbf{K}_s$ and $\mathbf{M}_s$, respectively. The formulation builds on the Variational Asymptotic Method (VAM) and has been described in detail by Hodges in [5] and validated by Yu and Hodges in [3] and Yu et al. [4]. The code is developed and maintained by Wenbin Yu and co-workers at Utah State University. Although VABS and BECAS are based on a different formulation, the same values of $\mathbf{K}_s$ are obtained (see Paper 4). VABS is distributed as a set of libraries and its source code is not available. As a consequence it is not possible to extend the code to include any modules necessary for the optimal design framework, like the analytical sensitivities of the cross section stiffness matrix.

1.2.3 Cross section mass matrix

The analysis of the cross section mass properties is significantly simpler than the analysis of the cross section stiffness parameters. The 6×6 cross section mass matrix $\mathbf{M}_s$ relates the linear and angular velocities in $\boldsymbol{\phi}$ to the inertial linear and angular momentum in $\boldsymbol{\gamma}$ through $\boldsymbol{\phi} = \mathbf{M}_s\boldsymbol{\gamma}$. The cross section mass matrix is given with respect to the cross section reference point as (cf. Hodges [5])

$$\mathbf{M}_s = \begin{bmatrix} m & 0 & 0 & 0 & 0 & -my_m \\ 0 & m & 0 & 0 & 0 & mx_m \\ 0 & 0 & m & my_m & -mx_m & 0 \\ 0 & 0 & my_m & I_{xx} & -I_{xy} & 0 \\ 0 & 0 & -mx_m & -I_{xy} & I_{yy} & 0 \\ -my_m & mx_m & 0 & 0 & 0 & I_{xx}+I_{yy} \end{bmatrix} \tag{1.32}$$

where m is the mass per unit length of the cross section. The cross section moments of inertia with respect to x and y are given by I_{xx} and I_{yy}, respectively,

while I_{xy} is the cross section product of inertia. The term $I_{xx} + I_{yy}$ is the polar moment of inertia associated with the torsion of the cross section. The mass and moments of inertia are obtained through integration of the mass properties on the cross section finite element mesh. The off-diagonal terms are associated with the offset between the mass center position $\mathbf{m}_c = (x_c, y_c)$ and the cross section reference point. The position of the mass center $\mathbf{m}_c$ is given as

$$\begin{aligned} x_c &= \left(\sum_{e=1}^{n_e} x_{c_e} v_e \varrho_e \right) / \left(\sum_{e=1}^{n_e} v_e \varrho_e \right) \\ y_c &= \left(\sum_{e=1}^{n_e} y_{c_e} v_e \varrho_e \right) / \left(\sum_{e=1}^{n_e} v_e \varrho_e \right) \end{aligned} \tag{1.33}$$

where (x_{c_e}, y_{c_e}), v_e and ϱ_e are the coordinates of the centroid, the volume and the density of element e, respectively, and n_e is the number of elements in the cross section mesh.

1.3 Implementation and validation

The structural model in Paper 1 is implemented in Fortran using VABS. The structural model in Papers 2 and 3 was implemented in MATLAB®. The beam structural model in Papers 1, 2 and 3 uses three-node quadratic beam finite elements with quadratic interpolation functions. This beam finite element implementation has been validated in Paper 1. The static and dynamic properties of laminated composite beams with different cross sections were validated against equivalent shell and solid finite element models. The results were found to be in very good agreement for all cases tested.

The cross section analysis code BECAS has been implemented in MATLAB®. It is built upon a finite element discretization of the cross sections using two dimensional four node isoparametric finite elements (see Bathe [20]). BECAS makes extensive use of the SuiteSparse libraries by Davis [16], and Davis and Natarajan [15]. Validation results for BECAS have been presented in Paper 4. The cross section stiffness parameters in $\mathbf{K}_s$ estimated by BECAS were validated against results from VABS. The validation results were obtained for solid, open and closed multi-cell cross sections made of isotropic and laminated orthotropic materials. The results were found to be in very good agreement for all cases tested.

Chapter 2

Optimal design of laminated composite structures

Laminated composite materials consist of a stack of laminae or layers. Each layer is composed of a stiff and strong fibrous material (e.g., glass or carbon fibers) binded by a compliant and weak matrix (e.g., Epoxy resin). The mechanical properties of the resulting composite material outstand the properties of the individual constituents. A schematic description of a composite laminate and its constituents is presented in Figure 2.1. The mechanical properties of the laminate depend on the mechanical properties of the constituent materials, the thickness of each of the individual layers, and the overall thickness of the laminate. Moreover, as the fibers are much stiffer along its length than they are in its transverse direction, the stiffness of the laminate depends also on the orientation of the fibers in each layer and its stacking sequence in the laminate. Thus, the optimal design of laminated composite structures should involve not only the optimization of the structural topology and shape but also the optimization of the each of laminate properties listed before.

This chapter describes two different models developed for the optimal design of laminated composite structures. Furthermore, the different objective functions and constraints are presented, and an optimal design problem which illustrates the type of problems considered throughout this thesis is formulated. Finally, the expressions for the gradients or sensitivities of each of the objective functions and constraints are described.

The chapter is organized as follows. Section 2.1 describes the optimization models developed in this thesis. The objective functions, constraints and problem formulation are presented next in Section 2.2. Finally, the expressions for the sensitivities of each of the objective functions and constraints is presented in Section 2.3.

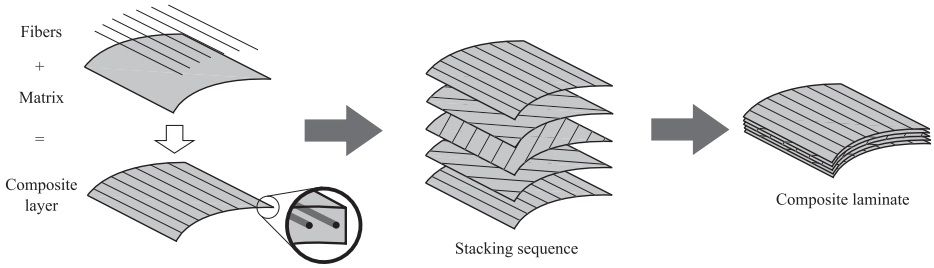

Figure 2.1: Schematic description of a laminate, its constituent layers, and the laminate stacking sequence. A layer is obtained from the assemblage of stiff fibers and a weak matrix (left). Each of the layers is then stacked with the fibers pointing in different directions. The order in which the layers are stacked is called the laminate stacking sequence (center). Finally, the resulting assemblage is called a laminate (right).

2.1 Optimization models

Two optimization models have been considered throughout this thesis. In the first optimization model two groups of design variables are defined representing the fiber orientations at each layer in the laminate and the overall laminate thickness, respectively. This model has been described and implemented in Paper 1 and is briefly described in Section 2.1.1. The second model has been employed in Paper 2 and 3 and is briefly described in Section 2.1.2. The model assumes that the design variables represent the volume fractions or amounts of a predefined set of candidate materials.

2.1.1 Continuous fiber angles and laminate thickness

The model is based on the assumption that at each element in the cross section mesh one type of laminated composite material is chosen from the start. The problem consists then of identifying the optimal orientations of the fibers in the laminate and the total laminate thickness.

Hence, two groups of design variables are considered. The first group is associated with the orientations $\boldsymbol{\alpha} = \{\alpha_p | p \in \{1, ..., n_p\}\}$ of the fibers at each patch p, where n_p is the number of patches in the cross section mesh. A patch is a group of elements in the cross section finite element mesh. It is assumed that the elements in a patch all share the same material properties (see Figure 2.2). The design variables are assumed to vary continuously between their bounds, i.e., $\underline{\alpha} \leq \alpha_p \leq \overline{\alpha}$, $\forall p = 1, ..., n_p$. The upper and lower bound are $\underline{\alpha} = 0°$ and $\overline{\alpha} = 180°$, respectively, where it is assumed that the fiber orientations in $\boldsymbol{\alpha}$ are defined in degrees. Now, assume that a given patch p has a material m, defined by its material constitutive matrix $\mathbf{Q}_m$, associated with it. Then, the properties $\mathbf{Q}_p$ of the laminate at patch

p are given by

$$\mathbf{Q}_p(\boldsymbol{\beta}) = \mathbf{T}_r^T(\alpha_p)\overline{\mathbf{Q}}_m\mathbf{T}_r(\alpha_p)$$

where the expression above is the typical three-dimensional rotation rule for orthotropic materials (cf. Bathe [20]), and $\mathbf{T}_r(\alpha_p)$ is the three-dimensional rotation matrix. Hence, at patch p, the laminate properties $\mathbf{Q}_p$ are obtained through a rotation of the original laminate material constitutive matrix $\overline{\mathbf{Q}}_m$.

Finally, the second group of design variables $\mathbf{t} = \{t_s | s \in \{1, ..., n_s\}\}$ represents the total thickness t_s of the laminate at face s for each of the n_s cross section faces. The variation of the laminate thickness is achieved by a rearrangement of the cross section finite element mesh (see Paper 1).

2.1.1.1 Projection method

The approach described in the previous section where the continuous design variables represent the fiber orientations is prone to generate problems with a large number of local minima. A strategy is suggested to improve the chances of obtaining a good design albeit the problems with local minima. The devised projection method is schematically described in Figure 2.2. The first step consists of defining a computationally inexpensive optimal design problem with very few design variables. This is achieved by defining large patches, each enclosing a large part of the cross section mesh. This problem is solved for a relatively large number of random starting points. The design presenting the lowest objective function value is then chosen as the starting point for the next step. A projection method is then used where a sequence of optimization problems is solved with increasing number of design variables. At each step the number of patches is increased as its individuals sizes are decreased. The optimal fiber orientations and thickness obtained in the previous problem are projected into the new design domain with a finer patch discretization. The optimization process is then restarted and a new optimized design is generated. The projection iterations are repeated until the variation in performance between consecutive designs is below a predefined tolerance.

The optimization model described in this section has been applied in the optimal design of laminated composite beams with stiffness and weight constraints in Paper 1. Solutions are presented for the maximum stiffness and minimum weight design of Carbon Fiber Reinforced Plastic beams with a hollow square, solid rectangular, and hollow elliptical cross section.

2.1.2 Multi-material topology optimization

The optimization model described in this section is based on multi-material topology optimization techniques. Similar approaches have been described by Lund and Stegmann [13] and Stegmann and Lund [12] for the optimal design of laminated composite structures using shell finite elements. The aim is to determine the optimal distribution of a predefined set of candidate materials within the cross section

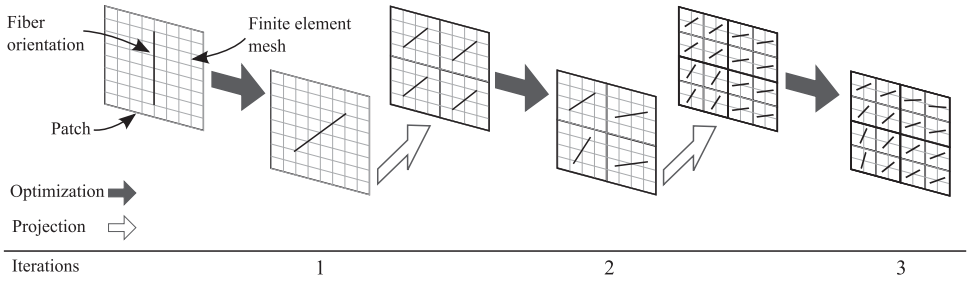

Figure 2.2: Schematic description of the projection method devised for the continuous fiber angles optimization approach. A sequence of problems is solved with increasing number of design variables. The optimal fiber orientations and thickness obtained in the previous problem are projected to generate a new starting point for the next optimal design problem. The optimization process is then restarted and a new optimized design is generated.

(see Figure 2.3). The result is a methodology which can simultaneously determine the optimal cross section topology and distribution of material therein. The optimization model comprises a material interpolation, penalization, and density filtering technique, each of which are described in the next sections. The optimization model described in this section has been used in Papers 2 and 3 for the optimal design of laminated composite beam cross sections with stiffness and eigenfrequency constraints.

2.1.2.1 Material interpolation

Hence, assume that a list of n_c candidate materials has been initially defined. The candidate materials must be linear elastic and no restrictions are imposed regarding anisotropy. Each of the candidates can correspond to a layer of the same composite material oriented in different directions. A possible extension of the Solid Isotropic Material with Penalization (SIMP) material interpolation model by Bendsøe and Kikuchi [10], and Rozvany and Zhou [8] is presented here to include multiple anisotropic materials. Hence, the material constitutive matrix $\mathbf{Q}_e$ at element e of the cross section mesh is given by the following material interpolation rule

$$\mathbf{Q}_e(\boldsymbol{\rho}) = \sum_{m=1}^{n_c} \rho_{em}^p \overline{\mathbf{Q}}_m \quad \forall e = 1, ..., n_e \tag{2.1}$$

where n_e is the number of elements in the cross section finite element mesh and $\overline{\mathbf{Q}}_m$ is the material constitutive matrix of candidate material m. The design variables $\boldsymbol{\rho} = \{\rho_{em} \in \mathbb{R} \mid e \in \{1, ..., n_e\}, \quad m \in \{1, ..., n_c\}\}$ represent the volume fractions of each of the candidate materials at each element of the cross section finite element mesh. The design variables are assumed to vary continuously between their

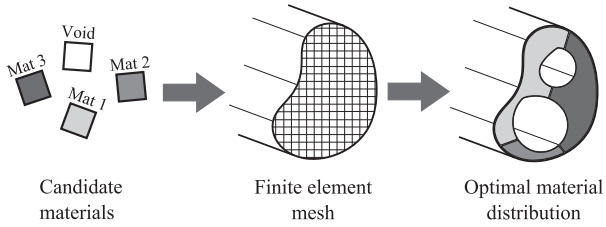

Figure 2.3: Schematic description of the multi-material topology optimization problem. The first step consists of defining a set of candidate materials (left). This set may include a material to represent void. The aim is then to determine the optimal distribution of each of the candidate materials in the cross section finite element mesh (center). The result is a methodology which allows for the simultaneous optimization of the cross section topology and material properties (right).

bounds, i.e., $0 \leq \rho_{em} \leq 1$, $\forall e = 1, ..., n_e$, $\forall m = 1, ..., n_c$. Finally, the role of the penalty parameter $p \geq 1$ is discussed later in Section 2.1.2.2.

The interpolation of the material density is slightly different as it does not include the penalization term p. Thus, the density ϱ_e at element e is given by

$$\varrho_e(\boldsymbol{\rho}) = \sum_{m=1}^{n_c} \rho_{em} \overline{\varrho}_m \quad \forall e = 1, ..., n_e \tag{2.2}$$

where $\overline{\varrho}_m$ is the density of material m.

The commonly used SIMP material interpolation expression for two phase problems (see Bendsøe and Sigmund [7]) implicitly controls the total amount of material or the sum of the design variables at each element. Here, the following linear equality constraints are included in the problem formulation in order to obtain the same relation between the design variables

$$\sum_{m=1}^{n_c} \rho_{em} = 1 \quad \forall e = 1, ..., n_e \tag{2.3}$$

The n_e linear constraints above ensure that the amount of material at each element remains constant.

The design variables $\boldsymbol{\rho}$ enter the structural model through the material constitutive matrix $\mathbf{Q}_e = \mathbf{Q}_e(\boldsymbol{\rho})$ and densities $\varrho_e = \varrho_e(\boldsymbol{\rho})$. The material constitutive matrix $\mathbf{Q}_e(\boldsymbol{\rho})$ is required for the determination of the coefficient matrices in (1.21) such that $\mathbf{K} = \mathbf{K}(\boldsymbol{\rho})$ and $\mathbf{G} = \mathbf{G}(\boldsymbol{\rho})$ in (1.26) and (1.29), respectively. Consequently, the cross section stiffness matrix is defined such that $\mathbf{K}_s = \mathbf{K}_s(\boldsymbol{\rho})$. The material densities $\varrho_e(\boldsymbol{\rho})$ are required in the evaluation of the cross section mass matrix in (1.32) such that $\mathbf{M}_s = \mathbf{M}_s(\boldsymbol{\rho})$. Finally at the beam finite element level, $\widehat{\mathbf{K}} = \widehat{\mathbf{K}}(\boldsymbol{\rho})$ and $\widehat{\mathbf{M}} = \widehat{\mathbf{M}}(\boldsymbol{\rho})$.

2.1.2.2 Penalization

Generally, designs obtained using the parameterization presented in the previous section (assuming $p = 1$) are not discrete, i.e., more than one material exists in the same element. The SIMP penalization works at the material interpolation level and has been extensively used in topology optimization problems. The penalization is realized by controling the value of the penalty parameter $p \geq 1$. Increasing the value of p corresponds to increasing the contrast between the different candidates and consequently in the penalization of intermediate values of the volume fractions. As a result the design variables are pushed into their bounds as p increases. The penalized problem, however, is in general non-convex and may have a large number of local minima. A continuation method is employed in order to increase the possibility of obtaining a good feasible design (see Sigmund and Petersson [23], Borrval and Petersson [25], and Hvejsel et al. [11]). The first step consists of solving the problem without penalization, i.e., $p = 1$. The resulting design is subsequently used as the starting point for the new optimal design problem. The penalty p_{i+1} for the new optimization problem is increased such that $p_{i+1} = p_i + \Delta p$ where p_i is the penalty value at the former iteration, and $\Delta p > 0$ is the penalty increase between iterations. The procedure is repeated until the design converges to a discrete solution.

2.1.2.3 Density based filtering

Two common issues in density based topology optimization concern the appearance of checkerboard patterns and the dependency of the results on the size of the elements in the finite element discretization (Sigmund [21]). A density filtering technique has been used in these thesis to address both of these issues. The technique has been originally introduced by Bruns and Tortorelli [22] and Bourdin [24] for two-phase topology optimization problems and it has been extended in this thesis (see Paper 2) to account for multiple material problems. Hence, the volume fraction of a given material at each element is a weighted average of the volume fractions of the same material in the neighboring elements and the element itself. This corresponds to imposing a length scale simultaneously for all candidate materials. The technique is briefly described next.

Let us define the set S_e of all elements at a distance f_r from element e as

$$S_e = \{\tilde{e} \in \{1, ..., n_e\} \mid \|\mathbf{x}_{\tilde{e}} - \mathbf{x}_e\|_2 \leq f_r\}$$

where f_r is the so-called filter radius, and $\mathbf{x}_{\tilde{e}}$ and $\mathbf{x}_e$ are the position vectors of element $\tilde{e}$ and e, respectively. The filtered volume fraction of material m at element e is $\widetilde{\rho}_{em} = \widetilde{\rho}_{em}(\rho_{\tilde{e}m}),\ \forall \tilde{e} \in S_e$ and defined as

$$\widetilde{\rho}_{em} = \frac{\sum_{\tilde{e} \in S_e} w(\mathbf{x}_{\tilde{e}}) v_{\tilde{e}} \rho_{\tilde{e}m}}{\sum_{\tilde{e} \in S_e} w(\mathbf{x}_{\tilde{e}}) v_{\tilde{e}}}$$

A linearly decaying weighting function $w(x_e)$ as suggested by Bruns and Tortorelli [22] and Bourdin [24] is used here and given by

$$w(\mathbf{x}_{\tilde{e}}) = f_r - \|\mathbf{x}_{\tilde{e}} - \mathbf{x}_e\|_2$$

The material interpolation expression presented before in (2.1) is rewritten here in terms of the filtered variables. Hence, the interpolated material constitutive matrix $\mathbf{Q}_e$ at element e is defined as

$$\mathbf{Q}_e(\boldsymbol{\rho}) = \sum_{m=1}^{n_c} \widetilde{\rho}_{em}^{p}(\boldsymbol{\rho})\overline{\mathbf{Q}}_m \quad , \quad \forall e = 1, ..., n_e$$

The same is done for the element density previously defined in (2.2) and now redefined as

$$\varrho_e(\boldsymbol{\rho}) = \sum_{m=1}^{n_c} \widetilde{\rho}_{em}(\boldsymbol{\rho})\overline{\varrho}_m \quad , \forall e = 1, ..., n_e$$

Finally, the linear constraints in (2.3) are also restated in function of the filtered design variables as

$$\sum_{m=1}^{n_c} \widetilde{\rho}_{em} = 1 \quad , \quad \forall e = 1, ..., n_e$$

Results have been presented in Paper 2 which specifically illustrate the behavior of the filtering technique presented above.

2.2 Problem formulation

Throughout this research the following functions have been used as either an objective function or constraint in the different optimal design formulations

- Compliance (Papers 1, 2, and 3);
- Eigenfrequencies (Paper 3);
- Shear center position (Papers 2 and 3);
- Mass center position (Paper 2);
- Weight (Papers 1, 2, and 3).

The shear and mass center positions have been defined in Sections 1.2.1.6 and 1.2.3, respectively. The remaining functions are defined in the next sections. Finally, an illustrative optimal design problem formulation is presented in the last section. Note that the functions and optimal design problem formulation presented are defined with respect to the design variables associated with the multi-material topology optimization model described in Section 2.1.2.

2.2.1 Compliance

The stiffness of the beam is evaluated in terms of the structural compliance. The structural compliance c_l for load case l is defined as the work done by the external forces $\widehat{\mathbf{f}}_l$ and written as

$$c_l(\boldsymbol{\rho}) = \widehat{\mathbf{f}}_l^T \widehat{\mathbf{u}}_l(\boldsymbol{\rho})$$

for load case l. The displacements $\widehat{\mathbf{u}}_l$ are obtained from the solution to the static equilibrium equation (1.10). Since $\widehat{\mathbf{K}}(\boldsymbol{\rho})$ is positive definite for all $\boldsymbol{\rho}$ within the specified bounds $0 \leq \rho_{em} \leq 1$, $\forall e = 1, ..., n_e$, $\forall m = 1, ..., n_c$, the displacement can determined from $\widehat{\mathbf{u}}_l(\boldsymbol{\rho}) = \widehat{\mathbf{K}}^{-1}(\boldsymbol{\rho})\widehat{\mathbf{f}}_l$, and the expression above can be re-written as

$$c_l(\boldsymbol{\rho}) = \widehat{\mathbf{f}}_l^T \widehat{\mathbf{K}}^{-1}(\boldsymbol{\rho})\widehat{\mathbf{f}}_l$$

The weighted average compliance C is then defined as

$$C(\boldsymbol{\rho}) = \sum_{l=1}^{n_l} \alpha_l c_l(\boldsymbol{\rho}) = \sum_{l=1}^{n_l} \alpha_l \widehat{\mathbf{f}}_l^T \widehat{\mathbf{K}}^{-1}(\boldsymbol{\rho})\widehat{\mathbf{f}}_l$$

where $\alpha_l \geq 0$ is the weight attributed to load case l.

2.2.2 Eigenfrequencies

The optimal design of structures with eigenfrequency constraints typically considers the maximization of the minimum eigenfrequency or the maximization of the distance between two specific eigenfrequencies. In both cases the order of the eigenfrequency may change throughout the optimization procedure leading to non-differentiability and consequently to a non-robust convergence of the optimization procedure. The Kreisselmeier-Steinhauser function (cf. Kreisselmeier and Steinhauser in [26]) is introduced in Paper 3 in order to address this issues and try to improve the convergence behavior of the optimization procedure. The KS function is a differentiable envelope function (Raspanti et al. in [19]) which gives a conservative representation of the maximum or minimum among a set of functions. It has been employed by Martins et al. in [17] and Maute et al. in [18] as a constraint aggregation function in structural optimization problems. The aim here is to use the KS function to approximate the maximum and minimum values of groups of eigenfrequencies.

The derivation presented next is for the form of the KS function approximating the minimum of a function – hereby denoted $\underline{\text{KS}}(\boldsymbol{\rho})$. Hence, assume that a group $\underline{\boldsymbol{\omega}} = \left\{\underline{\omega}_1, ..., \underline{\omega}_{n_g}\right\}$ of n_g frequencies has been defined. Furthermore, assume that $\underline{\boldsymbol{\omega}}$ is a subset of the eigenfrequencies $\boldsymbol{\omega} = \{\omega_1, ..., \omega_{n_u}\}$ obtained from (1.14), and that the frequencies are ordered such that $\underline{\omega}_1 \leq ... \leq \underline{\omega}_{n_g}$. The $\underline{\text{KS}}(\boldsymbol{\rho})$ is then

defined as

$$\underline{\mathrm{KS}}(\boldsymbol{\rho}) = \underline{\omega}_{n_g}(\boldsymbol{\rho}) - \frac{1}{\beta_s}\ln\left[\sum_{g=1}^{n_g} e^{-\beta_s(\underline{\omega}_g(\boldsymbol{\rho})-\underline{\omega}_{n_g}(\boldsymbol{\rho}))}\right] \tag{2.4}$$

The penalty parameter β_s is such that the function $\underline{\mathrm{KS}}(\boldsymbol{\rho})$ will tend to the minimum of $\underline{\boldsymbol{\omega}}$ as β_s increases. The function $\overline{\mathrm{KS}}(\boldsymbol{\rho})$ approximating the maximum of a group of frequencies $\overline{\boldsymbol{\omega}}$ is easily obtained from the expression above.

2.2.3 Weight

The total weight $w(\boldsymbol{\rho})$ of the beam finite element assemblage is defined as

$$w(\boldsymbol{\rho}) = \sum_{b=1}^{n_b}\sum_{e=1}^{n_e} v_e \varrho_e(\boldsymbol{\rho}) L_b$$

2.2.4 Optimal design problem formulation

The problem formulation presented here is an illustrative example of the type of problems addressed throughout this thesis. The formulation for the minimum compliance problem with constraints on frequency, mass, and shear and mass center positions, is

$$\begin{aligned}
\underset{\boldsymbol{\rho}\in\mathbb{R}^{n_e\times n_c}}{\text{minimize}} \quad & C(\boldsymbol{\rho}) \\
\text{subject to} \quad & \underline{\mathrm{KS}}(\underline{\boldsymbol{\omega}}(\boldsymbol{\rho})) \geq \underline{\omega} \\
& w(\boldsymbol{\rho}) \leq \overline{w} \\
& \mathbf{s}_c(\boldsymbol{\rho}) \leq \overline{\mathbf{s}} \\
& \mathbf{m}_c(\boldsymbol{\rho}) \leq \overline{\mathbf{m}} \\
& \sum_{m=1}^{n_c} \widetilde{\rho}_{em}(\boldsymbol{\rho}) = 1 \ , \ \forall e = 1, ..., n_e \\
& \underline{\rho} \leq \rho_{em} \leq \overline{\rho}, \ \forall e = 1, ..., n_e \ , \ \forall m = 1, ..., n_c
\end{aligned}$$

where the parameters $\underline{\omega}$, $\overline{w}$, $\overline{\mathbf{s}}$, and $\overline{\mathbf{m}}$ are the constraint values for the eigenfrequency, weight, and shear and mass center positions, respectively. Different problem formulations can be obtained by rearranging the objective and constraints functions above.

2.3 Sensitivity analysis

The expressions for the gradients or sensitivities of the objective function and constraints are presented in this section. The sensitivities are defined with respect to the design variables used in the multi-material topology optimization method described in Section 2.1.2.

2.3.1 Compliance

The structural compliance of the beam has been defined in Section 2.2.1. The gradients of the average compliance $C(\boldsymbol{\rho})$ with respect to ρ_{em} are

$$\frac{\partial C(\boldsymbol{\rho})}{\partial \rho_{em}} = \sum_{l=1}^{n_l} \alpha_l \frac{\partial c_l(\boldsymbol{\rho})}{\partial \rho_{em}}$$

The sensitivities of the compliance $c_l(\boldsymbol{\rho})$ for load case l is then given as

$$\frac{\partial c_l(\boldsymbol{\rho})}{\partial \rho_{em}} = \widehat{\mathbf{f}}_l^T \frac{\partial \widehat{\mathbf{u}}_l(\boldsymbol{\rho})}{\partial \rho_{em}} = \widehat{\mathbf{f}}_l^T \frac{\partial \widehat{\mathbf{K}}(\boldsymbol{\rho})^{-1}}{\partial \rho_{em}} \widehat{\mathbf{f}}_l$$

where it is assumed that the loads $\widehat{\mathbf{f}}_l$ are design independent. It can be shown (see, e.g., Bendsøe and Sigmund [7]) that the expression above can be further derived to yield

$$\frac{\partial c_l(\boldsymbol{\rho})}{\partial \rho_{em}} = -\widehat{\mathbf{u}}_l(\boldsymbol{\rho})^T \frac{\partial \widehat{\mathbf{K}}(\boldsymbol{\rho})}{\partial \rho_{em}} \widehat{\mathbf{u}}_l(\boldsymbol{\rho})$$

Thus the gradient of the beam compliance reduces to the evaluation of the gradient of the beam stiffness matrix $\widehat{\mathbf{K}}$. According to the definition of the beam stiffness matrix in (1.9), the gradient of $\widehat{\mathbf{K}}$ is

$$\frac{\partial \widehat{\mathbf{K}}(\boldsymbol{\rho})}{\partial \rho_{em}} = \sum_{b=1}^{n_b} \int_0^{L_b} \widehat{\mathbf{N}}_b^T \widehat{\mathbf{B}}^T \frac{\partial \mathbf{K}_s(\boldsymbol{\rho})}{\partial \rho_{em}} \widehat{\mathbf{B}} \widehat{\mathbf{N}}_b \, \mathrm{dz} \tag{2.5}$$

The sensitivities of the cross section stiffness matrix $\mathbf{K}_s(\boldsymbol{\rho})$ are presented in Section 2.3.4.

2.3.2 Eigenfrequencies

The eigenfrequency constraints are incorporated into the problem formulation through the KS function (see Section 2.2.2). The sensitivities are presented here for $\underline{\mathrm{KS}}(\boldsymbol{\rho})$ the form of the KS function approximating the minimum of a group $\underline{\boldsymbol{\omega}}$ of n_g eigenfrequencies.The sensitivities of $\underline{\mathrm{KS}}(\boldsymbol{\rho})$ with respect to the design variable ρ_{em} are obtained from the differentiation of (2.4) and defined as

$$\frac{\partial \underline{\mathrm{KS}}(\boldsymbol{\rho})}{\partial \rho_{em}} = \frac{\partial \underline{\omega}_{n_g}(\boldsymbol{\rho})}{\partial \rho_{em}} + \frac{\displaystyle\sum_{g=1}^{n_g} \left(\frac{\partial \underline{\omega}_g(\boldsymbol{\rho})}{\partial \rho_{em}} - \frac{\partial \underline{\omega}_{n_g}(\boldsymbol{\rho})}{\partial \rho_{em}} \right) e^{-\beta_s(\underline{\omega}_g(\boldsymbol{\rho}) - \underline{\omega}_{n_g}(\boldsymbol{\rho}))}}{\displaystyle\sum_{g=1}^{n_g} e^{-\beta_s(\underline{\omega}_g(\boldsymbol{\rho}) - \underline{\omega}_{n_g}(\boldsymbol{\rho}))}} \tag{2.6}$$

The gradients of the eigenfrequencies are presented next.

The eigenfrequencies $\boldsymbol{\omega}$ and associated eigenvectors $\widehat{\mathbf{v}}$ are obtained from the solution to the structural eigenvalue problem in (1.14). It is assumed that the eigenvectors are mass-normalized and thus

$$\widehat{\mathbf{v}}_p^T \widehat{\mathbf{M}}(\boldsymbol{\rho}) \widehat{\mathbf{v}}_q = \delta_{pq}, \ \forall p, q = 1, ..., n_d.$$

where n_d is the number of degrees of freedom in $\widehat{\mathbf{u}}$, and δ_{pq} is the Kronecker delta such that $\delta_{pq} = 1$ if $p = q$ and $\delta_{pq} = 0$ otherwise. For single eigenfrequencies the sensitivity of the eigenfrequency ω_p with respect to the design variable ρ_{em} is given by (cf. Seyranian et al. in [27])

$$\frac{\partial \omega_p^2(\boldsymbol{\rho})}{\rho_{em}} = \widehat{\mathbf{v}}_p^T \left(\frac{\partial \widehat{\mathbf{K}}(\boldsymbol{\rho})}{\partial \rho_{em}} - \omega_p^2(\boldsymbol{\rho}) \frac{\partial \widehat{\mathbf{M}}(\boldsymbol{\rho})}{\partial \rho_{em}} \right) \widehat{\mathbf{v}}_p \tag{2.7}$$

In the case of multiple eigenfrequencies we follow the technique outlined by Seyranian et al. [27]. Hence, assume that ω_M is an eigenfrequency with multiplicity n_ω such that $\omega_M = \omega_1 = ... = \omega_{n_\omega}$, where the eigenfrequencies are numbered from 1 to n_ω for convenience. The first step consists of assembling the auxiliary matrix $\boldsymbol{\Lambda}$ defined as

$$\Lambda_{rs} = \widehat{\mathbf{v}}_r^T \left(\frac{\partial \widehat{\mathbf{K}}(\boldsymbol{\rho})}{\partial \rho_{em}} - \omega_M^2 \frac{\partial \widehat{\mathbf{M}}(\boldsymbol{\rho})}{\partial \rho_{em}} \right) \widehat{\mathbf{v}}_s, \ r, s = 1, ..., n_\omega. \tag{2.8}$$

where $\widehat{\mathbf{v}}_r$ and $\widehat{\mathbf{v}}_s$, $r, s = 1, ..., n_\omega$, are the eigenvectors associated with the multiple eigenfrequency ω_M. Next, the following eigenvalue subproblem is subsequently solved

$$\left(\boldsymbol{\Lambda} - \tilde{\lambda} \mathbf{I} \right) \tilde{\mathbf{v}} = \mathbf{0}$$

yielding the eigenvalues $\widetilde{\boldsymbol{\lambda}} = \left\{ \tilde{\lambda}_1, ..., \tilde{\lambda}_{n_\omega} \right\}$ and corresponding eigenvectors $\widetilde{\mathbf{V}} = \{ \tilde{\mathbf{v}}_1, ..., \tilde{\mathbf{v}}_{n_\omega} \}$. The gradients of the multiple eigenfrequency ω_M are finally obtained as

$$\frac{\partial \omega_M^2(\boldsymbol{\rho})}{\rho_{em}} = \begin{cases} \tilde{\lambda}_1 \text{ with eigenvector } \mathbf{v}_1 = \sum_{q=1}^{n_\omega} \widehat{v}_q \tilde{v}_{1,q} \\ \quad \vdots \\ \tilde{\lambda}_{n_\omega} \text{ with eigenvector } \mathbf{v}_{n_\omega} = \sum_{q=1}^{n_\omega} \widehat{v}_q \tilde{v}_{n_\omega,q} \end{cases} \tag{2.9}$$

where $\tilde{v}_{n_\omega,q}$ is the entry (n_ω, q) of the eigenvector $\tilde{\mathbf{v}}$. The approach presented for multiple eigenfrequencies can be applied to single eigenfrequencies as well. In that case, $\boldsymbol{\Lambda}$ consists of only one eigenfrequency and the expression in (2.8) reduces to that derived for single eigenfrequencies in (2.7).

Finally, the gradients of the global beam finite element mass matrix $\widehat{\mathbf{M}}(\boldsymbol{\rho})$ in (2.7) and (2.8) are obtained through differentiation of (1.11) which yields

$$\frac{\partial \widehat{\mathbf{M}}(\boldsymbol{\rho})}{\partial \rho_{em}} = \sum_{b=1}^{n_b} \int_0^{L_b} \widehat{\mathbf{N}}_b^T \frac{\partial \mathbf{M}_s(\boldsymbol{\rho})}{\partial \rho_{em}} \widehat{\mathbf{N}}_b \, \mathrm{dz}$$

The sensitivities of the cross section mass matrix $\mathbf{M}_s$ are presented in Section 2.3.5. Inserting the results from either (2.7) or (2.9) into (2.6) for each of the eigenfrequencies in $\underline{\boldsymbol{\omega}}$ yields the gradients of $\underline{\mathrm{KS}}(\boldsymbol{\rho})$. The gradients of the global beam finite element stiffness matrix $\widehat{\mathbf{K}}(\boldsymbol{\rho})$ are given in (2.5).

2.3.3 Shear and mass center

The sensitivities of the shear center position with respect to the design variable ρ_{em} are obtained through differentiation of (1.31) to yield

$$\begin{aligned}
\frac{\partial x_s}{\partial \rho_{em}} = &- \left(\frac{\partial F_{s,62}}{\partial \rho_{em}} + \frac{\partial F_{s,64}}{\partial \rho_{em}} (L - z) \right) \frac{1}{F_{s,66}} \\
&+ \left(F_{s,62} + F_{s,64}(L - z) \right) \frac{1}{F_{s,66}^2} \frac{\partial F_{s,66}}{\partial \rho_{em}} \\
\frac{\partial y_s}{\partial \rho_{em}} = &\left(\frac{\partial F_{s,61}}{\partial \rho_{em}} + \frac{\partial F_{s,65}}{\partial \rho_{em}} (L - z) \right) \frac{1}{F_{s,66}} \\
&- \left(F_{s,61} + F_{s,65}(L - z) \right) \frac{1}{F_{s,66}^2} \frac{\partial F_{s,66}}{\partial \rho_{em}}
\end{aligned}$$

where the gradients $\partial F_{s,ij}/\partial \rho_{em}$ refer to the entries of $\partial \mathbf{F}/\partial \rho_{em}$ derived in Section 2.3.4. Finally, the sensitivities of the mass center position are obtained through differentiation of (1.33) which gives

$$\begin{aligned}
\frac{\partial x_c}{\partial \rho_{em}} &= \frac{x_{c_e} v_e}{\sum_{e=1}^{n_e} v_e \varrho_e} \frac{\partial \varrho_e}{\partial \rho_{em}} - \frac{\sum_{e=1}^{n_e} x_{c_e} v_e \varrho_e}{\left(\sum_{e=1}^{n_e} v_e \varrho_e \right)^2} \left(v_e \frac{\partial \varrho_e}{\partial \rho_{em}} \right) \\
\frac{\partial y_c}{\partial \rho_{em}} &= \frac{y_{c_e} v_e}{\sum_{e=1}^{n_e} v_e \varrho_e} \frac{\partial \varrho_e}{\partial \rho_{em}} - \frac{\sum_{e=1}^{n_e} y_{c_e} v_e \varrho_e}{\left(\sum_{e=1}^{n_e} v_e \varrho_e \right)^2} \left(v_e \frac{\partial \varrho_e}{\partial \rho_{em}} \right)
\end{aligned}$$

2.3.4 Cross section stiffness matrix

Two approaches were presented in Section 1.2 for the determination of the cross section stiffness matrix $\mathbf{K}_s$. The sensitivities of $\mathbf{K}_s$ when using VABS in Paper 1,

have been determined using finite differences. The reason is VABS is distributed as a "black-box" and hence it is not possible to implement the analytical sensitivities. The sensitivities presented here refer to the cross section analysis formulation presented in Section 1.2.1 using BECAS. This formulation was described and used first in Paper 2, and later employed in Paper 3.

The sensitivities of $\mathbf{K}_s$ with respect to ρ_{em} are defined as

$$\frac{\partial \mathbf{K}_s(\boldsymbol{\rho})}{\partial \rho_{em}} = \frac{\partial \mathbf{F}_s^{-1}(\boldsymbol{\rho})}{\partial \rho_{em}} = -\mathbf{K}_s(\boldsymbol{\rho}) \frac{\partial \mathbf{F}_s(\boldsymbol{\rho})}{\partial \rho_{em}} \mathbf{K}_s(\boldsymbol{\rho}) \tag{2.10}$$

where $\mathbf{K}_s = \mathbf{F}_s^{-1}$ and $\mathbf{F}_s$ is the cross section compliance matrix. The sensitivities of $\mathbf{F}_s$ are obtained from the differentiation of (1.30) to yield

$$\begin{aligned} \frac{\partial \mathbf{F}_s(\boldsymbol{\rho})}{\partial \rho_{em}} =& \frac{\partial \mathbf{W}^T(\boldsymbol{\rho})}{\partial \rho_{em}} \mathbf{G}(\boldsymbol{\rho}) \mathbf{W}(\boldsymbol{\rho}) + \mathbf{W}^T(\boldsymbol{\rho}) \frac{\partial \mathbf{G}(\boldsymbol{\rho})}{\partial \rho_{em}} \mathbf{W}(\boldsymbol{\rho}) \\ &+ \mathbf{W}^T(\boldsymbol{\rho}) \mathbf{G}(\boldsymbol{\rho}) \frac{\partial \mathbf{W}(\boldsymbol{\rho})}{\partial \rho_{em}} \end{aligned} \tag{2.11}$$

The evaluation of the second term in the expression above entails the evaluation of $\partial \mathbf{G}(\boldsymbol{\rho})/\partial \rho_{em}$. This can be obtained by evaluating the gradients of the sub-matrices in (1.21) and inserting the result into (1.29). The remaining terms can be efficiently evaluated as follows. The matrix $\mathbf{W}(\boldsymbol{\rho})$ is the solution to the linear system of equations in (1.27) such that $\mathbf{W}(\boldsymbol{\rho}) = \mathbf{K}(\boldsymbol{\rho})^{-1}\mathbf{F}$. Consequently, the sensitivities of $\mathbf{W}(\boldsymbol{\rho})$ are defined as

$$\frac{\partial \mathbf{W}(\boldsymbol{\rho})}{\partial \rho_{em}} = \frac{\partial \mathbf{K}^{-1}(\boldsymbol{\rho})}{\partial \rho_{em}} \mathbf{F} = -\mathbf{K}^{-1}(\boldsymbol{\rho}) \frac{\partial \mathbf{K}(\boldsymbol{\rho})}{\partial \rho_{em}} \mathbf{W}(\boldsymbol{\rho})$$

The gradients $\partial \mathbf{K}(\boldsymbol{\rho})/\partial \rho_{em}$ are determined by differentiation of (1.26) and corresponding sub-matrices in (1.21). Inserting the expression above into (2.11) yields

$$\begin{aligned} \frac{\partial \mathbf{F}_s(\boldsymbol{\rho})}{\partial \rho_{em}} =& -\mathbf{W}^T(\boldsymbol{\rho}) \frac{\partial \mathbf{K}^T(\boldsymbol{\rho})}{\partial \rho_{em}} \mathbf{K}^{-T}(\boldsymbol{\rho}) \mathbf{G}(\boldsymbol{\rho}) \mathbf{W}(\boldsymbol{\rho}) \\ &+ \mathbf{W}^T(\boldsymbol{\rho}) \frac{\partial \mathbf{G}(\boldsymbol{\rho})}{\partial \rho_{em}} \mathbf{W}(\boldsymbol{\rho}) \\ &- \mathbf{W}^T(\boldsymbol{\rho}) \mathbf{G}(\boldsymbol{\rho}) \mathbf{K}^{-1}(\boldsymbol{\rho}) \frac{\partial \mathbf{K}(\boldsymbol{\rho})}{\partial \rho_{em}} \mathbf{W}(\boldsymbol{\rho}) \end{aligned} \tag{2.12}$$

The first and last term can be dealt with efficiently by first solving the following sub-problem

$$\mathbf{V} = \mathbf{K}^{-T}(\boldsymbol{\rho}) \mathbf{G}(\boldsymbol{\rho}) \mathbf{W}(\boldsymbol{\rho})$$

The solution $\mathbf{V}$ to the set of linear equations above is the same for all design variables ρ_{em}. Hence, it can be evaluated once and stored to be reused in the calculation of the sensitivities for each of the design variables. The final expression

for the sensitivities of the compliance matrix is then obtained by inserting $\mathbf{V}$ into (2.12) to yield

$$\begin{aligned}\frac{\partial \mathbf{F}_s(\boldsymbol{\rho})}{\partial \rho_{em}} = &- \mathbf{W}^T(\boldsymbol{\rho})\frac{\partial \mathbf{K}^T(\boldsymbol{\rho})}{\partial \rho_{em}}\mathbf{V}(\boldsymbol{\rho}) + \mathbf{W}^T(\boldsymbol{\rho})\frac{\partial \mathbf{G}(\boldsymbol{\rho})}{\partial \rho_{em}}\mathbf{W}(\boldsymbol{\rho}) \\ &- \mathbf{V}^T(\boldsymbol{\rho})\frac{\partial \mathbf{K}(\boldsymbol{\rho})}{\partial \rho_{em}}\mathbf{W}(\boldsymbol{\rho})\end{aligned} \tag{2.13}$$

The gradient of the cross section stiffness matrix $\mathbf{K}_s$ are obtained by inserting (2.13) into (2.10). Inserting the result in (2.5) yields the sensitivities of the beam finite element stiffness matrix used for the evaluation of the sensitivities of the compliance and frequencies in Section 2.3.1 and 2.3.2, respectively. The gradients of the compliance matrix are required for the evaluation of the sensitivities of the shear center in Section 2.3.3.

2.3.5 Cross section mass matrix

The mass matrix $\mathbf{M}_s$ has been defined in (1.32). The gradient of $\mathbf{M}_s$ with respect to the design variable ρ_{em} is

$$\frac{\partial \mathbf{M}_s}{\partial \rho_{em}} = \begin{bmatrix} \frac{\partial m}{\partial \rho_{em}} & 0 & 0 & \frac{\partial I_{xx}}{\partial \rho_{em}} & -\frac{\partial I_{xy}}{\partial \rho_{em}} & 0 \\ 0 & \frac{\partial m}{\partial \rho_{em}} & 0 & -\frac{\partial I_{xy}}{\partial \rho_{em}} & \frac{\partial I_{yy}}{\partial \rho_{em}} & 0 \\ 0 & 0 & \frac{\partial m}{\partial \rho_{em}} & 0 & 0 & \frac{\partial I_{xx}}{\partial \rho_{em}} + \frac{\partial I_{yy}}{\partial \rho_{em}} \\ \frac{\partial I_{xx}}{\partial \rho_{em}} & -\frac{\partial I_{xy}}{\partial \rho_{em}} & 0 & 0 & 0 & -\frac{\partial m}{\partial \rho_{em}} y_m - m\frac{\partial y_m}{\partial \rho_{em}} \\ -\frac{\partial I_{xy}}{\partial \rho_{em}} & \frac{\partial I_{yy}}{\partial \rho_{em}} & 0 & 0 & 0 & \frac{\partial m}{\partial \rho_{em}} x_m + m\frac{\partial x_m}{\partial \rho_{em}} \\ 0 & 0 & \frac{\partial I_{xx}}{\partial \rho_{em}} + \frac{\partial I_{yy}}{\partial \rho_{em}} & \frac{\partial m}{\partial \rho_{em}} y_m + m\frac{\partial y_m}{\partial \rho_{em}} & -\frac{\partial m}{\partial \rho_{em}} x_m - m\frac{\partial x_m}{\partial \rho_{em}} & 0 \end{bmatrix}$$

Hence, the gradient of the cross section mass matrix reduces to the gradients of the mass per unit length, $\partial m/\partial \rho_{em}$, moments of inertia, $\partial I_{xx}/\partial \rho_{em}$ and $\partial I_{yy}/\partial \rho_{em}$, the product of inertia, $\partial I_{xy}/\partial \rho_{em}$, and the mass center $\partial x_m/\partial \rho_{em}$ and $\partial y_m/\partial \rho_{em}$.

2.4 Implementation and validation

The optimal design problem is solved using the sequential quadratic programming algorithm SNOPT (Gill et al. [14]). The gradients of each of the functions have been implemented both in Fortran (Paper 1) and MATLAB® (Papers 2 and 3). The MATLAB® implementation makes extensive used of the SuiteSparse libraries by Davis [16], and Davis and Natarajan [15]. Furthermore, the module for the evaluation of the sensitivities makes use of the parallel capabilities of the `parfor` command in the MATLAB® Parallel Computing Toolbox. The sensitivities have been consistently validated against values determined using finite differences.

An example is presented in Paper 2 which illustrates the amount of time involved in the computations. Consider a cross section finite element mesh with 6627 degrees of freedom, a beam finite element model with 390 degrees of freedom, and an optimal design problem with 18900 design variables. The current MATLAB® implementation takes approximately five seconds for each objective function evaluation including assembly of the finite element matrices and the solution of the linear system of equations. The sensitivity analysis takes about 20 seconds in total.

Chapter 3

Conclusions

The most important conclusions and contributions of this thesis are presented in this chapter along with suggestions for future research directions. This thesis describes work done in the field of structural analysis of beams and optimal design of laminated composite structures. The resulting optimal design framework combining a structural and optimization model has been applied to the optimal structural design of laminated composite beams.

This chapter is organized as follows. A summary of the results obtained in each individual publication is presented next in Section 3.1. The main contributions and impact of the research presented in this thesis is subsequently outlined in Section 3.2. Finally, in Section 3.3, several directions for future research are suggested.

3.1 Summary of the results

The most important results and conclusions from each of the publications are summarized here. At the date of submission of this thesis Paper 1 and 5 have been published in peer-reviewed international journals. Paper 2 has been submitted to a peer-reviewed international journal and Paper 3 is intended for submission in the near future. Finally, Paper 4 will be published as a technical report. The chronological order in which the research was produced is first Paper 5, then Paper 1, Paper 4, Paper 2, and finally Paper 3.

Paper 1: Maximum stiffness and minimum weight optimization of laminated composite beams using continuous fiber angles

This paper focuses on the optimal design of laminated composite beams for maximum stiffness and minimum weight. The structural analysis is performed using a beam finite element model. A three-node quadratic beam finite element is formulated which is able to correctly account for the effects of material anisotropy and inhomogeneity in the analysis of beams with arbitrary cross section geometry.

The static and dynamic response of the beam finite element model is validated against equivalent shell and solid finite element models and the results are in very good agreement. The main advantage of the beam model is the significant reduction in the size of the global finite element matrices when compared to equivalent shell and solid finite element models. This modeling approach is therefore an attractive alternative in computationally intensive applications like optimal design frameworks. A projection technique is proposed which aims at enabling the use of fiber angles as continuous design variables albeit the problems may have many local minima. The technique consists of solving a sequence problems with increasing number of design variables. At each step the results from the previous problem are projected to generate the starting point for the new optimal design problem. Results are presented for the minimum compliance and minimum weight design of laminated composite beams with different cross section geometries and load cases. The results suggest that the optimal design framework is suitable for the identification of optimal fiber orientations and laminate thickness in optimal design of laminated composite beams.

Remarks This paper presents the first iteration of the structural and optimization models. A short-coming of the structural model using VABS as a "black-box" concerned the evaluation of the sensitivities. The computational effort involved in the forward difference approach used here is significantly larger when compared to the analytical approach presented in Paper 2. Finally, the optimization model considers that the geometry and material properties are practically fixed and is therefore less versatile than the optmization approach presented in Paper 2.

Paper 2: Multi-material topology optimization of laminated composite beam cross sections

This paper presents an optimal design framework for the simultaneous identification of optimal cross section topology and material properties in structural design of laminated composite beams. The structural response of the beam is analyzed using a beam finite elements. A finite element based tool is described for the analysis of the cross section stiffness properties. The resulting beam finite element model is able to correctly account for the effects stemming from material anisotropy and inhomogeneity in the analysis of beams with arbitrary section geometry. An optimization framework based on multi-material topology optimization techniques is described. The design variables represent the volume fractions of each of a predefined set of candidate materials. Extensions of an existing material interpolation model, penalization method, and filtering technique are presented which can accommodate any number of anisotropic materials. The methodology is applied in the optimal design of laminated composite beams with different cross section shapes and load cases. Results are presented for the minimum compliance problem with constraints on weight, and the shear and mass center positions.

The methodology is also applied in the optimal design of an idealized wind turbine blade cross section subjected to static loading of aerodynamic nature. The results from the numerical experiments suggest that the devised optimal design framework is suitable for the simultaneous optimization of cross section topology and material properties in the structural design of laminated composite beams.

Remarks This paper described the incorporation of BECAS, the cross section analysis tool developed in Paper 4, into an optimal design framework. An important development in this thesis concerns the derivation of the sensitivities of the cross section stiffness matrix presented in this paper. This allowed for a significant decrease in the computation time involved in the evaluation of the sensitivities when compared to the approach described in Paper 1. Furthermore, the multi-material topology optimization model presented here addresses most of the short-comings of the model presented in Paper 1. Mostly, the fact that the cross section topology is not fixed together with the possibility of considering a wide range of different isotropic and anisotropic materials throughout the optimizaton process, makes this approach very versatile.

Paper 3: Multi-material topology optimization of laminated composite beams with frequency constraints

This paper presents a framework for the optimal structural design of laminated composite beam cross sections with stiffness and frequency constraints. The beam static and dynamic response is analyzed using a beam finite element model. The cross section stiffness and mass properties are estimated using a high-fidelity cross section analysis tool which is able to correctly estimate the effects of material anisotropy and inhomogeneity. The optimization is performed using the multi-material topology optimization framework presented in Paper 2. The design variables are the volume fractions of each of a predefined set of candidate materials at each point of the cross section. The frequency constraints are included in the optimal design problem formulation through the Kreisselmeyer-Steinhauser (KS) function. The KS function is a differentiable envelope function and is used here to approximate the maximum and the minimum of a group of eigenfrequencies. Results are initially presented for problems dealing with the maximization of the minimum eigenfrequency, and maximization of the gap between consecutive eigenfrequencies with constraints on weight and shear center position. Finally, solutions are presented for the minimum compliance problem with constraints on mass, frequency, and shear center position. The results indicate that the approach is suitable for the simultaneous optimization of the cross section topology and material properties in structural design of laminated composite beams with stiffness and frequency constraints.

Remarks This paper extends the work presented in Paper 2 to include frequency constraints. The beam finite element model is based on the cross section analysis tool presented in Paper 4.

Paper 4: BECAS - A cross section analysis tool for anisotropic and inhomogeneous sections of arbitrary geometry

The development, implementation and validation of the BEam Cross section Analysis Software – BECAS – is described. BECAS is a finite element based tool for the determination of the stiffness properties of beam cross sections with arbitrary geometry. Moreover, BECAS can account for the effects stemming from material anisotropy and the inhomogeneous distribution of material in the cross section. A thorough account of the underlying theory is presented first. Details on the practical implementation of the current version of BECAS are described next. Finally, validation results are presented for solid, hollow, open and multi-celled cross sections made of isotropic and anisotropic materials. The estimated stiffness parameters were found to be in very agreement when compared to the results obtained using an existing and extensively validated commercial cross section analysis tool.

Remarks BECAS is used in the beam finite element model of both Paper 2 and 3. The gradients of the cross section stiffness parameters are presented in Paper 2. BECAS is extended in Paper 3 to include the calculation of the mass matrix. The latter will be included in future versions of BECAS.

This report is intended to be a developers manual for future users of BECAS. The report will accompany the current open-source version of BECAS freely available for academic use. We hope that making the code publicly available will stimulate further research into the development of advanced beam finite element models.

Paper 5: Hydro-elastic analysis and optimization of a composite marine propeller

This paper describes the development of a framework for the hydro-elastic analysis and optimization of laminated composite marine propellers. A structural model of the marine composite propeller is developed using layered shell finite elements with varying thickness. The hydrodynamic model used for the evaluation of the hydrodynamic pressure acting on the face of the propeller is based on the panel method. The structural and hydrodynamic model are coupled in the hydro-elastic model in order to analyze the interaction between the elastic deformation of the blade and the hydrodynamic pressure distribution. An optimization model is presented where the design variables are the fiber orientations at different layers, and the blade pitch angle. The presented hydro-elastic and optimization models are employed in the design of a high-skew composite marine propeller. The laminate

properties are optimized to reduce the fuel consumption considering two operation conditions – cruising and maximum speed. The strength of the resulting optimized design is analyzed in terms of the Tsai-Wu strength index and the laminate in the most critical regions is rearranged. The numerical results show that the optimized composite marine propeller design allows for a reduction of the combined fuel consumption with respect to its metal counterpart, and is simultaneously able to resist the imposed hydrodynamic loads.

3.2 Contributions and impact

The main contribution of this thesis is the optimal design framework presented for the structural design of laminated composite beams. Although several design constraints are not yet accounted for in order to fully address problems like the aeroelastic tailoring of laminated composite wind turbine blades, we believe the work presented in this thesis represents a step towards this goal.

The contributions according to each individual paper are as follows. The main contribution of Paper 1 concerns the proposed projection technique. It can be employed in laminate optimization problems where the fiber angles are represented by continuous design variables. The first main contribution of Paper 2 concerns the integration of the cross section analysis tool, BECAS, into the optimal design framework. This is mostly achieved through the derivation and implementation of the analytical expressions for the sensitivities of the cross section stiffness matrix. The result is a significant reduction in computation time in the evaluation of the sensitivities which allows for the solution of problems with a larger number of design variables. This increase in computational efficiency paved the way for the development of the multi-material topology optimization model – the second contribution from this paper. Namely, the main contributions in this field are the proposed extensions of the material interpolation, penalization and filtering techniques to multiple anisotropic materials. Paper 3 extends the work of Paper 2 to include eigenfrequency constraints. The main contribution is the alternative approach for handling the eigenfrequency constraints based on the Kreisselmeier-Steinhauser function. The main contribution of Paper 4 concerns the the development, implementation, and validation of the cross section analysis tool BECAS. The development of BECAS allowed for a much deeper insight into the formulation of the beam model and a closer integration between the structural and optimization models. Paper 2 and Paper 4 represent perhaps the most important contributions from this thesis. The most important contribution of Paper 5 is the suggested hydro-elastic model for the analysis of composite marine propellers.

3.3 Future work

This section presents several topics for future research which are a continuation of the work or for which the work presented in this thesis can be used as a starting point.

Validation Further validation of the beam and cross section analysis models is required. The cross section stiffness parameters and warping displacements should be validated against numerical and experimental data, if possible. The efforts should focus on the validation of the effects stemming from material inhomogeneity and anisotropy as we feel there is a lack of physical insight concerning this phenomena.

Beam finite element model Future research should focus on the development of a beam finite element model which can account for the effects of tapering, pre-twist and curvature. This is relevant for the analysis of wind turbine blades as it is possible, using fewer beam finite elements, to accurately estimate the global response of the blade.

Cross section analysis tool A module for the analysis of the three-dimensional stresses in the cross section should be developed. It is possible based on these stresses to determine the magnitude of different failure index specific for the analysis of laminated composite structures (e.g., Tsai-Wu strength index). The results may give a valuable insight into the strength properties of the blade at the early stages of the design process.

The effects of tapering, pre-twist and curvature should also be included at the cross section analysis level. This is important for the correct estimation of the stiffness properties and cross section stresses.

Different types of finite elements should be developed for the cross section analysis. It should be possible to develop two-dimensional layered elements which would then be used in the estimation of the cross section properties. This would be an important step towards the exchange of information between the beam model and other existing shell or solid finite element models.

Optimization model The number of objective function evaluations and the overall computational effort could be reduced. One possibility is to improve the penalization approach used together with the continuation method. The information from the gradients of the objective function and constraints with respect to the penalty parameter p can perhaps be used to determine the correct step length between iterations in the continuation method.

Different shapes of the density filter, other than circular, should be considered. Layered structures can be realized using laminated composites and its appearance is being hindered when using a circular filter. Possibly, an elliptical filter whose

orientation is dependent on the orientation of the fiber plane could be an interesting alternative.

Optimal design problem formulations In order to address relevant physical problems like the optimal design of laminated composite wind turbine blades, further constraints should be included in the optimal design problem formulation. A possible first step concerns the incorporation of lift and drag in order to have a measure of aerodynamic performance.

Another important aspect is to account for the strength of the blade in the optimal design problem formulation. This can be done in two levels. The first is at the beam level where constraints can be imposed on the magnitude of the generalized transverse forces and moments at each node of the beam finite element model. This constraints would be computationally cheap as the analysis is done at the beam finite element level where the matrices are relatively small. The second approach concerns the analysis of the stresses at the cross section level. In this case, the use of failure criteria specifically developed for laminated composite materials (e.g., Tsai-Wu failure criteria) should be considered. This approach is more computationally expensive as in this case the determination of the sensitivities will entail the solution to the cross section equilibrium equations for each design variable.

Structural analysis of laminated composite beams Work is under way to couple the beam finite element model developed in this thesis with a micromechanics model for the analysis of debond damage growth in wind turbine blades. The aim is to investigate the effect of the debond damage on the global response of the blade and, furthermore, to analyze how the debond grows while the blade is under operation. The approach should be used for the fatigue analysis of wind turbine blades.

References

[1] Jung S.N., Nagaraj, V.T. Chopra, I., *Assessment of composite rotor blade modeling techniques*, Journal of the American Helicopter Society, 4(3), 188-205, 1999.

[2] Volovoi V.V., Hodges D.H., Cesnik C.E.S., Popescu B., *Assessment of beam modeling methods for rotor blade applications*, Mathematical and Computer Modelling, 33, 1099-1112, 2001.

[3] Yu W., Hodges D.H., *Generalized Timoshenko theory of the variational asymptotic beam sectional analysis*, Journal of the American Helicopter Society, 50(1), 46-55, 2005.

[4] Yu W., Volovoi V., Hodges D.H., Hong X., *Validation of the asymptotic beam sectional analysis (VABS)*, AIAA Journal, 40(10), 2002.

[5] Hodges D., *Nonlinear Composite Beam Theory*, Progress in Astronautics and Aeronautics Series, 213, AIAA, 2006.

[6] Giavotto V., Borri M., Mantegazza P., Ghiringhelli G., Carmaschi V., Maffiolu G.C., Mussi F., *Anisotropic beam theory and applications*, Composite Structures, 16(1-4), 403-413, 1983.

[7] Bendsøe M.P., Sigmund O., *Topology Optimization: Theory, Methods and Applications*, 2nd Edition, Springer-Verlag, Berlin, 2003.

[8] Rozvany G., Zhou M., *The COC algorithm .1. Cross-section optimization or sizing*, Computer Methods in Applied Mechanics and Engineering, 89(1-3), 281-308, 1991.

[9] Sigmund O., Torquato S., *Design of materials with extreme thermal expansion using a three-phase topology optimization method*, Journal of the Mechanics and Physics of Solids, 45(6), 1037-1067, 1997.

[10] Bendsøe M., Kikuchi N., *Generating optimal topologies in structural design using a homogenization method*, Computer Methods in Applied Mechanics and Engineering, 71 (2), 197-224, 1988.

[11] Hvejsel C.F., Lund E., Stolpe M., *Optimization strategies for discrete multi-material stiffness optimization*, Structural and Multidisciplinary Optimization, DOI 10.1007/s00158-011-0648-5, 2011.

[12] Stegmann J., Lund E., *Discrete material optimization of general composite shell structures*, International Journal for Numerical Methods in Engineering, 62(14), 2009-2007, 2005.

[13] Lund E., Stegmann J., *On structural optimization of composite shell structures using a discrete constitutive parametrization*, 8(1), 109-124, 2005.

[14] Gill P.E., Murray W., Saunders M.A., *SNOPT: An SQP algorithm for large scale constrained optimization*, SIAM Journal on Optimization, 121(4), 979-1006, 2002.

[15] Davis T.A., Natarajan E.P., *Algorithm 907: KLU, a direct sparse solver for circuit simulation problems*, ACM Transactions on Mathematical Software, 37 (3), 2010.

[16] Davis T.A., *Direct Methods for Sparse Linear Systems*, SIAM Book Series on the Fundamentals of Algorithms, Philadelphia, 2006.

[17] Martins J.R.R.A., Alonso J.J., Reuther J.J., *A coupled-adjoint sensitivity analysis method for high-fidelity aero-structural design*, Optimization and Engineering, 6(1), 33-ï¿½62, 2005.

[18] Maute K., Nikbay M., Farhat C., *Sensitivity analysis and design optimization of three dimensional non-linear aeroelastic systems by the adjoint method*, International Journal for Numerical Methods in Engineering, 56, 911-933, 2003.

[19] Raspanti C.G., Bandoni J.A., Biegler L.T., *New strategies for flexibility analysis and design under uncertainty*, Computers and Chemical Engineering, 24(9-10), 2193-2209, 2000.

[20] Bathe K.J., *Finite Element Procedures in Engineering Analysis*, Prentice-Hall, 1982.

[21] Sigmund O., *Morphology-based black and white filters for topology optimization*, Structural and Multidisciplinary Optimization, 33(4-5), 401-424, 2007.

[22] Bruns T. E., Tortorelli D. A., *Topology optimization of non-linear elastic structures and compliant mechanisms*, Computer Methods in Applied Mechanics and Engineering, 190(26-27), 3443-3459, 2001.

[23] Sigmund O., Petersson J., *Numerical instabilities in topology optimization: A survey on procedures dealing with checkerboards, mesh dependencies and local minima*, Structural Optimization, 16(1), 68-75, 1998.

[24] Bourdin B., *Filters in topology optimization*, International Journal for Numerical Methods in Engineering, 50 (9), 2143-2158, 2001.

[25] Borrval T., Petersson J., *Topology optimization using regularized intermediate density control*, Computer Methods in Applied Mechanics and Engineering, 190(37-38), 4911-4928, 2001.

[26] Kreisselmeier G., Steinhauser R., *Systematic control design by optimizing a vector performance index*, International Federation of Active Controls Symposium on Computer-Aided Design of Control Systems, Zurich, Switzerland, 1979.

[27] Seyranian A.P., Lund E., Olhoff N., *Multiple eigenvalues in structural optimization problems*, Structural Optimization, 8, 207-227, 1994.

[28] Hansen M.H., *Aeroelastic instability problems for wind turbines*, Wind Energy, 10, 551-577, 2007.

Part II

Publications

Paper 1

Blasques J.P., Stolpe M., Maximum stiffness and minimum weight optimization of laminated composite beams using continuous fiber angles, Structural and Multidisciplinary Optimization, 43 (4), 573-588, 2011.

Struct Multidisc Optim (2011) 43:573–588
DOI 10.1007/s00158-010-0592-9

RESEARCH PAPER

Maximum stiffness and minimum weight optimization of laminated composite beams using continuous fiber angles

José Pedro Blasques · Mathias Stolpe

Received: 14 June 2010 / Revised: 11 September 2010 / Accepted: 22 October 2010 / Published online: 20 November 2010

Abstract This paper deals with identification of optimal fiber orientations and laminate thicknesses in maximum stiffness and minimum weight design of laminated composite beams. The structural response is evaluated using beam finite elements which correctly account for the influence of the fiber orientation and cross section geometry. The resulting finite element matrices are significantly smaller than those obtained using equivalent finite element models. This modeling approach is therefore an attractive alternative in computationally intensive applications at the conceptual design stage where the focus is on the global structural response. An optimization strategy is presented which aims at enabling the use of fiber angles as continuous design variables albeit the problems may have many local minima. A sequence of closely related problems with an increasing number of design variables is treated. The design found for a problem in the sequence is projected to generate the starting point for the next problem in the sequence. Numerical results are presented for cantilever beams with different geometries and load cases. The results indicate that the devised strategy is well suited for finding optimal fiber orientations and laminate thicknesses in the design of slender laminated composite structures.

J. P. Blasques (✉)
Department of Mechanical Engineering,
Technical University of Denmark,
Nils Koppels Allé, Building 403, 2800
Kgs. Lyngby, Denmark
e-mail: jpbl@mek.dtu.dk

M. Stolpe
Department of Mathematics, Technical University of Denmark,
Matematiktorvet, Building 303S, 2800 Kgs. Lyngby, Denmark
e-mail: m.stolpe@mat.dtu.dk

Keywords Compliance and weight optimization · Beams · Laminated composites

1 Introduction

Composite laminates present different levels of elastic couplings which depend on the laminate lay-up. Using optimal design to tailor the orientation of the fibers in the laminate it is possible, to a certain extent, to improve the static and dynamic response of composite structures. This idea has been applied in the design of airplane wings and propeller blades. Shirk et al. (1985) present a review on this topic. The possibility of increasing the lift to drag ratio, improve maneuverability, and prevent wing divergence and flutter are among the possible issues aeroelastic tailoring may address. Maute et al. (2003) have recently presented a framework for the aeroelastic tailoring of composite airplane wings using a gradient-based technique. The benefits of aeroelastic tailoring have also been studied in the context of helicopter rotor blade design. Ganguli and Chopra (1995) and Murugan and Ganguli (2005) use laminate tailoring to reduce blade vibrations, improve aeroelastic stability and decrease stresses. In the field of wind turbine blade design, Jeronimidis et al. (1991) and Veers et al. (1998), argue for the use of laminate tailoring to design blades with passive pitch regulation. Incorporation of this design feature may lead to an increase in the energy production and more importantly to the mitigation of the effects of extreme gust loads. Hansen (2003) indicates that aeroelastic tailoring may also improve the dynamic properties of these type of blades. The idea was investigated and experimentally validated in the DAMPBLADE project (Chaviaropoulos et al. 2006) which used laminate tailoring among other, to improve the structural damping properties of a wind turbine blade.

In most of the references cited above, the analysis of the structural response is performed using either shell or beam finite element models. Shell elements are typically used when a relatively high level of detail is required, namely an accurate prediction of the stress field. Beam finite elements are specifically suited and thus often preferred for the global analysis of slender structures like helicopter and wind turbine rotor blades. Reviews of different beam modeling techniques are presented in Jung et al. (1999) and Volovoi et al. (2001). The correct prediction of the effect of the fiber orientations in the structural response of the beam is considered paramount and is specifically addressed in Jung et al. (1999) and Volovoi et al. (2001).

The objective is herein to establish a methodology for the identification of optimal fiber orientations in maximum stiffness and minimum weight design of laminated composite beams. The static structural response of the composite beam is evaluated using a beam finite element model capable of correctly predicting the effect of the fiber orientations. The aim is to set the foundations for future research which will extend the application to structural design of wind turbine blades with aeroelastic constraints.

Several approaches for optimization of laminate lay-ups have been reported in the literature. Some of these are based on the assumption that the design variables should only take discrete values. Algorithms used for these type of problems include genetic algorithms (Le Riche and Haftka 1993; Gürdal et al. 1999), particle swarm methods (Kathiravan and Ganguli 2007) and branch-and-bound methods (Stolpe and Stegmann 2007). Other approaches consider continuous design variables. In this case, it is often possible to compute the gradients (sensitivities) of the objective function and constraints. It is then possible to state nonlinear optimization problems which can be solved using robust and efficient numerical gradient-based optimization methods. The main advantage of these type of methods is that in general a relatively small number of objective and constraint function evaluations is required. This is a critical aspect when dealing with large, computationally expensive analysis models like nonlinear aeroelastic models of wind turbine blades. Different parameterizations have been put forward in this context. Pedersen (1991) presented an approach based on the minimization of the elastic strain energy in the optimal thickness and fiber orientations design of structures subjected to in-plane loads. Tsai and Pagano (1968) introduced the concept of lamination parameters or laminate invariants which allow for the definition of a convex design space in maximum stiffness design problems. Later, Miki and Sugiyama (1993) and Hammer et al. (1997) employed lamination parameters in the design optimization of laminated composite structures. Another approach inspired by the ideas of multi-phase topology optimization has been presented by Lund and Stegmann (2005) and Stegmann and Lund (2005). The so-called discrete material optimization approach uses a material interpolation model to force the continuous variables to approach discrete values.

In this paper, fiber orientations and layer thicknesses are used directly as design variables. This modeling approach is prone to generate optimal design problems with a large number of local minima. A strategy is presented which aims at enabling the use of fiber angles as design variables albeit the problem with local minima. A sequence of closely related problems with an increasing number of design variables is treated. The design found for a problem in the sequence is projected and used as the starting point for the next problem in the sequence. The strategy is applied in the optimal design of laminated composite beam-like structures subject to multiple load cases. Considering the overall aim of this research, gradient-based algorithms have been preferred for solving the optimization problems presented in this paper. Hence, each of the optimization problems is solved using a modern numerical optimization method for continuous constrained optimization—the robust and efficient sequential quadratic programming software SNOPT (Gill et al. 2002). Figure 1 shows an example of the results obtained when the devised methodology is applied to the design of a composite cantilever box beam.

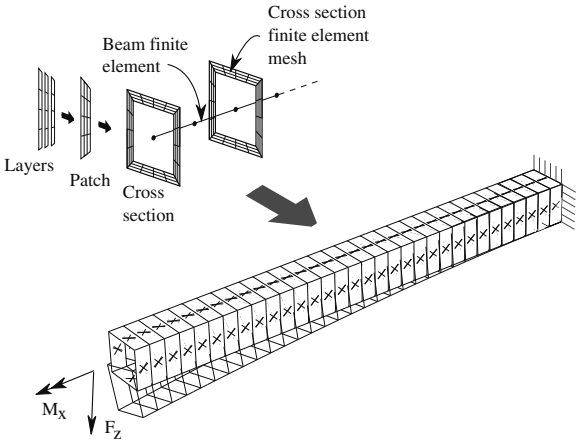

Fig. 1 An illustration of the developed methodology applied to the optimal design of a laminated composite box beam subject to a transverse load (F_z) and torsional moment (M_x). The structural analysis is performed using a beam finite element model. The geometry of each cross section is defined using plane finite elements. These elements are grouped to define the layers in the laminate of each face. The design variables are associated with fiber orientations in each layer. The devised optimization strategy is employed and the resulting optimal fiber orientations are finally identified

The structural analysis is performed in a beam finite element context. The cross section properties are evaluated using the Variational Asymptotic Beam Cross Sectional Analysis software, VABS (Yu and Hodges 2005; Yu et al. 2002). A three node quadratic beam finite element is consequently constructed and implemented. The presented beam finite element model is able to handle arbitrary cross section geometries and correctly predict the effect of the fiber orientations in the global static and dynamic response. In the beam element formulation the 2D analysis of the cross section properties is decoupled from the 1D integration of the cross section properties along the beam length. Consequently, the resulting system matrices are (much) smaller than those obtained using equivalent shell or solid finite element models. As a result, beam elements are very attractive in computationally intensive applications at stages of the design process focusing mostly on the the analysis of the global response of the beams. The possibility introduced by VABS of correctly predicting the effect of the fiber orientations, makes this whole approach attractive for the optimal design of slender laminated composite structures. Neto et al. (2008) presented the analytical sensitivities of the beam stiffness with respect to the fiber orientations using VABS. The fiber orientations of a cantilever laminated composite box beam were subsequently optimized to improve the buckling associated with the twist-bend instability. The largest problem in Neto et al. (2008) has four design variables and is solved using a gradient-based technique. Li et al. (2008) suggest a hybrid approach combining a gradient-based method and a genetic algorithm to design the cross section of a helicopter blade. The aim is to identify the optimal fiber orientations and internal spar shape which minimize the blade weight, reduce the distance between shear, mass and aerodynamic center, and respect a set of stiffness, stress and manufacturing constraints. The largest problem considers a total of 17 design variables. To the author's best knowledge, Neto et al. (2008) and Li et al. (2008) are the only publications to date combining fiber orientation optimization and a beam finite element formulation based on VABS.

The paper is organized as follows. The structural model and the validation thereof are described in Section 2. The formulation of the minimum weight problem with stiffness constraints is presented in Section 3. The sensitivity analysis of the constraint functions (compliance) and the objective function (weight) with respect to the design variables are described in Section 4. The setup of the numerical experiments and the employed optimization strategies are described in Section 5. In Section 6 numerical results for eight different combinations of cross section geometries, load cases and problem formulations are presented. Finally, a summary and an outline of future research are presented.

2 Structural model

A linear elastic three-node quadratic beam finite element is implemented. The construction of the beam finite element model is divided into two parts—the analysis of the cross section properties and the integration of these properties along the beam length. The cross section analysis is performed using the Variational Asymptotic Beam Cross Section Analysis (VABS) software (Yu and Hodges 2005). The cross section geometry is defined and meshed using plane finite elements. The material properties, plane of the laminate, and the orientation of the fibers are specified at each element of the cross section mesh. The software VABS returns, among other things, a generalized form of the Timoshenko beam stiffness and mass matrix, **A** and **E**, respectively (see e.g. Bathe 1982). The beam stiffness matrix includes and accounts for the anisotropic composite laminate couplings.

The cross section stiffness and mass matrices, **A** and **E**, are subsequently integrated along the beam length to generate a three node quadratic beam element. The element has three translational and three rotational degrees of freedom (dof) at each node. The beam element stiffness and mass matrices, $\mathbf{K}_e$ and $\mathbf{M}_e$, of element e are given by

$$\mathbf{K}_e(\boldsymbol{\theta}, \mathbf{t}) = \int_0^{L_b} \mathbf{B}^T \mathbf{A}(\boldsymbol{\theta}, \mathbf{t}) \mathbf{B} dl$$

$$\mathbf{M}_e(\mathbf{t}) = \int_0^{L_b} \mathbf{N}^T \mathbf{E}(\mathbf{t}) \mathbf{N} dl$$

The matrix **B** expresses the strain-displacement relation and incorporates the quadratic shape functions in matrix **N**, l is the direction along the length of the beam and L_b is the length of the beam. The design variable vectors $\boldsymbol{\theta} = \begin{pmatrix} \theta_1 & \dots & \theta_{n_\theta} \end{pmatrix}^T$ and $\mathbf{t} = \begin{pmatrix} t_1 & \dots & t_{n_t} \end{pmatrix}^T$ are associated with the fiber orientations and cross section face thickness design variables, respectively. Finally, the global stiffness and mass matrices are defined as

$$\mathbf{K}(\boldsymbol{\theta}, \mathbf{t}) = \sum_{e=1}^{n_e} \mathbf{K}_e(\boldsymbol{\theta}, \mathbf{t}) \tag{1}$$

$$\mathbf{M}(\mathbf{t}) = \sum_{e=1}^{n_e} \mathbf{M}_e(\mathbf{t}) \tag{2}$$

where n_e is the number of beam elements. The displacement field, $\mathbf{u}_k$, of the beam when subjected to the load, $\mathbf{f}_k$, is obtained by solving the linear system of equations

$$\mathbf{K}(\boldsymbol{\theta}, \mathbf{t}) \mathbf{u}_k = \mathbf{f}_k \tag{3}$$

where $k = 1, \dots, m$, indicates the load number.

2.1 Validation of the beam model

The static and dynamic response of the beam finite element model is validated by reproducing and extending some of the results presented by Yu (2007). The compliance and first six eigenfrequencies are compared against shell and solid finite element models. A cantilever beam with two different cross section geometries and laminate lay-ups is considered. The shell and solid finite element models are generated in ANSYS using SHELL99 and SOLID191 layered shell and solid finite elements, respectively. The compliance is evaluated for two load cases—a transverse load, F, and a torsional moment, M, applied at the free end of the beam. Results are first obtained for a solid rectangular cross section. The dimensions of the beam, fiber orientations, material mechanical properties, and magnitude of the loads are presented in Fig. 2. The finite element models are constructed using 20 elements along the length and width. In the thickness direction five elements are used in both the beam and solid finite element model. In the shell model five layers are defined through the thickness. The fibers are oriented at 30° with respect to the length (cf. Fig. 2). The results for each of the different models are presented in Table 1.

The beam finite element model is also validated using one of the optimal designs obtained later in this paper. The optimal design from example B2 (cf. Table 7) is reproduced using shell and solid finite elements. The geometrical properties, fiber orientations, material mechanical properties, and details concerning the imposed loads are presented in Fig. 3. The finite element discretization is the same for all three models. There are 32 elements along the length, 32 elements along the perimeter and six elements in the thickness direction. Only in the shell element model the six layers are defined across the thickness.

As reported in Tables 1 and 2 the results indicate that there is a good agreement between the values of the three models irrespective of the cross section geometry or laminate lay-up. Note that the unconstrained warping boundary condition present in the beam model is difficult to reproduce using the shell and solid model. Hence it has been disregarded. This fact may explain the discrepancy in the results. The validation results serve to show that the modeling approach is suited for the analysis of the global response of slender laminated composite structures. The optimal results obtained using the beam finite element model can be transferred to an equivalent shell or solid model if a more detailed analysis is required. The main advantage of the beam element model in comparison to its shell and solid counterparts is the reduced problem size. For example, in the first case (solid rectangular cross section) the beam, shell and solid finite element models have 1,293, 2,200 and 29,673 dof, respectively. Moreover, note that the 1D beam finite element model has only 390 dof. The remaining 903 correspond to the cross section mesh.

Table 1 Validation results obtained for the solid rectangular cross section. Comparison between the compliance and first six eigenfrequencies using equivalent beam, shell and solid finite element models. The relative difference is with respect to the beam model results

	Beam	Shell	Error (%)	Solid	Error (%)
Load					
F	221.9	217.3	2.05	215.5	2.87
M	0.666	0.664	0.26	0.653	2.03
Eigenfrequency					
# 1	52.6	54.439	3.55	54.5	3.58
# 2	209.8	214.34	2.16	214.4	2.18
# 3	326.3	339.87	4.14	339.8	4.13
# 4	900.3	948.34	5.34	947.6	5.26
# 5	1,285.2	1,317.9	2.55	1,318.0	2.56
# 6	1,661.6	1,732.8	4.29	1,686.4	1.49

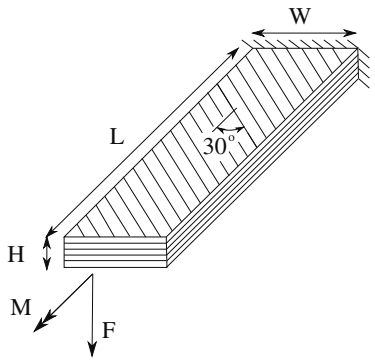

Fig. 2 Solid rectangular beam used for validation of the beam finite element. Geometrical lay-out, fiber orientations and direction of transverse load (F) and torsional moment (M) (*left*). Material mechanical properties, geometrical dimensions, and magnitude of the loads (*right*)

E_{11}	126 GPa
$E_{22} = E_{33}$	9.49 GPa
G_{12}	5.16 GPa
G_{13}	4.2 GPa
G_{23}	2.54 GPa
$\nu_{12} = \nu_{13} = \nu_{23}$	0.3
ρ	1549 kg/m^3
Length (L)	0.1905 m
Width (W)	0.0127 m
Height (H)	0.003175 m
F	20 N
M	0.127 Nm

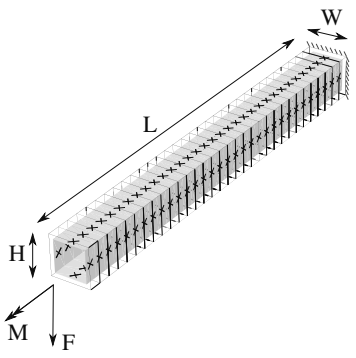

E_{11}	126 GPa
$E_{22} = E_{33}$	11 GPa
G_{12}	7 GPa
G_{13}	5.5 GPa
G_{23}	2.9 GPa
ν_{12}	0.3
$\nu_{13} = \nu_{23}$	0.02
ρ	1800 kg/m^3
Length (L)	40 m
Width (W)	1 m
Height (H)	1 m
Thickness	0.1 m
F	1000 N
M	9300 Nm

Fig. 3 Box beam used for validation which is a reproduction of example B2 (cf. Table 7) presented later in this paper. Geometrical lay-out, fiber orientations, and direction of transverse load (F) and torsional moment (M) (*left*). Material mechanical properties, dimensions and magnitude of the loads (*right*)

3 Problem formulation

The minimum weight problem with a constraint on the weighted average of the compliances for each load case is formulated next. The total weight of the structure, $w(\mathbf{t})$, is only a function of the thickness variables, $\mathbf{t}$, of the cross section faces whereas the compliance of load case k, $c_k(\boldsymbol{\theta}, \mathbf{t})$, is function of the thickness and also the fiber orientations $\boldsymbol{\theta}$. The structural compliance is a measure of stiffness defined as the work performed by the external loads

$$c_k(\boldsymbol{\theta}, \mathbf{t}) = \mathbf{f}_k^T \mathbf{u}_k(\boldsymbol{\theta}, \mathbf{t})$$

The design variable values are bounded within given values, i.e., $\underline{\theta} \le \theta_i \le \overline{\theta}\ ,\ \forall i = 1, \ldots, n_\theta$ and $\underline{t} \le t_j \le \overline{t},\ \forall j = 1, \ldots, n_t$. We assume herein that $\underline{t} > 0$ and $\mathbf{K}(\boldsymbol{\theta}, \mathbf{t})$ is positive definite for all $(\boldsymbol{\theta}, \mathbf{t})$ within the specified bounds. It is then possible to define the function $\mathbf{u}_k(\boldsymbol{\theta}, \mathbf{t}) = \mathbf{K}^{-1}(\boldsymbol{\theta}, \mathbf{t})\mathbf{f}_k$ and rewrite the compliance as

$$c_k(\boldsymbol{\theta}, \mathbf{t}) = \mathbf{f}_k^T \mathbf{K}^{-1}(\boldsymbol{\theta}, \mathbf{t})\mathbf{f}_k \tag{4}$$

The nested problem formulation of the minimum weight problem with compliance constraints (P1) is

$$(P1) \quad \begin{aligned} &\underset{\boldsymbol{\theta}\in\mathbb{R}^{n_\theta}, \mathbf{t}\in\mathbb{R}^{n_t}}{\text{minimize}} && w(\mathbf{t}) \\ &\text{subject to} && \sum_{k=1}^{m} \alpha_k \mathbf{f}_k^T \mathbf{K}^{-1}(\boldsymbol{\theta}, \mathbf{t})\mathbf{f}_k \le \overline{c} \\ & && \underline{\theta} \le \theta_i \le \overline{\theta}\ ,\ \forall i = 1, \ldots, n_\theta \\ & && \underline{t} \le t_j \le \overline{t}\ ,\ \forall j = 1, \ldots, n_t \end{aligned} \tag{5}$$

The value $\overline{c}$ is the maximum allowed value of the average of the compliances weighted by the factors $\alpha_k \ge 0,\ \forall k = 1, \ldots, m$.

In formulation (P1) the objective function is the total weight of the structure while the constraint function is the weighted average of the compliances for each load case. Interchanging the objective and constraint functions yields the minimum compliance optimization problem with a constraint on the total weight of the structure. The latter problem shall be herein referred to as (P2). Note that only the thickness design variables affect the weight of the structure. Thus, if the vector $\mathbf{t}$ is fixed, the weight will remain unchanged and (P2) is simply the minimum compliance optimization problem. Furthermore, instead of using the averaged compliance as in formulation (P1), the compliance constraints may be imposed independently for each load case. The minimum weight problem with a compliance constraint for each load case shall be referred to as problem formulation (P3). Finally, it is also possible to minimize the maximum compliance value while constraining the total weight of the structure. This will be referred to as formulation (P4). Since this formulation has a non-smooth objective

Table 2 Validation results obtained for the box beam. Comparison between the compliance and first six eigenfrequencies using equivalent beam, shell, and solid finite element models. The relative difference is with respect to the beam model results

	Beam	Shell	Error (%)	Solid	Error (%)
Load					
F	17.8	17.6	0.92	17.7	0.42
M	1.523	1.490	2.17	1.537	0.91
Eigenmode					
# 1	15.0	14.6	2.55	15.0	0.18
# 2	15.0	14.8	1.65	15.2	0.93
# 3	93.9	91.5	2.57	93.8	0.13
# 4	93.9	92.4	1.65	94.9	0.99
# 5	261.5	254.9	2.55	261.5	0.01
# 6	261.6	257.4	1.61	264.5	1.11

function we reformulate it as a smooth problem, using the so-called bound formulation.

4 Sensitivity analysis

The gradients (sensitivities) of the objective and constraint functions are presented in this section. In our implementation the sensitivities are computed semi-analytically. The reason is that sensitivity analysis is currently not implemented in VABS and furthermore, the VABS source code is not available to the authors.

4.1 Compliance

The sensitivity of the compliance with respect to the design variables is presented first. Consider the vector $\mathbf{h} = \left(\boldsymbol{\theta}^T, \mathbf{t}^T\right)^T$ which gathers both types of design variables. If

$$C(\mathbf{h}) = \sum_{k=1}^{m} \alpha_k c_k(\mathbf{h})$$

then the corresponding gradient with respect to the design variables is

$$\frac{\partial C(\mathbf{h})}{\partial h_i} = \sum_{k=1}^{m} \alpha_k \frac{\partial c_k(\mathbf{h})}{\partial h_i} \tag{6}$$

Assuming that the loads are design independent and according to the definition of compliance in (4), the sensitivity of $c_k(\mathbf{h})$ with respect to the design variable, h_i, can then be defined as

$$\frac{\partial c_k(\mathbf{h})}{\partial h_i} = \mathbf{f}_k^T \frac{\partial \mathbf{u}_k(\mathbf{h})}{\partial h_i} = \mathbf{f}_k^T \frac{\partial \mathbf{K}(\mathbf{h})^{-1}}{\partial h_i} \mathbf{f}_k$$

Furthermore, it is possible to show (see Bendsøe and Sigmund 2003) that in this case

$$\frac{\partial c_k(\mathbf{h})}{\partial h_i} = -\mathbf{u}_k(\mathbf{h})^T \frac{\partial \mathbf{K}(\mathbf{h})}{\partial h_i} \mathbf{u}_k(\mathbf{h})$$

If the design variable h_i affects only the element stiffness matrix of element e then the derivative of the compliance with respect to the design variable h_i becomes

$$\begin{aligned} \frac{\partial c_k(\mathbf{h})}{\partial h_i} &= -\mathbf{u}_k(\mathbf{h})^T \frac{\partial \mathbf{K}_e(\mathbf{h})}{\partial h_i} \mathbf{u}_k(\mathbf{h}) \\ &= -\mathbf{d}_e(\mathbf{h})^T \frac{\partial \mathbf{K}_e(\mathbf{h})}{\partial h_i} \mathbf{d}_e(\mathbf{h}) \end{aligned} \tag{7}$$

where $\mathbf{d}_e$ are the components of the displacement vector $\mathbf{u}_k$ associated with the degrees of freedom of the element e. It is possible to further simplify (7) by noting the manner in which the element stiffness matrix was defined in (1). Thus in this case,

$$\frac{\partial \mathbf{K}_e(\mathbf{h})}{\partial h_i} = \int_0^L \mathbf{B}^T \frac{\partial \mathbf{A}(\mathbf{h})}{\partial h_i} \mathbf{B} dl$$

which consists in differentiating the generalized Timoshenko beam stiffness matrix directly. Consequently, it is possible to avoid integrating and building the element stiffness matrix twice. In the current implementation the sensitivities $\partial \mathbf{A}(\mathbf{h})/\partial h_i$ are determined by numerical differentiation, namely using forward differences. This is due to the fact that VABS is given as a "black-box" and consequently it is not possible to establish a complete analytical version. The numerical differentiation using a forward difference scheme is implemented as follows

$$\frac{\partial \mathbf{A}(\mathbf{h})}{\partial h_i} \approx \frac{\mathbf{A}(\mathbf{h} + s \cdot \mathbf{e}_i) - \mathbf{A}(\mathbf{h})}{s}$$

where s is the step size and $\mathbf{e}_i$ is the i-th unit vector. The step size s has been set to 1×10^{-6} in our implementation. The sensitivity of the weighted average of the compliance is obtained by replacing (7) in (6).

4.2 Mass

The weight of the structure is only function of the thickness design variables. The sensitivity of the weight with respect to the thickness of the cross section face is hence

$$\frac{\partial w(\mathbf{t})}{\partial t_j} = \sum_{e=1}^{n_e} \sum_{e_c=1}^{n_c} \rho \frac{\partial A_{e_c}(\mathbf{t})}{\partial t_j} \cdot L_e$$

where n_c is number of elements in the cross section mesh, L_e is the length of beam element e or distance between cross sections. The material density is given by ρ while the area of the element e_c in the cross section mesh is defined as A_{e_c}. The sensitivity of the weight with respect to the thickness of the cross section faces is obtained by numerical differentiation in a procedure similar to that described before for the compliance sensitivity analysis.

5 Numerical experiments

The setup for the numerical experiments and the optimization strategy is described next. The beam geometry and the loads are generally kept simple to facilitate the interpretation of the results and give an insight into the behavior of the proposed strategy. Hence, a cantilever beam with three different cross section geometries is considered. These are representative of the type of load carrying structural elements found in wing-like structures. Moreover, optimal

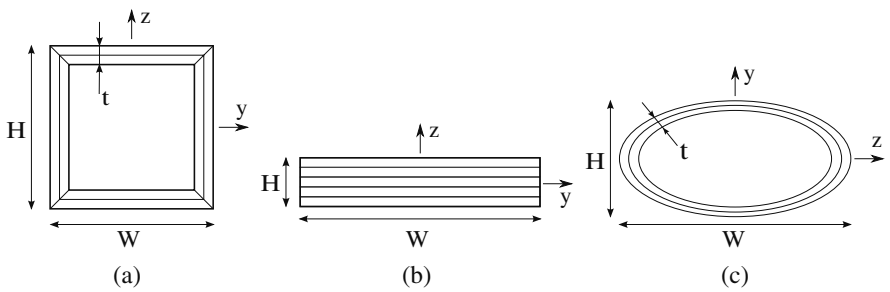

Fig. 4 Geometry of the three cross sections considered: Box (**a**), Rectangle (**b**) and Ellipse (**c**). The cross section dimensions are presented in Table 3

designs are initially presented for beams subjected to either transverse loads, torsional moments, or to a combination of both. These initial results give an insight into how the optimal fiber orientations are affected by the imposed load conditions. The procedure is repeated considering the thickness of the cross section faces as a design variable as well. It is then possible to compare the effect of the thickness variation on the optimal fiber orientations. Finally a load case is considered which mimics the general properties of aerodynamic loading.

5.1 Geometries and material properties

The three different types of cross section geometries considered are presented in Fig. 4. The cross sections shall henceforth be referred to as Box (Fig. 4a), Rectangle (Fig. 4b) and Ellipse (Fig. 4c). The cross section dimensions are presented in Table 3. All beams are laminated using a type of uni-directional carbon fiber reinforced epoxy whose mechanical properties are stated in Table 4.

When using VABS, attributes like material properties and fiber orientations are specified for each element in the cross section mesh. The design variables, however, may be associated with more than one finite element. As such, there is a finite element discretization and a discretization associated with the optimization problem. In this sense, a *layer* is hereby defined as a group of elements in the cross section mesh. All elements in a layer share the same attributes and design variables. Layers are stacked through the thickness of the cross section faces. A *patch* is defined as a group of layers along the perimeter of the cross section. There may be several patches along the cross section perimeter. Furthermore, patches and layers are grouped in *cross sections* distributed along the length. In sum, each design variable is associated with a layer belonging to a patch which in its turn belongs to a cross section. Henceforth, the number of layers, patches and cross sections for a given problem are respectively identified by the letters L, P and S each preceded by a number. This nomenclature is introduced to facilitate the reference to the results. For example, *Box 16S 4P 3L* corresponds to the case where there are 16 cross sections with a Box geometry along the length, and four patches along the perimeter each composed of three layers (cf. Fig. 5). Each layer has an angle design variable, θ_i, associated with it. Thus, in this case there would be $4(patches) \times 3(layers) = 12$ fiber angle design variables in the cross section and a total of $12 \times 16(cross\ sections) = 800$ fiber angle design variables in the whole model. The thickness design variables, on the other hand, are associated with the cross sections. There are two thickness design variables per cross section. In the example before there would be $16(cross\ sections) \times 2 = 32$ thickness design variables.

A schematic representation of the variation of the cross section thickness is presented for each cross section type in Fig. 6. In the *Rectangle* case (Fig. 6b) the dimensions

Table 3 Geometrical dimensions of the beams (cf. Fig. 4)

Geometry	Dimensions (m)	
Box	Width	1
	Height	1
	Length	40
	Thickness	0.1
Rectangle	Width	0.5
	Height	0.125
	Length	40
Ellipse	Width	2
	Height	0.5
	Length	40
	Thickness	0.04

Table 4 General material properties of a type of uni-directional carbon reinforced epoxy

E_{11}	126 GPa
$E_{22} = E_{33}$	11 GPa
G_{12}	7 GPa
G_{13}	5.5 GPa
G_{23}	2.9 GPa
ν_{12}	0.3
$\nu_{13} = \nu_{23}$	0.02
ρ	1,800 kg/m^3

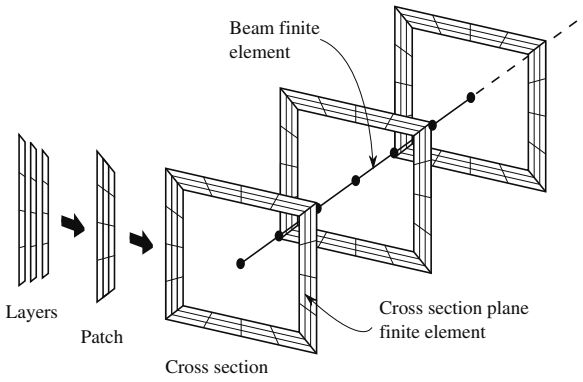

Fig. 5 A *layer*, *patch*, and a *cross section* superimposed on the finite element mesh. The fiber angle design variables are associated with the layers and patches whereas the thickness design variables are associated with the cross sections

of the cross section can vary both in the thickness and width direction. In the case of the *Box* and *Ellipse* cross section geometries (Fig. 6a and c, respectively), the thickness design variables control the shape of the inner face of the cross section. One design variable is associated with variations of thickness in the vertical direction (top and bottom faces) while the other is associated with variations in the horizontal direction (side faces). It is assumed in all cases that the outer faces remain unchanged. Note that a change in the thickness of the cross section faces requires a rearrangement of the cross section mesh.

The beam finite element model is composed of 32 beam elements and the 1D problem consists therefore of 390 dof. All cross sections are meshed using eight node plane finite elements. The total number of elements and its disposition throughout each of the cross sections is presented in Table 5. The beam is a cantilever beam for all cases. The translation and rotation degrees of freedom are constrained at the clamped end of the beam. Note, however, that the cross section is free to warp at the clamped end. The considered load cases are presented in Table 6. The loads are identified by the letters F, M, P and T followed by a subscript indicating the direction. The letters F and M correspond to transverse loads and moments, respectively, applied at the free end of the beam. The letters P and T indicate distributed loads and moments applied along the length of the beam, respectively.

Table 5 Number of elements and corresponding arrangement for each cross section geometry

Geometry	Number of elements		
	Thickness	Perimeter	Total
Box	6	32	192
Rectangle	20	20	400
Ellipse	12	88	1,056

5.2 Optimization strategies

Using fiber angles as design variables may lead to optimal design problems with a large number of (bad) local minima. In our computational experience, problems with a large number of design variables will typically converge to a design which is very close to the starting point and far from optimal. A strategy is hereby put forward which aims at increasing the possibility of converging to a good design using fiber angles as design variables. The strategy consists of solving a sequence of problems with an increasing number of design variables. The starting point of each problem is the final point of the former. The approach is illustrated in Fig. 7. In the initial problem, 1 CS, all beam finite elements share the same cross section properties. The initial problem has a very small number of design variables ($\leq$ 15) and is therefore inexpensive to solve. Thus, 100 random starting points are generated and a design is found for each. The design with the lowest objective function value is then chosen as the starting point for the subsequent problem. The number of cross sections along the length is then doubled. The optimal angle orientation found in the initial problem is used as the initial fiber orientations at both halves of the beam. The problem is solved once more. In the 2 CS case the resulting optimal fiber orientations for both halves of the beam are different although the starting point is the same. The number of cross sections is once again doubled and

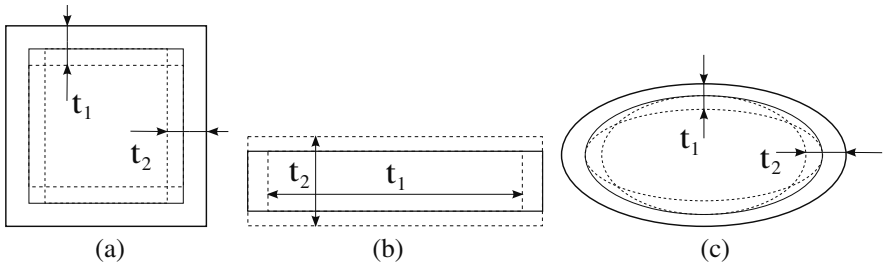

Fig. 6 Representation of the thickness design variables for the Box (**a**), Rectangle (**b**) and Ellipse (**c**) geometries

Table 6 Direction and magnitude of the load cases and its association with each cross section geometry

Geometry	Ref.	Load cases	
		Direction	Magnitude
Box	BLC1	F_z	1,000 N
	BLC2	M_x	9,300 Nm
	BLC3	F_z	1,000 N
		M_x	9,300 Nm
Rectangle	RLC1	F_z	50 N
		F_z	−50 N
		M_x	900 N
		M_x	−900 N
Ellipse	ELC1	P_z	25 N/m
		P_y	10 N/m
		T_x	100 Nm/m

the same procedure is repeated. The strategy is described here for an increasing number of cross sections. It is also applicable for an increasing number of layers and patches.

All random starting points used for the initial problems were generated so that $\theta_i \in [0°, 180°]$, $\forall i = 1, \ldots, n_\theta$. Throughout the optimization process, however $\theta_i \in [-90°, 270°]$, $\forall i = 1, \ldots, n_\theta$. Initial tests conducted for $\theta_i \in [0°, 180°]$, $\forall i = 1, \ldots, n_\theta$, show that a large number of design variables converge to their bounds. A broader interval between lower and upper bound results in better designs. The thickness design variables are allowed to vary around the initial values reported in Table 3. Thus, if t is the initial thickness value then for all cases $t - 0.05 \leq t_i \leq t + 0.05, \forall i = 1, \ldots, n_t$ where t_i is a thickness design variable. The range of variation is chosen so that the quality of the cross section mesh is not significantly affected.

Finally, the fibers are said to be oriented at 0° when aligned along the length of the beam and at 90° when transverse to the beam length. All problems are solved by SNOPT (Gill et al. 2002) with the optimality and feasibility tolerance set to 1×10^{-5}.

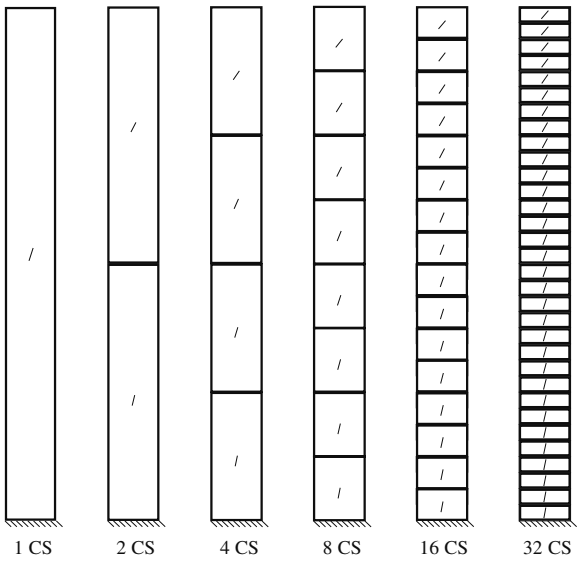

Fig. 7 Example illustrating the optimization strategy. Fiber orientations are propagated through a succession of solutions to problems with increasing number of cross sections along the length

6 Results

Results are initially presented for eight different combinations of cross section, load cases, and problem formulations (see Table 7). The resulting fiber orientations and cross section thickness are presented in Figs. 8, 9, 10, 11 and 12. Details concerning the number of design variables, number of objective function evaluations (corresponding to the number of global stiffness matrix assemblies) and the resulting values of compliance and weight are summarized in Table 8. The remaining numerical experiments—B7, R2 and E2—are discussed in Section 6.4.

Table 7 Catalogue of numerical experiments as combinations of cross section type (see Fig. 4), problem formulations and load cases (see Table 6)

Reference	Geometry	Problem formulation	Load cases
B1	Box	Minimum compliance (P2)	BLC1
B2	Box	Minimum compliance (P2)	BLC2
B3	Box	Minimum compliance (P2)	BLC3
B4	Box	Minimum weight with constraint on average compliance (P1)	BLC1
B5	Box	Minimum weight with constraint on average compliance (P1)	BLC2
B6	Box	Minimum weight with constraint on average compliance (P1)	BLC3
B7	Box	Minimum maximum compliance with weight constraint (P4)	BLC3
R1	Rectangle	Minimum weight with constraint on average compliance (P1)	RLC1
R2	Rectangle	Minimum weight with multiple compliance constraints (P3)	RLC1
E1	Ellipse	Minimum weight with constraint on average compliance (P1)	ELC1
E2	Ellipse	Minimum weight with multiple compliance constraints (P3)	ELC1

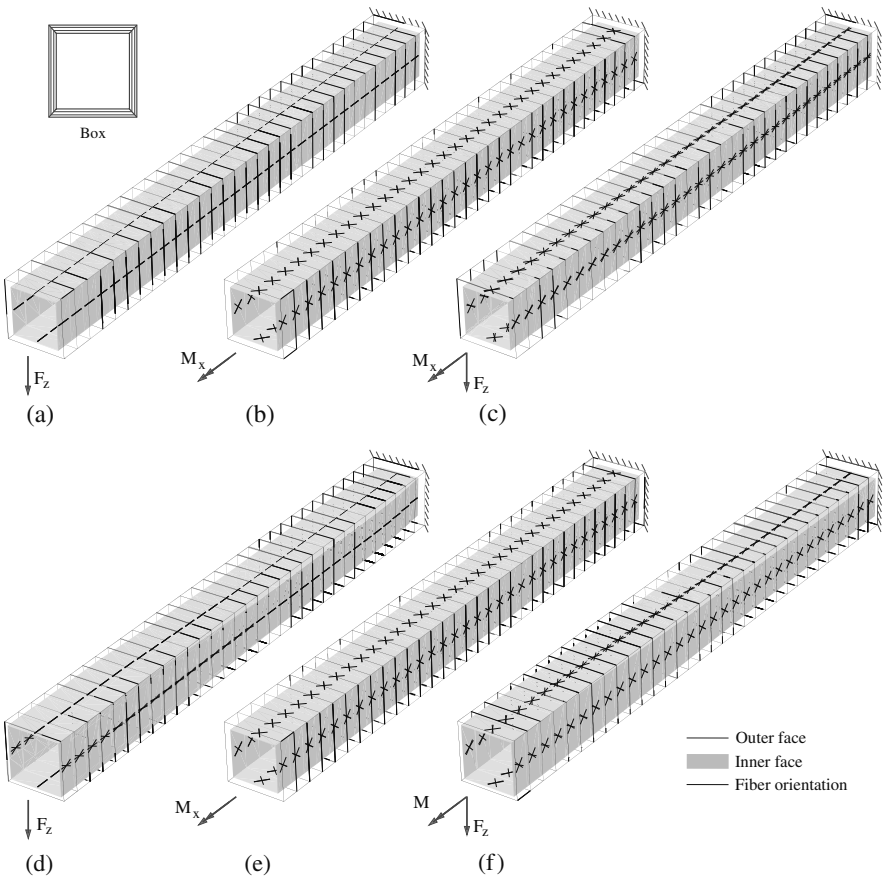

Fig. 8 Optimal fiber orientations, laminate thickness and load cases for each of the examples using the *Box* geometry. **a–c** Results for the minimum compliance problem with fixed thickness (Examples B1–B3). **d–f** Results for the minimum weight optimal design problem with compliance constraints (Examples B4–B6). The dimensions are not to scale

6.1 Box

The first six problems (B1 to B6) are solved using the *Box* geometry. The thickness is fixed in the first three problems, B1–B3 (Fig. 8a–c). The problem consists of identifying the optimal fiber orientations which maximize the stiffness (or minimize the compliance) of the beam. In the subsequent examples, B4 to B6 (see Fig. 8d–f), the thickness design variables are allowed to vary and results are presented for the minimum weight problem with a compliance constraint.

In Fig. 8a and d, the transverse force induces a bending moment which has the largest value at the root of the beam and varies linearly along the length vanishing at the tip. Consequently, the top and bottom faces are subjected to normal stress while the side faces are subjected to a combination of normal and shear stress. In Fig. 8a the fibers at all faces orient along the length direction to resist the normal stresses. In Fig. 8d, the thickness of the faces adjusts to compensate for the bending moment. The top and bottom faces are consequently thicker at the root and progressively

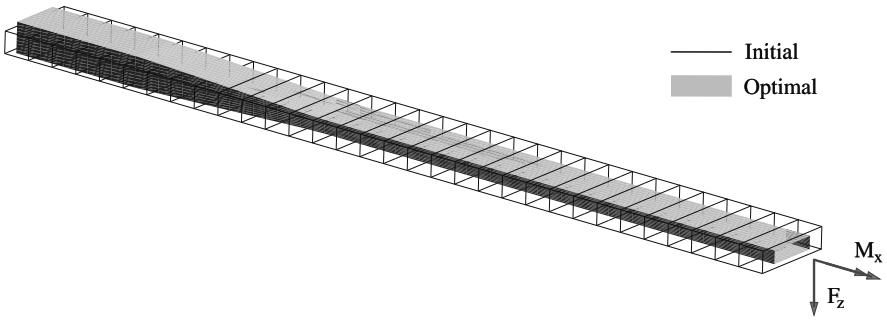

Fig. 9 Optimal thickness distribution for a cantilever beam with the *Rectangle* cross section geometry. The beam is subject to a combination of transverse forces and torsional moments (Example R1). Results obtained for the minimum weight problem with compliance constraints. Dimensions are not to scale

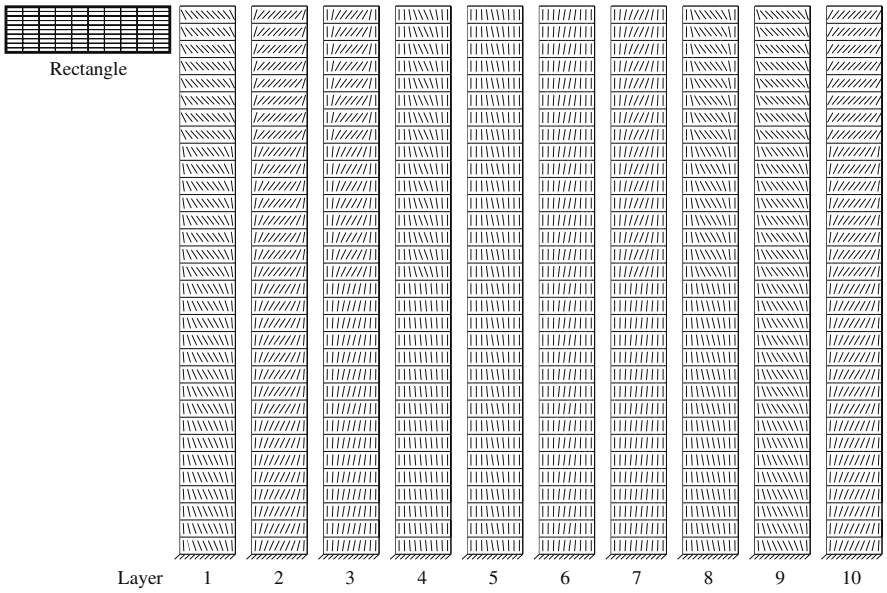

Fig. 10 Optimal fiber orientations for a cantilever beam with the *Rectangle* cross section geometry. The beam is subject to a combination of transverse forces and torsional moments (Example R1). Results obtained for the minimum weight problem with compliance constraints. Dimensions are not to scale

thinner towards the free end. The side faces are as thin as possible along the whole length excepting the cross section at the root where the thickness increases slightly. In this case, shear stress dominates in the thin side faces. As a result, the optimal fiber directions tend to 45° and −45° orientations corresponding to the orientation of the principal stresses.

In the cases B2 and B5, the torsional moment applied at the free end induces a constant torsional moment distribution along the length of the beam. The resulting designs can been seen in Fig. 8b and e. All faces are subjected to shear stress and the laminate on the faces arranges accordingly. The solution consists of [45°, −45°, 45°] or [−45°, 45°, −45°] laminates. Once again, this is in accordance with the orientation of the principal stresses for a structure subject to shear stress. The thickness remains constant throughout the length of the beam due to the constant torsional moment distribution along the length.

Finally, in the cases B3 and B6 the beam is subjected to a combination of transverse force and torsional moment. The results are presented in Fig. 8c and f. In this case, shear stress induced by both the transverse force and the torsional moment dominates on the side faces. As such, and as discussed before for the torsion case, the resulting optimal laminates are composed of −45° and 45° all throughout the length. The fibers in top and bottom face align in the length direction close to the root where the bending moment is larger. Closer to the free end the magnitude of the bending moment is decreased and the fibers align at −45° and 45° to compensate for the shear stress induced by the torsional

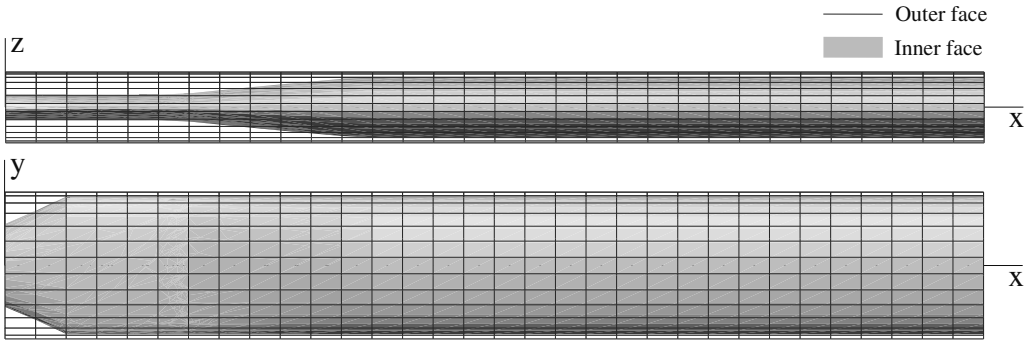

Fig. 11 Optimal thickness distribution for a cantilever beam with the *Ellipse* cross section geometry. The beam is subject to distributed loads in two directions and a distributed torsional moment (Example E1). Results obtained for the minimum weight problem with compliance constraints. Dimensions are not to scale

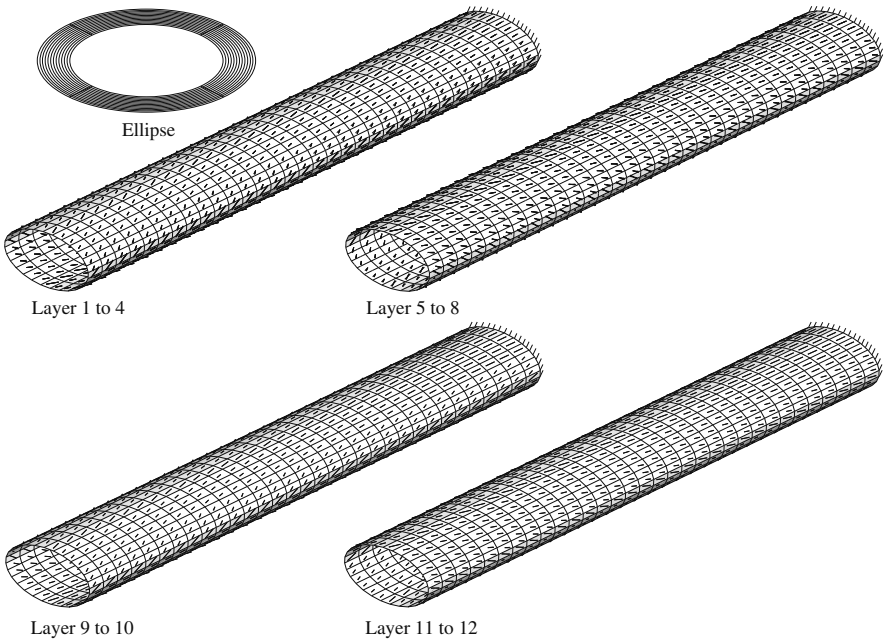

Fig. 12 Optimal fiber orientations for a cantilever beam with the *Ellipse* cross section geometry. The beam is subject to distributed loads in two directions and a distributed torsional moment (Example E1). Results obtained for the minimum weight problem with compliance constraints. Dimensions are not to scale

moment. As before, the thickness variation is dictated by the bending moment distribution. The top and bottom faces become thicker towards the free end whereas the side faces have a constant thickness equal to the allowable minimum. Once again it is observable the influence of the thickness variation on the resulting fiber orientations.

In the next examples much of the features observed before will be repeated. The variation of thickness is dictated mostly by the bending moment distribution. Laminates in regions away from the neutral axis and close to the root will tend to be thicker. In general, the fibers will tend to align in the direction of the principle stresses. In the regions where normal stress dominates the fibers will typically align in the direction of the beam length. Regions of the beam subjected to shear stresses will have lower thickness and the laminate will tend to align close to the $-45°$ and $45°$ directions.

6.2 Rectangle

The next problem concerns the design optimization of a laminated composite beam with the *Rectangle* cross section geometry—example R1. The beam is subjected to a symmetric loading comprising transverse forces and torsional moments. In this example, the results are propagated along the thickness, width, and length of the beam. The problem is initially solved using one cross section with one patch and 5 layers (1S 1P 5L case). The number of layers along the thickness is increased first (1S 1P 10L) and then the patches along the width (1S 10P 10L). Finally, the optimal fiber orientations are identified for problems with a growing number of cross sections along the length. The optimal thickness distribution is presented in Fig. 9 while the optimal fiber orientations can be seen in Fig. 10 for each of the ten layers. The result is a symmetric laminate across the thickness. The shear stress is larger in the outer layers which consequently align away from the $0°$ direction. Note the difference on the fiber orientation across the width where the fibers at the edges of all layers tend to align in the length direction (the reason for this is not clear).

6.3 Ellipse

Finally, the beam with the *Ellipse* cross section geometry is optimized—example E1. The resulting thickness distribution and fiber orientations are presented in Figs. 11 and 12. The beam is subject to distributed loads in two directions and a distributed torsional moment. This loading condition mimics the general properties of the wind loading typically acting on a wind turbine blade. The number of layers is increased progressively from three to 12. Results obtained with 24 layers showed a negligible reduction in weight. The number of cross sections along the length is gradually increased from one to 32. The thickness distribution is presented in Fig. 11. The thicker section is at the root. Moving towards the free end, the thickness first decreases in the y direction and then in the z direction. The resulting

Table 8 Summary of results for all numerical experiments obtained for the minimum weight problem with a constraint on the average compliance (*P1*), and the minimum compliance problem (*P2*). The discretization column describes the number of cross sections (*S*), patches (*P*), and layers (*L*) considered in each problem. The number of design variables associated with fiber orientations and thickness are given as n_θ and n_t, respectively. The number of objective function and constraint evaluations (# O.F.E.), the final compliance and weight values, are given next

Ref.	Discretization	n_θ	n_t	# O.F.E.	Compliance	Weight
B1	1S 4P 3L	12	Fixed	≈ 10	3.477	–
B2	1S 4P 3L	12	Fixed	≈ 10	1.523	–
B3	1S 4P 3L	12	Fixed	≈ 10	7.266	–
	2S 4P 3L	24	Fixed	22 (22)	7.010	–
	4S 4P 3L	48	Fixed	19 (41)	6.919	–
	8S 4P 3L	96	Fixed	24 (65)	6.896	–
	16S 4P 3L	192	Fixed	14 (79)	6.889	–
	32S 4P 3L	384	Fixed	11 (90)	6.888	–
B4	1S 4P 3L	12	2	≈ 10	3.069	25.919
	2S 4P 3L	24	4	111 (111)	3.069	23.976
	4S 4P 3L	48	8	50 (161)	3.069	22.740
	8S 4P 3L	96	16	60 (221)	3.069	22.573
	16S 4P 3L	192	32	16 (237)	3.069	22.533
	32S 4P 3L	384	64	17 (254)	3.069	22.521
B5	1S 4P 3L	12	2	≈ 10	1.523	25.919
B6	1S 4P 3L	12	2	≈ 10	6.523	25.919
	2S 4P 3L	24	4	153 (153)	6.523	23.666
	4S 4P 3L	48	8	182 (335)	6.523	22.927
	8S 4P 3L	96	16	228 (563)	6.523	22.689
	16S 4P 3L	192	32	310 (873)	6.523	22.631
	32S 4P 3L	384	64	387 (1,260)	6.523	22.617
R1	1S 1P 5L	5	2	≈ 10	26.786	4.500
	1S 10P 10L	100	2	37 (37)	26.786	4.321
	2S 10P 10L	200	4	20 (57)	26.786	4.205
	4S 10P 10L	400	8	18 (75)	26.786	4.182
	8S 10P 10L	800	16	18 (93)	26.786	4.181
	16S 10P 10L	1,600	32	9 (102)	26.786	4.180
E1	1S 4P 3L	12	2	≈ 10	6.266	10.944
	1S 4P 6L	24	2	126 (126)	6.266	10.935
	1S 4P 12L	48	2	38 (164)	6.266	10.934
	2S 4P 12L	96	4	46 (210)	6.266	9.573
	4S 4P 12L	192	8	93 (303)	6.266	9.271
	8S 4P 12L	384	16	77 (380)	6.266	9.214
	16S 4P 12L	768	32	93 (473)	6.266	9.200
	32S 4P 12L	1,536	64	16 (489)	6.266	9.197

layer groups suggest that the results are not simply repeated between the increasingly larger problems. Instead, the fiber orientations are sufficiently free to vary between iterations.

6.4 Other problem formulations

All results presented before have been obtained for the minimum weight problem with a constraint on the average compliance (P1), and the minimum compliance problem (P2). Some of the examples have also been solved for the minimum weight problem with a constraint on the compliance for each load case (P3), and the minimum maximum compliance with a constraint on the total weight (P4). The results are presented in Table 9 where the stated compliance values are the weighted average of each load case as calculated in (P1).

Table 9 Summary of results obtained for the minimum weight problem with a constraint on the compliance for each load case (*P3*), and minimum maximum compliance with a constraint on the total weight (*P4*). The discretization column describes the number of cross sections (*S*), patches (*P*), and layers (*L*) considered in each problem. The number of design variables associated with fiber orientations and thickness are given as n_θ and n_t, respectively. The number of objective function and constraint evaluations (# O.F.E.), the final weighted average compliance and weight values, are given next

Ref.	Discretization	n_θ	n_t	# O.F.E.	Compliance	Weight
B7	1S 4P 3L	12	2	≈ 10	6.731	25.919
	2S 4P 3L	24	4	138 (138)	6.492	25.919
	4S 4P 3L	48	8	200 (338)	6.350	25.919
	8S 4P 3L	96	16	178 (516)	6.302	25.919
	16S 4P 3L	192	32	171 (687)	6.292	25.919
	32S 4P 3L	384	64	126 (813)	6.290	25.919
R2	1S 1P 5L	5	2	≈ 10	26.814	4.500
	1S 10P 10L	100	2	69 (69)	26.814	4.341
	2S 10P 10L	200	4	34 (103)	26.814	4.213
	4S 10P 10L	400	8	17 (120)	26.814	4.189
	8S 10P 10L	800	16	31 (151)	26.814	4.185
	16S 10P 10L	1,600	32	11 (162)	26.814	4.184
E2	1S 4P 3L	12	2	≈ 10	6.266	10.944
	1S 4P 6L	24	2	49 (49)	6.266	10.935
	1S 4P 12L	48	2	32 (81)	6.266	10.934
	2S 4P 12L	96	4	30 (111)	6.266	9.573
	4S 4P 12L	192	8	73 (184)	6.266	9.272
	8S 4P 12L	384	16	38 (222)	6.266	9.216
	16S 4P 12L	768	32	65 (287)	6.265	9.204
	32S 4P 12L	1,536	64	26 (313)	6.264	9.201

The compliance values are very similar for all load cases. Thus, there are no significant differences in the optimal fiber orientations for the results obtained using the different problem formulations. A comparison between the optimal width and height distribution for case B6 and B7 are presented in Fig. 13. The optimal thickness distribution for case R2 and E2, do not present significant variations when compared to the corresponding case, R1 and E1, respectively. These results serve to illustrate that the proposed approach can also be used with different problem formulations.

6.5 Discussion

All numerical results and the procedure adopted in each of the numerical experiments are summarized in Table 8. The discretization column specifies the way in which the number of layers, patches and cross sections is increased at each step. The following two columns indicate the number of design variables associated with fiber orientation and laminate thickness, n_θ and n_t, respectively. The number of objective function evaluations (# O.F.E.) is given next. This corresponds also to the number of times the global stiffness matrix is assembled and factorized. Finally, the resulting compliance and weight values are presented.

Note that problems B1, B2, and B5 do not benefit from an increase in the number of design variables. The design presented is that obtained using one cross section only along

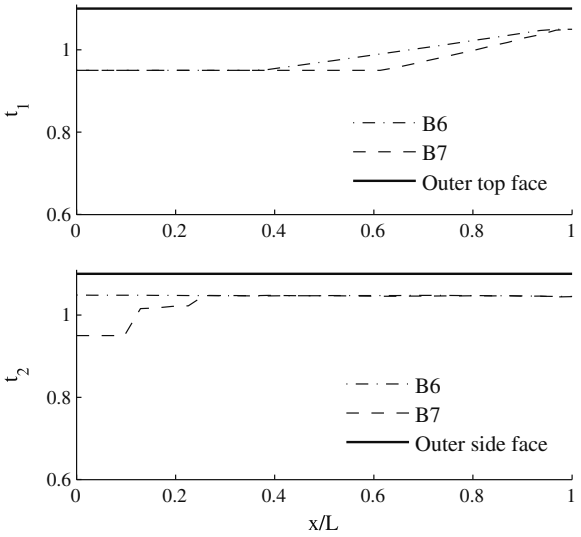

Fig. 13 Optimal variation of top and side face thickness along the beam length for B6 and B7 cases

the length. The number of objective function evaluations, in most of the smaller problems, is less than 10. Problem B6, on the other hand, requires a total of 1,260 objective function evaluations and is the most difficult problem to solve. Problems with a larger number of design variables, like R1 and E1, require around two and ten times less objective function evaluations, respectively. Finally, note in example E1 how an increase in the number of layers from six to 12 results in a very small increase in stiffness and consequent decrease in the total weight.

The number of objective function evaluations may be reduced by increasing the optimality and feasibility tolerances. Example B6 is solved again using an optimality tolerance of 1×10^{-4} (instead of 1×10^{-5}). In this case only 589 objective function evaluations are required to reach the final design. The objective function value or the final weight, however, is slightly higher reaching 22.627. Another possibility consists of interchanging the objective and constraint functions. That is, to solve the minimum compliance problem with weight constraints instead. The example B6 is used again. A total of 957 objective function evaluations are required in this case corresponding to a decrease of about 20% in the number of objective function evaluations. The objective function values are not comparable in this case.

The use of optimization techniques may lead to designs which are sensitive to perturbations of the design variables. The robustness of the optimal designs with respect to the fiber orientations is therefore evaluated. Two types of perturbations are considered. In a first case the design variables are randomly perturbed by a given amount. In the random perturbation case two different perturbation magnitudes are considered — $\pm 4.5°$ and $\pm 9°$ corresponding to 2.5 and 5% of the design variable range, respectively. The optimal design of problem E1 and R1 are used as the baseline designs. The compliance of 100 randomly perturbed designs is evaluated for each baseline design and the maximum value is recorded. In the E1 case the maximum compliance value is 6.304 and 6.423 for $\pm 4.5°$ and $\pm 9°$ perturbations, respectively. This corresponds to a relative difference of 0.72 and 2.61%, respectively, when compared to the values presented in Table 8. In the R1 case the maximum compliance values were 27.212 and 28.140 for $\pm 4.5°$ and $\pm 9°$ perturbations, respectively. This corresponds to a relative difference of 1.6 and 5%, respectively, when compared to the baseline values. Finally, in the second case all design variables are offset by the same amount and the corresponding compliance is evaluated. Using the E1 case as the baseline design and adding $\pm 4.5°$ and $\pm 9°$ to all fiber angle design variables, the resulting compliance values are 6.572 and 7.326. This corresponds to a relative difference of 5 and 17%. In the R1 case, the resulting compliance values are 29.275 and 29.060 which corresponds to an increase of 9.29 and 8.49%, respectively.

Finally, from a manufacturing standpoint, the incorporation of varying fiber orientations along the length of the beams, and the small tolerances in the fiber orientations may prove impractical. Concerning the latter, an approach is suggested where the fiber angles are rounded to a predefined set of angles, say, 0°, 45°, −45° and 90°. This approach has been applied to the optimal result of case R1. The resulting fiber orientations are presented in Fig. 14. The compliance of the obtained design is 9.3% larger than the original. In summary, the devised approach intends to be a valuable tool at the conceptual design phase where manufacturing

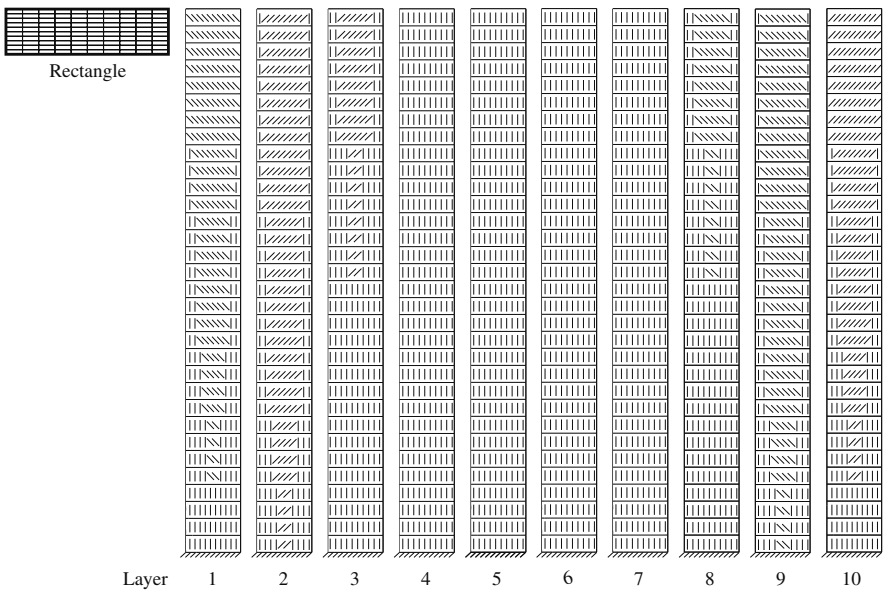

Fig. 14 Optimal fiber orientations obtained by rounding up the optimal angles of R1 (see Fig. 10) to 0°, 45°, −45° and 90°

constraints are not necessarily accounted for. The resulting optimal designs highlight important structural design features which should be considered at later stages of the design process.

7 Summary and future work

A beam finite element model has been implemented and validated. The formulation of the minimum weight optimal design problem with a constraint on the weighted average of the compliances for multiple load cases is described. The design variables are the fiber orientations and the total laminate thickness of the cross sections. Three different cantilever beam geometries have been considered—box, solid rectangular, and elliptic. An optimization strategy is devised which consists of solving a succession of problems with an increasing number of design variables. The optimal design of the former is the initial point for the next problem in the sequence. The numerical results indicate that the devised strategy succeeds in overcoming the problem with local minima inherent to the use of fiber angles as design variables. Furthermore, this work highlights the possibility and advantages of incorporating a beam finite element model in an optimal design framework to solve large-scale structural optimization problems.

In future work, the design variables will represent volume fractions of different materials. This approach will allow for the simultaneous optimization of laminate stacking sequence and material distribution. Design dependent aerodynamic loads will moreover be included. The benefits of the beam finite element model will be apparent in this case as the reduced size of the resulting structural matrices will allow for a significant decrease in computation time. The framework will be applied to simultaneously optimize the structural lay-out and the aerodynamic loading of wind turbine blades.

Acknowledgments The authors would like to thank the two anonymous reviewers for their constructive comments and suggestions. The computer resources were funded by the Danish Center for Scientific Computing (www.dcsc.dk) grant CPU-0107-07 “Optimal design of composite structures”.

References

Bathe KJ (1982) Finite element procedures in engineering analysis. Prentice-Hall, Englewood Cliffs

Bendsøe MP, Sigmund O (2003) Topology optimization: theory, methods and applications, 2nd edn. Springer, Berlin

Chaviaropoulos PK et al (2006) Enhancing the damping of wind turbine rotor blades—the DAMPBLADE project. Wind Energy 9:163–177

Ganguli R, Chopra I (1995) Aeroelastic optimization of a helicopter rotor with composite coupling. J Aircr 32(6):1326–1334

Gill PE, Murray W, Saunders MA (2002) SNOPT: an SQP algorithm for large scale constrained optimization. SIAM J Optim 121(4):979–1006

Gürdal Z, Haftka RT, Hajela P (1999) Design and optimization of laminated composite materials, 1st edn. Wiley, New York

Hammer VB, Bendsøe MP, Lipton R, Pedersen P (1997) Parametrization in laminate design for optimal compliance. Int J Solids Struct 34(4):415–434

Hansen MH (2003) Improved modal dynamics of wind turbines to avoid stall-induced vibrations. Wind Energy 6:179–195

Jeronimidis G, Karaolis NM, Musgrove PJ (1991) Power control of wind turbine blades through structural design. In: Smart structures and materials. ASME, New York, p 123

Jung SN, Nagaraj VT, Chopra I (1999) Assessment of composite rotor blade modeling techniques. J Am Helicopter Soc 4(3):188–205

Kathiravan R, Ganguli R (2007) Strength design of composite beams using gradient and particle swarm optimization. Compos Struct 81(4):471–479

Le Riche R, Haftka RT (1993) Optimization of laminate stacking sequence for buckling load maximization by genetic algorithm. AIAA J 51(5):951–956

Li L, Volovoi VV, Hodges DH (2008) Cross-sectional design of composite rotor blades. J Am Helicopter Soc 53(3):240–251

Lund E, Stegmann J (2005) Discrete material optimization of general composite shell structures. Int J Numer Methods Eng 62(14): 2009–2027

Maute K, Nikbay M, Farhat C (2003) Sensitivity analysis and design optimization of three dimensional non-linear aeroelastic systems by the adjoint method. Int J Numer Methods Eng 56:911–933

Miki M, Sugiyama Y (1993) Optimum design of laminated composite plates using lamination parameters. AIAA J 31:921–922

Murugan SM, Ganguli R (2005) Aeroelastic stability enhancement and vibration supression in a composite helicopter rotor. J Aircr 42(4):1013–1024

Neto MA, Yu W, Leal RP (2008) Generalized Timoshenko modelling of composite beam structures: analysis and optimal design. Eng Optim 40(10):891–906

Pedersen P (1991) On thickness and orientational design with orthotropic materials. Struct Optim 3:69–78

Shirk M, Hertz T, Weisshaar T (1985) Aeroelastic tailoring—theory, practice and promise. J Aircr 23(1):6–18

Stegmann J, Lund E (2005) On structural optimization of composite shell structures using a discrete constitutive parametrization. Wind Energy 8(1):109–124

Stolpe M, Stegmann J (2007) A Newton method for solving continuous multiple material minimum compliance problems. Struct Multidisc Optim 35(2):93–106

Tsai SW, Pagano NJ (1968) Invariant properties of composite materials. In: Tsai SW, Halpin JC, Pagano NJ (eds) Composite materials workshop. Technomic Publishing Co., Westport, pp 233–253

Veers P, Bir G, Lobitz D (1998) Aeroelastic tailoring in windturbine blade applications. Presented at Windpower 98, American Wind Energy Association meeting and exhibition, Bakersfield, California, 28 April–1 May 1998

Volovoi VV, Hodges DH, Cesnik CES, Popescu B (2001) Assessment of beam modeling methods for rotor blade applications. Math Comput Model 33:1099–1112

Yu W (2007) Efficient high-fidelity simulation of multibody systems with composite dimensionally reducible components. J Am Helicopter Soc 52(1):49–58

Yu W, Hodges DH (2005) Generalized Timoshenko theory of the variational asymptotic beam sectional analysis. J Am Helicopter Soc Society 50(1):46–55

Yu W, Volovoi V, Hodges DH, Hong X (2002) Validation of the variational asymptotic beam sectional analysis (VABS). AIAA J 40(10):2105–2113

Paper 2

Blasques J.P., Stolpe M., Multi-material topology optimization of laminated composite beam cross sections, submitted, 2011.

Multi-material topology optimization of laminated composite beam cross sections

José Pedro Blasques
Risø National Laboratory for Sustainable Energy
Technical University of Denmark
Frederiksborgvej 399, P.O. Box 49, Building 114, 4000 Roskilde
jpb@risoe.dtu.dk

Mathias Stolpe
Department of Mathematics
Technical University of Denmark
Matematiktorvet, Building 303S, DK-2800 Kgs. Lyngby, Denmark
m.stolpe@mat.dtu.dk

November 10, 2011

Abstract

This paper presents a novel framework for simultaneous optimization of topology and material properties in structural design of beam cross sections. The structural response of the beam is evaluated using a beam finite element model comprising a cross section analysis tool which is suitable for the analysis of anisotropic and inhomogeneous sections of arbitrary geometry. The optimization framework is based on a multi-material topology optimization model in which the design variables represent the amount of the given materials in the cross section. Existing material interpolation, penalization, and filtering schemes have been extended to accommodate any number of anisotropic materials. The methodology is applied to the optimal design of several laminated composite beams with different cross sections. Solutions are presented for a minimum compliance (maximum stiffness) problem with constraints on the weight, and the shear and mass center positions. The practical applicability of the method is illustrated by performing optimal design of an idealized wind turbine blade subjected to static loading of aerodynamic nature. The numerical results suggest that the proposed framework is suitable for simultaneous optimization of cross section topology and identification of optimal material properties in structural design of laminated composite beams.

Keywords: Beams, Cross section analysis, Laminated composites, Multi-material topology optimization

1 Introduction

This paper describes a methodology for simultaneous optimization of the topology and the material properties of beam cross sections. The objective in the considered optimal design problems is to minimize the compliance of the beam, i.e. to maximize stiffness, with constraints on the weight and the shear and mass center positions. The design variables represent the volume fractions of each of a predefined set of candidate materials in the cross section. The structural response of the beam is computed using a beam finite element model which incorporates an efficient and accurate cross section analysis tool able to account for the effects of material anisotropy and inhomogeneity in sections of arbitrary geometry.

The work presented here is based on the developments in the field of multi-material topology optimization, see e.g. Bendsøe and Sigmund [20] and Sigmund and Torquato [23]. The work is also inspired by the ideas for optimal design of composite structures suggested by Lund and Stegmann [26] and Stegmann and Lund [27]. We follow a common approach in topology optimization and replace the discrete design variables by continuous variables and attempt to force the variables to their bounds by an appropriate material model. The model is based on an extension of the SIMP material interpolation scheme to problems with multiple (anisotropic) materials. For an overview of material interpolation schemes we refer you to Bendsøe and Sigmund [22, 20]. Certain problems in topology optimization suffer from undesirable features such as mesh-dependency and checkerboard patterns in the design, see e.g. Sigmund and Petersson [34]. These issues can be resolved by regularization of the problem, for example by filtering of the design variables as described in Bourdin [35]. The filtering technique of Bruns and Tortorelli [33] is here extended to multi-material problems and utilized to avoid mesh-dependency and the appearance of checkerboard patterns. Analytical expressions for the gradients of the cross section stiffness parameters and shear and mass center position are derived. The optimal design problems can therefore be solved using any modern and robust numerical optimization method for continuous constrained optimization.

The proposed methodology is applied to the design of laminated composite beams. Several numerical results are presented which illustrate the ability of the method in solving the problem of identifying the optimal cross section topology and the material properties (see Figure 1). The applicability of the method is attested by the results presented for the maximum stiffness optimization of an idealized wind turbine rotor blade cross section with prescribed weight and, shear and mass center placement constraints.

Several approaches have been presented in the literature for optimal design of beams combining different structural models and optimization problems. A methodology combining a beam finite element model and a cross section analysis tool was presented by Blasques and Stolpe [12] for maximum stiffness and minimum weight design of laminated composite beams. The three dimensional

variation of laminate thickness, stacking sequence, and fiber orientation of several composite beams with different cross section shapes were optimized. Based on the same cross section analysis tool, Li et al. [17] optimized the cross sectional stiffness and inertia properties of a helicopter rotor blade. The aim was to improve the static and dynamic properties of the blade. Similarly, the work by Ganguli and Chopra [18] and Murugan and Ganguli [19] addressed optimal design of laminated composite beams with stiffness and aeroelastic constraints. The design variables were the fiber orientations of the laminate on the walls of the internal blade spar.

The references in the preceding paragraph all assumed that the topology of the beam was to a large extent fixed and the problem consisted mostly of optimizing the material properties. That is, the optimal design of the cross section topology or structural lay-out was not fully addressed. The work by Kim and Kim [14] is perhaps the first reference using topology optimization in the optimal design of the structural lay-out of thin-walled beam cross sections. The bending and torsional stiffnesses were obtained based on Euler beam theory and a finite element representation of the Saint-Venant's torsion problem, respectively. The same authors have later used a model based on Poisson's equations and Prandtl's stress function to analyze the deformation of cross sections subjected to torsion (Kim and Kim [13]). The structural lay-out of beam cross sections was optimized using topology optimization to simultaneously increase torsional stiffness and reduce cross section distortion. Donoso and Sigmund [16] have used a similar approach to optimize the cross section topology and maximize the cross section distortion to produce "warping mechanisms".

The references in the previous paragraph consider only isotropic materials and do not address optimization of material properties. The methodology described in this paper allows for the simultaneous optimization of the cross section topology and distribution of given (anisotropic) materials.

Three different analysis models have been generally considered in the literature for the structural analysis of beam structures – beam, shell, and solid finite elements. Solid and shell finite element models offer high accuracy. These are suitable for the simultaneous estimation of the global response of the beam and analysis of localized effects like local buckling or stress concentrations. The main disadvantage is that these analysis models can become computationally expensive. Beam finite elements, on the other hand, are built on specific assumptions and suitable only for the analysis of relatively long and slender structures. These assumptions allow for a significant reduction in the size of the resulting global finite element matrices. This type of analysis model is therefore attractive in applications requiring a large number of evaluations of the equilibrium equations such as wind turbine aeroelastic analysis codes (see, e.g., Hansen et al. [40]). When combined with advanced cross section analysis techniques, it is possible to obtain accurate estimates of both the global response of the beam and, to a certain extent, the three dimensional stress field.

Reviews on the different cross section analysis tools described in the literature

are presented by Jung et al. [1] and Volovoi et al. [2]. Probably the most comprehensive work in this field is that by Hodges (Hodges [6]) and co-workers (Yu and Hodges [4]). The beam formulation builds on the Variational Asymptotic Method (VAM) which was first used in this context by Berdichevskii [3]. The theory has served as the basis for the development of the Variational Asymptotic Beam Section analysis tool (VABS) decribed and validated in Yu and Hodges [4] and Yu et al. [5].

The cross section analysis tool used in this paper is based on the theory introduced by Giavotto et al. [7], and further detailed by Ghiringelli and Mantegazza [8], and Ghiringelli [9]. The formulation is based on the Saint-Venant's principle where only solutions away from the ends of the beam are considered. The cross section warping displacements are approximated using a finite element discretization of the cross section geometry. The formulation is able to account for the effects of material anisotropy and inhomogeneity in cross sections of arbitrary geometry. The theory has been implemented in BECAS – BEam Cross section Analysis Software (Blasques and Lazarov [10]). BECAS has been validated against VABS and exactly the same magnitude of the cross section stiffness parameters has been obtained for a series of cases including, anisotropic, inhomogeneous, closed, open, and multi-celled, cross sections (Blasques and Lazarov [10]). Effects like tapering, pre-twist, and curvature have not yet been accounted for.

The paper is organized as follows. The structural model, with special emphasis on the cross section analysis, is described in Section 2. The formulation of the optimal design problems and the material interpolation and filtering techniques are presented in Section 3. The analytical expressions for the sensitivities of the beam stiffness matrix and specifically of the cross section stiffness parameters are presented in Section 4. The implementation is described in Section 5. The setup of the numerical experiments and the corresponding results and discussion is presented in Section 6. Finally, the main conclusions of this paper and suggestions for future research topics are summarized in Section 7.

2 Structural model

The structural model is described in detail in order to keep the manuscript self-contained. A formulation for a linear elastic beam finite element of arbitrary section geometry accounting for the effects of material anisotropy and inhomogeneity is presented here. The construction of the beam finite element model is divided into two parts - the analysis of the cross section properties and the consequent generation of the beam finite element model by integration of these properties along the beam length. The analysis of the cross section properties is performed according to the theory by Giavotto et al. [7]. Based on the present formulation it is possible to retrieve a generalized form of the Timoshenko cross section compliance matrix, $\mathbf{F}_s$, which accounts for any elastic effects induced by material anisotropy and inhomogeneity, for sections of arbitrary geometry. Finally, the beam finite

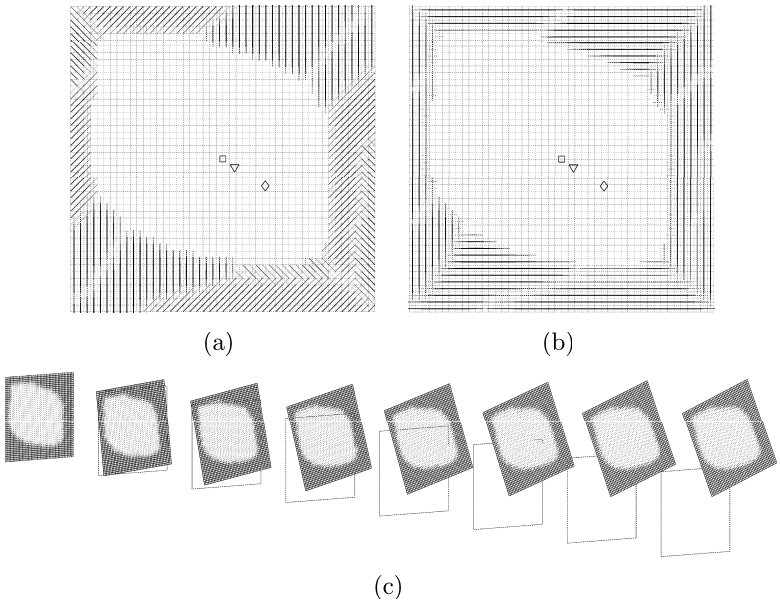

(a) (b)

(c)

Figure 1: Optimal material distribution and deformed shape for a beam with a square cross section. The presented design is a solution to the minimum compliance problem with a weight constraint. The beam is subjected to a distributed horizontal transverse force F_x, vertical transverse force F_y, and torsional moment M_z. Nine different candidate materials have been considered: orthotropic laminate (as solid lines) may be stacked in two directions parallel to either horizontal or vertical plane and may be oriented at $0°$, $45°$, $-45°$ and $90°$, and isotropic material (in white). (a) Optimal fiber orientation (lines) and distribution of isotropic material (white). Vertical and horizontal orientation are coincident with length and transverse directions, respectively. (b) Optimal fiber plane orientation (lines) and distribution of isotropic material. Horizontal and vertical lines indicate the laminate is stacked parallel to horizontal and vertical planes, respectively. (c) The deformed shape of the beam. The dimensions and magnitude of deformations are not to scale.

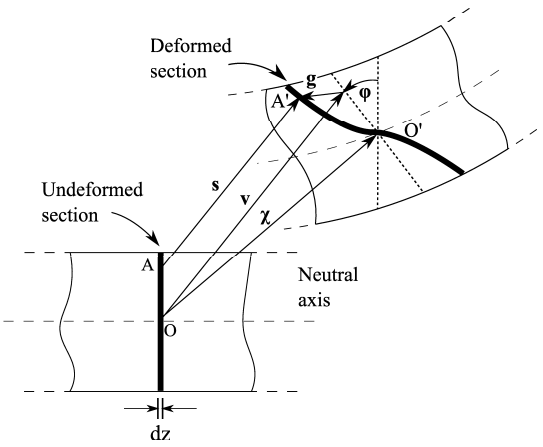

Figure 2: Total displacement $\mathbf{s}$ of a point in the cross section. The displacement is composed of a translation $\boldsymbol{\chi}$, a rotation $\boldsymbol{\varphi}$, and a warping displacement $\mathbf{g}$.

element stiffness matrix is generated by integration of the cross section properties following the isoparametric approach (see, e.g., Bathe [31]). The devised model is based on the assumptions that the loads are static, displacements are small, and that the material is linear elastic.

2.1 Cross section analysis

The theory presented in this section assumes that the beam structure is relatively long and slender and does not present abrupt variations in cross section geometry, load distribution and material properties along its length. Consequently, the resulting displacement and strain gradients along the beam axis are assumed to be relatively small. In the case where these assumptions are not fulfilled care should be taken in the interpretation of the results. The assumptions mentioned before are not imposed along the cross section coordinates in the cross section plane. For clarity, the notation throughout this section has been kept close to that adopted by Giavotto et al. in [7].

2.1.1 General properties

Let us consider a slice dz of a beam (cf. Figure 2). The strain and stresses acting at a point in the slice representing the cross section of the beam are $\boldsymbol{\epsilon} = [\epsilon_{xx}\ \epsilon_{yy}\ 2\epsilon_{xy}\ 2\epsilon_{xz}\ 2\epsilon_{yz}\ \epsilon_{zz}]^T$, $\boldsymbol{\sigma} = [\sigma_{xx}\ \sigma_{yy}\ \sigma_{xy}\ \sigma_{xz}\ \sigma_{yz}\ \sigma_{zz}]^T$ which are related by the stress-strain relation or Hooke's law as $\boldsymbol{\sigma} = \mathbf{Q}\boldsymbol{\epsilon}$. In this case, $\mathbf{Q}$ is the material constitutive matrix.

The internal forces $\mathbf{T} = [T_x\ T_y\ T_z]^T$ and moments $\mathbf{M} = [M_x\ M_y\ M_z]^T$ acting at a beam section are described in Figure 3(a). The components of the force vector consist of the transverse forces T_x and T_y acting in the plane of the section, and the tension force T_z. The moment vector is defined by the bending moment

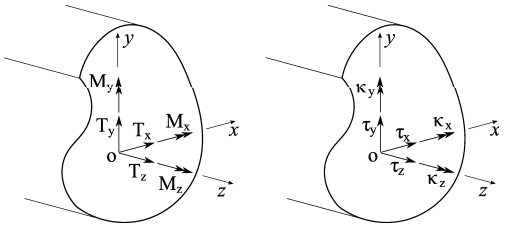

(a) Forces and moments (b) Strains and curvatures

Figure 3: Section coordinate system, forces and moments (a) and corresponding strains and curvatures (b).

components M_x and M_y, and the torsion moment M_z. These forces and moments are statically equivalent to the stress components $\mathbf{p} = [\sigma_{xz}\ \sigma_{yz}\ \sigma_{zz}]^T$ acting on the section face and defined as

$$\mathbf{T} = \int_A \mathbf{p}\ \mathrm{dA}, \quad \mathbf{M} = \int_A \mathbf{n}^T\mathbf{p}\ \mathrm{dA}$$

where

$$\mathbf{n} = \begin{bmatrix} 0 & -z & y \\ z & 0 & -x \\ -y & x & 0 \end{bmatrix} \tag{1}$$

and A is the cross section area. The coordinates x and y in the section plane are given with respect to the cross section reference point O (cf. Figure 2). The vector of section forces $\boldsymbol{\theta} = \begin{bmatrix}\mathbf{T}^T\ \mathbf{M}^T\end{bmatrix}^T$ is thus defined as

$$\boldsymbol{\theta} = \int_A \mathbf{Z}^T\mathbf{p}\ \mathrm{dA}$$

where the matrix $\mathbf{Z} = \begin{bmatrix}\mathbf{I}_3 & \mathbf{n}^T\end{bmatrix}$, and $\mathbf{I}_3$ is an identity matrix of size 3×3.

The cross section deformations associated with the load vector $\boldsymbol{\theta}$ are described by the cross section strain-curvature vector $\boldsymbol{\psi} = \begin{bmatrix}\boldsymbol{\tau}^T\ \boldsymbol{\kappa}^T\end{bmatrix}^T$ (as described in Figure 3(b)). The shear component $\boldsymbol{\tau} = [\tau_x\ \tau_y\ \tau_z]^T$ is composed of the shear strains τ_x and τ_y, and the tension strain τ_z. The components of the vector of curvatures $\boldsymbol{\kappa} = [\kappa_x\ \kappa_y\ \kappa_z]^T$ are the bending curvatures κ_x and κ_y, and the twist rate κ_z. The section forces and moments in $\boldsymbol{\theta}$, and the strains and curvatures in $\boldsymbol{\psi}$ are related through the constitutive relation $\boldsymbol{\psi} = \mathbf{F}_s\boldsymbol{\theta}$ where $\mathbf{F}_s$ is the 6×6 cross section compliance matrix. For most practical applications $\mathbf{F}_s$ is symmetric positive definite. Hence $\mathbf{K}_s = \mathbf{F}_s^{-1}$, where $\mathbf{K}_s$ is the cross section stiffness matrix, and consequently the following relation holds $\boldsymbol{\theta} = \mathbf{K}_s\boldsymbol{\psi}$.

A methodology is presented in the next sections for the estimation of the parameters in $\mathbf{F}_s$. This formulation accounts for effects stemming from material anisotropy and inhomogeneity and is valid for cross sections of arbitrary geometry.

2.1.2 Beam kinematics

The total displacement $\mathbf{s} = [s_x \; s_y \; s_z]^T$ of a point in the cross section is (cf. Figure 2)

$$\mathbf{s} = \mathbf{v} + \mathbf{g}$$

where the displacement components $\mathbf{v} = [v_x \; v_y \; v_z]^T$ are associated with the rigid body translations and rotations of the cross section. Assuming small displacements and rotations,

$$\mathbf{v} = \mathbf{Z}\mathbf{r}$$

where $\mathbf{r} = \left[\boldsymbol{\chi}^T \; \boldsymbol{\varphi}^T\right]^T$. The components $\boldsymbol{\chi} = [\chi_x \; \chi_y \; \chi_z]^T$ represent the translations of the cross section reference point, while $\boldsymbol{\varphi} = [\varphi_x \; \varphi_y \; \varphi_z]^T$ are the cross section rotations. Finally, $\mathbf{g} = [g_x \; g_y \; g_z]^T$ is the displacement vector associated with the in- and out-of-plane cross section distortion or warping. The total displacement expression is restated as

$$\mathbf{s} = \mathbf{Z}\mathbf{r} + \mathbf{g} \tag{2}$$

Assuming small displacements, the strain-displacement relation is

$$\epsilon_{\alpha\beta} = \frac{1}{2}\left(\frac{\partial s_\alpha}{\partial \beta} + \frac{\partial s_\beta}{\partial \alpha}\right), \qquad (\alpha, \beta = x, y, z)$$

Replacing the total displacement expression in (2) in the equation above yields

$$\boldsymbol{\epsilon} = \mathbf{S}\mathbf{Z}\boldsymbol{\psi} + \mathbf{B}\mathbf{g} + \mathbf{S}\frac{\partial \mathbf{g}}{\partial z}$$

The strain-displacement matrices $\mathbf{B}$ and $\mathbf{S}$ are defined as

$$\mathbf{B} = \begin{bmatrix} \partial/\partial x & 0 & 0 \\ 0 & \partial/\partial y & 0 \\ \partial/\partial y & \partial/\partial x & 0 \\ 0 & 0 & \partial/\partial x \\ 0 & 0 & \partial/\partial y \\ 0 & 0 & 0 \end{bmatrix}, \quad \mathbf{S} = \begin{bmatrix} 0 & 0 & 0 \\ 0 & 0 & 0 \\ 0 & 0 & 0 \\ 1 & 0 & 0 \\ 0 & 1 & 0 \\ 0 & 0 & 1 \end{bmatrix}$$

where the derivatives $\partial/\partial z$ along the length of the beam have been conveniently separated and left unsolved. The vector of strains and curvatures $\boldsymbol{\psi} = \left[\boldsymbol{\tau}^T \; \boldsymbol{\kappa}^T\right]^T$ (cf. Figure 3(b)) is defined in function of the rigid body motions, $\mathbf{r}$, as

$$\boldsymbol{\psi} = \left(\mathbf{T}_r + \frac{\partial}{\partial z}\right)\mathbf{r} \tag{3}$$

where

$$\mathbf{T}_r = \begin{bmatrix} \mathbf{0}_3 & \mathbf{t}_r \\ \mathbf{0}_3 & \mathbf{0}_3 \end{bmatrix}, \quad \mathbf{t}_r = \begin{bmatrix} 0 & -1 & 0 \\ 1 & 0 & 0 \\ 0 & 0 & 0 \end{bmatrix},$$

and $\mathbf{0}_3$ is the 3×3 zero matrix. The resulting strain and curvature components in (3) are recognizable from typical beam theory and given as

$$\tau_x = \frac{\partial \chi_x}{\partial z} - \varphi_y, \quad \tau_y = \frac{\partial \chi_y}{\partial z} + \varphi_x, \quad \tau_z = \frac{\partial \chi_x}{\partial z}$$
$$\kappa_x = \frac{\partial \boldsymbol{\varphi}_x}{\partial z}, \quad \kappa_y = \frac{\partial \boldsymbol{\varphi}_y}{\partial z}, \quad \kappa_z = \frac{\partial \boldsymbol{\varphi}_z}{\partial z}$$

2.1.3 Finite element formulation

The continuous formulation presented in the previous section is herein approximated based on a finite element discretization of the cross section. It is assumed that the cross section geometry is discretized using, e.g., two dimensional isoparametric finite elements. The three dimensional warping displacements $\mathbf{g}$ is given by

$$\mathbf{g}(x, y) \approx \mathbf{N}(x, y)\mathbf{u} \tag{4}$$

where $\mathbf{N}$ is the matrix of finite element shape functions and $\mathbf{u}$ the nodal warping displacements. Inserting (4) in the expression for the total displacement in (2) yields

$$\mathbf{s} = \mathbf{Z}\mathbf{r} + \mathbf{N}\mathbf{u} \tag{5}$$

The corresponding finite element form of the three dimensional strain field $\boldsymbol{\epsilon}$ at the cross section level is

$$\boldsymbol{\epsilon} = \mathbf{S}\mathbf{Z}\boldsymbol{\psi} + \mathbf{B}\mathbf{N}\mathbf{u} + \mathbf{S}\mathbf{N}\frac{\partial \mathbf{u}}{\partial z}$$

2.1.4 Principle of virtual displacements

The principle of virtual displacements is subsequently invoked to derive the cross section equilibrium equations. The principle states that, at equilibrium, the total external virtual work per unit length, $\partial W_{ext}/\partial z$, has to be equal to the total internal virtual work per unit length, $\partial W_{int}/\partial z$, for any compatible, small virtual displacements. Hence, the following must hold

$$\frac{\partial W_{ext}}{\partial z} = \frac{\partial W_{int}}{\partial z} \tag{6}$$

The only contribution for the total external virtual work per unit length is stemming from the work done by the section stresses $\mathbf{p}$ going through the virtual displacements $\delta\mathbf{s}$. Hence,

$$\frac{\partial W_{ext}}{\partial z} = \int_A \frac{\partial \left(\delta \mathbf{s}^T \mathbf{p}\right)}{\partial z}\, \mathrm{dA} = \begin{bmatrix} \delta\frac{\partial \mathbf{u}^T}{\partial z} \\ \delta\mathbf{u} \\ \delta\boldsymbol{\psi} \end{bmatrix}^T \begin{bmatrix} \mathbf{P} \\ \frac{\partial \mathbf{P}}{\partial z} \\ \boldsymbol{\theta} \end{bmatrix} + \delta\mathbf{r}^T \left(\frac{\partial \boldsymbol{\theta}}{\partial z} - \mathbf{T}_r^T \boldsymbol{\theta}\right) \tag{7}$$

where

$$\mathbf{P} = \int_A \mathbf{N}^T \mathbf{p}\, \mathrm{dA}, \quad \frac{\partial \mathbf{P}}{\partial z} = \int_A \mathbf{N}^T \frac{\partial \mathbf{p}}{\partial z}\, \mathrm{dA}$$

are the nodal stresses acting in the cross section finite element discretization, and δ is the virtual operator.

The total internal virtual work per unit length corresponds to the elastic strain energy of the cross section. It is defined as the work done by the stresses $\boldsymbol{\sigma}$ along the virtual strains $\delta\boldsymbol{\epsilon}$ (associated with the virtual displacements), and given as

$$\frac{\partial W_{int}}{\partial z} = \int_A \delta\boldsymbol{\epsilon}^T \boldsymbol{\sigma}\, \mathrm{dA} = \begin{bmatrix} \delta\mathbf{u} \\ \delta\boldsymbol{\psi} \\ \delta\frac{\partial \mathbf{u}}{\partial z} \end{bmatrix}^T \begin{bmatrix} \mathbf{E} & \mathbf{R} & \mathbf{C} \\ \mathbf{R}^T & \mathbf{A} & \mathbf{L} \\ \mathbf{C}^T & \mathbf{L}^T & \mathbf{M} \end{bmatrix} \begin{bmatrix} \mathbf{u} \\ \boldsymbol{\psi} \\ \frac{\partial \mathbf{u}}{\partial z} \end{bmatrix} \tag{8}$$

Each of the system matrices presented above is defined as

$$\begin{aligned}
\underset{(6\times 6)}{\mathbf{A}} &= \sum_{e=1}^{n_e} \int_A \mathbf{Z}_e^T \mathbf{S}_e^T \mathbf{Q}_e \mathbf{S}_e \mathbf{Z}_e\, \mathrm{dA} & \underset{(n_d\times 6)}{\mathbf{R}} &= \sum_{e=1}^{n_e} \int_A \mathbf{N}_e^T \mathbf{B}_e^T \mathbf{Q}_e \mathbf{S}_e \mathbf{Z}_e\, \mathrm{dA} \\
\underset{(n_d\times n_d)}{\mathbf{E}} &= \sum_{e=1}^{n_e} \int_A \mathbf{N}_e^T \mathbf{B}_e^T \mathbf{Q}_e \mathbf{B}_e \mathbf{N}_e\, \mathrm{dA} & \underset{(n_d\times n_d)}{\mathbf{C}} &= \sum_{e=1}^{n_e} \int_A \mathbf{N}_e^T \mathbf{B}_e^T \mathbf{Q}_e \mathbf{S}_e \mathbf{N}_e\, \mathrm{dA} \\
\underset{(6\times n_d)}{\mathbf{L}} &= \sum_{e=1}^{n_e} \int_A \mathbf{Z}_e^T \mathbf{S}_e^T \mathbf{Q}_e \mathbf{S}_e \mathbf{N}_e\, \mathrm{dA} & \underset{(n_d\times n_d)}{\mathbf{M}} &= \sum_{e=1}^{n_e} \int_A \mathbf{N}_e^T \mathbf{S}_e^T \mathbf{Q}_e \mathbf{S}_e \mathbf{N}_e\, \mathrm{dA}
\end{aligned} \tag{9}$$

where e is the element number and n_e is the number of finite elements in the cross section mesh. The total number of degrees of freedom associated with the cross section finite element mesh is $n_d = n_n \times 3$ where the number of nodes n_n multiplies the number of degrees of freedom at each node – the three dimensional nodal displacements u_x, u_y, and u_z. The finite element matrices can be successfully built using, e.g., four node isoparametric finite elements. The sums in (9) refer to the typical assembly procedure used in finite element analysis.

The cross section equilibrium equations are obtained by inserting (7) and (8) in (6). The result must be true for any admissible virtual displacements – $\delta\boldsymbol{\psi}$, $\delta\mathbf{u}$, $\delta\frac{\partial \mathbf{u}^T}{\partial z}$ and $\delta\mathbf{r}$ – and hence the following set of equations is obtained

$$\begin{cases} \mathbf{M}\frac{\partial^2 \mathbf{u}}{\partial z^2} + \left(\mathbf{C} - \mathbf{C}^T\right)\frac{\partial \mathbf{u}}{\partial z} + \mathbf{L}\frac{\partial \boldsymbol{\psi}}{\partial z} - \mathbf{E}\mathbf{u} - \mathbf{R}\boldsymbol{\psi} = \mathbf{0} \\ \mathbf{L}^T\frac{\partial \mathbf{u}}{\partial z} + \mathbf{R}^T\mathbf{u} + \mathbf{A}\boldsymbol{\psi} = \boldsymbol{\theta} \\ \frac{\partial \boldsymbol{\theta}}{\partial z} = \mathbf{T}_r^T\boldsymbol{\theta} \end{cases}$$

The second order linear differential equation above renders two types of solutions – an homogeneous and a particular (or *extremities* and *central* solutions, respectively, as originally coined by Giavotto et al. [7]) – corresponding to two different physical phenomena. For a relatively long and slender beam, the homogeneous solution is associated with the deformations at the ends or extremities of the beam. These are decaying solutions which become negligible at a certain distance from the ends of the beam (see, e.g., Choi and Horgan [11] for a discussion on this topic). The particular solution, on the other hand, will yield the displacement field at the central part of the beam where end effects become negligible. This solution can be used to derive the stiffness properties of beam sections and consequently construct finite elements suitable for the analysis of the global behavior of relatively long and slender structures.

Before proceeding with the derivation note that the displacement definition as stated first in (2) and later in its finite element form in (5) is six times redundant. The warping displacements, $\mathbf{u}$, are able to replicate the six rigid body motions already included in $\boldsymbol{\psi}$ (cf. (3)). The following set of constraint equations is included

$$\begin{bmatrix} \mathbf{D}^T & \mathbf{0} \\ \mathbf{0} & \mathbf{D}^T \end{bmatrix} \begin{bmatrix} \mathbf{u} \\ \frac{\partial \mathbf{u}}{\partial z} \end{bmatrix} = \begin{bmatrix} \mathbf{0} \\ \mathbf{0} \end{bmatrix}, \text{ where } \mathbf{D} = \begin{bmatrix} \mathbf{I}_3 & \dots & \mathbf{I}_3 \\ \mathbf{n}_1 & \dots & \mathbf{n}_{n_n} \end{bmatrix}^T$$

where $\mathbf{I}_3$ is the 3×3 identity matrix, and $\mathbf{n}_n$ is obtained from (1) using the nodal coordinates of node n. These constraints ensure that the warping displacements do not contribute to the rigid-body displacements of the cross section.

After some manipulation, the resulting equilibrium equations for a section in the central part of the beam are defined in matrix form as

$$\mathbf{K}\mathbf{w} = \mathbf{f} \Leftrightarrow \begin{bmatrix} \mathbf{K}_{11} & \mathbf{K}_{12} \\ \mathbf{0} & \mathbf{K}_{11} \end{bmatrix} \begin{bmatrix} \mathbf{w}_1 \\ \mathbf{w}_2 \end{bmatrix} = \begin{bmatrix} \mathbf{f}_1 \\ \mathbf{f}_2 \end{bmatrix} \tag{10}$$

where

$$\mathbf{K}_{11} = \begin{bmatrix} \mathbf{E} & \mathbf{R} & \mathbf{D} \\ \mathbf{R}^T & \mathbf{A} & \mathbf{0} \\ \mathbf{D}^T & \mathbf{0} & \mathbf{0} \end{bmatrix}, \ \mathbf{K}_{12} = \begin{bmatrix} (\mathbf{C}^T - \mathbf{C}) & -\mathbf{L} & \mathbf{0} \\ \mathbf{L}^T & \mathbf{0} & \mathbf{0} \\ \mathbf{0} & \mathbf{0} & \mathbf{0} \end{bmatrix} \tag{11}$$

and, $\mathbf{w}_1 = \begin{bmatrix} \mathbf{u}^T & \boldsymbol{\psi}^T & \boldsymbol{\lambda}_1^T \end{bmatrix}^T$, $\mathbf{w}_2 = \begin{bmatrix} \partial \mathbf{u}^T/\partial z & \partial \boldsymbol{\psi}^T/\partial z & \boldsymbol{\lambda}_2^T \end{bmatrix}^T$, $\mathbf{f}_1 = \begin{bmatrix} \mathbf{0}^T & \boldsymbol{\theta}^T & \mathbf{0}^T \end{bmatrix}^T$, and $\mathbf{f}_2 = \begin{bmatrix} \mathbf{0}^T & (\mathbf{T}_r^T \boldsymbol{\theta})^T & \mathbf{0}^T \end{bmatrix}^T$. The vectors of Lagrange multipliers $\boldsymbol{\lambda}_1$, and $\boldsymbol{\lambda}_2$ refer to the first and second set of constraint equations, respectively. The set of equations above will yield the warping displacements and strains, $\mathbf{u}$ and $\boldsymbol{\psi}$ respectively, for given internal section forces $\boldsymbol{\theta}$. The coefficient matrix $\mathbf{K}_{11}$ is the same for both sets. An efficient solution procedure can be devised by factorizing $\mathbf{K}_{11}$ once and then determine the solutions using two forward-backward substitutions.

2.1.5 Cross section properties

A procedure is presented next for the derivation of the cross section compliance matrix $\mathbf{F}_s$ based on the cross section equilibrium equations derived in the previous section (cf. Giavotto et al. in [7]).

Consider the case where the set of equations (10) is solved for different right-hand sides each corresponding to setting one of the entries of $\boldsymbol{\theta}$ to unity and the remaining to zero. This procedure is similar to the stiffness method in the finite element method. It can be realized by replacing the cross section load vector $\boldsymbol{\theta}$ by the 6×6 identity matrix $\mathbf{I}_6$ and solving the following set of equations

$$\mathbf{KW} = \mathbf{F} \Leftrightarrow \begin{bmatrix} \mathbf{K}_{11} & \mathbf{K}_{12} \\ \mathbf{0} & \mathbf{K}_{11} \end{bmatrix} \begin{bmatrix} \mathbf{W}_1 \\ \mathbf{W}_2 \end{bmatrix} = \begin{bmatrix} \mathbf{F}_1 \\ \mathbf{F}_2 \end{bmatrix} \tag{12}$$

where $\mathbf{W}_1 = \begin{bmatrix} \mathbf{U}^T & \boldsymbol{\Psi}^T & \boldsymbol{\Lambda}_1^T \end{bmatrix}^T$, $\mathbf{W}_2 = \begin{bmatrix} \partial\mathbf{U}^T/\partial z & \partial\boldsymbol{\Psi}^T/\partial z & \boldsymbol{\Lambda}_2^T \end{bmatrix}^T$, $\mathbf{F}_1 = \begin{bmatrix} \mathbf{0}^T & \mathbf{I}_6 & \mathbf{0}^T \end{bmatrix}^T$, and $\mathbf{F}_2 = \begin{bmatrix} \mathbf{0}^T & \mathbf{T}_r & \mathbf{0}^T \end{bmatrix}^T$. The resulting solution matrices $\mathbf{U}$, $\partial\mathbf{U}/\partial z$, $\boldsymbol{\Psi}$ and $\partial\boldsymbol{\Psi}/\partial z$ have six columns each corresponding to one of the right-hand sides. The displacement solutions $\mathbf{u}$, $\partial\mathbf{u}/\partial z$, $\boldsymbol{\psi}$ and $\partial\boldsymbol{\psi}/\partial z$ can be retrieved for any $\boldsymbol{\theta}$ using the following relations

$$\mathbf{u} = \mathbf{U}\boldsymbol{\theta}, \qquad \frac{\partial\mathbf{u}}{\partial z} = \frac{\partial\mathbf{U}}{\partial z}\boldsymbol{\theta}, \qquad \boldsymbol{\psi} = \boldsymbol{\Psi}\boldsymbol{\theta}, \qquad \frac{\partial\boldsymbol{\psi}}{\partial z} = \frac{\partial\boldsymbol{\Psi}}{\partial z}\boldsymbol{\theta} \tag{13}$$

Restating the cross section equilibrium in (6) as

$$\delta\boldsymbol{\theta}^T\mathbf{F}_s\boldsymbol{\theta} = \int_A \delta\boldsymbol{\epsilon}^T\boldsymbol{\sigma} \ \mathrm{dA}$$

where the left-hand term is the complimentary form of the cross section internal elastic energy. The right-hand term is the internal virtual work or the elastic strain energy as defined in (8). The cross section equilibrium equations are obtained by inserting the relations in (13) into (8) and replacing the result into the equation above to yield

$$\delta\boldsymbol{\theta}\mathbf{F}_s\boldsymbol{\theta} = \delta\boldsymbol{\theta}^T \begin{bmatrix} \mathbf{W}_1 \\ \mathbf{W}_2 \end{bmatrix}^{'T} \begin{bmatrix} \mathbf{G}_{11} & \mathbf{G}_{12} \\ \mathbf{G}_{12}^T & \mathbf{G}_{22} \end{bmatrix} \begin{bmatrix} \mathbf{W}_1 \\ \mathbf{W}_2 \end{bmatrix} \boldsymbol{\theta} = \delta\boldsymbol{\theta}^T\mathbf{W}^T\mathbf{G}\mathbf{W}\boldsymbol{\theta}$$

where

$$\mathbf{G}_{11} = \begin{bmatrix} \mathbf{E} & \mathbf{R} & \mathbf{0} \\ \mathbf{R}^T & \mathbf{A} & \mathbf{0} \\ \mathbf{0} & \mathbf{0} & \mathbf{0} \end{bmatrix}, \mathbf{G}_{12} = \begin{bmatrix} \mathbf{C} & \mathbf{L} & \mathbf{0} \\ \mathbf{L}^T & \mathbf{0} & \mathbf{0} \\ \mathbf{0} & \mathbf{0} & \mathbf{0} \end{bmatrix}, \mathbf{G}_{22} = \begin{bmatrix} \mathbf{M} & \mathbf{0} & \mathbf{0} \\ \mathbf{0} & \mathbf{0} & \mathbf{0} \\ \mathbf{0} & \mathbf{0} & \mathbf{0} \end{bmatrix}$$

The following expression for the cross section compliance matrix is obtained

$$\mathbf{F}_s = \mathbf{W}^{'T}\mathbf{G}\mathbf{W} \tag{14}$$

This concludes the derivation of the cross section stiffness matrix. In practice the procedure for the evaluation of $\mathbf{F}_s$ consists of first assembling the matrices in (9).

This can be done very efficiently using standard finite element techniques. The next step consists of assembling the matrices $\mathbf{K}_{11}$ and $\mathbf{K}_{12}$ in (11), and finding the solutions for (12). Finally, having assembled matrix $\mathbf{G}$, the cross section compliance matrix $\mathbf{F}_s$ is computed by replacing the solutions obtained into (14) .

2.1.6 Shear and mass center positions

The shear and elastic center positions are determined based on the entries of the cross section compliance matrix (cf. Hodges [6]). The shear center, $\mathbf{s}_c = (x_s, y_s)$, of a given cross section is defined such that a transverse load applied at this point will not induce a torsional moment. It is given as a function of the cross section entries and defined as

$$\begin{aligned} x_s &= -\frac{F_{s,62} + F_{s,64}(L-z)}{F_{s,66}} \\ y_s &= \frac{F_{s,61} + F_{s,65}(L-z)}{F_{s,66}} \end{aligned} \tag{15}$$

where $F_{s,ij}$ is the entry (i,j) of the compliance matrix $\mathbf{F}_s$, and L is the beam length. Finally, the position of the mass center $\mathbf{m}_c = (x_c, y_c)$ is given as

$$\begin{aligned} x_c &= \left(\sum_{e=1}^{n_e} x_{c_e} v_e \varrho_e\right) / \left(\sum_{e=1}^{n_e} v_e \varrho_e\right) \\ y_c &= \left(\sum_{e=1}^{n_e} y_{c_e} v_e \varrho_e\right) / \left(\sum_{e=1}^{n_e} v_e \varrho_e\right) \end{aligned} \tag{16}$$

where (x_{c_e}, y_{c_e}), v_e and ϱ_e are the coordinates of the centroid, the volume and the density of element e, respectively.

2.2 Beam finite element model

The last step in the construction of the structural model entails the generation of the beam finite element matrices. Employing the typical finite element approach, assume that the rigid body translations and rotations in $\mathbf{r}$ may be approximated within a beam finite element b as

$$\mathbf{r}(z) \approx \widehat{\mathbf{N}}_b(z)\widehat{\mathbf{u}}_b \tag{17}$$

where $\widehat{\mathbf{N}}_b(z)$ is the matrix of shape functions. The displacement vector $\widehat{\mathbf{u}}_b(x,y,z)$ yields the beam translational and rotational nodal degrees of freedom.

Invoking the principle of virtual work, at equilibrium the total internal virtual work of the beam, $\widehat{W}_{int}$, must be equal to the total external virtual work , $\widehat{W}_{ext}$, i.e., $\widehat{W}_{ext} = \widehat{W}_{int}$. The total internal virtual work or the elastic strain energy of the beam is given as

$$\widehat{W}_{int} = \int_0^{L_b} \delta\boldsymbol{\psi}^T \boldsymbol{\theta} \ \mathrm{dz} = \int_0^{L_b} \delta\boldsymbol{\psi}^T \mathbf{K}_s \boldsymbol{\psi} \ \mathrm{dz}$$

where the cross section constitutive relation $\boldsymbol{\theta} = \mathbf{K}_s\boldsymbol{\psi}$ has been invoked. The strains and curvatures in $\boldsymbol{\psi}$ are associated with the translations and rotations in $\mathbf{r}$ through (3) which inserted in the equation above yields

$$\widehat{W}_{int} = \sum_{b=1}^{n_b} \int_0^{L_b} \delta\mathbf{r}^T \left(\mathbf{T}_r + \frac{\partial}{\partial z}\right)^T \mathbf{K}_s \left(\mathbf{T}_r + \frac{\partial}{\partial z}\right) \mathbf{r} \; \mathrm{dz}$$

where n_b is the number of beam finite elements, and L_b is the length of the beam finite element b. The finite element form of this expression is obtained inserting (17) in the expression above to obtain

$$\widehat{W}_{int} = \delta\widehat{\mathbf{u}}^T \sum_{b=1}^{n_b} \int_0^{L_b} \widehat{\mathbf{N}}_b^T \left(\mathbf{T}_r + \frac{\partial}{\partial z}\right)^T \mathbf{K}_s \left(\mathbf{T}_r + \frac{\partial}{\partial z}\right) \widehat{\mathbf{N}}_b \; \mathrm{dz} \; \widehat{\mathbf{u}} \tag{18}$$

Following the same approach, the total external virtual work of the beam, or the work done by the the loads $\mathbf{f}^s$ through the virtual displacements, is

$$\widehat{W}_{ext} = \int_0^{L_b} \delta\mathbf{r}^T \mathbf{f}^s \; \mathrm{dz} \; = \delta\widehat{\mathbf{u}}^T \sum_{b=1}^{n_b} \int_0^{L_b} \widehat{\mathbf{N}}_b^T \mathbf{f}_b^s \; \mathrm{dz} \tag{19}$$

Hence, observing that the result must be true for any admissible displacement $\delta\widehat{\mathbf{u}}$ and that at equilibrium (18) and (19) must balance each other, the following holds

$$\sum_{b=1}^{n_b} \int_0^{L_b} \widehat{\mathbf{N}}_b^T \left(\mathbf{T}_r + \frac{\partial}{\partial z}\right)^T \mathbf{K}_s \left(\mathbf{T}_r + \frac{\partial}{\partial z}\right) \widehat{\mathbf{N}}_b \; \mathrm{dz} \; \widehat{\mathbf{u}} = \sum_{b=1}^{\widehat{n}_b} \int_0^{L_b} \widehat{\mathbf{N}}_b^T \mathbf{f}_b^s \; \mathrm{dz}$$

Based on the above it is possible to define the beam element stiffness matrix $\widehat{\mathbf{K}}_b$ as

$$\widehat{\mathbf{K}}_b = \int_0^{L_b} \widehat{\mathbf{N}}_b^T \left(\mathbf{T}_r + \frac{\partial}{\partial z}\right)^T \mathbf{K}_s \left(\mathbf{T}_r + \frac{\partial}{\partial z}\right) \widehat{\mathbf{N}}_b \; \mathrm{dz}$$

The global stiffness matrix of the beam model, $\widehat{\mathbf{K}}$, is obtained from

$$\widehat{\mathbf{K}} = \sum_{b=1}^{n_b} \widehat{\mathbf{K}}_b \tag{20}$$

following the typical assembly procedure from finite element analysis. The global load vector $\widehat{\mathbf{f}}$ considering only pressure loads, is defined as

$$\widehat{\mathbf{f}} = \sum_{b=1}^{n_b} \int_0^{L_b} \widehat{\mathbf{N}}^T \mathbf{f}_b^s \; \mathrm{dz}$$

The nodal translations and rotations in $\widehat{\mathbf{u}}_l$ for a beam subject to the load, $\widehat{\mathbf{f}}_l$, is obtained by solving the linear system of equations

$$\widehat{\mathbf{K}}\widehat{\mathbf{u}}_l = \widehat{\mathbf{f}}_l$$

where $l = 1, \ldots, n_l$, indicates the load case number from the n_l load cases considered.

3 Formulation of the optimal design problem

The formulation of the minimum compliance problem with constraints on weight and positions of shear and mass center is presented next. The aim is to identify the optimal distribution of a predefined number of candidate materials within a given cross section. The devised methodology should yield a solution where only one of the candidate materials has been chosen at each point of the design domain. In order to avoid the complications associated with the solution of discrete problems a relaxation has been suggested where the continuous design variables are allowed to vary between zero and one. Intermediate values are penalized by a material interpolation scheme thus forcing the design variables to converge to a discrete valued solution. The parameterization, the penalization, and a filtering technique are described next.

3.1 Parameterization

A SIMP-like material interpolation scheme (see Bendsøe and Kikuchi [24], Rozvany and Zhou [21]) is employed which can accommodate any number of anisotropic candidate materials. The 6×6 material constitutive matrix $\mathbf{Q}_e$ at element e is assumed to be defined as

$$\mathbf{Q}_e(\boldsymbol{\rho}) = \sum_{m=1}^{n_c} \rho_{em}^p \overline{\mathbf{Q}}_m \quad \forall e = 1, ..., n_e \tag{21}$$

where n_c is the number of candidate materials and n_e the number of elements in the cross section finite element mesh. The design variables $\boldsymbol{\rho} = \{\rho_{em} \in \mathbb{R} \mid e \in \{1, ..., n_e\}, \quad m \in \{1, ..., n_c\}\}$ represent the volume fractions of each of the candidate materials m represented by the constitutive matrix $\overline{\mathbf{Q}}_m$, at element e. The design variables are assumed to vary continuously between given bounds, i.e., $\underline{\rho} \leq \rho_{em} \leq \overline{\rho}$, $\forall e = 1, ..., n_e$, $\forall m = 1, ..., n_c$. The upper and lower bound are $\underline{\rho} = 0$ and $\overline{\rho} = 1$, respectively. The list of candidate materials is defined a priori and may include any type of anisotropic material as well as the same material aligned in different directions. The following linear equality constraints are included in the problem formulation

$$\sum_{m=1}^{n_c} \rho_{em} = 1 \quad \forall e = 1, ..., n_e$$

These equalities ensure that the sum of the volume fractions of the candidate materials at each element or patch add to unity. Finally, the parameter $p \geq 1$ is a penalty term whose role will be discussed in further detail in the next section.

The element density ϱ_e is given by

$$\varrho_e(\boldsymbol{\rho}) = \sum_{m=1}^{n_c} \rho_{em} \overline{\varrho}_m \quad \forall e = 1, ..., n_e \tag{22}$$

where $\overline{\varrho}_m$ is the density of candidate material m. The interpolation schemes for both stiffness and density are similar although the penalty parameter p used in (21) is not considered in the density interpolation expression above.

The design variables $\boldsymbol{\rho}$ enter the structural model through the material constitutive matrices $\mathbf{Q}_e = \mathbf{Q}_e(\boldsymbol{\rho})$ as part of the definition of the finite element matrices in (9). Hence, $\mathbf{A} = \mathbf{A}(\boldsymbol{\rho})$, $\mathbf{M} = \mathbf{M}(\boldsymbol{\rho})$, $\mathbf{C} = \mathbf{C}(\boldsymbol{\rho})$, $\mathbf{E} = \mathbf{E}(\boldsymbol{\rho})$, $\mathbf{R} = \mathbf{R}(\boldsymbol{\rho})$, and $\mathbf{L} = \mathbf{L}(\boldsymbol{\rho})$. Consequently, $\mathbf{F}_s = \mathbf{F}_s(\boldsymbol{\rho})$ at the cross section level and finally, $\widehat{\mathbf{K}} = \widehat{\mathbf{K}}(\boldsymbol{\rho})$ at the beam finite element level.

3.1.1 Penalization

The parameterization presented before (assuming $p = 1$) is prone to generate optimal designs where the solution is not discrete, i.e., where several candidate materials exist simultaneously in the same element. The SIMP penalization approach has been extensively used in topology optimization problems (see Bendsøe and Sigmund [20]) to force the design variables to their bounds and hence towards a discrete design. It works at the material interpolation level and is realized by controlling the penalty term $p \geq 1$ in (21). Increasing the value of p corresponds to increasing the contrast between the different candidates and consequently in the penalization of intermediate densities.

The penalized problem is in general non-convex and may have a large number of local minima. Continuation methods have been suggested in this context as a way to increase the possibility of obtaining a good feasible design to the discrete problem (see Sigmund and Petersson [34], Borrvall and Petersson [36], and Hvejsel et al. [25]). In practice the problem is initially solved for $p = 1$ corresponding to the case where no penalization is imposed. Subsequently, the penalty is increased and the found design of the former optimal design problem is used as the starting point of the new problem. As p is increased the variables are forced to their bounds. This process is repeated until a discrete valued design is obtained where all but one candidate material have been eliminated at each point of the design domain. In the implementation all optimal design problems are solved until either some optimality conditions are satisfied or the maximum number of iterations is reached.

3.2 Filtering scheme

Typical issues in density based topology optimization include, among other, the appearance of checkerboards and mesh-dependency (Sigmund and Petersson [34]). Several regularization techniques have been proposed which introduce, in some way or another, a length scale on the optimal solution which eliminates these effects (see Sigmund and Petersson [34], Bruns and Tortorelli [33], Bourdin [35], and Sigmund [32]). Most of the approaches have been devised for the typical two phase or material-void topology optimization problems. An extension of the filtering scheme described in Bruns and Tortorelli [33] for multi-material topol-

ogy optimization problems is suggested here. The multi-material problem differs from the typical material-void topology optimization problem in that there can be more than one design variables, or volume fractions, of each candidate material, competing at each element of the design domain. In this case, the volume fraction of a candidate material at element e is given as a function of the volume fractions of the same candidate material, m, at the surrounding elements and the element itself. This is valid for any material m appearing at that element. This corresponds to imposing a length scale simultaneously for all candidate materials.

The set of elements surrounding element e within a given radius f_r is defined by the set S_e such that,

$$S_e = \{\tilde{e} \in \{1, ..., n_e\} \mid \|\mathbf{x}_{\tilde{e}} - \mathbf{x}_e\|_2 \leq f_r\}$$

where $\mathbf{x}_{\tilde{e}}$ and $\mathbf{x}_e$ are the coordinates of the centroid of element $\tilde{e}$ and e, respectively. The volume fraction of material m at element e is

$$\widetilde{\rho}_{em} = \widetilde{\rho}_{em}(\rho_{\tilde{e}m}), \quad \forall \tilde{e} \in S_e$$

The filtered density for material m at element e is hence

$$\widetilde{\rho}_{em} = \frac{\sum_{\tilde{e} \in S_e} w(\mathbf{x}_{\tilde{e}}) v_{\tilde{e}} \rho_{\tilde{e}m}}{\sum_{\tilde{e} \in S_e} w(\mathbf{x}_{\tilde{e}}) v_{\tilde{e}}}$$

The weighting function $w(x_e)$ is given by the linearly decaying function

$$w(\mathbf{x}_{\tilde{e}}) = f_r - \|\mathbf{x}_{\tilde{e}} - \mathbf{x}_e\|_2$$

as suggested by Bruns and Tortorelli [33] and Bourdin [35]. The material interpolation scheme presented in (21) is then restated to include the filtered design variables

$$\mathbf{Q}_e(\boldsymbol{\rho}) = \sum_{m=1}^{n_c} \widetilde{\rho}_{em}^p(\boldsymbol{\rho}) \overline{\mathbf{Q}}_m \quad , \quad \forall e = 1, ..., n_e$$

The element density is also redefined as a function of the filtered variables and hence the expression in (22) is restated as

$$\varrho_e(\boldsymbol{\rho}) = \sum_{m=1}^{n_c} \widetilde{\rho}_{em}(\boldsymbol{\rho}) \overline{\varrho}_m \quad , \forall e = 1, ..., n_e$$

Finally, note that in the problem formulation presented next the constraint ensuring that the sum of the variables is equal to unity is now imposed on the filtered volume fractions

$$\sum_{m=1}^{n_c} \widetilde{\rho}_{em} = 1 \quad , \quad \forall e = 1, ..., n_e \tag{23}$$

The solution to a numerical example is presented in Figure 4 which illustrates the behavior of the density filter. The minimum compliance problem with weight constraints is solved for a beam with a square cross section. Five candidate materials are considered – four candidates corresponding to four different fiber orientations of the orthotropic material, and an isotropic material. The beam is subjected to a distributed horizontal transverse force F_x, vertical transverse force F_y, and torsional moment M_z. The problem is first solved for three different mesh sizes using the same filter radius, $f_r = 0.15$. The meshes considered have 20×20, 30×30, and 40×40 elements (Figures 4(a), (c), and (e), respectively). The results indicate that the solution is independent of the mesh size. The problem is then solved for a fixed mesh size (40×40) but using different filter sizes – $f_r = 0$, $f_r = 0.1$, and $f_r = 0.2$ (Figures 4(b), (d), and (f)). The results show the influence of the filter radius on the topology of the different material regions. Moreover, some checkerboard regions appear when no filtering is used ($f_r = 0$ in Figure 4(b)). These are removed in the subsequent examples when filtering is active. In summary, the results suggest that the extended filtering technique presented here is a viable option when dealing with multi-material topology optimization problems.

3.3 Problem formulation

The structural compliance of load case l,

$$c_l(\boldsymbol{\rho}) = \widehat{\mathbf{f}}_l^{T} \widehat{\mathbf{u}}_l(\boldsymbol{\rho})$$

is a measure of the stiffness of the beam defined as the work performed by the external loads. It is assumed herein that $\widehat{\mathbf{K}}(\boldsymbol{\rho})$ is positive definite for all $\boldsymbol{\rho}$ within the specified bounds $\underline{\rho} \leq \rho_{em} \leq \overline{\rho}$, $\forall e = 1, ..., n_e$, $\forall m = 1, ..., n_c$. Hence, it is possible to define the function $\widehat{\mathbf{u}}_k(\boldsymbol{\rho}) = \widehat{\mathbf{K}}^{-1}(\boldsymbol{\rho})\widehat{\mathbf{f}}_k$ such that

$$c_l(\boldsymbol{\rho}) = \widehat{\mathbf{f}}_l^{T} \widehat{\mathbf{K}}^{-1}(\boldsymbol{\rho})\widehat{\mathbf{f}}_l \tag{24}$$

The weighted average of the compliances $C(\boldsymbol{\rho})$, for a given set of load cases is defined as

$$C(\boldsymbol{\rho}) = \sum_{l=1}^{n_l} \alpha_l c_l(\boldsymbol{\rho}) = \sum_{l=1}^{n_l} \alpha_l \widehat{\mathbf{f}}_l^{T} \widehat{\mathbf{K}}^{-1}(\boldsymbol{\rho})\widehat{\mathbf{f}}_l \tag{25}$$

where $\alpha_l \geq 0$ is the given weight attributed to load case l. The formulation of the optimal design problem (P1) is then

$$\begin{aligned} \underset{\boldsymbol{\rho} \in \mathbb{R}^{n_e \times n_c}}{\text{minimize}} \quad & C(\boldsymbol{\rho}) \\ \text{subject to} \quad & w(\boldsymbol{\rho}) \leq \overline{w} \\ & \mathbf{s}_c(\boldsymbol{\rho}) \leq \overline{\mathbf{s}} \\ & \mathbf{m}_c(\boldsymbol{\rho}) \leq \overline{\mathbf{m}} \end{aligned} \tag{P1}$$

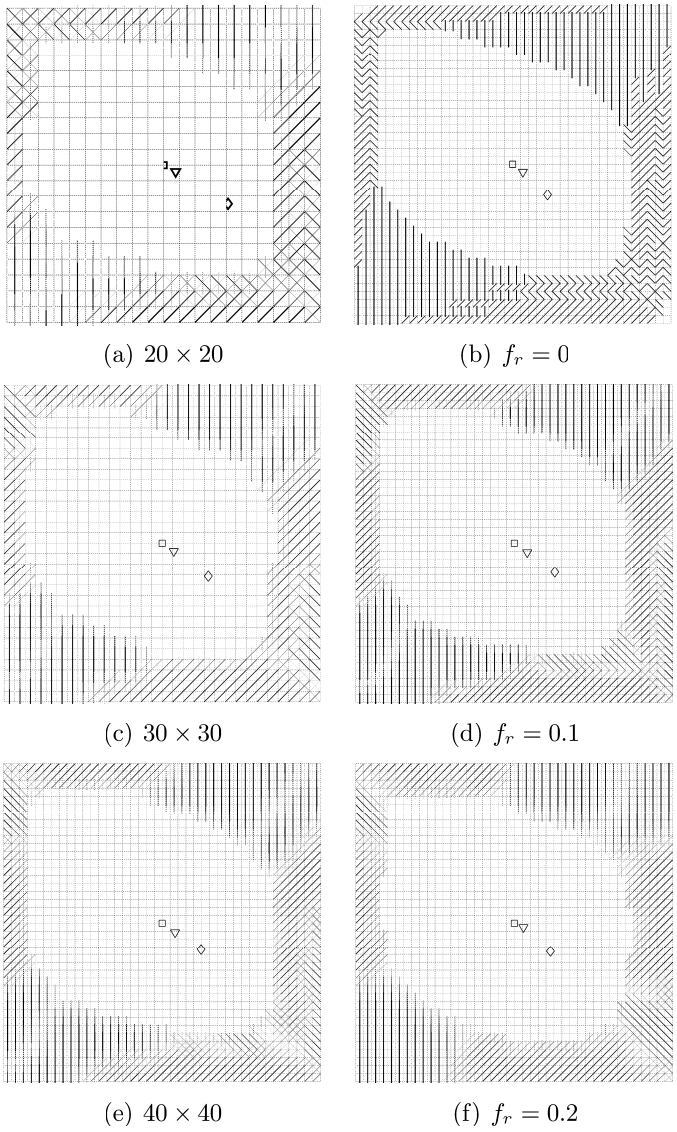

(a) 20×20 (b) $f_r = 0$

(c) 30×30 (d) $f_r = 0.1$

(e) 40×40 (f) $f_r = 0.2$

Figure 4: Numerical example illustrating the behavior of the multi-material density filter. Five different candidate materials have been considered: orthotropic laminate (as solid lines) at $0°$, $45°$, $-45°$ and $90°$, and an isotropic material (in white). The beam is subjected to a distributed horizontal transverse force F_x, vertical transverse force F_y, and torsional moment M_z. Figures (a), (c), and (e), show the optimal material distribution for a beam with a square cross section using three different mesh sizes – 20×20, 30×30, and 40×40 elements, respectively. The filter radius size is fixed at $f_r = 0.15$ for these cases. Figures (b), (d), and (f), show the result for different magnitudes of the filter radius – $f_r = 0$, $f_r = 0.1$, and $f_r = 0.2$, respectively. The mesh size is fixed at 40×40 for these cases.

$$\sum_{m=1}^{n_c} \widetilde{\rho}_{em}(\boldsymbol{\rho}) = 1 \ , \ \forall e = 1, ..., n_e$$
$$\underline{\rho} \leq \rho_{em} \leq \overline{\rho}, \ \forall e = 1, ..., n_e \ , \ \forall m = 1, ..., n_c$$

where the total beam weight $w(\boldsymbol{\rho})$ is defined as

$$w(\boldsymbol{\rho}) = \sum_{b=1}^{n_b} \sum_{e=1}^{n_e} v_e \varrho_e(\boldsymbol{\rho}) L_b$$

The parameters $\overline{\mathbf{w}}$, $\overline{\mathbf{s}}$ and $\overline{\mathbf{m}}$ are the constraint values for the weight and, shear and mass center positions, respectively.

Finally, removing the shear and mass center position constraints from problem formulation (P1) will yield the formulation for the minimum compliance with weight constraints problem (P2).

4 Sensitivity analysis

The gradients (or sensitivities) of the beam compliance and, shear and mass center positions are presented here.

4.1 Compliance

The gradient of the compliance is derived in two steps. The first step consists of determining the partial derivative of the beam stiffness matrix, $\widehat{\mathbf{K}}(\boldsymbol{\rho})$. The second step consists of the determining an expression for the partial derivative of the cross section stiffness matrix, $\mathbf{K}_s(\boldsymbol{\rho})$.

According to the definition of the average compliance in (25), the partial derivative of $C(\boldsymbol{\rho})$ with respect to design variables ρ_{em} is

$$\frac{\partial C(\boldsymbol{\rho})}{\partial \rho_{em}} = \sum_{l=1}^{n_l} \alpha_l \frac{\partial c_l(\boldsymbol{\rho})}{\partial \rho_{em}}$$

The loads are assumed to be design independent and so, according to the definition of compliance in (24), the derivative of $c_l(\boldsymbol{\rho})$ is

$$\frac{\partial c_l(\boldsymbol{\rho})}{\partial \rho_{em}} = \widehat{\mathbf{f}}_l^T \frac{\partial \widehat{\mathbf{u}}_l(\boldsymbol{\rho})}{\partial \rho_{em}} = \widehat{\mathbf{f}}_l^T \frac{\partial \widehat{\mathbf{K}}(\boldsymbol{\rho})^{-1}}{\partial \rho_{em}} \widehat{\mathbf{f}}_l$$

In this case the following holds (see, e.g., Bendsøe and Sigmund [20])

$$\frac{\partial c_l(\boldsymbol{\rho})}{\partial \rho_{em}} = -\widehat{\mathbf{u}}_l(\boldsymbol{\rho})^T \frac{\partial \widehat{\mathbf{K}}(\boldsymbol{\rho})}{\partial \rho_{em}} \widehat{\mathbf{u}}_l(\boldsymbol{\rho}) \tag{26}$$

According to the definition of the global beam stiffness matrix in (20), the partial derivative of $\widehat{\mathbf{K}}$ is

$$\frac{\partial \widehat{\mathbf{K}}(\boldsymbol{\rho})}{\partial \rho_{em}} = \sum_{b=1}^{n_b} \int_0^{L_b} \widehat{\mathbf{N}}_b^T \left(\mathbf{T}_r + \frac{\partial}{\partial z}\right)^T \frac{\partial \mathbf{K}_s(\boldsymbol{\rho})}{\partial \rho_{em}} \left(\mathbf{T}_r + \frac{\partial}{\partial z}\right) \widehat{\mathbf{N}}_b \, \mathrm{dz} \tag{27}$$

Computing the gradient of the beam compliance boils down to evaluating partial derivatives of the cross section stiffness matrix $\mathbf{K}_s(\boldsymbol{\rho})$.

4.1.1 Cross section stiffness matrix

The derivative of the cross section stiffness matrix $\mathbf{K}_s$ with respect to the design variable ρ_{em} is

$$\frac{\partial \mathbf{K}_s(\boldsymbol{\rho})}{\partial \rho_{em}} = \frac{\partial \mathbf{F}_s^{-1}(\boldsymbol{\rho})}{\partial \rho_{em}} = -\mathbf{K}_s(\boldsymbol{\rho}) \frac{\partial \mathbf{F}_s(\boldsymbol{\rho})}{\partial \rho_{em}} \mathbf{K}_s(\boldsymbol{\rho}) \tag{28}$$

where $\mathbf{F}_s^{-1} = \mathbf{K}_s$. From (14), the cross section compliance matrix is defined as $\mathbf{F}_s = \mathbf{W}^T(\boldsymbol{\rho}) \mathbf{G}(\boldsymbol{\rho}) \mathbf{W}(\boldsymbol{\rho})$. Employing the chain rule yields

$$\begin{aligned} \frac{\partial \mathbf{F}_s(\boldsymbol{\rho})}{\partial \rho_{em}} =& \frac{\partial \mathbf{W}^T(\boldsymbol{\rho})}{\partial \rho_{em}} \mathbf{G}(\boldsymbol{\rho}) \mathbf{W}(\boldsymbol{\rho}) + \mathbf{W}^T(\boldsymbol{\rho}) \frac{\partial \mathbf{G}(\boldsymbol{\rho})}{\partial \rho_{em}} \mathbf{W}(\boldsymbol{\rho}) \\ &+ \mathbf{W}^T(\boldsymbol{\rho}) \mathbf{G}(\boldsymbol{\rho}) \frac{\partial \mathbf{W}(\boldsymbol{\rho})}{\partial \rho_{em}} \end{aligned} \tag{29}$$

The solution vectors in $\mathbf{W}(\boldsymbol{\rho})$ are computed as $\mathbf{W}(\boldsymbol{\rho}) = \mathbf{K}^{-1}(\boldsymbol{\rho}) \mathbf{F}$ from (12). Accordingly, the gradient of $\mathbf{W}(\boldsymbol{\rho})$ is

$$\frac{\partial \mathbf{W}(\boldsymbol{\rho})}{\partial \rho_{em}} = \frac{\partial \mathbf{K}^{-1}(\boldsymbol{\rho})}{\partial \rho_{em}} \mathbf{F} = -\mathbf{K}^{-1}(\boldsymbol{\rho}) \frac{\partial \mathbf{K}(\boldsymbol{\rho})}{\partial \rho_{em}} \mathbf{W}(\boldsymbol{\rho}) \tag{30}$$

Replacing (30) in (29) yields

$$\begin{aligned} \frac{\partial \mathbf{F}_s(\boldsymbol{\rho})}{\partial \rho_{em}} =& - \mathbf{W}^T(\boldsymbol{\rho}) \frac{\partial \mathbf{K}^T(\boldsymbol{\rho})}{\partial \rho_{em}} \mathbf{K}^{-T}(\boldsymbol{\rho}) \mathbf{G}(\boldsymbol{\rho}) \mathbf{W}(\boldsymbol{\rho}) \\ &+ \mathbf{W}^T(\boldsymbol{\rho}) \frac{\partial \mathbf{G}(\boldsymbol{\rho})}{\partial \rho_{em}} \mathbf{W}(\boldsymbol{\rho}) \\ &- \mathbf{W}^T(\boldsymbol{\rho}) \mathbf{G}(\boldsymbol{\rho}) \mathbf{K}^{-1}(\boldsymbol{\rho}) \frac{\partial \mathbf{K}(\boldsymbol{\rho})}{\partial \rho_{em}} \mathbf{W}(\boldsymbol{\rho}) \end{aligned} \tag{31}$$

where $\mathbf{G}(\boldsymbol{\rho})$ is symmetric, i.e., $\mathbf{G}^T(\boldsymbol{\rho}) = \mathbf{G}(\boldsymbol{\rho})$. The first and third terms of the equation above can be dealt with by defining $\mathbf{V}(\boldsymbol{\rho})$ as

$$\mathbf{V}(\boldsymbol{\rho}) = \mathbf{K}^{-T}(\boldsymbol{\rho}) \mathbf{G}(\boldsymbol{\rho}) \mathbf{W}(\boldsymbol{\rho}) \tag{32}$$

Hence, $\mathbf{V}(\boldsymbol{\rho})$ is the solution to

$$\mathbf{K}^T(\boldsymbol{\rho}) \mathbf{V} = \mathbf{G}(\boldsymbol{\rho}) \mathbf{W}(\boldsymbol{\rho})$$

which is solved only once regardless of the number of design variables. This approach is the most convenient for the problem at hand where the number of design variables is much larger than the number of state variables. Alternatively, $\mathbf{V}(\boldsymbol{\rho})$ can be obtained from the solution to $\mathbf{K}(\boldsymbol{\rho})\mathbf{V} = \partial\mathbf{K}(\boldsymbol{\rho})/\partial\rho_{em}$. In this approach a forward-backward substitution is required for each design variable. This approach is viable only in the case when the number of design variables is smaller than the number of state variables. This was the approach employed by Liu et al. in [15]. Replacing (32) in (31) yields

$$\begin{aligned}\frac{\partial\mathbf{F}_s(\boldsymbol{\rho})}{\partial\rho_{em}} =& -\mathbf{W}^T(\boldsymbol{\rho})\frac{\partial\mathbf{K}^{'T}(\boldsymbol{\rho})}{\partial\rho_{em}}\mathbf{V}(\boldsymbol{\rho}) + \mathbf{W}^T(\boldsymbol{\rho})\frac{\partial\mathbf{G}(\boldsymbol{\rho})}{\partial\rho_{em}}\mathbf{W}(\boldsymbol{\rho}) \\ & -\mathbf{V}^T(\boldsymbol{\rho})\frac{\partial\mathbf{K}(\boldsymbol{\rho})}{\partial\rho_{em}}\mathbf{W}(\boldsymbol{\rho})\end{aligned} \tag{33}$$

The gradient of the cross section stiffness matrix is obtained by inserting the result from (33) into (28). Finally, replacing (28) in (27) and the corresponding result in (26) yields the gradient of the beam compliance for load case l.

4.2 Shear and mass center position

The sensitivities of the shear center position with respect to the design variable ρ_{em} are obtained from differentiation of (15) yielding

$$\begin{aligned}\frac{\partial x_s}{\partial\rho_{em}} =& -\left(\frac{\partial F_{s,62}}{\partial\rho_{em}} + \frac{\partial F_{s,64}}{\partial\rho_{em}}(L-z)\right)\frac{1}{F_{s,66}} \\ & + \left(F_{s,62} + F_{s,64}(L-z)\right)\frac{1}{F_{s,66}^2}\frac{\partial F_{s,66}}{\partial\rho_{em}} \\ \frac{\partial y_s}{\partial\rho_{em}} =& \left(\frac{\partial F_{s,61}}{\partial\rho_{em}} + \frac{\partial F_{s,65}}{\partial\rho_{em}}(L-z)\right)\frac{1}{F_{s,66}} \\ & - \left(F_{s,61} + F_{s,65}(L-z)\right)\frac{1}{F_{s,66}^2}\frac{\partial F_{s,66}}{\partial\rho_{em}}\end{aligned}$$

where the gradients $\partial F_{s,ij}/\partial\rho_{em}$ are the entries of $\partial\mathbf{F}/\partial\rho_{em}$ derived in the previous section. Finally, by differentiation of (16) the sensitivities of the mass center

position are

$$\frac{\partial x_c}{\partial \rho_{em}} = \frac{x_{c_e} v_e}{\sum_{e=1}^{n_e} v_e \varrho_e} \frac{\partial \varrho_e}{\partial \rho_{em}} - \frac{\sum_{e=1}^{n_e} x_{c_e} v_e \varrho_e}{\left(\sum_{e=1}^{n_e} v_e \varrho_e \right)^2} \left(v_e \frac{\partial \varrho_e}{\partial \rho_{em}} \right)$$

$$\frac{\partial y_c}{\partial \rho_{em}} = \frac{y_{c_e} v_e}{\sum_{e=1}^{n_e} v_e \varrho_e} \frac{\partial \varrho_e}{\partial \rho_{em}} - \frac{\sum_{e=1}^{n_e} y_{c_e} v_e \varrho_e}{\left(\sum_{e=1}^{n_e} v_e \varrho_e \right)^2} \left(v_e \frac{\partial \varrho_e}{\partial \rho_{em}} \right)$$

5 Implementation

The structural model described in Section 2 and the sensitivity analysis presented in Section 4 have been implemented in MATLAB®. The implementation of the cross section analysis tool is detailed in Blasques and Lazarov [10]. The beam finite element discretization consists of three node quadratic beam finite elements. The cross section finite element discretization is based on two dimensional four node isoparametric finite elements (see Bathe [31]). The solution for the cross section equilibrium equations in (12) are obtained by LU factorization of the corresponding matrix. The sensitivity analysis has been parallelized using the `parfor` command in MATLAB®and allocating eight processors. The parallel loop is implemented so that the gradients of the objective function and constraints with respect to the design variables are calculated in parallel. The code makes extensive use of the SuiteSparse libraries by Davis [30], and Davis and Natarajan [29]. The optimal design problems stated in Section 3.3 are solved using the robust and efficient sequential quadratic programming algorithm SNOPT by Gill et al. [28]. The SNOPT algorithm is suitable for solving optimization problems incorporating a large number of linear constraints. The n_e sparse linear constraints in (23) are therefore efficiently handled.

As an example, consider a problem with a cross section discretized using 2 116 finite elements (corresponding to 6 627 degrees of freedom), a beam finite element model using 32 three node quadratic beam finite elements (corresponding to 390 degrees of freedom), and 18 900 design variables. The current implementation, running on a platform using eight Intel XEON X5550 CPU's at 2.66 GHz takes approximately five seconds for each objective function evaluation. Each objective function evaluation includes the assembly of finite element matrices and the solution of the corresponding linear system of equations at both the cross section and beam levels, respectively. The sensitivities of the beam compliance with respect to all design variables are evaluated in approximately 20 seconds.

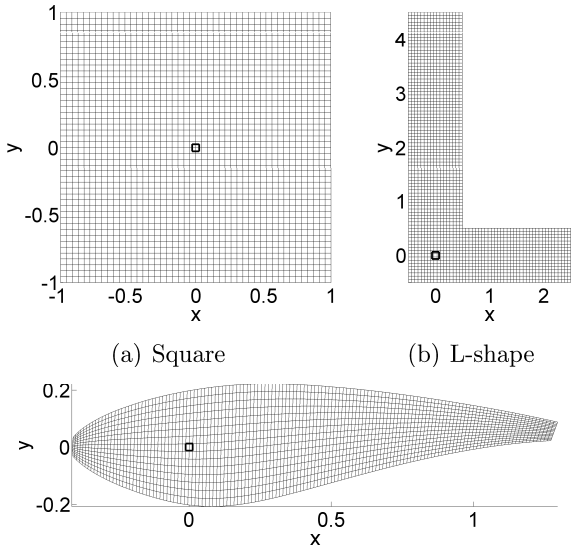

(a) Square (b) L-shape

(c) Profile

Figure 5: Cross section dimensions and finite element discretization of the studied cross sections. (a) Square cross section with 2116 elements, (b) L-shape cross section with 2023 elements, and (c) wing profile with 2100 elements. The square marker indicates the position of the beam node or point of application of the loads.

6 Numerical experiments

In this section we present a set of numerical experiments which illustrate the behavior of the devised methodology for optimal design of laminated composite beams. The setup of the experiments, namely the beam geometries, load cases, and material properties, is presented first. Details regarding the organization and visualization of the results are discussed next. Finally, all numerical results are presented and discussed.

6.1 Beam geometries

Three different cross section geometries have been considered – a square, an L-shape, and a wing profile from a section of a wind turbine blade. The finite element discretizations of the cross sections are presented in Figure 5. The dimensions of each of the cross sections are given in Table 1. The beam finite element model for all cases is composed of 32 three node quadratic beam finite elements. In Figure 5 the position of the beam node with respect to the cross section geometry is marked with a square marker.

Table 1: Dimensions of the considered beams.

Square		L-shape		Profile	
Width	2 m	Width	3 m	Chord	2 m
Height	2 m	Height	5 m	Thickness	0.43 m
Length	20 m	Thickness	1 m	Length	20 m
		Length	20 m		

Table 2: Load cases and direction and magnitude of the loads, for two of the beam geometries. The distributed transverse forces $\widehat{f}_x$ and $\widehat{f}_y$, and the torsional moment $\widehat{m}_z$ have been considered.

Load cases	Direction	Magnitude	
		Square	L-shape
LC1	$\widehat{f}_y$	0.3	–
LC2	$\widehat{f}_x + \widehat{f}_y$	0.2+0.3	0.2+0.35
LC3	$\widehat{m}_z$	1.5	1
LC4	$\widehat{f}_y + \widehat{m}_z$	0.3+1.5	–
LC5	$\widehat{f}_x + \widehat{f}_y + \widehat{m}_z$	0.2+0.3+1.5	–
LC6	$\widehat{f}_x, \widehat{f}_y$	0.2, 0.3	0.2, 0.35
LC7	$\widehat{f}_y, \widehat{m}_z$	0.3, 1.5	–

6.2 Load cases

All loads are applied as distributed pressure loads along the beam length. The direction of the loads is according to the cross section coordinate system shown in Figure 3. The load cases for the square and the L-shape cross sections are presented in Table 2.

The beam with the wing profile cross section is subjected to 15 static load cases. The load cases are defined based on the aerodynamic loading generated by an airfoil of the same shape exposed to a constant incoming wind speed of $W_s =$ 20m/s at 15 different angles of attack. For each angle of attack the aerodynamic loads are computed as

$$L_a = \frac{1}{2}\varrho_a W_s^2 c C_L, \quad D_a = \frac{1}{2}\varrho_a W_s^2 c C_D, \quad M_a = \frac{1}{2}\varrho_a W_s^2 c^2 C_M$$

where L_a, D_a, and M_a, are the aerodynamic lift, drag, and moment, respectively. The aerodynamic lift, drag and moment coefficients, C_L, C_D, and C_M, respectively, are obtained from the experimental data in Ramsay et al. [41]. The experimental data is presented in Figure 6 for several values of angle of attack α_w. The air density is assumed to be $\varrho_a = 1.2041\text{kg/m}^3$. The magnitude of lift and drag is defined with respect to the wind direction as described in Figure 7(a). Its components with respect to the cross section coordinate system are computed to define the corresponding resultant load vector R_a. The magnitude and orientation of the aerodynamic lift and drag loads, and corresponding resultant

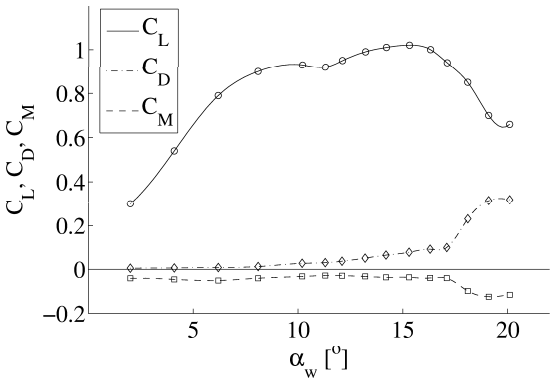

Figure 6: Aerodynamic lift, drag, and moment coefficients – C_L, C_D, and C_M, respectively – as function of the angle of attack α_w. Experimental values for the S809 wind turbine airfoil (Ramsay et al. [41]).

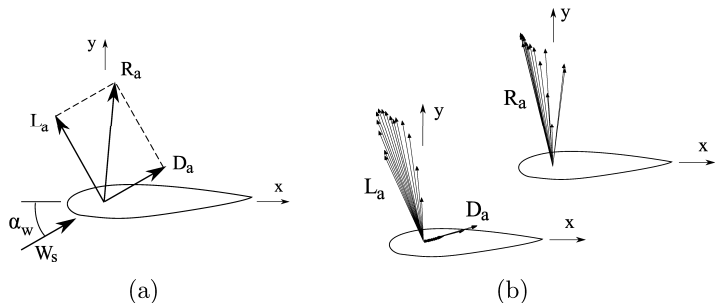

Figure 7: Definition of aerodynamic lift, drag and resultant forces. (a) Description of aerodynamic lift and drag forces, L_a and D_a, and corresponding resultant force R_a, generated by a profile exposed to a wind speed W_s at an angle of attack α_w. (b) Magnitude and orientation of the lift, drag, and corresponding resultant forces for each of the 15 load cases applied in the optimization procedure.

vector, for each of the 15 load cases are presented in Figure 7(b). Note that the aerodynamic moment is not depicted in these figures.

The idealized wind turbine blade is represented by a cantilever beam of constant cross section along the length. The static pressure loads are also assumed to be constant along the length of the beam. The beam node or the point of application of the loads is coincident with the aerodynamic center positioned at a distance equal to a quarter of the chord from the leading edge.

6.3 Material properties

The material properties are specified at each element of the cross section finite element discretization. The candidate materials may be isotropic, anisotropic, or even the same anisotropic material oriented in different directions. In the

Table 3: Material properties for the orthotropic material (scaled values for E-glass reinforced Epoxy laminate according to the Handbook of Composites [37]), and the isotropic material (scaled values for DIAB H100 PVC Core according to DIAB mechanical property sheets [38]).

Material	Orthotropic		Isotropic	
$E_{xx} = E_{yy}$	120	Gpa	0.130	Gpa
E_{zz}	480	Gpa	0.130	Gpa
$G_{zx} = G_{zy}$	60	Gpa	0.035	Gpa
G_{xy}	50	Gpa	0.035	Gpa
$\nu_{zx} = \nu_{zy}$	0.19	-	0.35	-
ν_{xy}	0.26	-	0.35	-
$\overline{\varrho}$	1.78	10^3 kg/m^3	0.1	10^3 kg/m^3

numerical experiments, two material types have been considered – one orthotropic material and one isotropic material. Their stiffness properties are presented in Table 3. The orthotropic material corresponds to a type of E-Glass reinforced Epoxy laminate (cf. Peters [37]). The isotropic material corresponds to a type of polyvinyl chloride (PVC) core material (cf. DIAB H100 [38]) typically used in sandwich structures of wind turbine blades.

6.3.1 Generating candidates

A candidate material constitutive matrix $\overline{\mathbf{Q}}_j$ is generated in the following manner. The material constitutive matrices, $\mathbf{Q}_m$, for each material m are based on the material properties in Table 3. This will initially yield two candidates – the orthotropic material and the isotropic material, respectively. The remaining candidates are generated by orienting the material constitutive matrix $\mathbf{Q}_m$ of the orthotropic material in different directions. Hence, the material constitutive matrix of candidate j is obtained from the rotation of the material constitutive matrix $\mathbf{Q}_m$ as

$$\overline{\mathbf{Q}}_j = \mathbf{R}_t \mathbf{Q}_m \mathbf{R}_t^T$$

where $\mathbf{R}_t$ is the three dimensional transformation matrix for a rotation about a given axis. This is a convenient approach in the design of laminated composite structures. A laminate consists of different layers of fibers aligned in different directions. The layers will be stacked in different directions defined by the different fiber plane orientations. In this case, a different matrix $\overline{\mathbf{Q}}_j$ will be associated with each different combination of fiber and fiber plane orientation generated from the same matrix $\mathbf{Q}_m$. The procedure is illustrated in Figure 8. First, the fiber plane orientation is defined by the rotation α_p. Then the fibers are rotated in their own plane by α_f and the final fiber orientation is obtained.

In total eight orthotropic candidate materials have been considered during the numerical experiments. These materials correspond to two different fiber plane

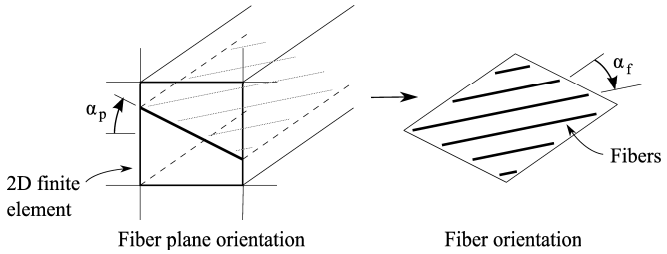

Figure 8: Three-dimensional rotation of fiber plane and fiber orientation in the cross section mesh. The fiber plane orientation is defined by the angle α_p while the orientation of the fibers in the fiber plane are defined by the angle α_f.

orientations (0° and 90°) and four different in-plane fiber orientations (0°, 45°, −45°, and 90°). The list of candidate materials is described in Figure 9 where the resulting spatial orientation of the fibers for each of the orthotropic candidates are listed.

6.4 Optimization strategy

The optimization strategy consists of first solving the unpenalized problem, i.e., assuming $p_1 = 1$ in the material interpolation scheme in (21). The penalty parameter is gradually increased such that at step $i+1$ the penalty value is $p_{i+1} = p_i + \Delta p$, where $\Delta p \geq 0$. Each problem is solved until some optimality criteria is satisfied or the maximum number iterations is met. In SNOPT, the major optimality tolerance and maximum number of major iterations (number of solved quadratic sub-problems) at each step of the continuation method is set to 1×10^{-5} and 500, respectively. The remaining parameters in SNOPT are set to the default values. Our numerical experiences indicate that the resulting design will depend on the step length Δp. In general, designs with lower compliance values can be attained using a larger number of steps with a smaller step length. The disadvantage is that the number of objective function evaluations increases. In the numerical experiments using the square and L-shape cross sections a $\Delta p = 0.1$ has been used. In the case of the wing profile a smaller step length of $\Delta p = 0.075$ is used. For all cases the final penalty value is such that $p \geq 3$ (see Table 5). Finally, the starting point for all cases is such that the same volume fraction is given to all materials.

6.5 Presentation of the results

Devising a succinct presentation of the results for multi-material topology optimization problems is not trivial. The aim here is to describe the organization of the result figures and corresponding legends which are used in the presentation of the results for all numerical experiments.

The optimal distribution of candidate materials are presented using two groups of figures. As described in Figure 10, each figure in the bottom group corresponds

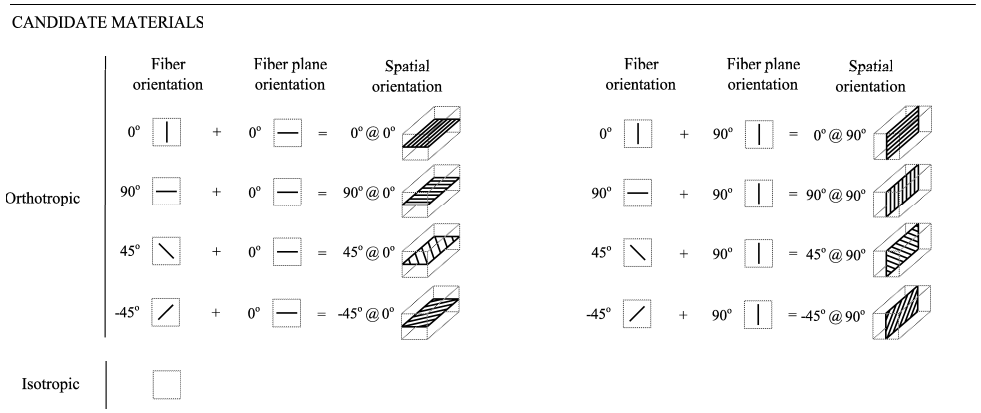

Figure 9: Legend for the figures depicting the designs. Visualization of the spatial orientation of the fibers at each element based on the resulting fiber and fiber plane orientations, for each of the candidate orthotropic materials.

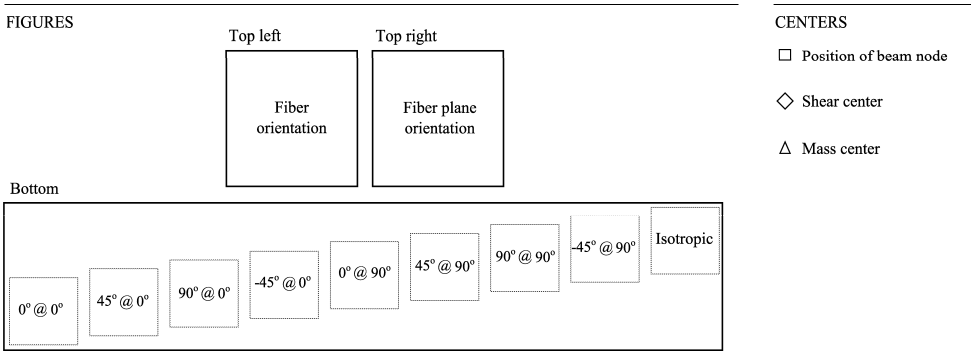

Figure 10: Legend for the figures depicting the designs. Three figures are presented to describe the results of each numerical experiment. The definition of each of the figures can be seen on the left. The symbols used to indicate the beam node, shear center and mass center positions can be seen on the right.

to one candidate material. In these figures an element is darker where that material exists. This is essentially an extension of the visualization procedure used in two phase topology optimization to the multiple material case. The two figures in the top row show the fiber and fiber plane orientations at each element, respectively. In both cases the orientation is marked with a line on the element. The orientation of these lines define the spatial orientation of the fibers of the orthotropic material at each element. The spatial orientation of the fibers of the orthotropic material is visualized using the legend presented in Figure 9. The thickness and darkness of the line is weighted by the value of filtered design variable at the corresponding element. It is consequently possible to visualize the effect of the density filter in the areas of transition between different materials. Finally, the element is white in case the material is isotropic.

Table 4: Catalog of problems combining different cross sections (square, L-shape, and wing profile as described in Figure 5), load cases (cf. Table 2), and problem formulations. The minimum compliance problem with constraints on weight and positions of shear and mass center is denoted (P1), and the minimum compliance problem with weight constraints is denoted (P2).

Ref.	Cross section	Load case	Problem formulation
S1	Square	LC1	(P2)
S2	Square	LC2	(P2)
S3	Square	LC3	(P2)
S4	Square	LC4	(P2)
S5	Square	LC5	(P2)
S6	Square	LC6	(P2)
S7	Square	LC7	(P2)
S8	Square	LC6	(P1)
L1	L-shape	LC2	(P2)
L2	L-shape	LC3	(P2)
L3	L-shape	LC6	(P2)
L4	L-shape	LC2	(P1)
W1	Profile	Aerodynamic	(P2)
W2	Profile	Aerodynamic	(P1)

Note that for all cases, the presented designs correspond to the penalized filtered volume fractions. The use of the filtered values is motivated by the fact that these represent the actual volume fractions multiplying each of the candidates. Regarding the use of penalized values, for discrete designs the magnitude of the penalty will not affect the value of the compliance or the position of the shear center. However, inherent to the use of the density filter is the fact that the edges of the different material regions will consist of material mixtures. These will not be eliminated through increased penalization. The magnitude of the compliance and position of the shear center center will therefore show some dependence on the penalty value. Thus, the designs obtained with the penalized values are presented since these are the basis for the evaluation of the values and feasibility of the constraints.

6.6 Results

The 14 different numerical experiments are listed in Table 4 as a combination between the different cross sections, load cases, and problem formulations. Details regarding the step length and maximum penalty size in the continuation method, and the chosen constraint values are presented in Table 5. The number of design variables, resulting number of objective function evaluations, and constraint values for all the optimal design problems are summarized in Table 6. Note that in the MATLAB® interface to SNOPT each evaluation of the objective function and constraints entails necessarily an evaluation of its gradients. The steps included

Table 5: Details of all the numerical experiments (cf. Table 4). The first column indicates the number of degrees of freedom (cross section/beam). The next two columns indicate the step size and maximum penalty (Δp and p_{max}, respectively) associated with the continuation method. The remaining columns indicate the values of the constraints on weight (defined by the ratio of orthotropic material), shear center and mass center positions ($\overline{w}$, $\mathbf{s}_c = (x_s, y_s)$, and $\mathbf{m}_c = (x_c, y_c)$, respectively).

Ref.	Number of d.o.f.'s	Penalization		Constraints		
		Δp	p_{max}	$\overline{w}$	$\overline{\mathbf{s}}_c$	$\overline{\mathbf{m}}_c$
S1-7	6624/390	0.1	3	1/2	–	–
S8	6624/390	0.1	3	1/2	$x_s = 0$, $y_s = 0$	$x_c = 0$, $y_c = 0$
L1-3	6480/390	0.1	3	1/2	–	–
L4	6480/390	0.1	3	1/2	$0 \leq x_s \leq 1$, $0 \leq y_s \leq 1$	$0 \leq x_c \leq 1$, $0 \leq y_c \leq 1$
W1	6768/390	0.075	8.5	1/3	–	–
W2	6768/390	0.075	8.5	1/3	$x_s \geq -0.2$	$x_c \leq 0.1$

in one objective function evaluation have been described in Section 5.

The results obtained for the minimum compliance problem with weight constraints (P2) are presented first. The results for the minimum compliance problem with constraints on weight and shear and mass center positions (P1), are presented next. Finally, the devised methodology is applied in the optimal design of the structural lay-out of a wind turbine blade cross section.

6.6.1 Minimum compliance with weight constraints

The optimal designs presented in Figures 11 and 12, correspond to the cases where the beam is subjected to a distributed transverse force (case S1 and S2). The normal stresses induced by the bending moment dominate in the regions away from the neutral axis. In the central part of the beam, close to the neutral axis, the normal stresses approach zero and the shear stresses dominate. The resulting topology is, in both cases, a variation of the typical I-beam or box-beam with the flanges resisting the normal stresses and the webs resisting the shear stresses. In the S1 case, the laminates at the flanges orient at 0°@90° along the length of the beam to resist the normal stresses. In the case S2 the laminates in the flanges orient at both 0°@0° and 0°@90°. The fibers remain aligned along the beam length while the fiber plane rotates around the corner of the cross section. In the webs a laminate structure composed of 45°@90° and −45°@90° appears in both cases. These patterns in terms of fiber and fiber plane orientations are common to most of the solutions where a transverse load dominates the load case. The optimal distribution of materials are presented for the L-shape section cases L1 and L3 in Figures 16 and 18, respectively. Note that the same type of pattern is emerging here. The regions away from the neutral axis are composed of 0°@0° and 0°@90° laminates. The fiber plane orientation changes as the fibers go around

Table 6: Summary of numerical results for all cases in Table 4. The second and third columns indicate the number of design variables and objective function evaluations, respectively. The resulting compliance (C), weight (w) defined by the ratio of orthotropic material, shear center position ($\mathbf{s}_c = (x_s, y_s)$), and mass center position ($\mathbf{m}_c = (x_c, y_c)$). The compliance and shear center position values are obtained with the penalized densities, i.e., $p = p_{max}$ (cf. Table 5).

Ref.	Number of D.V.'s	Obj. func. eval.'s	C	w	x_s	y_s	x_c	y_c
S1	19044	1204	15.235	1/2	–	–	–	–
S2	19044	469	18.046	1/2	–	–	–	–
S3	19044	913	41.479	1/2	–	–	–	–
S4	19044	1536	19.986	1/2	–	–	–	–
S5	19044	1134	43.813	1/2	–	–	–	–
S6	19044	880	22.184	1/2	–	–	–	–
S7	19044	763	48.307	1/2	–	–	–	–
S8	19044	1193	44.336	1/2	0	0	0	0
L1	18216	1252	8.275	1/2	–	–	–	–
L2	18216	1316	8.060	1/2	–	–	–	–
L3	18216	1067	7.058	1/2	–	–	–	–
L4	18216	1291	8.326	1/2	0.0093	0	0.6043	1.0000
W1	18900	3158	13.978	1/3	–	–	–	–
W2	18900	2784	14.621	1/3	-0.1187	0.0164	0.1000	0.0134

a corner of the cross section. The shear webs in these cases also present the same type of laminate structure with two separate regions of $45°@90°$ and $-45°@90°$ for vertical webs, and $45°@0°$ and $-45°@0°$ for horizontal ones.

Note that for case S1 and S2 (see Figures 11 and 12) the relative position of the shear center coincides with the beam node, or the point of application of the loads. Thus, an applied transverse force, irrespective of the direction, will not induce a torsional moment. In case L1 (see Figure 16) the shear center position is aligned with the beam node along the direction of the applied transverse load (load case LC2, $\widehat{f}_x + \widehat{f}_y$). Hence, the specific load combination in LC2 will not induce a torsional moment, but the coupling will occur for a transverse load in any other direction.

The results obtained for the square and L-shape cross sections subject to a torsional moment (case S3 and L2, respectively) are presented in Figures 13 and 17, respectively. As expected, the resulting optimal designs are closed cross sections. This is due to the fact that for a closed cross section subjected to torsion the shear flow is constant through the thickness. In open cross sections the shear flow varies linearly through the thickness. Hence, the torsional stiffness is a function of the area for closed cross sections and of the thickness for open cross sections. Thus, closed cross sections are stiffer in torsion. An assumption of the Saint-Venant theory underlying the structural model used here is that the warping deformation is unconstrained. As such, for a beam subjected to a torsional moment, the normal stresses are zero and the cross section walls are subject to shear stresses

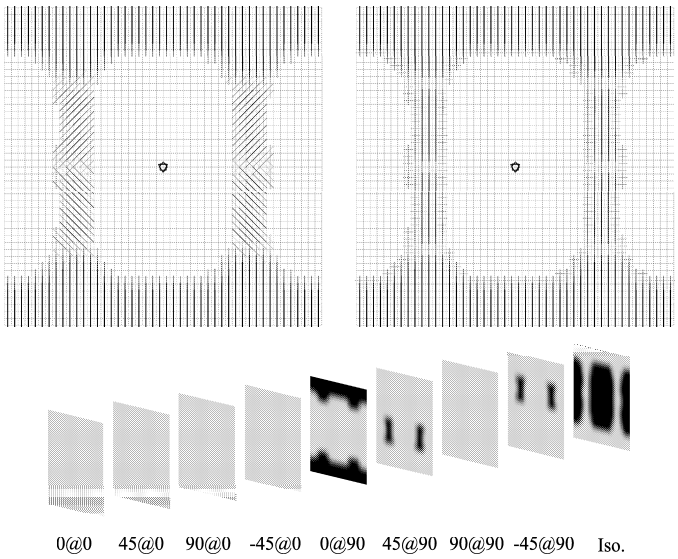

Figure 11: Optimal material distribution for square cross section subject to vertical transverse force $\widehat{f}_y$ (case S1, cf. Table 4) with $f_r = 0.15$. Solution to the minimum compliance problem with a weight constraint (P2). The legend to the figure is described in Figures 9 and 10.

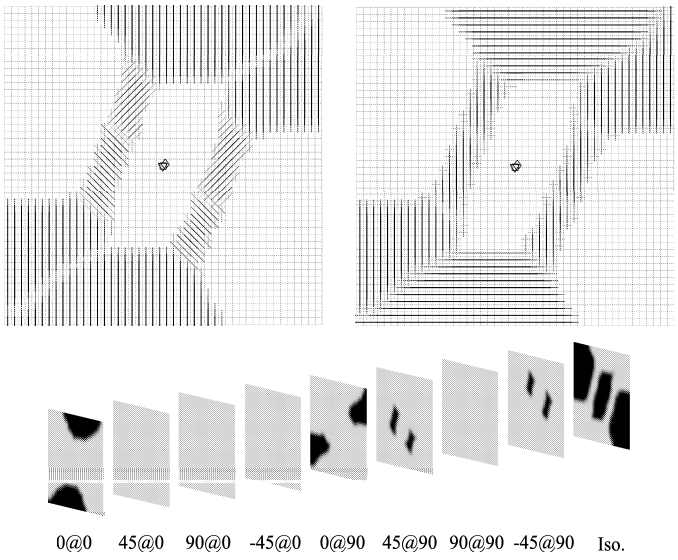

Figure 12: Optimal material distribution for square cross section subject to combined horizontal transverse force $\widehat{f}_x$ and vertical transverse force $\widehat{f}_y$ (case S2, cf. Table 4) with $f_r = 0.1$. Solution to the minimum compliance problem with a weight constraint (P2). The legend to the figure is described in Figures 9 and 10.

only. The resulting optimal results for both cross sections consist therefore only of laminates oriented at $45°@0°$, $-45°@0°$, $45°@90°$, and $-45°@90°$. In this way

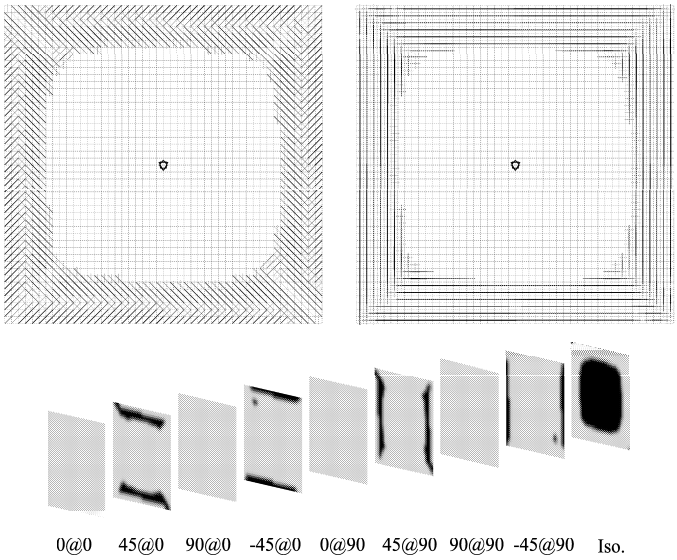

Figure 13: Optimal material distribution for square cross section subject to torsional moment $\widehat{m}_z$ (case S3, cf. Table 4) with $f_r = 0.1$. Solution to the minimum compliance problem with a weight constraint (P2). The legend to the figure is described in Figures 9 and 10.

the fibers align in the direction of the principal stresses. Moreover, in both the S3 and L2 cases, a layered structure is visible. This is in agreement with the common engineering intuition. Since both $45°$ and $-45°$ directions are equally stiff, a stacking of interchanging layers of $45°$ and $-45°$ increases stiffness and avoids any elastic anisotropic material couplings.

Contrarily to the results obtained for case S1, S2 and S3, the shear center does not coincide with the point of application of the loads in the resulting designs for cases S4 and S5 (Figures 14 and 15). The position of the shear center $\mathbf{s}_c$ is a function of the magnitude of the entries of the cross section compliance matrix $\mathbf{F}_s$ (cf. (15) in Section 2.1.6), $F_{s,61}$ and $F_{s,62}$ for the shear-torsion couplings, and, $F_{s,64}$ and $F_{s,65}$ for the bending-torsion couplings. The magnitude of these entries depends on both the cross section topology and the elastic couplings stemming from material anisotropy. In the S4 (see Figure 14) case it is clearly visible that the optimal solution has exploited both effects. The topology has changed when compared to the S1 and S3 cases so that there is an asymmetry with respect to the vertical axis. Moreover, existence of a layer of $-45°@0°$ in both top and bottom will result in non-zero shear- and bend-torsion coupling coefficients. Both these features contribute to the horizontal shift in the position of the shear center. The same mechanisms play the same role in the optimal solution of case S5 (see Figure 15). In summary, the beams of case S4 and S5 will present couplings between both shear and torsion and, bending and torsion. In these cases, and based on the position of the shear center, these couplings are such that the applied transverse

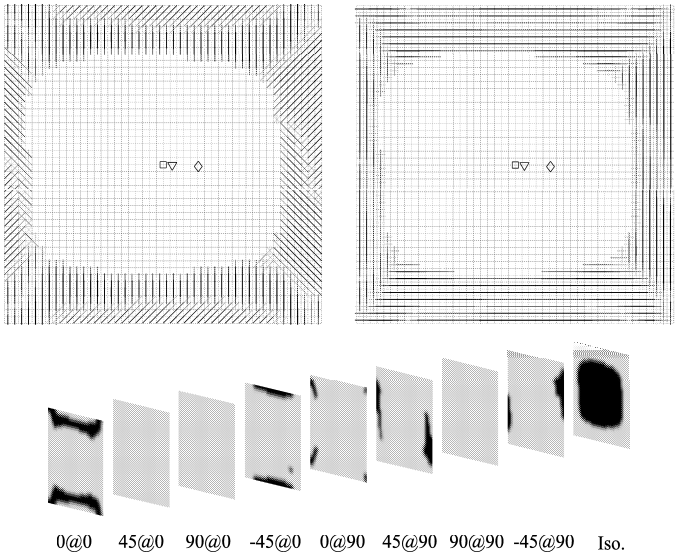

Figure 14: Optimal material distribution for square cross section subject to combined vertical transverse force $\widehat{f}_y$ and torsional moment $\widehat{m}_z$ (case S4, cf. Table 4) with $f_r = 0.1$. Solution to the minimum compliance problem with a weight constraint (P2). The legend to the figure is described in Figures 9 and 10.

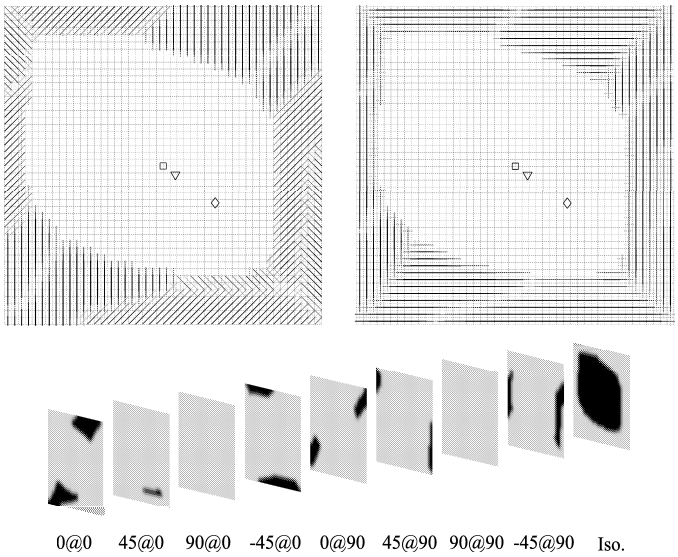

Figure 15: Optimal material distribution for square cross section subject to combined horizontal transverse force $\widehat{f}_x$, vertical transverse force $\widehat{f}_y$, and torsional moment $\widehat{m}_z$ (case S5, cf. Table 4) with $f_r = 0.1$. Solution to the minimum compliance problem with a weight constraint (P2). The legend to the figure is described in Figures 9 and 10.

force ($\widehat{f}_y$ in S4 and, $\widehat{f}_x$ and $\widehat{f}_y$ in S5) and resulting bending moment, will induce a torsional rotation of the cross section which opposes the applied torsional moment.

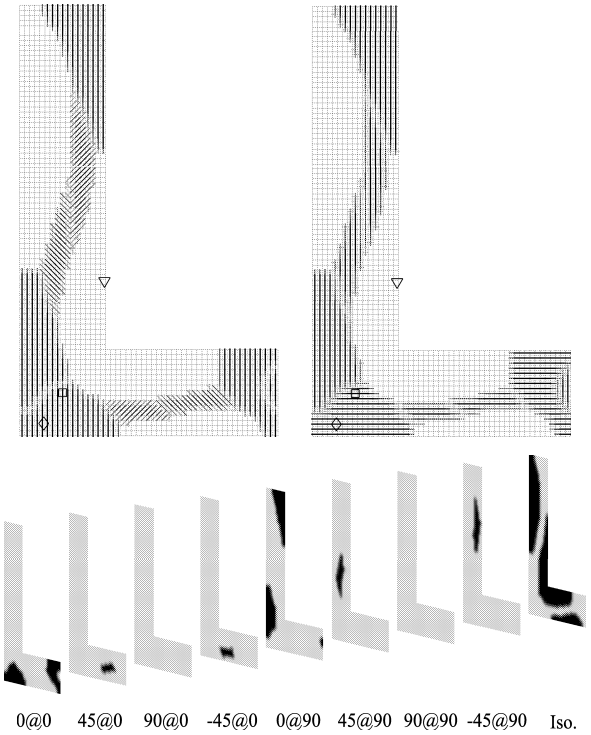

Figure 16: Optimal material distribution for L-shape cross section subject to combined horizontal transverse force $\widehat{f}_x$ and vertical transverse force $\widehat{f}_y$ (case L1, cf. Table 4) with $f_r = 0.125$. Solution to the minimum compliance problem with a weight constraint (P2). The legend to the figure is described in Figures 9 and 10.

A larger number of numerical experiments were conducted, mostly with the L-shape cross section. The differences in the results, in terms of material distribution and cross section topology, were however not significant and these results have therefore been omitted.

6.6.2 Minimum compliance problem with constraints on mass and positions of shear and mass centers.

The S5 and L2 cases (see Figures 15 and 16, respectively) are revisited here but now the positions of the shear and mass center are constrained. The resulting optimal designs are presented in Figures 19 and 20, for case S8 and L4, respectively. The resulting values of the constraints are presented in Table 5. In the S8 case the shear and mass center positions are constrained such that its position is coincident with the beam node, i.e., $x_s = 0$, $y_s = 0$, $x_c = 0$, and $y_c = 0$. The resulting design satisfies all constraints. Compared to the S5 case (see Figure 15), the orientation of the fibers is similar in the different regions. The thickness of the faces however has changed to satisfy the constraints in the mass center position. The resulting compliance for the S8 case is, as a consequence, slightly higher than that of case

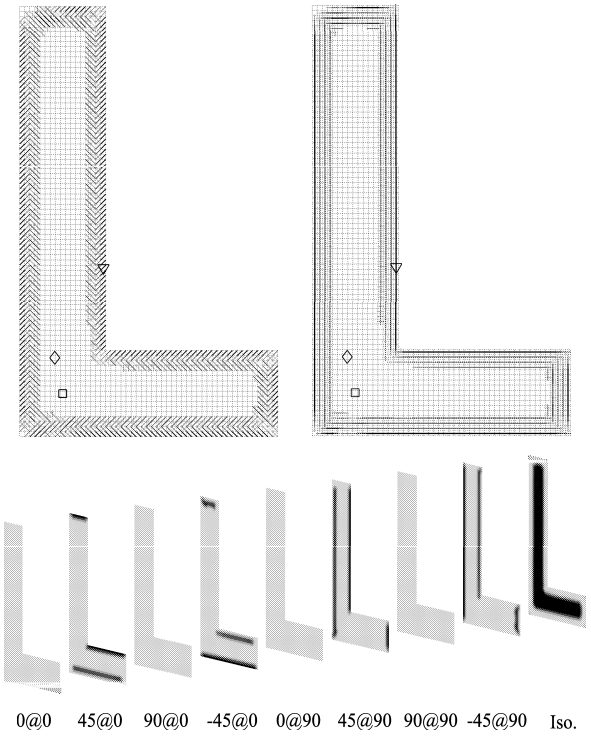

Figure 17: Optimal material distribution for L-shape cross section subject to a torsional moment $\widehat{m}_z$ (case L2, cf. Table 4) with $f_r = 0.125$. Solution to the minimum compliance problem with a weight constraint (P2). The legend to the figure is described in Figures 9 and 10.

S5 (cf. the results in Table 6).

In the L4 case (see Figure 16) the shear and mass center are constrained such that $0 \leq x_s \leq 1$, $0 \leq y_s \leq 1$, $0 \leq x_c \leq 1$, and $0 \leq y_c \leq 1$. The resulting optimal design satisfies all the constraints. The resulting cross section topology fiber orientations are similar to the unconstrained case L2 (see Figure 16). The material however has been redistributed to satisfy the constraint on the mass center position which is now placed lower than in the L2 case.

6.6.3 Application to the structural design of the cross section of a wind turbine blade

The same methodology is now applied in the design of the cross section of an idealized wind turbine blade. The blade is subject to 15 static load cases as described in Section 6.2.

For the minimum compliance problem with weight constraints (problem formulation (P2)) the ratio between the stiffness and density of the materials does not affect the results. This is not the case when the constraints on shear and mass center positions are included (problem formulation (P1)). Both the shear and

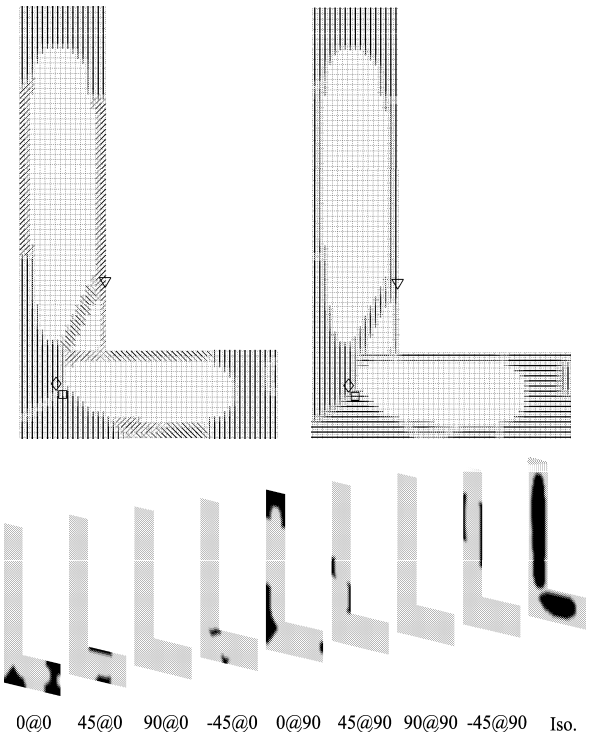

Figure 18: Optimal material distribution for square cross section subject to horizontal transverse force $\widehat{f}_x$ and vertical transverse force $\widehat{f}_y$, separately (case L3, cf. Table 4), with $f_r = 0.125$. Solution to the minimum compliance problem with a weight constraint (P2). The legend to the figure is described in Figures 9 and 10.

mass center positions are functions of the relative difference between the stiffness and density of the candidate materials. In order to obtain realistic values a second isotropic material is included which scales the first isotropic materials stiffness and density by a factor of 1×10^{-3}. The aim is to include a "material" which mimics void as commonly done in topology optimization. Thus, in both the W1 and W2 cases ten candidate materials have been considered (eight orthotropic and two isotropic materials) instead of the nine considered in the formed cases.

Note that the aim here is to design the load carrying structure of the wind turbine blade. It is therefore assumed that the aerodynamic shell is non-structural and exists around the perimeter of the cross section shape outside the design domain.

The results are presented in Figures 21 and 22 for cases W1 and W2, respectively. In both cases only the void material (or second and weaker isotropic material) exists in both final optimal designs. Furthermore, both results suggest that the effect of the aerodynamic moment M_a is small and that the distributed transverse forces R_a are the dominating loads. Hence, the resulting optimal designs are present patterns similar to the obtained for the square cross section under

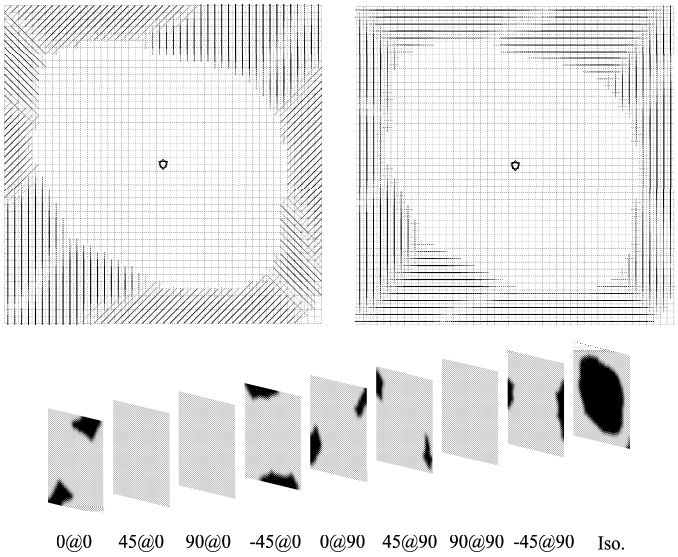

Figure 19: Optimal material distribution for square cross section subject to combined horizontal transverse force $\widehat{f}_x$, vertical transverse force $\widehat{f}_y$, and torsional moment $\widehat{m}_z$ (case S8, cf. Table 4) with $f_r = 0.125$. Solution to the minimum compliance problem with constraints on weight and, shear and mass center positions (P1). The legend to the figure is described in Figures 9 and 10.

a transverse load (case S1 and S2, Figures 11 and 12, respectively). The laminates in top and bottom form the flanges of the box beam resisting the normal stresses. The fibers in these regions are oriented along the length of the blade and stacked in an horizontal plane, i.e., the 0°@0° laminate. The webs or side faces of the box beam resist the shear stresses. The laminates here are mostly composed of fibers oriented at 45° and −45° and stacked in a vertical plane, i.e., laminates 45°@90°, and −45°@90°. The resulting optimal designs are similar to existing wind turbine blade designs where the load carrying structure consists of a box beam or spar, see, e.g., [42].

The position of shear and aerodynamic center have an impact on the dynamic characteristics of wind turbine blades. According to Hansen [39], flutter and divergence speed limits are strongly associated with the relative positions of the mass, aerodynamic, and shear centers. For a fixed position of the aerodynamic and shear centers, the divergence speed is the limiting factor in case the mass center is placed for (closer to the leading edge) of the aerodynamic center. In case the mass center is aft of the aerodynamic center, the flutter speed is the limiting factor. The flutter limit speed has an asymptote when the mass and aerodynamic center are coincident, and decreases as the mass center moves towards the trailing edge. In the W2 case (see Figure 22) these considerations on the dynamic performance of the wind turbine blade are incorporated into the structural design by controlling the position of the shear and mass centers. Hence, the distance from the mass

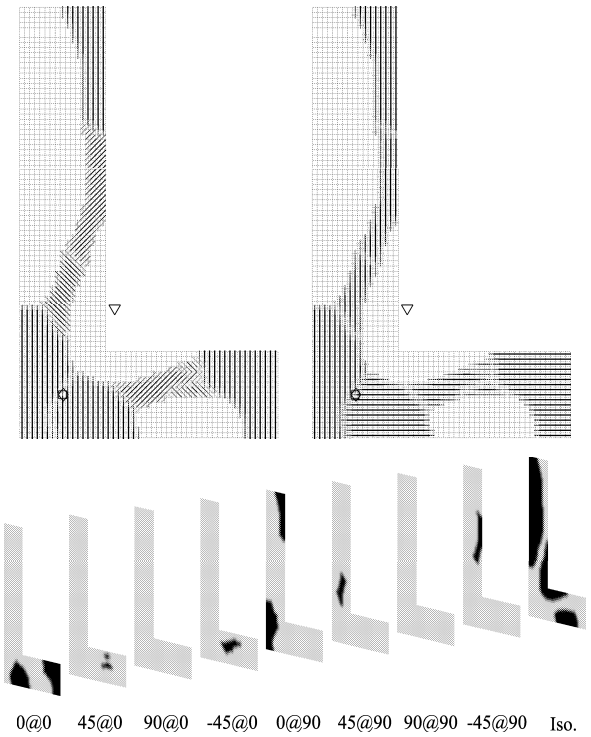

Figure 20: Optimal material distribution for L-shape cross section subject to combined horizontal transverse force $\widehat{f}_x$ and vertical transverse force $\widehat{f}_y$ (case L4, cf. Table 4) with $f_r = 0.125$. Solution to the minimum compliance problem with constraints on weight and, shear and mass center positions (P1). The legend to the figure is described in Figures 9 and 10.

center to the aerodynamic center is reduced to about half the distance obtained in W1, i.e., $x_c \leq 0.1$. In order to avoid strong couplings between the transverse (or flap wise) and torsional deformation, the shear center is constrained so that it remains within a given distance of the aerodynamic center, i.e., $x_s \geq -0.2$. The aim is to design the cross section structural lay-out and simultaneously accounts for the static and dynamic properties of the wind turbine blade. The resulting optimal design satisfies both constraints. The difference in the results from the W1 and W2 case can be interpreted as a shift towards the leading edge in the position of the box beam. However, note that the resulting optimal design W2 is more compliant than the optimal design from case W1. In future research a measure of the dynamic performance should be included so that an optimal compromise between the static and dynamic performance is achieved.

6.7 Discussion

The results presented suggest that the proposed methodology is suitable for simultaneous optimization of the topology and material distribution for maximum stiff-

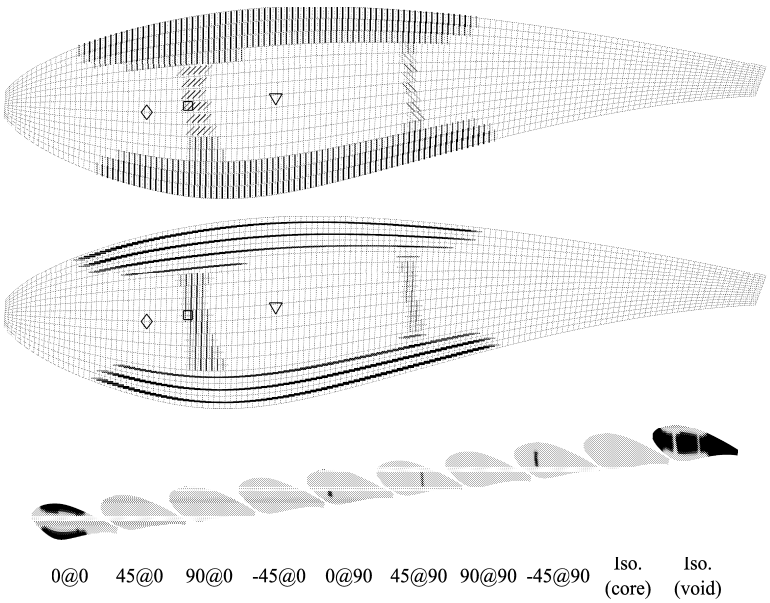

Figure 21: Optimal material distribution for a wing profile cross section subject to 15 static aerodynamic load cases (case W1, cf. Table 4) with $f_r = 0.035$. Solution to the minimum compliance problem with a weight constraint (P2). The legend to the figure is described in Figures 9 and 10.

ness design of anisotropic and inhomogeneous beam cross sections. The method has been applied to optimize laminated composite beams subjected to stiffness, weight and, shear and mass center placement constraints.

The resulting optimal designs reflect the generality of the formulation and its consequent ability to capture the three-dimensional elastic phenomena underlying the deformation of inhomogeneous anisotropic beams. The model allows for the solution of a three-dimensional problem while requiring only the solution to two smaller one- and two-dimensional problems.

Our numerical experience indicates that the multi-material topology optimization formulation as presented here is prone to converge to poorly performing designs if proper care is not taken. The results suggests that the continuation method is an effective approach to avoid these low-performing designs. In general, the performance of the different designs improved when the magnitude of the increase in the penalty value between steps in the continuation method was reduced. The disadvantage of the approach is the increase in the number of objective function evaluations when compared to typical material-void topology optimization problems. A decrease in the number of objective function evaluations is attainable through an increase in the major optimality criteria or a reduction of the number of maximum iterations.

The proposed penalization technique also proved effective in generating designs where only one material has been chosen at each point of the design domain. Note

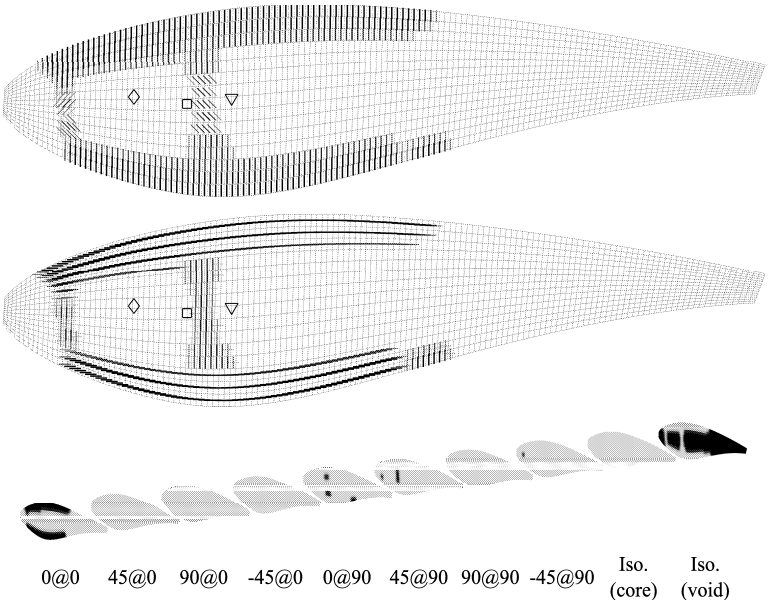

Figure 22: Optimal material distribution for a wing profile cross section subject to 15 static aerodynamic load cases (case W2, cf. Table 4) with $f_r = 0.035$. Solution to the minimum compliance problem with constraints on weight and, shear and mass center positions (P1). The legend to the figure is described in Figures 9 and 10.

however that a consequence of the application of the density filter is that the edges of the different regions will consist of material mixtures which will not be eliminated through increased penalization. An alternative would be to extend the formulation to use the Heaviside projection technique (see, e.g., Sigmund [32]). Nonetheless, the results indicate that the devised filtering technique is suitable for multi-material topology optimization problems.

7 Conclusions and Future Research

We have presented a beam finite element formulation for the analysis of anisotropic and inhomogeneous beams with arbitrary cross section geometries. The formulation builds on a finite element discretization of the cross section geometry and is therefore suitable for topology optimization. We have also formulated a minimum compliance multi-material topology optimization problem with constraints on the weight and shear and mass center positions. The design variables represent the volume fractions of each of the members in a predefined list of candidate materials. An extension of the SIMP material interpolation scheme and density filtering has been presented which can accommodate any number of (anisotropic) materials.

A large set of numerical experiments have been presented to illustrate the numerical behavior of the proposed framework. The cross section topology and material properties have been optimized for two different basic structures – a

square and L-shape beam sections – subjected to different load cases. The applicability of the framework has also been demonstrated in the optimal design of the cross section of an idealized wind turbine blade. The results indicate that the proposed methodology is suitable for the optimization of cross section topology and material distribution in minimum compliance design of laminated composite beams with prescribed weight and, shear and mass center placement constraints.

The next step in the research includes optimal design of beams with varying cross section properties along the length, and the incorporation of frequency and aeroelastic constraints. The advantages of the beam finite element model will be evident in the latter case due to the reduced size of the beam finite element matrices necessary for the estimation of the global beam response.

Acknowledgements

The authors wish to thank Christian Frier Hvejsel at Aalborg University for fruitful discussions and suggestions. The computer resources were funded by the Danish Center for Scientific Computing (www.dcsc.dk) under the grant CPU-0107-07 *Optimal design of composite structures*.

References

[1] Jung S.N., Nagaraj, V.T. Chopra, I., *Assessment of composite rotor blade modeling techniques*, Journal of the American Helicopter Society, 4(3), 188-205, 1999.

[2] Volovoi V.V., Hodges D.H., Cesnik C.E.S., Popescu B., *Assessment of beam modeling methods for rotor blade applications*, Mathematical and Computer Modelling, 33, 1099-1112, 2001.

[3] Berdichevskii V.L., *On the energy of an elastic rod*, Journal of Applied Mathematics and Mechanics, 45(4), 518-529, 1981.

[4] Yu W., Hodges D.H., *Generalized Timoshenko theory of the variational asymptotic beam sectional analysis*, Journal of the American Helicopter Society, 50(1), 46-55, 2005.

[5] Yu W., Volovoi V., Hodges D.H., Hong X., *Validation of the asymptotic beam sectional analysis (VABS)*, AIAA Journal, 40(10), 2105-2112, 2002.

[6] Hodges D.H., *Nonlinear Composite Beam Theory*, Progress in Astronautics and Aeronautics Series, 213, AIAA, 2006.

[7] Giavotto V., Borri M., Mantegazza P., Ghiringhelli G., Carmaschi V., Maffiolu G.C., Mussi F., *Anisotropic beam theory and applications*, Composite Structures, 16(1-4), 403-413, 1983.

[8] Ghiringhelli G., Mantegazza P., *Linear, straight and untwisted anisotropic beam section properties from solid finite elements*, Composites Engineering, 4(12), 1225-1239, 1994.

[9] Ghiringhelli G., *On the linear three dimensional behaviour of composite beams*, Composites Part B, 28B, 613-626, 1997.

[10] Blasques J.P., Lazarov B., *BECAS - A beam cross section analysis tool for anisotropic and inhomogeneous sections of arbitrary geometry*, RISØ-R 1785 DTU-RISØ Technical Report, 2011.

[11] Choi I., Horgan C.O., *Saint-Venant's principle and end effects in anisotropic elasticity*, Transactions of the ASME, 424-430, 1977.

[12] Blasques J.P., Stolpe M., *Maximum stiffness and minimum weight optimization of laminated composite beams using continuous fiber angles*, Structural and Multidisciplinary Optimization, 43(4), 573-588, 2011.

[13] Kim T.S., Kim Y.Y., *Multiobjective topology optimization of beam under torsion and distortion*, AIAA Journal, 40(2), 376-381, 2002.

[14] Kim Y.Y., Kim T.S., *Topology optimization of beam cross sections*, International Journal of Solids and Structures, 37, 477-493, 2000.

[15] Liu S., An X., Jia H., *Topology optimization of beam cross-section considering warping deformation* Structural and Multidisciplinary Optimization, 35(5), 403-411, 2008.

[16] Donoso A., Sigmund O., *Topology optimization of multiple physics problems modeled by Poisson's equation*, Latin American Journal of Solids and Structures, 1(2), 169-189, 2004.

[17] Li L., Volovoi V.V., Hodges D.H., *Cross-sectional design of composite rotor blades*, Journal of the American Helicopter Society, 53(3), 240-251, 2008.

[18] Ganguli R., Chopra I., *Aeroelastic optimization of a helicopter rotor with composite coupling*, Journal of Aircraft, 32(6), 1326-1334, 1995.

[19] Murugan S.M., Ganguli R., *Aeroelastic stability enhancement and vibration supression in a composite helicopter rotor*, Journal of Aircraft, 42(4), 1013-1024, 2005.

[20] Bendsøe M.P., Sigmund O., *Topology Optimization: Theory, Methods and Applications*, 2nd Edition, Springer-Verlag, Berlin, 2003.

[21] Rozvany G., Zhou M., *The COC algorithm .1. Cross-section optimization or sizing*, Computer Methods in Applied Mechanics and Engineering, 89(1-3), 281-308, 1991.

[22] Bendsøe M. P., Sigmund O., *Material interpolation schemes in topology optimization*, Archive of Applied Mechanics, 69(9-10), 635-654, 1999.

[23] Sigmund O., Torquato S., *Design of materials with extreme thermal expansion using a three-phase topology optimization method*, Journal of the Mechanics and Physics of Solids, 45(6), 1037-1067, 1997.

[24] Bendsøe M., Kikuchi N., *Generating optimal topologies in structural design using a homogenization method*, Computer Methods in Applied Mechanics and Engineering, 71(2), 197-224, 1988.

[25] Hvejsel C.F., Lund E., Stolpe M., *Optimization strategies for discrete multi-material stiffness optimization*, Structural and Multidisciplinary Optimization, DOI 10.1007/s00158-011-0648-5, 2011.

[26] Lund E., Stegmann J., *Discrete material optimization of general composite shell structures*, International Journal for Numerical Methods in Engineering, 62(14), 2009-2007, 2005.

[27] Stegmann J., Lund E., *On structural optimization of composite shell structures using a discrete constitutive parametrization*, 8(1), 109-124, 2005.

[28] Gill P.E., Murray W., Saunders M.A., *SNOPT: An SQP algorithm for large scale constrained optimization*, SIAM Journal on Optimization, 121(4), 979-1006, 2002.

[29] Davis T.A., Natarajan E.P., *Algorithm 907: KLU, a direct sparse solver for circuit simulation problems*, ACM Transactions on Mathematical Software, 37(3), 1-17, 2010.

[30] Davis T.A., *Direct Methods for Sparse Linear Systems*, SIAM Book Series on the Fundamentals of Algorithms, Philadelphia, 2006.

[31] Bathe K.J., *Finite Element Procedures in Engineering Analysis*, Prentice-Hall, 1982.

[32] Sigmund O., *Morphology-based black and white filters for topology optimization*, Structural and Multidisciplinary Optimization, 33(4-5), 401-424, 2007.

[33] Bruns T. E., Tortorelli D. A., *Topology optimization of non-linear elastic structures and compliant mechanisms*, Computer Methods in Applied Mechanics and Engineering, 190(26-27), 3443-3459, 2001.

[34] Sigmund O., Petersson J., *Numerical instabilities in topology optimization: A survey on procedures dealing with checkerboards, mesh dependencies and local minima*, Structural Optimization, 16(1), 68-75, 1998.

[35] Bourdin B., *Filters in topology optimization*, International Journal for Numerical Methods in Engineering, 50(9), 2143-2158, 2001.

[36] Borrvall T., Petersson J., *Topology optimization using regularized intermediate density control*, Computer Methods in Applied Mechanics and Engineering, 190(37-38), 4911-4928, 2001.

[37] Peters S., *Handbook of composites*, 2nd Edition, Chapman & Hall, London, 1998.

[38] DIAB Group, Divinycell H100 Data sheet, www.diabgroup.com, 2011.

[39] Hansen M.H., *Aeroelastic instability problems for wind turbines*, Wind Energy, 10, 551-577, 2007.

[40] Hansen M.O.L., Sørensen J.N., Voutsinas S., Sørensen N., Madsen H.Aa., *State of the art in wind turbine aerodynamics and aeroelasticity*, Progress in Aerospace Sciences, 42(4), 285-330, 2006.

[41] Ramsay R.R., Hoffmann M.J., Gregorek G.M., *Effects of Grit Roughness and Pitch Oscillations on the S809 Airfoil: Airfoil Performance Report*, The Ohio State University, December 1999.

[42] All Points Energy, Company focus, allpoints-energy.com/focus, 2011.

Paper 3

Blasques J.P., Stolpe M., Multi-material topology optimization of laminated composite beams with eigenfrequency constraints, to be submitted, 2011.

Multi-material topology optimization of laminated composite beams with eigenfrequency constraints

José Pedro Blasques
Department of Mechanical Engineering
Technical University of Denmark
Nils Koppels Allé, Building 403, DK-2800 Kgs. Lyngby, Denmark
jpb@mek.dtu.dk

Mathias Stolpe
Department of Mathematics
Technical University of Denmark
Matematiktorvet, Building 303S, DK-2800 Kgs. Lyngby, Denmark
m.stolpe@mat.dtu.dk

August 2, 2011

Abstract

This paper describes a methodology for optimal design of laminated composite beam cross sections with eigenfrequency constraints. The static and dynamic structural response of the beam is analyzed using beam finite elements. The sectional properties are evaluated using a finite element based cross section analysis tool which is able to account for the effects stemming from material anisotropy and inhomogeneity. The optimization is performed using a multi-material topology optimization model where the continuous design variables represent the volume fractions of different candidate materials at each point in the cross section. An approach based on the Kreisselmeier-Steinhauser function is proposed to deal with the convergence issues typically encountered when dealing with eigenfrequency constraints. The framework is applied to the optimal design of a laminated composite cantilever beam. Solutions are initially presented for problems dealing with the maximization of the minimum eigenfrequency and maximization of the gap between consecutive eigenfrequencies with constraints on the weight and shear center position. Finally, results are presented for the minimum compliance problem with constraints on the gap between eigenfrequencies, weight, and shear center position. The results suggest that the devised methodology is suitable for simultaneous optimization of the cross section topology and material properties in the design of laminated composite beams with stiffness and eigenfrequency constraints.

Keywords: Beams, Laminated composites, Multi-material topology optimization, Eigenfrequency constraints

1 Introduction

A typical objective in the design of structures subjected to dynamic loads concerns the maximization of the minimum eigenfrequency or the maximization of the gap between consecutive eigenfrequencies. A methodology is presented in this paper for the simultaneous optimization of the cross section topology and material properties in the design of laminated composite beams with eigenfrequency constraints.

The structural response of the beam is evaluated using a beam finite element model. The cross section properties are analyzed using the BEam Cross section Analysis Software (BECAS), an implementation by Blasques and Lazarov [11] of the original theory by

Giavotto et al. [10]. BECAS is a finite element based tool which is able to account for the effects of material anisotropy and inhomgeneity in the analysis of sections of arbitrary geometry. Several other approaches for the determination of the cross section properties have been reported in the litterature. For a review on different beam modelling techniques the reader should refer to Jung et al. in [2], Volovoi et al. in [3], and the comprehensive work by Hodges in [4].

The optimization framework used here and described by Blasques and Stolpe in [12] is based on the principles of topology optimization (you are referred to the monograph by Bendsøe and Sigmund [13]). The multi-material topology optimization framework relies on extensions of the Solid Isotropic Material with Penalization (SIMP) material interpolation technique (Bendsøe and Kikuchi [14] and Rozvany and Zhou [15]), and the density filtering scheme by Bruns and Tortorelli [18] to include multiple anisotropic materials. A similar approach has been described by Lund and Stegmann [32] and Stegmann and Lund [33] and applied to the optimal design of laminated composite shell structures.

A common issue when dealing with eigenfrequency constraints concerns the fact that the order of the eigenfrequencies may change throughout the optimization procedure thus leading to non-differentiability a non-robust convergence behavior. A typical approach consists of applying the so-called bound formulation (Bendsøe and Sigmund in [13]). An alternative approach is proposed here using the Kreisselmeier-Steinhauser (KS) function (Kreisselmeier and Steinhauser [6]) to approximate the maximum and minimum values of groups of eigenfrequencies. The KS function is a continuously differentiable envelope function which approximates the maximum or minimum of a set of functions. The functions should be continuous but need not be continuously differentiable. The aim is to try to improve the convergence behavior by rewriting the eigenfrequency constraints to take advantage of the mathematical properties of the KS function. The mathematical properties of the KS function have been discussed by Raspanti et al. in [7]. Moreover, it has been used in similar optimal structural design contexts as a constraint aggregation function by, e.g., Martins et al. [8] and Maute et al. [9].

Examples of eigenfrequency optimization using topology optimization have been presented by, e.g., Diaz and Kikuchi [29] for two dimensional structures, and Pedersen [28] and Du and Olhoff [31] for the control of the dynamic properties of plates. Furthermore, Stegmann and Lund [33] and Pedersen [30] have presented solutions for the maximum minimum eigenfrequency design of laminated composite plates. The optimal design of beams with frequency constraints, however, has mostly concerned two dimensional problems and addressed only the optimization of the cross section areas along the beam (see, e.g., Olhoff [26] and Bendsøe and Olhoff [27]).

The paper is organized as follows. The beam finite element structural model is described in Section 2. The multi-material topology optimization framework and problem formulations are described next in Section 3, where the KS function is also presented. The sensitivities for each of the objective functions and constraints are presented in Section 4. Section 5 describes the setup of the numerical experiments, presents the optimized cross section designs, and discusses the results. Finally, the most important conclusions of the work presented in this paper are summarized in Section 6.

2 Structural model

The structural response of the beam is analyzed based on the beam finite element model presented by Blasques and Stolpe in [12]. The model is extended here for the analysis of the beam natural vibration frequencies and modes.

When using beam models it is assumed that the original beam structure is represented by a reference line going through the reference points of a given number of representative cross sections. In this context, the analysis of the beam is performed in two steps. The first step concerns the evaluation of the cross section stiffness and mass properties as discussed in Section 2.1. The second part concerns the integration of these properties to generate the beam finite element model. The latter is addressed in Section 2.2 where the derivation of the beam finite element stiffness and mass matrices is presented along with the equations of motion for the analysis of the static and dynamic response of the beam.

2.1 Cross section analysis

For a linear elastic beam there exists a linear relation between the cross section generalized forces $\mathbf{T}$ and moments $\mathbf{M}$ in $\boldsymbol{\theta} = \left[\mathbf{T}^T \mathbf{M}^T\right]^T$, and the resulting strains $\boldsymbol{\tau}$ and curvatures $\boldsymbol{\kappa}$ in $\boldsymbol{\psi} = \left[\boldsymbol{\tau}^T \boldsymbol{\kappa}^T\right]^T$. This relation is given in its stiffness form as $\mathbf{K}_s \boldsymbol{\psi} = \boldsymbol{\theta}$, where $\mathbf{K}_s$ is the 6×6 cross section stiffness matrix. In the most general case, considering material anisotropy and inhomogeneity, all the 21 stiffness parameters in $\mathbf{K}_s$ may be required to describe the deformation of the beam cross section. In the current research, the entries of $\mathbf{K}_s$ are determined using the BEam Cross section Analysis Software (BECAS). BECAS is an implementation by Blasques and Lazarov [11] of the theory by Giavotto et al. [10]. The formulation relies on a finite element discretization of the cross section to approximate the cross section in-plane and out-of-plane deformation or warping. BECAS is able to estimate the stiffness properties of beam sections with arbitrary geometry and correctly account for the effects stemming from material anisotropy and inhomogeneity. A brief outline of the theory underlying the determination of $\mathbf{K}_s$ is presented.

The determination of $\mathbf{K}_s$ entails the solution to the following linear system of equations

$$\mathbf{K}\mathbf{W} = \mathbf{F} \tag{1}$$

where the coefficient matrices $\mathbf{K}$ and the parameter matrix $\mathbf{F}$ have been defined in Blasques and Stolpe [12]. The linear system of equations above is obtained from the cross section equilibrium equations which yield the cross section rigid body motions and three dimensional warping displacements for a given vector $\boldsymbol{\theta}$ of forces and moments. The solution to (1) yields the matrix $\mathbf{W}$ which is subsequently used in the determination of the cross section compliance matrix $\mathbf{F}_s$ defined as

$$\mathbf{F}_s = \mathbf{W}^T \mathbf{G} \mathbf{W} \tag{2}$$

where the coefficient matrix $\mathbf{G}$ is also defined in Blasques and Stolpe [12]. For most practical applications, and in all cases considered in this paper, $\mathbf{F}_s$ is symmetric positive definite. Hence, the cross section stiffness matrix is consequently obtained from. $\mathbf{K}_s = \mathbf{F}_s^{-1}$.

The 6×6 cross section mass matrix $\mathbf{M}_s$ relates the linear and angular velocities in $\boldsymbol{\phi}$ to the generalized inertial linear and angular momentum in $\boldsymbol{\gamma}$ through $\boldsymbol{\phi} = \mathbf{M}_s \boldsymbol{\gamma}$. The analysis of the cross section mass properties is relatively simpler. According to Hodges in [4], the coefficients of $\mathbf{M}_s$ are

$$\mathbf{M}_s = \begin{bmatrix} m & 0 & 0 & 0 & 0 & -my_m \\ 0 & m & 0 & 0 & 0 & mx_m \\ 0 & 0 & m & my_m & -mx_m & 0 \\ 0 & 0 & my_m & I_{xx} & -I_{xy} & 0 \\ 0 & 0 & -mx_m & -I_{xy} & I_{yy} & 0 \\ -my_m & mx_m & 0 & 0 & 0 & I_{xx} + I_{yy} \end{bmatrix} \tag{3}$$

where m is the mass per unit length, I_{xx} and I_{yy} are the moment of inertia with respect to x and y, respectively, and I_{xy} is the product of inertia. All of the terms in $\mathbf{M}_s$ are determined through integration of the mass properties in the cross section finite element mesh. The off-diagonal terms are due to the offset between the position of the cross section reference point and the mass center $\mathbf{m}_c = (x_m, y_m)$.

2.2 Beam finite element analysis

The equations of static and dynamic equilibrium presented in this section have been derived based on the principle of virtual displacements and using standard finite element techniques (cf. Blasques and Stolpe in [12]). Hence, the beam finite element nodal displacements and rotations in $\widehat{\mathbf{u}}$ which balance the applied external loads in $\widehat{\mathbf{f}}$ are obtained from the solution to

$$\widehat{\mathbf{K}}\widehat{\mathbf{u}} = \widehat{\mathbf{f}} \tag{4}$$

In the expression above $\widehat{\mathbf{K}}$ is the global beam stiffness matrix defined as

$$\widehat{\mathbf{K}} = \sum_{b=1}^{n_b} \widehat{\mathbf{K}}_b \tag{5}$$

where n_b is the number of elements in the beam finite element assemblage. The summation refers to the typical finite element assembly. The beam finite element stiffness matrix $\widehat{\mathbf{K}}_b$ for element b is given by

$$\widehat{\mathbf{K}}_b = \int_0^{L_b} \widehat{\mathbf{N}}_b^T \widehat{\mathbf{B}}^T \mathbf{K}_s \widehat{\mathbf{B}} \widehat{\mathbf{N}}_b \, \mathrm{dz}$$

where L_b is the length of element b, $\widehat{\mathbf{N}}_b$ is the matrix of finite element shape functions, and $\widehat{\mathbf{B}}$ is the strain-displacement matrix. The cross section stiffness matrix $\mathbf{K}_s$ has been presented in the previous section.

The finite element form of the beam structural eigenvalue problem is (cf. Bathe [16])

$$\left(\widehat{\mathbf{K}} - \omega_f^2 \widehat{\mathbf{M}}\right) \widehat{\mathbf{v}}_f = 0, \ \forall f = 1, ..., n_d \tag{6}$$

where n_d is the number of degrees of freedom associated with the finite element system matrices $\widehat{\mathbf{K}}$ and $\widehat{\mathbf{M}}$. The problem above yields the eigenfrequencies $\boldsymbol{\omega} = \{\omega_1, ..., \omega_{n_d}\}$ associated with the eigenvectors $\widehat{\mathbf{V}} = \{\widehat{\mathbf{v}}_1, ..., \widehat{\mathbf{v}}_{n_d}\}$. It is assumed that the eigenfrequencies in $\boldsymbol{\omega}$ are given in ascending order of magnitude, i.e., $\omega_1 \leq \omega_2 \leq ... \leq \omega_{n_d}$. The beam global finite element mass matrix $\widehat{\mathbf{M}}$ is defined as

$$\widehat{\mathbf{M}} = \sum_{b=1}^{n_b} \widehat{\mathbf{M}}_b$$

where the beam finite element mass matrix for element b is

$$\widehat{\mathbf{M}}_b = \int_0^{L_b} \widehat{\mathbf{N}}_b^T \mathbf{M}_s \widehat{\mathbf{N}}_b \, \mathrm{dz} \tag{7}$$

The cross section mass matrix $\mathbf{M}_s$ has been defined in the previous section.

3 Optimization model

The optimal design problem is formulated based on the multi-material topology optimization framework presented by Blasques and Stolpe [12]. The aim is to determine the optimal distribution of a predefined set of candidate materials within the beam cross section. The design requirements entail the minimization of the beam compliance and the maximization or minimization of specific frequencies of vibration of the beam.

A brief outline of the optimization framework is presented in Section 3.1. The optimal design problem formulations considered in this paper are subsequently presented in Section 3.2.

3.1 Multi-material topology optimization

It is assumed that a set of n_c candidate materials has been defined. The candidate materials may be anisotropic or even the same anisotropic material oriented in different directions. A candidate material m is defined by its constitutive matrix $\overline{\mathbf{Q}}_m$ and density $\overline{\varrho}_m$. An extension of the SIMP material interolation model (Bendsøe and Kikuchi [14], and Rozvany and Zhou [15]) to multiple anisotropic materials is used. Hence, the material constitutive matrix $\mathbf{Q}_e$ at element e is defined as

$$\mathbf{Q}_e(\boldsymbol{\rho}) = \sum_{m=1}^{n_c} \rho_{em}^p(\boldsymbol{\rho})\overline{\mathbf{Q}}_m \quad , \quad \forall e = 1, ..., n_e \tag{8}$$

where ρ_{em} is the volume fraction of material m at element e, and p is a penalization parameter. The volume fractions $\boldsymbol{\rho} = \{\rho_{em} \in \mathbb{R} \mid e \in \{1, ..., n_e\}, \ m \in \{1, ..., n_c\}\}$ are the design variables of the optimization problem. It is assumed that the design variables vary continuously between their bounds, i.e., $0 \leq \rho_{em} \leq 1$, $\forall e = 1, ..., n_e$, $\forall m = 1, ..., n_c$.

The density ϱ_e at element e is similarly defined as

$$\varrho_e(\boldsymbol{\rho}) = \sum_{m=1}^{n_c} \rho_{em}(\boldsymbol{\rho})\overline{\varrho}_m \quad , \forall e = 1, ..., n_e$$

where the penalty parameter is not included.

In the typical SIMP formulation for two phase problems an increase in the volume fraction of one material corresponds to a decrease in the volume fractions of the second material. The same effect is achieved here through the inclusion of the following set of n_e linear constraints in the optimal design problem formulation

$$\sum_{m=1}^{n_c} \rho_{em} = 1 \quad , \quad \forall e = 1, ..., n_e$$

The role of p in (8) is to penalize intermediate material densities or volume fractions. As the magnitude of p increases the design variables are pushed towards their bounds. The result is a discrete solution where one material only exists at each element of the cross section mesh. The penalized problem, however, may have a large number of local minima. A continuation approach is therefore employed to increase the possibility of obtaining a good feasible design (see Sigmund and Petersson [19], Borrval and Peterson [22], and Hvejsel et al. [21]). The practical use of the penalty parameter p within the continuation approach is further discussed in Section 5.2.

Common issues in density based topology optimization problems concern the appearance of checkerboard patterns and the dependency of the results on the resolution of the

finite element mesh (Sigmund [17]). The extension presented by Blasques and Stolpe in [12] of the density filtering technique by Bruns and Tortorelli [18] is employed here to address these issues. Essentially, the volume fractions at an element are a function of the volume fractions of the surrounding elements within a given distance f_r (the filter radius) and the element itself. In summary, $\widetilde{\rho}_{em} = \widetilde{\rho}_{em}(\rho_{em})$, where $\widetilde{\rho}_{em}$ are the filtered volume fractions. Finally, a linear support function (cf. Bruns and Tortorelli [18] and Bourdin [20]) is used to weight the volume fractions.

Finally, the design variables $\boldsymbol{\rho}$ enter the structural model through the material constitutive matrix $\mathbf{Q}_e = \mathbf{Q}_e(\boldsymbol{\rho})$ and densities $\varrho_e = \varrho_e(\boldsymbol{\rho})$. The material constitutive matrix $\mathbf{Q}_e(\boldsymbol{\rho})$ is required for the determination of the coefficient matrices in (1) and (2) such that $\mathbf{K} = \mathbf{K}(\boldsymbol{\rho})$ and $\mathbf{G} = \mathbf{G}(\boldsymbol{\rho})$, respectively. Consequently, the cross section stiffness matrix is defined such that $\mathbf{K}_s = \mathbf{K}_s(\boldsymbol{\rho})$. The material densities $\varrho_e(\boldsymbol{\rho})$ are required in the evaluation of the cross section mass matrix in (3) such that $\mathbf{M}_s = \mathbf{M}_s(\boldsymbol{\rho})$. Finally at the beam finite element level, $\widehat{\mathbf{K}} = \widehat{\mathbf{K}}(\boldsymbol{\rho})$ and $\widehat{\mathbf{M}} = \widehat{\mathbf{M}}(\boldsymbol{\rho})$.

3.2 Problem formulation

The stiffness of the beam is evaluated in terms of the structural compliance. The structural compliance c_l for load case l is defined as the work done by the external forces $\widehat{\mathbf{f}}_l$ going through the displacements $\widehat{\mathbf{u}}_l$ such that

$$c_l(\boldsymbol{\rho}) = \widehat{\mathbf{f}}_l^T \widehat{\mathbf{u}}_l(\boldsymbol{\rho})$$

The displacements $\widehat{\mathbf{u}}_l$ are obtained from the solution to the static equilibrium equation in (4). Since $\widehat{\mathbf{K}}(\boldsymbol{\rho})$ is positive definite for all $\boldsymbol{\rho}$ within the specified bounds $0 \leq \rho_{em} \leq 1$, $\forall e = 1, ..., n_e$, $\forall m = 1, ..., n_c$, the expression above can be re-written as

$$c_l(\boldsymbol{\rho}) = \widehat{\mathbf{f}}_l^T \widehat{\mathbf{K}}^{-1}(\boldsymbol{\rho}) \widehat{\mathbf{f}}_l$$

The weighted average compliance C is defined as

$$C(\boldsymbol{\rho}) = \sum_{l=1}^{n_l} \alpha_l c_l(\boldsymbol{\rho}) = \sum_{l=1}^{n_l} \alpha_l \widehat{\mathbf{f}}_l^T \widehat{\mathbf{K}}^{-1}(\boldsymbol{\rho}) \widehat{\mathbf{f}}_l$$

where $\alpha_l \geq 0$ is the weight attributed to load case l.

The natural frequencies of vibration of the beam $\boldsymbol{\omega}(\boldsymbol{\rho})$ are introduced in the optimal design problem through the Kreisselmeier-Steinhauser (KS) function (cf. Kreisselmeier and Steinhauser [6]). The KS function is a differentiable envelope function (see Raspanti et al. in [7]) which gives a conservative representation of the maximum or minimum of a set of functions. It is used here to approximate the maximum or minimum of a group of frequencies. The derivation presented next is for the form of KS approximating the minimum of a function – hereby denoted $\underline{\mathrm{KS}}(\boldsymbol{\rho})$. Hence, assume that $\underline{\boldsymbol{\omega}} = \left\{\underline{\omega}_1, ..., \underline{\omega}_{n_g}\right\}$ is a subset of the eigenfrequencies $\boldsymbol{\omega} = \{\omega_1, ..., \omega_{n_d}\}$ obtained from (6). Furthermore, it is also assumed that the n_g frequencies in $\underline{\boldsymbol{\omega}}$ are ordered such that $\underline{\omega}_1 \leq ... \leq \underline{\omega}_{n_g}$. In this case, $\underline{\mathrm{KS}}(\boldsymbol{\rho})$, is defined as

$$\underline{\mathrm{KS}}(\boldsymbol{\rho}) = -\frac{1}{\beta_s} \ln \left[\sum_{g=1}^{n_g} e^{-\beta_s \underline{\omega}_g(\boldsymbol{\rho})} \right]$$

In order to reduce numerical difficulties (Raspanti et al. in [7]) $\underline{\text{KS}}(\boldsymbol{\rho})$ can be rewritten as

$$\underline{\text{KS}}(\boldsymbol{\rho}) = \underline{\omega}_{n_g}(\boldsymbol{\rho}) - \frac{1}{\beta_s}\ln\left[\sum_{g=1}^{n_g} e^{-\beta_s(\underline{\omega}_g(\boldsymbol{\rho})-\underline{\omega}_{n_g}(\boldsymbol{\rho}))}\right] \tag{9}$$

The penalty parameter β_s is such that the function $\underline{\text{KS}}(\boldsymbol{\rho})$ will tend to the minimum of $\underline{\boldsymbol{\omega}}$ as β_s increases. The function $\overline{\text{KS}}(\boldsymbol{\rho})$ approximating the maximum of a group of frequencies $\overline{\boldsymbol{\omega}}$ is easily obtained from the expressions above.

Finally, the position of the shear center $\mathbf{s}_c(\boldsymbol{\rho}) = (x_s(\boldsymbol{\rho}), y_s(\boldsymbol{\rho}))$ is defined in function of the entries $F_{s,ij}$ of the compliance matrix $\mathbf{F}_s(\boldsymbol{\rho})$ (from (2)) as

$$x_s(\boldsymbol{\rho}) = -\frac{F_{s,62}(\boldsymbol{\rho}) + F_{s,64}(\boldsymbol{\rho})(L-z)}{F_{s,66}(\boldsymbol{\rho})}, \quad y_s(\boldsymbol{\rho}) = \frac{F_{s,61}(\boldsymbol{\rho}) + F_{s,65}(\boldsymbol{\rho})(L-z)}{F_{s,66}(\boldsymbol{\rho})} \tag{10}$$

where L is the beam length (cf. Hodges [4]). The shear center is defined such that a transverse load applied at the shear center will not induce a torsional moment.

The first optimal design problem formulation (problem P1-1) concerns the maximization of the gap $\underline{\text{KS}}(\underline{\boldsymbol{\omega}}(\boldsymbol{\rho})) - \overline{\text{KS}}(\overline{\boldsymbol{\omega}}(\boldsymbol{\rho}))$ between the minimum and maximum of the two groups of eigenfrequencies $\underline{\boldsymbol{\omega}}(\boldsymbol{\rho})$ and $\overline{\boldsymbol{\omega}}(\boldsymbol{\rho})$, respectively. The problem P1-1 including constraints on the shear center position, and total weight of the beam is formulated as

$$\begin{aligned}
\underset{\boldsymbol{\rho}\in\mathbb{R}^{n_e\times n_c}}{\text{maximize}} \quad & \underline{\text{KS}}(\underline{\boldsymbol{\omega}}(\boldsymbol{\rho})) - \overline{\text{KS}}(\overline{\boldsymbol{\omega}}(\boldsymbol{\rho})) \\
\text{subject to} \quad & \underline{\mathbf{s}} \leq \mathbf{s}_c(\boldsymbol{\rho}) \leq \overline{\mathbf{s}} \\
& w(\boldsymbol{\rho}) = \overline{w} \\
& \sum_{m=1}^{n_c} \widetilde{\rho}_{em}(\boldsymbol{\rho}) = 1 \ , \ \forall e = 1, ..., n_e \\
& 0 \leq \rho_{em} \leq 1, \ \forall e = 1, ..., n_e \ , \ \forall m = 1, ..., n_c
\end{aligned} \tag{P1-1}$$

where the parameters $\overline{w}$ and, $\overline{\mathbf{s}}$ and $\underline{\mathbf{s}}$ are the constraint values for the weight and shear center position, respectively. The compliance is not considered in these formulation. The aim is to present results where the focus is solely in the optimization of the dynamic properties of the beam.

The second problem formulation concerns the minimum compliance problem with constraints on frequency, weight, and shear center position (problem P2-1) is formulated as

$$\begin{aligned}
\underset{\boldsymbol{\rho}\in\mathbb{R}^{n_e\times n_c}}{\text{minimize}} \quad & C(\boldsymbol{\rho}) \\
\text{subject to} \quad & \overline{\text{KS}}(\overline{\boldsymbol{\omega}}(\boldsymbol{\rho})) \leq \overline{\omega} \\
& \underline{\text{KS}}(\underline{\boldsymbol{\omega}}(\boldsymbol{\rho})) \geq \underline{\omega} \\
& \mathbf{s}_c(\boldsymbol{\rho}) \leq \overline{\mathbf{s}} \\
& w(\boldsymbol{\rho}) = \overline{w} \\
& \sum_{m=1}^{n_c} \widetilde{\rho}_{em}(\boldsymbol{\rho}) = 1 \ , \ \forall e = 1, ..., n_e \\
& \underline{\rho} \leq \rho_{em} \leq \overline{\rho}, \ \forall e = 1, ..., n_e \ , \ \forall m = 1, ..., n_c
\end{aligned} \tag{P2-1}$$

where the parameter $\underline{\omega}$ and $\overline{\omega}$ are the constraint values associated with the lower and upper bound on the frequencies, respectively. This problem formulation considers both

compliance and eigenfrequency constraints. The aim is to show that it is possible to simultaneously tailor the static and dynamic properties of the beam.

Alternative problem formulations can be obtained by rearranging the objective functions and constraints in P1-1 and P2-1. The following problem formulations have also been considered in this paper. Problem formulation P1-2, P1-3, and P1-4 are based on P1-1. Problem formulation P1-2 concerns the maximization of the gap between two groups of eigenfrequencies with constraints on the weight. Problem formulation P1-3 concerns the maximization of the minimum eigenfrequency with a constraint on the weight. Finally, problem formulation P1-4 concerns the maximization of the minimum eigenfrequency subject to constraints on weight and shear center position. The remaining problem formulations P2-2, P2-3 and P2-4 are based on problem P2-1. Problem formulation P2-2 refers to the minimum compliance problem with weight constraints. Problem formulation P2-3 refers to the minimum compliance problem with constraints on weight and shear center position. Problem formulation P2-4 refers to the minimum compliance problem with frequency and weight constraints. Numerical results are presented in Section 5 for each of the problem formulation mentioned before.

The aim in this paper is to present proofs-of-concept for later research, namely, in the field of wind turbine blade design. Tailoring the position of the shear center and controlling the magnitude of certain frequencies it is possible, e.g., to limit the risk of flutter and divergence instabilities (see Hansen [34]).

4 Sensitivities

The sensitivities of the beam natural frequencies, KS function and cross section mass matrix are derived in this section. The gradients or sensitivities of the beam compliance, cross section stiffness matrix and shear center position have been derived in Blasques and Stolpe [12]. Hence, only a brief outline is presented here.

4.1 Compliance

The sensitivities of the average compliance C with respect to the design variable ρ_{em} is given by

$$\frac{\partial C(\boldsymbol{\rho})}{\partial \rho_{em}} = \sum_{l=1}^{n_l} \alpha_l \frac{\partial c_l(\boldsymbol{\rho})}{\partial \rho_{em}}$$

It can be shown (see, e.g., Bendsøe and Sigmund in [13]) that the sensitivities of the compliance c_l for load load case l are given by

$$\frac{\partial c_l(\boldsymbol{\rho})}{\partial \rho_{em}} = -\widehat{\mathbf{u}}_l(\boldsymbol{\rho})^T \frac{\partial \widehat{\mathbf{K}}(\boldsymbol{\rho})}{\partial \rho_{em}} \widehat{\mathbf{u}}_l(\boldsymbol{\rho})$$

The sensitivities of the global beam finite element stiffness matrix $\widehat{\mathbf{K}}$ are obtained through differentiation of (5) to yield

$$\frac{\partial \widehat{\mathbf{K}}(\boldsymbol{\rho})}{\partial \rho_{em}} = \sum_{b=1}^{n_b} \int_0^{L_b} \widehat{\mathbf{N}}_b^T \widehat{\mathbf{B}}^T \frac{\partial \mathbf{K}_s(\boldsymbol{\rho})}{\partial \rho_{em}} \widehat{\mathbf{B}} \widehat{\mathbf{N}}_b \, \mathrm{dz} \tag{11}$$

Hence, the sensitivities of the compliance reduce to the determination of the gradients of the cross section stiffness matrix $\mathbf{K}_s$ which is described later in Section 4.4.

4.2 Eigenfrequencies

The solution to the structural eigenvalue problem in (6) yields the eigenfrequencies and eigenvectors $\boldsymbol{\omega} = \{\omega_1, ..., \omega_{n_d}\}$ and $\widehat{\mathbf{V}} = \{\widehat{\mathbf{v}}_1, ..., \widehat{\mathbf{v}}_{n_d}\}$, respectively. It is assumed that the eigenvectors are mass-normalized such that

$$\widehat{\mathbf{v}}_p^T \widehat{\mathbf{M}}(\boldsymbol{\rho}) \widehat{\mathbf{v}}_q = \delta_{pq}, \ \forall p, q = 1, ..., n_d.$$

where n_d is the number of degrees of freedom in $\widehat{\mathbf{u}}(\boldsymbol{\rho})$, and δ_{pq} is the Kronecker delta such that $\delta_{pq} = 1$ if $p = q$ and $\delta_{pq} = 0$ otherwise. The gradient of a single eigenfrequency ω_p with respect to the design variable ρ_{em} is given by (cf. Seyranian et al. [5])

$$\frac{\partial \omega_p^2(\boldsymbol{\rho})}{\rho_{em}} = \widehat{\mathbf{v}}_p^T \left(\frac{\partial \widehat{\mathbf{K}}(\boldsymbol{\rho})}{\partial \rho_{em}} - \omega_p^2(\boldsymbol{\rho}) \frac{\partial \widehat{\mathbf{M}}(\boldsymbol{\rho})}{\partial \rho_{em}} \right) \widehat{\mathbf{v}}_p \tag{12}$$

In the case of a multiple eigenfrequency, i.e., $\omega_M = \omega_1 = ... = \omega_{n_\omega}$, where the eigenfrequencies are numbered from 1 to n_ω for convenience and n_ω indicates the multiplicity of ω_M, a different technique is applied (cf. Seyranian et al. [5]). The first step consists of evaluating the entries of the auxiliary matrix $\boldsymbol{\Lambda}$ defined as

$$\Lambda_{rs} = \widehat{\mathbf{v}}_r^T \left(\frac{\partial \widehat{\mathbf{K}}(\boldsymbol{\rho})}{\partial \rho_{em}} - \omega_M^2 \frac{\partial \widehat{\mathbf{M}}(\boldsymbol{\rho})}{\partial \rho_{em}} \right) \widehat{\mathbf{v}}_s, \ r, s = 1, ..., n_\omega.$$

where $\widehat{\mathbf{v}}_r$ and $\widehat{\mathbf{v}}_s$, $r, s = 1, ..., n_\omega$, are the eigenvectors associated with the multiple eigenfrequency ω_M. The next step consists of determining the solution to the following eigenvalue sub-problem

$$\left(\boldsymbol{\Lambda} - \tilde{\lambda} \mathbf{I} \right) \tilde{\mathbf{v}} = \mathbf{0}$$

which yields the eigenvalues $\widetilde{\boldsymbol{\lambda}} = \left\{ \tilde{\lambda}_1, ..., \tilde{\lambda}_{n_\omega} \right\}$ and corresponding eigenvectors $\widetilde{\mathbf{V}} = \{\tilde{\mathbf{v}}_1, ..., \tilde{\mathbf{v}}_{n_\omega}\}$. It is assumed herein that the eigenvalues $\tilde{\boldsymbol{\lambda}}$ are given in ascending order of magnitude such that $\tilde{\lambda}_1 < ... < \tilde{\lambda}_{n_\omega}$. The gradients of the multiple eigenfrequency ω_M are finally obtained as

$$\frac{\partial \omega_M^2(\boldsymbol{\rho})}{\rho_{em}} = \begin{cases} \tilde{\lambda}_1 \text{ with eigenvector } \mathbf{v}_1 = \displaystyle\sum_{q=1}^{n_\omega} \widehat{v}_q \tilde{v}_{1,q} \\ \qquad \vdots \\ \tilde{\lambda}_{n_\omega} \text{ with eigenvector } \mathbf{v}_{n_\omega} = \displaystyle\sum_{q=1}^{n_\omega} \widehat{v}_q \tilde{v}_{n_\omega,q} \end{cases}$$

where $\tilde{v}_{n_\omega,q}$ is the entry (n_ω, q) of the eigenvector $\tilde{\mathbf{v}}$.

The two techniques presented above are used for the evaluation of the beam eigenfrequencies throughout the optimization procedure. Two or more eigenfrequencies are considered multiple eigenfrequencies if the relative difference between them is below a predefined threshold.

The gradients of the global beam finite element mass matrix $\widehat{\mathbf{M}}(\boldsymbol{\rho})$ in (12) are obtained through differentiation of (7) which yields

$$\frac{\partial \widehat{\mathbf{M}}(\boldsymbol{\rho})}{\partial \rho_{em}} = \sum_{b=1}^{n_b} \int_0^{L_b} \widehat{\mathbf{N}}_b^T \frac{\partial \mathbf{M}_s(\boldsymbol{\rho})}{\partial \rho_{em}} \widehat{\mathbf{N}}_b \, \mathrm{dz} \tag{13}$$

The sensitivities of the cross section mass matrix $\mathbf{M}_s$ are presented in Section 4.5. The gradients of the global beam finite element stiffness matrix $\widehat{\mathbf{K}}(\boldsymbol{\rho})$ are given in (11).

Finally, the eigenfrequencies are included in the optimal design problem formulation through the KS function $\underline{\mathrm{KS}}(\boldsymbol{\rho})$ (see Section 3.2). The sensitivities of $\underline{\mathrm{KS}}(\boldsymbol{\rho})$ defined in (9) with respect to the design variables ρ_{em} for a set $\underline{\boldsymbol{\omega}}$ of n_g eigenfrequencies is given as

$$\frac{\partial \underline{\mathrm{KS}}(\boldsymbol{\rho})}{\partial \rho_{em}} = \frac{\partial \underline{\omega}_{n_g}(\boldsymbol{\rho})}{\partial \rho_{em}} + \frac{\displaystyle\sum_{g=1}^{n_g} \left(\frac{\partial \underline{\omega}_g(\boldsymbol{\rho})}{\partial \rho_{em}} - \frac{\partial \underline{\omega}_{n_g}(\boldsymbol{\rho})}{\partial \rho_{em}} \right) e^{-\beta_s(\underline{\omega}_g(\boldsymbol{\rho}) - \underline{\omega}_{n_g}(\boldsymbol{\rho}))}}{\displaystyle\sum_{g=1}^{n_g} e^{-\beta_s(\underline{\omega}_g(\boldsymbol{\rho}) - \underline{\omega}_{n_g}(\boldsymbol{\rho}))}}$$

The gradients of $\overline{\mathrm{KS}}(\boldsymbol{\rho})$ are easily obtained from the expression above.

4.3 Shear center

The sensitivities of the shear center position with respect to the design variable ρ_{em} are obtained through differentiation of (10) to yield

$$\begin{aligned}
\frac{\partial x_s}{\partial \rho_{em}} &= -\left(\frac{\partial F_{s,62}}{\partial \rho_{em}} + \frac{\partial F_{s,64}}{\partial \rho_{em}}(L - z) \right) \frac{1}{F_{s,66}} \\
&\quad + (F_{s,62} + F_{s,64}(L - z)) \frac{1}{F_{s,66}^2} \frac{\partial F_{s,66}}{\partial \rho_{em}} \\
\frac{\partial y_s}{\partial \rho_{em}} &= \left(\frac{\partial F_{s,61}}{\partial \rho_{em}} + \frac{\partial F_{s,65}}{\partial \rho_{em}}(L - z) \right) \frac{1}{F_{s,66}} \\
&\quad - (F_{s,61} + F_{s,65}(L - z)) \frac{1}{F_{s,66}^2} \frac{\partial F_{s,66}}{\partial \rho_{em}}
\end{aligned}$$

where the gradients $\partial F_{s,ij}/\partial \rho_{em}$ refer to the entries of $\partial \mathbf{F}/\partial \rho_{em}$ derived in (15).

4.4 Cross section stiffness matrix

A brief account of the steps involved in the derivation of the sensitivities of the cross section stiffness matrix $\mathbf{K}_s$ is presented here. The reader is referred to Blasques and Stolpe [12] for more details on the derivation.

The sensitivities of the cross section stiffness matrix $\mathbf{K}_s(\boldsymbol{\rho})$ with respect to ρ_{em} are defined in function of the cross section compliance matrix $\mathbf{F}_s(\boldsymbol{\rho})$ as

$$\frac{\partial \mathbf{K}_s(\boldsymbol{\rho})}{\partial \rho_{em}} = \frac{\partial \mathbf{F}_s^{-1}(\boldsymbol{\rho})}{\partial \rho_{em}} = -\mathbf{K}_s(\boldsymbol{\rho}) \frac{\partial \mathbf{F}_s(\boldsymbol{\rho})}{\partial \rho_{em}} \mathbf{K}_s(\boldsymbol{\rho}) \tag{14}$$

The gradients of the cross section compliance matrix are obtained through differentiation of (2) which yields

$$\begin{aligned}
\frac{\partial \mathbf{F}_s(\boldsymbol{\rho})}{\partial \rho_{em}} &= -\mathbf{W}^T(\boldsymbol{\rho}) \frac{\partial \mathbf{K}^{'T}(\boldsymbol{\rho})}{\partial \rho_{em}} \mathbf{V}(\boldsymbol{\rho}) + \mathbf{W}^T(\boldsymbol{\rho}) \frac{\partial \mathbf{G}(\boldsymbol{\rho})}{\partial \rho_{em}} \mathbf{W}(\boldsymbol{\rho}) \\
&\quad - \mathbf{V}^T(\boldsymbol{\rho}) \frac{\partial \mathbf{K}(\boldsymbol{\rho})}{\partial \rho_{em}} \mathbf{W}(\boldsymbol{\rho})
\end{aligned} \tag{15}$$

The matrix $\mathbf{W}(\boldsymbol{\rho})$ is the solution to the linear system of equations in (1) such that $\mathbf{W}(\boldsymbol{\rho}) = \mathbf{K}(\boldsymbol{\rho})^{-1}\mathbf{F}$. The matrix $\mathbf{V}$ is obtained from the evaluation of $\mathbf{V}(\boldsymbol{\rho}) = \mathbf{K}^{-T}(\boldsymbol{\rho})\mathbf{G}(\boldsymbol{\rho})\mathbf{W}(\boldsymbol{\rho})$, where the coefficient matrix $\mathbf{G}(\boldsymbol{\rho})$ has been defined in (2). Both $\mathbf{W}(\boldsymbol{\rho})$ and $\mathbf{V}(\boldsymbol{\rho})$ are determined only once and then reused in the evaluation of (15) for each of the design variables ρ_{em}. Finally, inserting the result of (15) into (14) yields the gradients of the cross section stiffness matrix $\mathbf{K}_s$.

4.5 Cross section mass matrix

The sensitivities of the mass matrix with respect to the design variable ρ_{em} are

$$\frac{\partial \mathbf{M}_s}{\partial \rho_{em}} = \begin{bmatrix} \frac{\partial m}{\partial \rho_{em}} & 0 & 0 & 0 & 0 & -\frac{\partial m}{\partial \rho_{em}} y_m - m\frac{\partial y_m}{\partial \rho_{em}} \\ 0 & \frac{\partial m}{\partial \rho_{em}} & 0 & 0 & 0 & \frac{\partial m}{\partial \rho_{em}} x_m + m\frac{\partial x_m}{\partial \rho_{em}} \\ 0 & 0 & \frac{\partial m}{\partial \rho_{em}} & \frac{\partial m}{\partial \rho_{em}} y_m + m\frac{\partial y_m}{\partial \rho_{em}} & -\frac{\partial m}{\partial \rho_{em}} x_m - m\frac{\partial x_m}{\partial \rho_{em}} & 0 \\ 0 & 0 & \frac{\partial m}{\partial \rho_{em}} y_m + m\frac{\partial y_m}{\partial \rho_{em}} & \frac{\partial I_{xx}}{\partial \rho_{em}} & -\frac{\partial I_{xy}}{\partial \rho_{em}} & 0 \\ 0 & 0 & -\frac{\partial m}{\partial \rho_{em}} x_m - m\frac{\partial x_m}{\partial \rho_{em}} & -\frac{\partial I_{xy}}{\partial \rho_{em}} & \frac{\partial I_{yy}}{\partial \rho_{em}} & 0 \\ -\frac{\partial m}{\partial \rho_{em}} y_m - m\frac{\partial y_m}{\partial \rho_{em}} & \frac{\partial m}{\partial \rho_{em}} x_m + m\frac{\partial x_m}{\partial \rho_{em}} & 0 & 0 & 0 & \frac{\partial I_{xx}}{\partial \rho_{em}} + \frac{\partial I_{yy}}{\partial \rho_{em}} \end{bmatrix} \tag{16}$$

Hence, the gradient of the cross section mass matrix reduces to the evaluation of the partial derivatives of the mass per unit length, $\partial m/\partial \rho_{em}$, moments of inertia, $\partial I_{xx}/\partial \rho_{em}$ and $\partial I_{yy}/\partial \rho_{em}$, the product of inertia, $\partial I_{xy}/\partial \rho_{em}$, and the mass center $\partial x_m/\partial \rho_{em}$ and $\partial y_m/\partial \rho_{em}$. Finally, inserting (16) into (13) yields the gradients of the beam finite element mass matrix.

5 Numerical experiments

The optimal design framework described in the previous sections is employed now in the optimal design of laminated composite beams. The geometrical properties of the beam are presented first. The mechanical properties of the considered materials are detailed next along with a description of the procedures entailed in the generation of the candidate materials. A brief description of the optimization strategy and details regarding the presentation of the results are subsequently presented. Finally, all the results are presented and discussed for the different problem formulations considered.

5.1 Setup

We consider the optimal design of a cantilever beam of constant cross section. The beam finite element model is composed of 16 three-node quadratic beam finite elements corresponding to 198 degrees of freedom. The coordinate system, finite element mesh and dimensions of the rectangular cross section or design domain are presented in Figure 1. The cross section is meshed using 2116 four-node isoparametric finite elements corresponding to 6627 degrees of freedom. The dimensions of the beam are given in Table 1.

Two different materials have been considered – an orthotropic and an isotropic material – with the mechanical properties presented in Table 2. The mechanical properties of the orthotropic material are based on that of an E-glass reinforced Epoxy laminate (cf. Peters in [23]). The mechanical properties of the isotropic material correspond to that of DIAB H100 PVC Core [24].

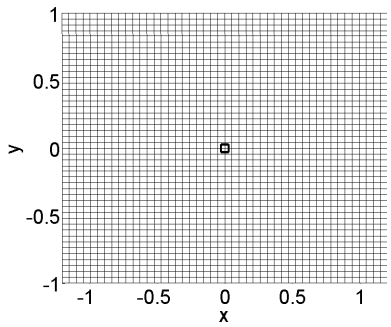

Figure 1: Cross section coordinate system and finite element mesh. The cross section is meshed using 2116 four-node isoparametric finite elements corresponding to 6627 degrees of freedom. The square marker indicates the position of the cross section reference point or beam node.

Table 1: Dimensions of the beam.

Width	2.2 m
Height	2 m
Length	20 m

Table 2: Material properties for orthotropic material (scaled values for E-glass reinforced Epoxy laminate according to the Handbook of Composites [23]), and isotropic material (scaled values for DIAB H100 PVC Core according to DIAB mechanical property sheets [24]) (Table from Blasques and Stolpe [12]).

Material	Orthotropic		Isotropic	
$E_{xx} = E_{yy}$	120	Gpa	0.130	Gpa
E_{zz}	480	Gpa	0.130	Gpa
$G_{zx} = G_{zy}$	60	Gpa	0.035	Gpa
G_{xy}	50	Gpa	0.035	Gpa
$\nu_{zx} = \nu_{zy}$	0.19	-	0.35	-
ν_{xy}	0.26	-	0.35	-
$\overline{\varrho}$	1.78	10^3 kg/m^3	0.1	10^3 kg/m^3

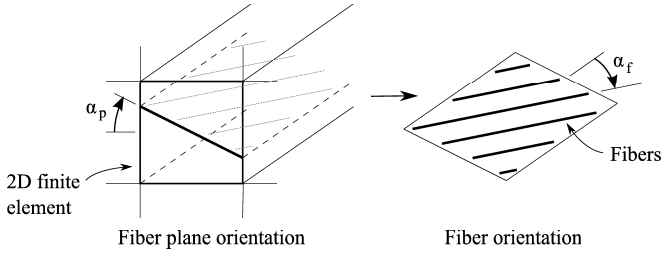

Figure 2: Three-dimensional rotation of fiber plane and fiber orientation in the cross section mesh. The fiber plane orientation is defined by the angle α_p while the orientation of the fibers in the fiber plane are defined by the angle α_f. (Figure from Blasques and Stolpe [12])

Nine candidate materials have been considered for all numerical experiments. The candidate materials are generated based on the material properties of the orthotropic layer and isotropic core material in Table 2. One of the candidates is the isotropic material itself. The remaining eight candidate materials are generated by rotation of the orthotropoic layer. The orientation of the orthotropic layer in the cross section plane is specified based on the orientation of the fiber plane α_p, and the orientation α_f of the fibers in the plane, cf. Figure 2 . The eight candidate materials considered correspond to four different layer or fiber orientations – 0°, 45° −45°, and 90° – stacked in either an horizontal (0°) or vertical (90°) fiber plane . Henceforth the nomenclature $\alpha_f@\alpha_p$ will be used when referring to an orthotropic candidate materials. For example, a layer oriented at 45° stacked on a vertical plane (90°) is referred to as 45°@90° (cf. Figure 3).

5.2 Optimization strategy

The first step in the optimization is to solve the unpenalized problem corresponding to the case where $p_1 = 1$. At each of the subsequent steps, the penalty parameter p is increased such that $p_{i+1} = p_i + \Delta p$ until $p = p_{max}$. For all numerical experiments presented here it is assumed that the maximum penalty $p_{max} = 5$. The step length is $\Delta p = 0.5$ for the numerical experiments S1, S2, S3 and S4, and $\Delta p = 0.1$ for S5, S6, S7 and S8 (cf. Table 3). Furthermore, at the starting point all materials have the same volume fractions for all cases. The optimal design problems are solved using the sequential quadratic programming algorithm SNOPT by Gill et al. [25]. Each problem is solved until the major optimality tolerance is satisfied or the maximum number of major iterations is reached. The major optimality tolerance, like the major feasibility tolerance, is set to 1×10^{-5} in SNOPT. The maximum number of major iterations is set to 500 in the first iteration and to 100 in the remaining. The remaining parameters are set to the default values.

5.3 Presentation of the results

The visualization of the results is done based on two groups of figures for each numerical experiment. The first group consists of two figures which indicate the fiber and fiber plane orientation, respectively. The orientations are represented by lines at each element. The thickness and darkness of the line is weighted by the value of the filtered design variable. It is possible in this way to visualize the effect of the filter. Based on the orientation of the lines and resorting to Figure 3, it is possible to visualize the spatial orientation of the fibers. The element is white if the material is isotropic. Finally, the position of the cross section reference point, shear center, and mass center is indicated in these group of figures with a square, triangle and diamond marker, respectively (cf. Figure 3).

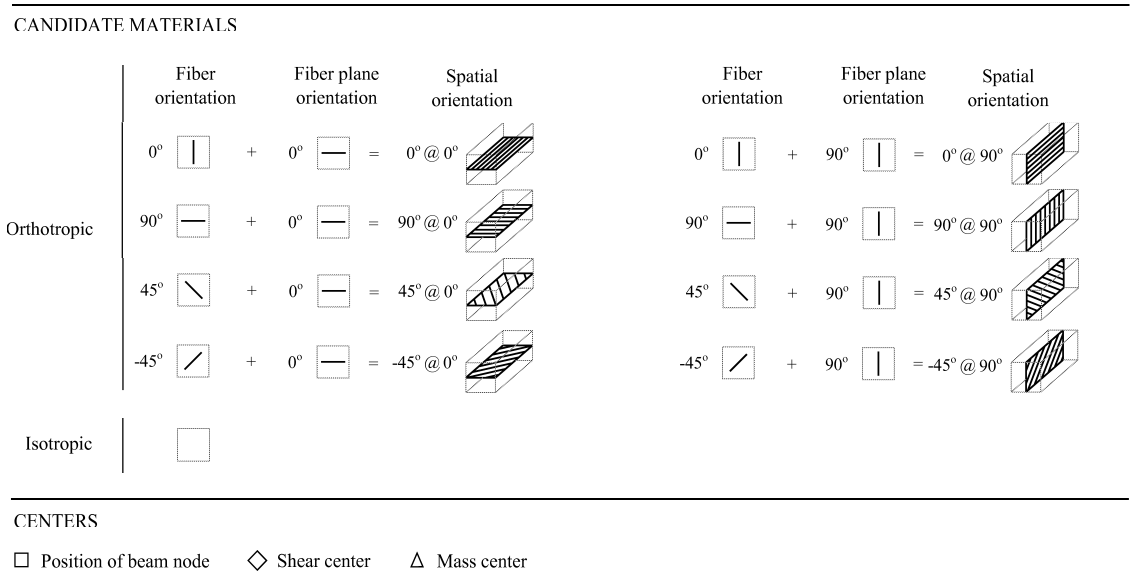

Figure 3: Legend for the figures depicting the solutions. Visualization of the spatial orientation of the fibers at each element based on the resulting fiber and fiber plane orientations, for each of the candidate orthotropic materials. Description of the markers used to define the cross section reference point or beam node (square), shear center (diamond), and mass center (triangle). (Figure from Blasques and Stolpe [12])

The last group consists of nine figures each corresponding to a different material. The aim is to visualize the results following the black and white representation commonly used in two phase material topology optimization. Thus, at each figure the elements are black where the corresponding material exists, and white otherwise.

5.4 Results

All 12 numerical experiments considered in this paper are defined in Table 3. The corresponding objective function and constraints for each numerical experiment are defined in Table 4. All the numerical experiments are solved for 19044 design variables associated with the nine materials at each of the 2116 elements of the cross section. The filter radius is set to $f_r = 0.15$ for the numerical experiments S1, S2, S3 and S4, and to $f_r = 0.1$ in the remaining cases. Furthermore, the value of $\overline{w}$ indicates the portion of the total weight which is orthotropic material. An equality constraint is used for the weight in order to avoid designs where only the isotropic material exists. Moreover, it is assumed that the frequency groups used in conjunction with the KS function are subsets of $\boldsymbol{\omega}$ determined in (6). The frequency groups are denoted $\boldsymbol{\omega}_{i,j} = \{\omega_i, ..., \omega_j\}$ where the subscripts i and j indicate the order of the lowest and higher frequencies in the group, respectively. The order number refers to the order placement in $\boldsymbol{\omega}$. Only groups of consecutive frequencies have been considered such that $\boldsymbol{\omega}_{i,j}$ includes the frequencies i, j, and all frequencies in between. The value of the parameter β_s introduced in the definition of the KS function in (9) is set to unity for all cases. The sensitivity analysis technique for multiple eigenfrequencies presented in Section 4.2 is employed whenever the relative difference between two or more eigenfrequencies is below 1×10^{-5}. In case S5, S6, S7, and S8 it is assumed that the beam is subjected to one load case combining the distributed transverse forces $\widehat{f}_x = 2$ and $\widehat{f}_y = 3$, and the distributed torsional moment $\widehat{m}_z = 15$.

The resulting values of compliance, frequencies, shear center position, and number of

Table 3: Catalogue of numerical experiments combining the different problem formulations.

Ref.	Problem formulation
S1	Maximize minimum eigenfrequency with a weight constraint (P1-3)
S2-1	Maximize gap between two eigenfrequencies with constraints on weight (P1-2)
S2-2	Maximize gap between two eigenfrequencies with constraints on weight (P1-2)
S2-3	Maximize gap between two eigenfrequencies with constraints on weight (P1-2)
S3	Maximize minimum eigenfrequencies with constraints on weight and shear center position (P1-4)
S4-1	Maximize gap between two eigenfrequencies with constraints on weight and shear center position (P1-1)
S4-2	Maximize gap between two eigenfrequencies with constraints on weight and shear center position (P1-1)
S4-3	Maximize gap between two eigenfrequencies with constraints on weight and shear center position (P1-1)
S5	Minimize compliance with a weight constraint (P2-2)
S6	Minimize compliance with constraints on eigenfrequencies and weight (P2-4)
S7	Minimize compliance with constraints on weight and shear center position (P2-3)
S8	Minimize compliance with constraints on weight, eigenfrequencies, and shear center position (P2-1)

Table 4: Details for all numerical experiments (cf. Table 3). The first column indicates the objective function. The frequency groups are denoted $\boldsymbol{\omega}_{i,j} = \{\omega_i, ..., \omega_j\}$ where the subscripts i and j indicate the order of the lowest and higher frequencies in the group, respectively. The second column indicates the value of the weight constraint where $\overline{w}$ refers to the ratio of orthotropic material. The third and fourth column indicate the constraints on the maximum and minimum values of the frequency groups, $\overline{\boldsymbol{\omega}}$ and $\underline{\boldsymbol{\omega}}$, respectively. The last column indicates the constraints on the shear center position $\mathbf{s}_c = (x_s, y_s)$.

Ref.	Obj. func.	$\overline{w}$	$\overline{\boldsymbol{\omega}}$	$\underline{\boldsymbol{\omega}}$	$\bar{\mathbf{s}}_c$
S1	$\underline{\mathrm{KS}}(\boldsymbol{\omega}_{1,5})$	2/5	–	–	–
S2-1	$\underline{\mathrm{KS}}(\boldsymbol{\omega}_{3,4}) - \underline{\mathrm{KS}}(\boldsymbol{\omega}_{1,2})$	2/5	–	–	–
S2-2	$\underline{\mathrm{KS}}(\boldsymbol{\omega}_{4,6}) - \underline{\mathrm{KS}}(\boldsymbol{\omega}_{1,3})$	2/5	–	–	–
S2-3	$\underline{\mathrm{KS}}(\boldsymbol{\omega}_{5,7}) - \underline{\mathrm{KS}}(\boldsymbol{\omega}_{2,4})$	2/5	–	–	–
S3	$\underline{\mathrm{KS}}(\boldsymbol{\omega}_{1,5})$	2/5	–	–	$x_s = -0.2$, $y_s = 0$
S4-1	$\underline{\mathrm{KS}}(\boldsymbol{\omega}_{1,2}) - \underline{\mathrm{KS}}(\boldsymbol{\omega}_{3,4})$	2/5	–	–	$x_s = -0.2$, $y_s = 0$
S4-2	$\underline{\mathrm{KS}}(\boldsymbol{\omega}_{1,3}) - \underline{\mathrm{KS}}(\boldsymbol{\omega}_{4,6})$	2/5	–	–	$x_s = -0.2$, $y_s = 0$
S4-3	$\underline{\mathrm{KS}}(\boldsymbol{\omega}_{2,4}) - \underline{\mathrm{KS}}(\boldsymbol{\omega}_{5,7})$	2/5	–	–	$x_s = -0.2$, $y_s = 0$
S5	C	2/5	–	–	–
S6	C	2/5	$\overline{\mathrm{KS}}(\boldsymbol{\omega}_{1,3}) \leq 75.95$	$\underline{\mathrm{KS}}(\boldsymbol{\omega}_{4,6}) \geq 115.07$	–
S7	C	2/5	–	–	$x_s = -0.2$ $y_s = 0$
S8	C	2/5	$\overline{\mathrm{KS}}(\boldsymbol{\omega}_{1,3}) \leq 76.33$	$\underline{\mathrm{KS}}(\boldsymbol{\omega}_{4,6}) \geq 134.92$	$x_s = -0.2$ $y_s = 0$

objective function evaluations are presented in Tables 5 and 6. Note that in the MATLAB interface to SNOPT each objective function evaluation entails also the evaluation of the function gradients. Furthermore, all compliance and frequency values presented refer to the penalized case, i.e., $p = p_{max}$

The next section presents results for the optimal design problems concerning the maximization of the minimum eigenfrequency and maximization of the gap between the minimum and maximum of different groups of frequencies. Finally, in Section 5.4.2 results are presented for the minimum compliance problem with frequency constraints.

5.4.1 Maximization of the minimum frequency and of the gap between frequencies

The resulting values of the first seven frequencies, total weight, shear center position, and the number of objective function evaluations for case S1, S2, S3, S4 and all sub-cases therein are presented in Table 5. The resulting designs are presented in Figures 4 through 7. The cases S1 and S3 refer to the maximization of the minimum eigenfrequency. The cases S2 and S4 refer to the maximization of the gap between two frequency groups (cf. Table 3).

The resulting designs for case S1 are presented in Figures 4(a), 4(b), and 5(a). The optimized cross section topology and material distribution for case S3 can be observed in Figures 6(a) 6(b), and 7(a). As can be seen, the results are very similar in both cases. The slight difference is motivated by the constraints on the shear center in S3. Otherwise, note that the mass center position remains the same in both cases. Furthermore, in both cases, the lowest eigenfrequency, ω_1, is associated with the bending deformation of the beam in the y or vertical direction. The fibers align at $0°@0°$ and $0°@90°$ where the normal stresses dominate – away from the neutral axis, in the top and bottom faces of the beam. In the side faces closer to the neutral axis the shear stresses dominate and the characteristic $45°@90°$ and $-45°@90°$ fibers appear. The resulting design is similar to that obtained by Blasques and Stolpe [12] for the minimum compliance optimization of a square beam with an applied vertical transverse load $\widehat{f}_y$.

The numerical experiments S2-1, S2-2 and S2-3 consider the maximization of the gap between groups of frequencies. The cases S3-1, S3-2 and S3-3 address the same problem although in these numerical experiments a constraint in the shear center position is included. The resulting cross section topology and material distribution for cases S2-1, S2-2, and S2-3 are presented in Figures 4(c) through (h), and Figures 5(b) through (d). The resulting optimized designs for cases S4-1, S4-2, and S4-3 are presented in Figures 6(c) through (h), and Figures 7(b) through (d). The sub-problems 1, 2 and 3 for both case S2 and S4 refer to the different frequency groups being considered in the optimal design problem (see Table 4).

As expected in both the S2 and S4 cases the optimized cross section topology and material distributions change significantly depending on the groups of frequencies being considered. Furthermore, note that the resulting designs for cases S2-2, S2-3, S4-2, and S4-3 present a depart from the typical box like cross section topology seen before (see Figures 4(e) through (h), and Figures 6(e) through (h)). In these cases, the constraint on the shear center does not seem to affect the results significantly when comparing to the S2-1 and S2-2 cases with the S4-1 and S4-2 cases, respectively ((see Figures 4(c) through (f), and Figures 6(c) through (f))). Cases S2-3 and S4-3 however, present a significant difference between the two resulting designs (cf. Figures 4(g) and (h), and Figures 6(g) through (h), respectively). This is also reflected in the magnitude of the resulting gaps between ω_4 and ω_5 (cf. Table 5). In case S2-3 the frequencies ω_4 and ω_5 are associated with

Table 5: Summary of numerical results for cases S1, S2, S3, S4 and all sub-cases therein (cf. Table 4). The first seven rows indicated the lowest seven eigenfrequencies for the optimized designs (the lines are place between the frequencies that have been separated). The weight (w) and shear center position ($\mathbf{s}_c = (x_s, y_s)$) are presented in row eight through ten. The last row presents the number of objective function evaluations. The frequency values and the shear center position values are obtained with the penalized densities, i.e., $p = p_{max} = 5$.

	S1	S2-1	S2-2	S2-3	S3	S4-1	S4-2	S4-3
ω_1	5.89	4.21	0.69	0.49	5.91	3.72	1.16	0.73
ω_2	7.34	4.39	2.94	0.52	7.47	3.92	3.59	7.88
ω_3	69.50	98.98	23.47	18.07	66.33	82.73	38.36	20.79
ω_4	99.67	111.02	71.69	19.34	96.17	98.52	100.59	25.51
ω_5	170.00	114.02	85.74	76.03	176.09	100.03	105.11	159.89
ω_6	439.89	579.85	154.53	128.86	413.69	495.82	244.19	161.04
ω_7	629.48	591.43	298.70	139.56	606.23	519.86	319.25	198.88
w	3/5	3/5	3/5	3/5	3/5	3/5	3/5	3/5
x_s	0.0	0.0	0.0	0.0	-0.2	-0.2	-0.2	-0.2
y_s	0.0	0.0	0.0	0.0	0.0	0.0	0.0	0.0
Func. Evals.	546	1736	2336	2269	760	1682	2213	2869

the bending and torsional vibration modes of the beam, respectively. Hence, a increase in the difference between the two frequencies is achieved through a decrease in bending stiffness and an increase in torsional stiffness. The resulting nearly cylindrical topology with small radius visible in Figures 4(g) and (h) achieves just that. The small radius reduces the cross section bending stiffness while the cylindrical shape can be shown to be the stiffer in torsion (see, e.g., Timoshenko and Goodier [1]). Moreover, the resulting laminates consist of interleaving layers of $45°$ and $-45°$ fibers aligned to resist the shear stresses which orient at a $45°$ helical angle around the cylinder.

In case S4-3, the frequencies ω_4 and ω_5 are associated with two bending modes orthogonal to each other. In order to maximize the gap between the two frequencies, the bending stiffness in one direction has to be increased while the bending stiffness in the orthogonal direction has to be decreased. The resulting design is a type of "I-beam" oriented diagonally with respect to the cross section coordinate system (see Figures Figures 6(g) and (h), and 7(d)). The diagonal orientation is such that the height of the cross section, and consequently the bending stiffness in the negative x and positive y direction, is maximized. The fiber orientations are such that the fibers align at $0°@0°$ and $0°@90°$ in the "flanges", or top left and bottom right regions of the cross section, where the normal stresses are higher. In the central part, the shear stresses dominate an the laminates consisting of $45°$ and $-45°$ fibers emerge. The resulting optimized topology and material distribution is in fact similar to the results obtained by Blasques and Stolpe in [12] for the minimum compliance optimization of a square beam subjected to a diagonal transverse load.

The results presented in this section indicate that the devised optimal design framework is able to simultaneously optimize the cross section topology and material properties to precisely tailor the frequency spectrum of laminated composite beams.

5.4.2 Minimum compliance with frequency constraints

The results for the S5, S6, S7 and S8 cases are presented in this section. The resulting compliance and frequency values, shear center position, and number of objective function evaluations are presented in Table 6. The resulting optimized cross section topologies and material distributions are presented in Figures 8 and 9. It is assumed in all cases that the beam is subjected to one load case combining the distributed transverse forces $\widehat{f}_x = 2$ and

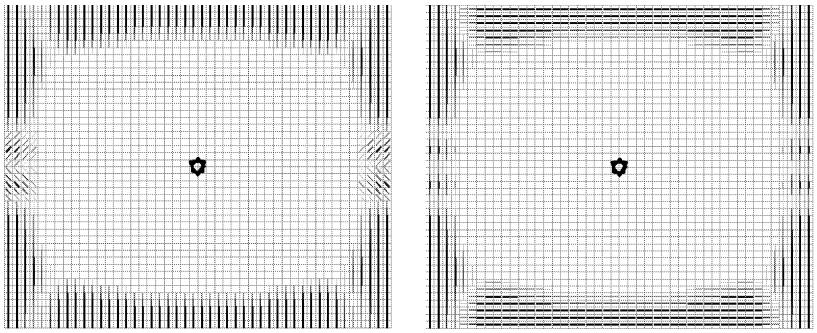

(a) S1 Fiber angles

(b) S1 Fiber plane angles

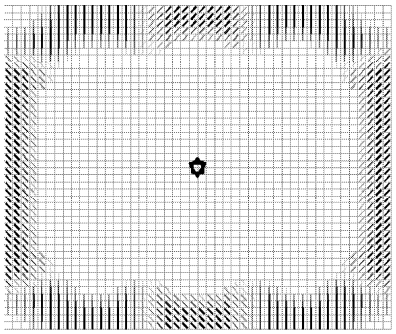

(c) S2-1 Fiber angles

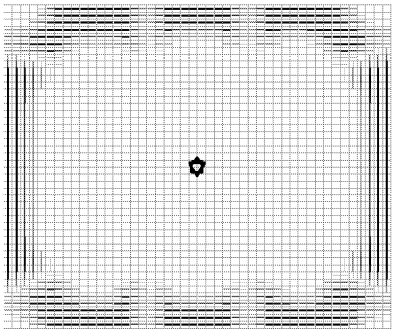

(d) S2-1 Fiber plane angles

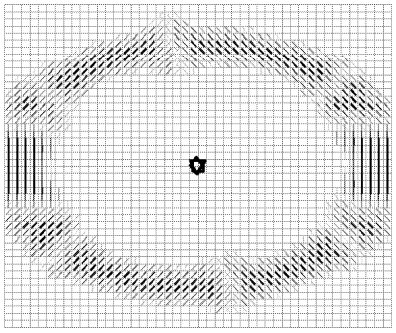

(e) S2-2 Fiber angles

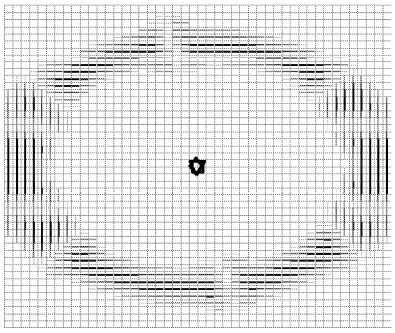

(f) S2-2 Fiber plane angles

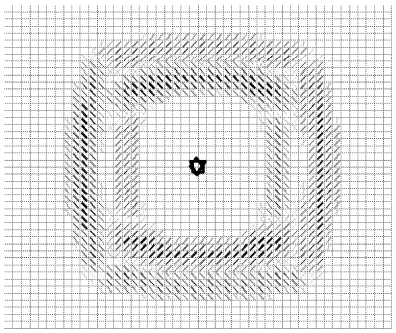

(g) S2-3 Fiber angles

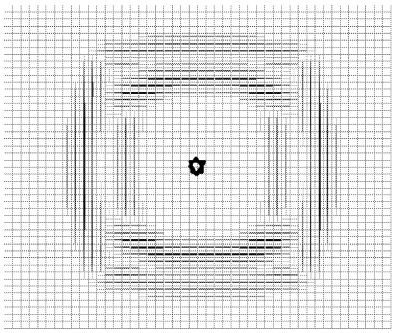

(h) S2-3 Fiber plane angles

Figure 4: Optimal material distribution for cases S1, S2-1, S2-2, and S2-3 (cf. Tables 3 and 4). Case S1 is the solution to the maximization of the minimum eigenfrequecy problem with a weight constraint (P1-3). The remaining cases S2-1, S2-2, and S2-3 are the solutions to the maximization of the gap between two eigenfrequencies with weight constraints (P1-2). The legend to the figures is described in Figure 3.

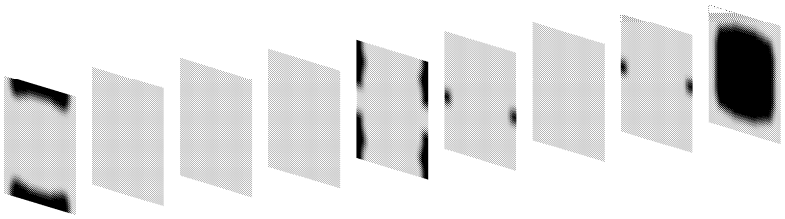

(a) S1

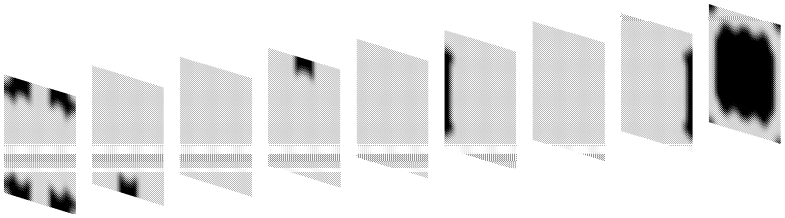

(b) S2-1

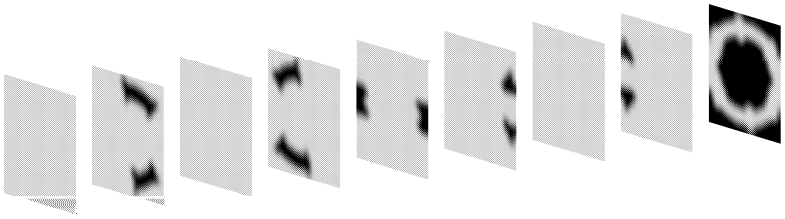

(c) S2-2

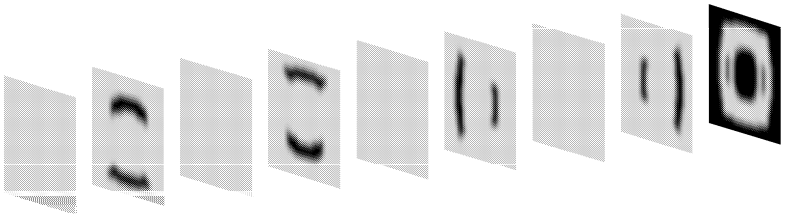

(d) S2-3

0@0 45@0 90@0 -45@0 0@90 45@90 90@90 -45@90 Iso.

Figure 5: (continue from Figure 4) Volume fractions for each candidate material for cases S1, S2-1, S2-2, and S2-3 (cf. Tables 3 and 4). Case S1 is the solution to the maximization of the minimum eigenfrequecy problem with a weight constraint (P1-3). The remaining cases S2-1, S2-2, and S2-3 are the solutions to the maximization of the gap between two eigenfrequencies with weight constraints (P1-2). The legend to the figures is described in Figure 3.

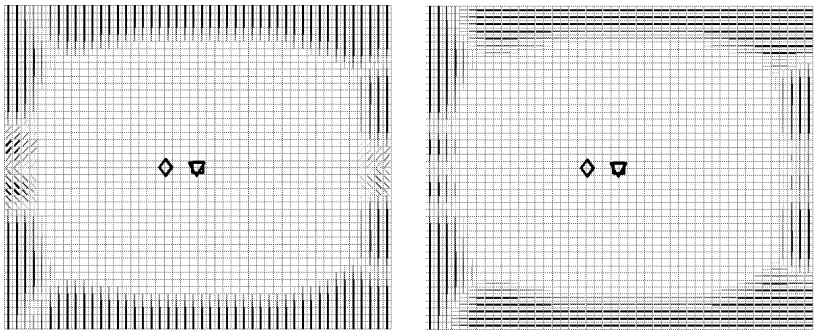

(a) S3 Fiber angles

(b) S3 Fiber plane angles

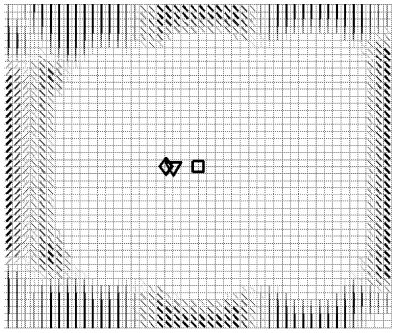

(c) S4-1 Fiber angles

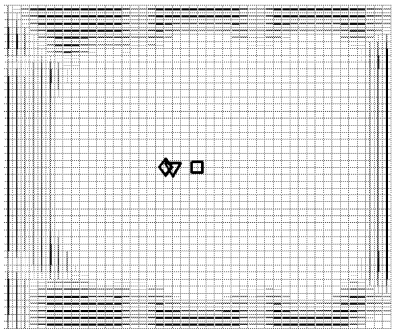

(d) S4-1 Fiber plane angles

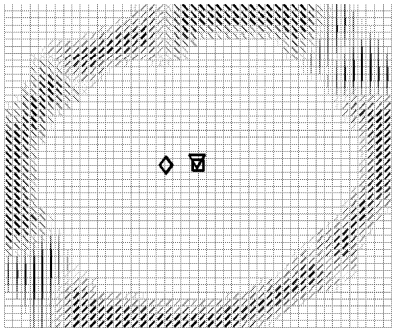

(e) S4-2 Fiber angles

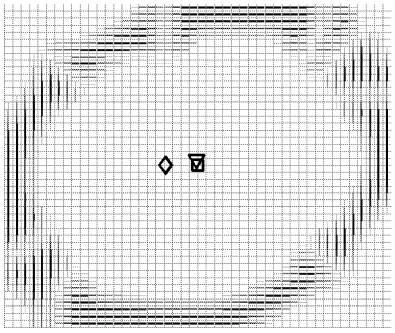

(f) S4-2 Fiber plane angles

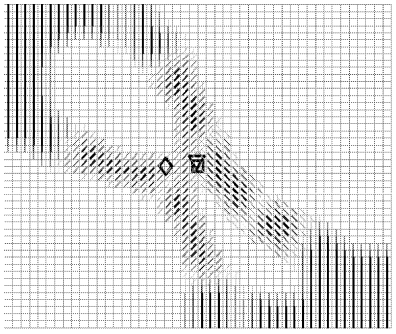

(g) S4-3 Fiber angles

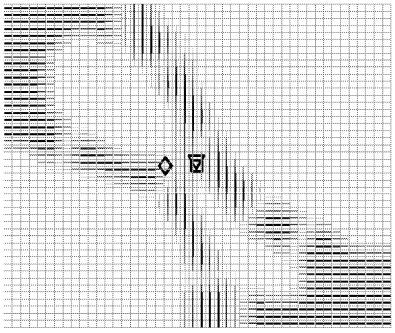

(h) S4-3 Fiber plane angles

Figure 6: Optimal material distribution for cases S3, S4-1, S4-2, and S4-3 (cf. Tables 3 and 4). Case S3 is the solution to the maximization of the minimum eigenfrequecy problem with constraints on weight and shear center position (P1-4). The remaining cases S4-1, S4-2, and S4-3 are the solutions to the maximization of the gap between two eigenfrequencies with constraints on weight and shear center position (P1-1). The legend to the figures is described in Figure 3.

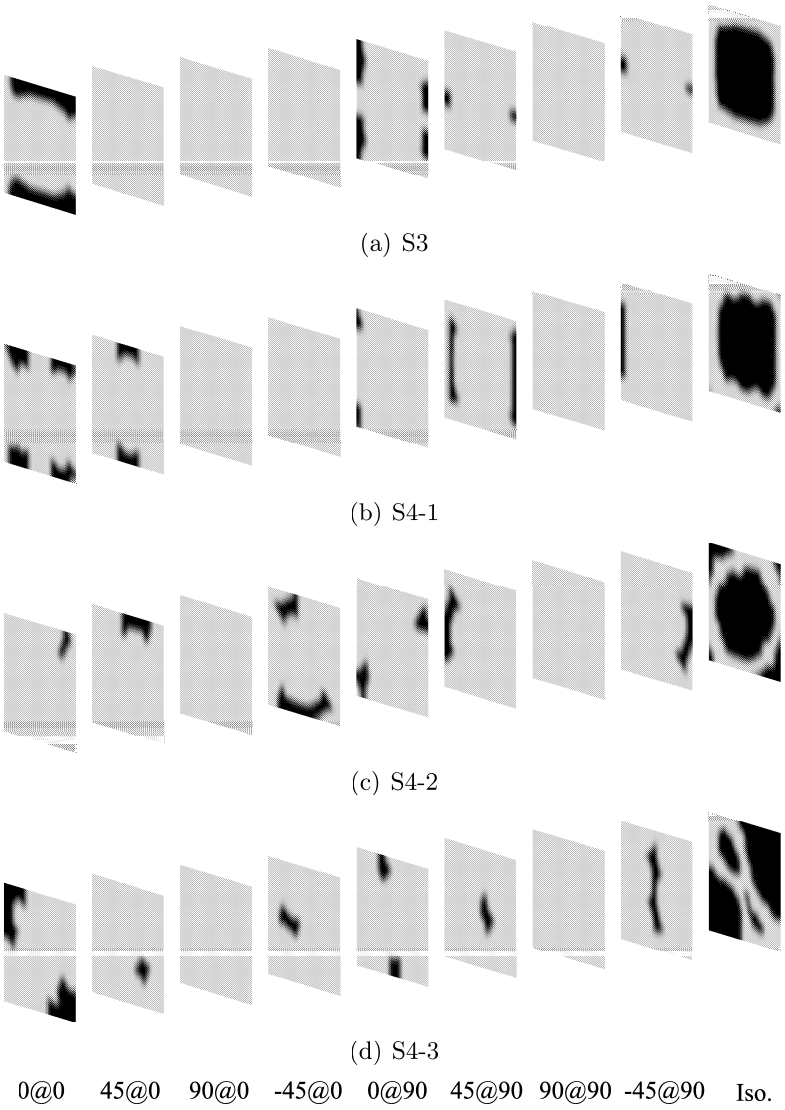

Figure 7: (continue from Figure 6) Volume fractions for each candidate material for cases S3, S4-1, S4-2, and S4-3 (cf. Tables 3 and 4). Case S3 is the solution to the maximization of the minimum eigenfrequecy problem with constraints on weight and shear center position (P1-4). The remaining cases S4-1, S4-2, and S4-3 are the solutions to the maximization of the gap between two eigenfrequencies with constraints on weight and shear center position (P1-1). The legend to the figures is described in Figure 3.

$\widehat{f}_y = 3$, and the distributed torsional moment $\widehat{m}_z = 15$.

The numerical experiments are designed so that it is possible to observe the influence of the frequency constraints on the resulting optimized cross section designs. Hence, results are obtained first for the reference cases S5 and S7 (cf. Table 3). The resulting designs presented in Figures 8 and 9 are in agreement with similar results presented by Blasques and Stolpe in [12]. The value of the frequency constraints presented in Table 4 for the numerical examples S6 and S8 are subsequently chosen based on the resulting frequencies presented in Table 6 for cases S5 and S7, respectively. Hence, in both the S6 and S8 cases the upper bound on $\overline{\mathrm{KS}}(\boldsymbol{\omega}_{1,3})$ is set to the value of ω_3 determined in S5 and S7, respectively. The lower bound on $\underline{\mathrm{KS}}(\boldsymbol{\omega}_{4,6})$ is set to be 5% larger than the value of ω_4 determined in S5 and S7, respectively. This corresponds to imposing an increase of 11%

Table 6: Summary of numerical results for all cases in Table 4. The second and third columns indicate the number of design variables and objective function evaluations, respectively. The resulting compliance (C), weight (w) defined by the ratio of orthotropic material, shear center position ($\mathbf{s}_c = (x_s, y_s)$), and mass center position ($\mathbf{m}_c = (x_c, y_c)$). The compliance and shear center position values are obtained with the penalized densities, i.e., $p = p_{max}$ (cf. Table 4).

	S5	S6	S7	S8
C	11.42	11.25	12.51	12.52
ω_1	2.42	2.27	2.41	2.33
ω_2	7.28	6.99	7.15	6.53
ω_3	75.95	72.44	76.33	74.00
ω_4	109.59	115.07	128.50	135.61
ω_5	165.69	167.31	170.15	165.46
ω_6	457.01	443.50	469.16	456.80
ω_7	696.45	649.60	634.25	574.99
w	3/5	3/5	3/5	3/5
x_s	0.49	0.47	-0.2	-0.2
y_s	-0.17	-0.16	0.0	0.0
Func. Evals.	997	2369	1589	3659

in the relative difference between the ω_3 and ω_4 frequencies when comparing case S6 with S5, and an increase of 14% when comparing case S8 with S7.

As can be seen in Table 6, the frequency constraints are satisfied in both the S6 and S8 cases. In fact, most of the constraints on $\underline{\text{KS}}(\boldsymbol{\omega}_{1,3})$ and $\overline{\text{KS}}(\boldsymbol{\omega}_{1,3})$ are not active at the final optimized designs. As a result the gap between ω_3 and ω_4 in both the S6 and S8 case is larger than that imposed by the constraints. The result is a 21% and 15% increase in the relative difference between the ω_3 and ω_4 frequencies for case S6 and S8, respectively.

In terms of the material distribution, there is no significant difference in the material properties and cross section topology between the cases S5 and S7, and S6 and S8. This is clear when comparing the resulting position of the shear and mass center in S5 and S7, and the mass center in S6 and S8.

In summary, the results suggest that the devised optimal design framework is suitable for the identification of the optimal cross section topology and material properties in problems dealing with the simultaneous design of the static and dynamic properties of the beam.

5.5 Discussion

Note that the compliance values in case S5 is larger than the value of case S6 (cf. Table 6). This is contrary to the expected. The S5 case does not include the frequency constraints and should therefore result in a lower compliance value. The same happens when comparing the value of the lowest frequency in cases S1 and S3 (cf. Table 5). The design obtained in S1 presents a lower minimum eigenfrequency than the case S3 where the constraints on the shear center position are enforced. Further investigation into the correct choice of the step Δp in the continuation method may help solve this problem.

Finally, the numerical experiments indicate that the KS function is a suitable alternative for addressing the convergence issues commonly encountered when dealing with eigenfrequency constraints.

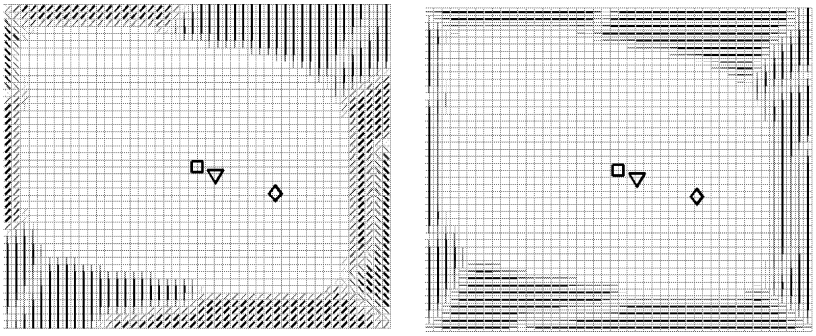

(a) S5 Fiber angles

(b) S5 Fiber plane angles

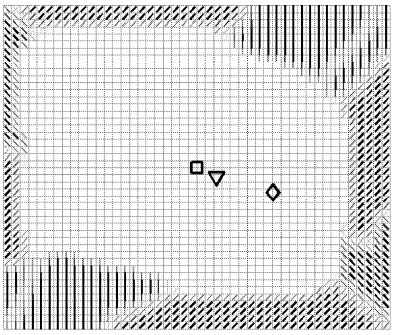

(c) S6 Fiber angles

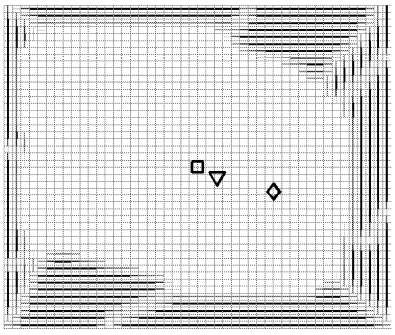

(d) S5 Fiber plane angles

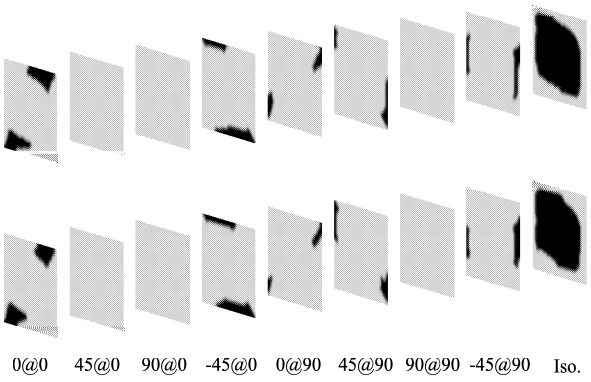

(g) Volume fractions for each candidate material for S5 (top) and S6 (bottom) cases.

Figure 8: Optimal material distribution for case S5 and S6 (cf. Tables 3 and 4). Case S5 is the solution to the minimum compliance problem with weight constraints (P2-2). Case S6 is the solution to the the minimum compliance problem with frequency and weight constraints (P2-4). The legend to the figures is described in Figure 3.

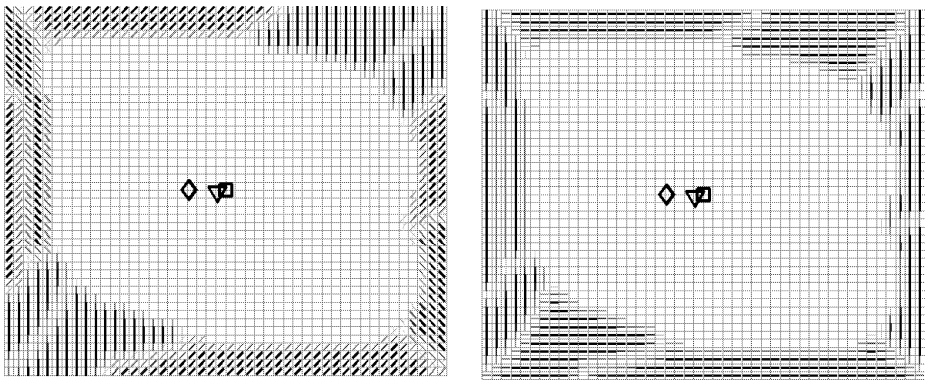

(a) S7 Fiber angles

(b) S7 Fiber plane angles

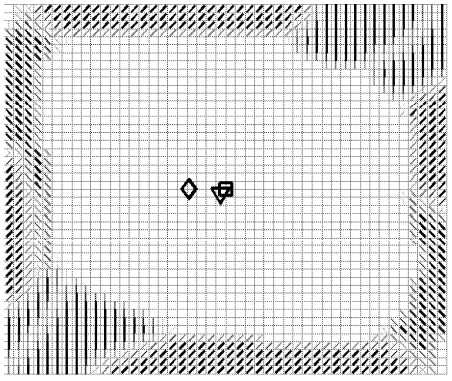

(c) S8 Fiber angles

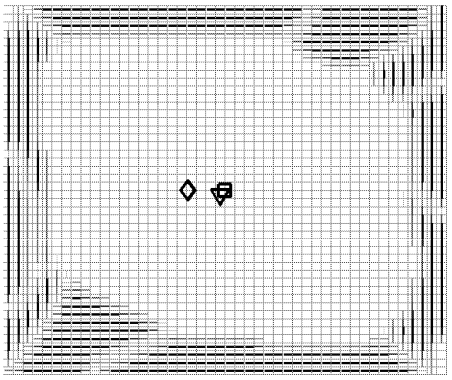

(d) S8 Fiber plane angles

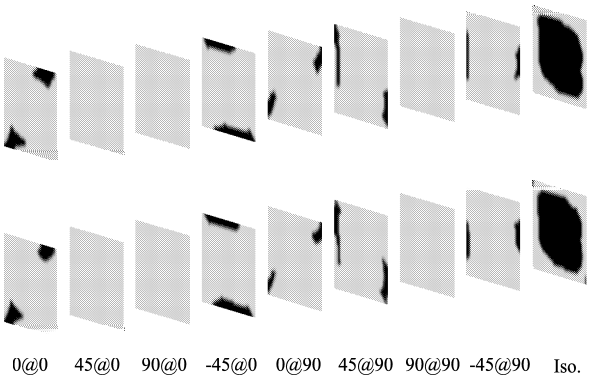

(g) Volume fractions for each candidate material for S7 (top) and S8 (bottom) cases.

Figure 9: Optimal material distribution for case S7 and S8 (cf. Tables 3 and 4). Case S7 is the solution to the minimum compliance problem with constraints on weight and shear center position (P2-3). Case S8 is the solution to the the minimum compliance problem with constraints on the frequency, weight, and shear center position (P2-4). The legend to the figures is described in Figure 3.

6 Conclusions

A framework has been presented for the optimal design of laminated composite beams with stiffness and frequency constraints. The static and dynamic structural response of the beam is analyzed using beam finite elements. The cross section stiffness and mass properties are determined using a finite element based cross section analysis tool. The resulting beam model is able to account for effects stemming from material anisotropy and inhomogeneity in the analysis of beams with arbitrary section geometry.

The optimal design problem is formulated in a multi-material topology optimization context. The suggested approach is suitable for the simultaneous determination of the optimal cross section topology and material properties. An alternative approach is proposed to handle the eigenfrequencies constraints based on the the Kreisselmeier-Steinhauser function.

Optimized cross section designs are presented first for optimal design problems dealing with the maximization of the minimum frequency, and the maximization of the gap between consecutive frequencies. Furthermore, results are also presented where the same problems are solved but the position of the shear center is constrained. Finally, optimized designs are presented for the minimum compliance problem with constraints on frequency, shear center position and weight.

The numerical examples suggest that the devised optimal design framework is suitable for the simultaneous optimization of the cross section topology and material properties in the design of laminated composite beams with stiffness and frequency constraints. The next step consists of applying the presented methodology for the aeroelastic tailoring of laminated composite wind turbine blades.

References

[1] Timoshenko S.P., Goodier J.N., *Theory of Elasticity*, McGraw-Hill Book Company, 1st Ed., 1934.

[2] Jung S.N., Nagaraj V.T. Chopra I., *Assessment of composite rotor blade modeling techniques*, Journal of the American Helicopter Society, 4(3), 188-205, 1999.

[3] Volovoi V.V., Hodges D.H., Cesnik C.E.S., Popescu B., *Assessment of beam modeling methods for rotor blade applications*, Mathematical and Computer Modelling, 33, 1099-1112, 2001.

[4] Hodges D., *Nonlinear Composite Beam Theory*, Progress in Astronautics and Aeronautics Series, 213, AIAA, 2006.

[5] Seyranian A.P., Lund E., Olhoff N., *Multiple eigenvalues in structural optimization problems*, Structural Optimization, 8, 207-227, 1994.

[6] Kreisselmeier G., Steinhauser R., *Systematic control design by optimizing a vector performance index*, International Federation of Active Controls Symposium on Computer-Aided Design of Control Systems, Zurich, Switzerland, 1979.

[7] Raspanti C.G., Bandoni J.A., Biegler L.T., *New strategies for flexibility analysis and design under uncertainty*, Computers and Chemical Engineering, 24(9-10), 2193-2209, 2000.

[8] Martins J.R.R.A., Alonso J.J., Reuther J.J., *A coupled-adjoint sensitivity analysis method for high-fidelity aero-structural design*, Optimization and Engineering, 6(1), 3362, 2005.

[9] Maute K., Nikbay M., Farhat C., *Sensitivity analysis and design optimization of three dimensional non-linear aeroelastic systems by the adjoint method*, International Journal for Numerical Methods in Engineering, 56, 911-933, 2003.

[10] Giavotto V., Borri M., Mantegazza P., Ghiringhelli G., Carmaschi V., Maffiolu G.C., Mussi F., *Anisotropic beam theory and applications*, Composite Structures, 16(1-4), 403-413, 1983.

[11] Blasques J.P., Lazarov B., *BECAS - A beam cross section analysis tool for anisotropic and inhomogeneous sections of arbitrary geometry*, RISØ-R 1785 Technical Report, 2011.

[12] Blasques J.P., Stolpe M., *Multi-material topology optimization of laminated composite beam cross sections*, submitted, 2011.

[13] Bendsøe M.P., Sigmund O., *Topology Optimization: Theory, Methods and Applications*, 2nd Edition, Springer-Verlag, Berlin, 2003.

[14] Bendsøe M., Kikuchi N., *Generating optimal topologies in structural design using a homogenization method*, Computer Methods in Applied Mechanics and Engineering, 71 (2), 197-224, 1988.

[15] Rozvany G., Zhou M., *The COC algorithm .1. Cross-section optimization or sizing*, Computer Methods in Applied Mechanics and Engineering, (89), (1-3), 281-308, 1991.

[16] Bathe K.J., *Finite Element Procedures in Engineering Analysis*, Prentice-Hall, 1982.

[17] Sigmund O., *Morphology-based black and white filters for topology optimization*, Structural and Multidisciplinary Optimization, 33(4-5), 401-424, 2007.

[18] Bruns T. E., Tortorelli D. A., *Topology optimization of non-linear elastic structures and compliant mechanisms*, Computer Methods in Applied Mechanics and Engineering, 190(26-27), 3443-3459, 2001.

[19] Sigmund O., Petersson J., *Numerical instabilities in topology optimization: A survey on procedures dealing with checkerboards, mesh dependencies and local minima*, Structural Optimization, 16(1), 68-75, 1998.

[20] Bourdin B., *Filters in topology optimization*, International Journal for Numerical Methods in Engineering, 50(9), 2143-2158, 2001.

[21] Hvejsel C.F., Lund E., Stolpe M., *Optimization strategies for discrete multi-material stiffness optimization*, Structural and Multidisciplinary Optimization, DOI 10.1007/s00158-011-0648-5, 2011.

[22] Borrval T., Petersson J., *Topology optimization using regularized intermediate density control*, Computer Methods in Applied Mechanics and Engineering, 190(37-38), 4911-4928, 2001.

[23] Peters S., *Handbook of composites*, 2nd Edition, Chapman & Hall, London, 1998.

[24] http://www.diabgroup.com/, 2011.

[25] Gill P.E., Murray W., Saunders M.A., *SNOPT: An SQP algorithm for large scale constrained optimization*, SIAM Journal on Optimization, 121(4), 979-1006, 2002.

[26] Olhoff N., *Optimization of vibrating beams with respect to higher order natural frequencies*, Journal of Structural Mechanics, 4, 87-122, 1976.

[27] Bendsøe M.P., Olhoff N., *A method of design against vibration resonance of beams and shafts*, Optimal Control Applications and Methods, 6, 191-200, 1985.

[28] Pedersen N.L., *Maximization of eigenvalues using topology optimization*, Structural and Multidisciplinary Optimization, 20, 2-11, 2000.

[29] Diaz A.R., Kikuchi N., *Solutions to shape and topology eigenvalue optimization problems using a homogenization method*, International Journal of Numerical Methods in Engineering, 35, 1487-1502, 1992.

[30] Pedersen N.L., *On design of fiber-nets and orientation for eigenfrequency optimization of plates*, Computational Mechanics, 39(1), 1-13, 2006.

[31] Du J., Olhoff N., *Topological design of freely vibrating continuum structures for maximum values of simple and multiple eigenfrequencies and frequency gaps*, Structural and Multidisciplinary Optimization, 34(2), 91-110.

[32] Lund E., Stegmann J., *Discrete material optimization of general composite shell structures*, International Journal for Numerical Methods in Engineering, 62(14), 2009-2007, 2005.

[33] Stegmann J., Lund E., *On structural optimization of composite shell structures using a discrete constitutive parametrization*, Wind Energy, 8(1), 109-124, 2005.

[34] Hansen M.H., *Aeroelastic instability problems for wind turbines*, Wind Energy, 10, 551-577, 2007.

Paper 4

Blasques J.P., Lazarov B., BECAS – A beam cross section analysis tool for anisotropic and inhomogeneous sections of arbitrary geometry, RISØ-R 1785 Technical Report, 2011.

BECAS

A cross section analysis tool for anisotropic and inhomogeneous sections of arbitrary geometry

José Pedro Blasques
RISØ – National Laboratory for Sustainable Energy
Technical University of Denmark
Frederiksborgvej 399, P.O. Box 49, Building 114,
DK-4000 Roskilde, Denmark
jpb@mek.dtu.dk

Boyan Lazarov
Department of Mechanical Engineering
Technical University of Denmark
Nils Koppels Allé, Building 404,
DK-2800 Kgs. Lyngby, Denmark
bsl@mek.dtu.dk

RISØ-R 1785

Project funded by:
EFP 2007 Project 33033-0075
Anisotropic beam model for analysis and design of passive controlled wind turbine blades (ANBAVI)

Contents

List of Symbols

x, y, z	Coordinates of a point in the cross section	10
A	Cross section area	10
$\boldsymbol{\epsilon}$	Strain vector	10
$\boldsymbol{\sigma}$	Stress vector	10
$\mathbf{Q}$	Material tensor	10
$\mathbf{p}$	Tractions on cross section	10
$\mathbf{T}$	Section forces - shear and axial forces	10
$\mathbf{M}$	Section forces - bending moments and torque	10
$\boldsymbol{\theta}$	Vector of section forces	10
$\mathbf{n}$	Two dimensional cross product matrix	10
$\mathbf{Z}$	Auxiliary matrix for evaluation of cross section forces	11
$\mathbf{s}$	Total displacement of a point in the cross section	11
$\mathbf{v}$	Rigid body displacement of a point in the cross section	11
$\mathbf{g}$	Warping displacement of a point in the cross section	11
$\mathbf{r}$	Cross section translation and rotation	11
$\boldsymbol{\chi}$	Translation of a reference point in the cross section	11
$\boldsymbol{\varphi}$	Cross section rotation angles	11
$\mathbf{B}$	Two dimensional strain-displacement matrix	11
$\mathbf{S}$	One dimensional strain-displacement matrix	11
$\mathbf{T}_r$	Sixth order auxiliary matrix for definition of the section strains	12
$\boldsymbol{\psi}$	Section strain parameters	12
$\mathbf{N}$	Matrix of finite element interpolation functions	12
$\mathbf{u}$	Nodal degrees of freedom in cross section finite element mesh	12
W_e	External work per unit length	13
W_i	Internal work or elastic energy per unit length	14
W_t	Total virtual work per unit length	15
n_n	Number of nodes in the cross section finite element mesh	19
$\mathbf{F}$	Cross section compliance matrix	26
$\mathbf{K}$	Cross section stiffness matrix	26
x_t, y_t	Coordinates of elastic center	26
x_s, y_s	Coordinates of shear center	26
n_q	Number of nodes in the cross section finite element mesh	30
n_e	Number of elements in the cross section finite element mesh	31

Chapter 1

Introduction

This report describes the development and implementation of the **BE**am **C**ross section **A**nalysis **S**oftware – **BECAS**.

Cross section analysis tools are commonly employed in the development of beam models for the analysis of long slender structures. These type of models can be very versatile when compared against its equivalent counterparts as they generally offer a very good compromise between accuracy and computational efficiency. When suited, beam models can be advantageously used in an optimal design context (see, e.g., Ganguli and Chopra [1], Li et al. [2], Blasques and Stolpe [3]) or in the development of complex multiphysics codes. Wind turbine aeroelastic codes, for example, commonly rely on these types of models for the representation of most parts of the wind turbine, from the tower to the blades (see, e.g., Hansen et al. [4], Chaviaropoulos et al. [5]). In specific, the development of beam models which correctly describe the behaviour of the wind turbine blades have been the focus of many investigations. The estimation of the properties of these types of structures becomes more complex as the use of different combinations of advanced materials becomes a standard. It is therefore paramount to develop cross section analysis tools which can correctly account for all geometrical and material effects. BECAS is a general purpose cross section analysis tool specifically developed for these types of applications. BECAS is able to handle a large range of arbitrary section geometries and correctly predict the effects of inhomogeneous material distribution and anisotropy. Based on a definition of the cross section geometry and material distribution, BECAS is able to determine the cross section stiffness properties while accounting for all the geometrical and material induced couplings. These properties can be consequently utilized in the development of beam models to accurately predict the response of wind turbine blades with complex geometries and made of advanced materials.

BECAS is based on the theory originally presented by Giavotto et al. [6] for the analysis of inhomogeneous anisotropic beams. The theory leads to the definition of two types of solutions of which, and in accordance to Saint-Venant's principle, the non-decaying solutions are the basis for the evaluation of the cross section stiffness properties. A slight modification to the theory was introduced later by Borri and Merlini [7] where the concept of *intrinsic warping* is introduced in the derivation of the cross section stiffness matrix. Despite the modifications, no difference in the results was reported. The theory was subsequently extended by Borri et al [8] to account for large displacements, curvature and twist. Ghiringhelli and Mantegazza in [9] presented an implementation of the theory for commercial finite element codes. Finally Ghiringhelli in [10, 11] and Ghiringhelli et al. [12] presented a formulation incorporating thermoelastic and piezo-electric effects, respectively. The validation results presented throughout each of the previously mentioned publications highlight the robustness of the method in the analysis of the stiffness and strength properties of anisotropic and inhomogeneous beam cross sections. According to

Yu et al. [13] implementations of this theory have been in fact used as a benchmark for the validation of any new tool emerging since the early 1980's (see, e.g., Yu et al. [13, 14] and Chen et al. [15]).

Many other cross section analysis tools have been described in the litterature. The reader is referred to Jung et al. [16] and Volovoi et al. [17] for an assessment of different cross section analysis tools. Nonetheless, at this stage the Variational Asymptotic Beam Section analysis commercial package VABS by Yu et al. [13] is perhaps the state of the art for these type of tools. VABS has been extensively validated (see Yu et al. [13, 14], Chen et al. [15]) and is therefore used in this report as the benchmark for the validation of BECAS. As shall be seen the cross section properties estimated by both tools are in very good agreement.

The theory presented in this report concerns only the determination of the cross section stiffness properties for inhomogeneous and anisotropic beam cross sections of arbitrary geometry, i.e., the theory implemented in BECAS. Most of the relevant information which is spread across the different publications (namely [6]-[12]) and which concerns the estimation of the cross section stiffness properties is compiled here. The aim was to produce a self-contained document which can serve as a developer's manual for the readers wishing to use, understand and further develop BECAS.

This report is organized as follows:

Chapter 2 Theory Manual All the theory leading to the evaluation of the cross section stiffness properties is presented in this chapter. The assumptions underlying the presented theory are stated first in Section 2.1. The equibilibrium equations are established next in Section 2.2 and consequently resolved in Section 2.3. Some of the mathematical properties invoked in the resolution of the equilibrium equations are described in detail in Section 2.4. Finally, the expressions for the cross section stiffness matrix, and positions of shear and elastic centers, are determined in Section 2.5.

Chapter 3 Implementation Manual The details concerning the numerical implementation of the theory are presented in this chapter. A two dimensional implementation based on four node plane finite elements is presented in Section 3.1. Furthermore, an implementation of the method for commercial finite element codes is described next in Section 3.2. Finally, in Section 3.3, the constitutive matrix is defined and some important conventions utilized in its transformation are stated.

Chapter 4 Validation All numerical experiments performed for the validation of VABS are presented in this Chapter. The general setup for the numerical experiments is described first in Section 4.1. The validation results obtained for the different cross sections are finally presented in Section 4.2.

Appendix A BECAS The MATLAB implementation of BECAS is described here.

Chapter 2

Theory manual

This chapter describes the theory underlying the implementation of the cross section analysis tool BECAS. The chapter is organized as follows. In the first section, Section 2.2, some general definitions are introduced. The beam kinematics are subsequently described. The displacement of a point in the cross section is described as the sum of a rigid body motion and a warping displacement accounting for the cross section deformation. A two dimensional discretization of the warping following the typical finite element approach is introduced. The principle of virtual work is then invoked in the derivation of the expressions for the external and internal virtual work per unit length. The equilibrium equations for the cross section are consequently established.

The solution to the equilibrium equations, a set of second order linear differential equations, is discussed in Section 2.3. As shall be seen, the solution is defined by a particular integral which depends on the boundary conditions – or internal force resultants in this case – and a general integral which resolves into an eigenvalue problem. The particular integral corresponds to solutions far from the ends of the beam where the end effects are negligible– the *central* solutions – while the general integrals corresponds to the solutions at the extremities of the beam are applied – *extremity* solutions (nomencalture according to Giavotto et al. [6]). At this point some mathematical properties of the solutions are invoked which are only detailed later in Section 2.4. The reader may wish to avoid this section if only a general overview of the method is required.

The equations for the cross section stiffness matrix are presented in Section 2.5. Based on the cross section stiffness properties it is possible to compute the positions of the shear and elastic center.

2.1 Assumptions

The theory presented in the next sections is valid for long slender structures which present a certain level of geometric and structural continuity. Thus, there should not be abrupt variations of the cross section geometry and material properties along the beam length. Moreover, the same should be valid for the loads applied. Consequently, the gradients of the resulting strains and displacement along the beam axis should also be small. All the assumptions mentioned before are not imposed along the cross section coordinates in the cross section plane. Finally, the theory is based on the assumptions of small displacements and rotations.

2.2 Equilibrium equations

The derivation of the equilibrium equations for the beam cross section are presented in this section.

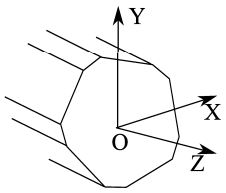

Figure 2.1: Cross section coordinate system.

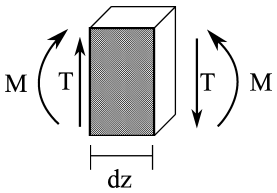

Figure 2.2: Cross section resultant forces for a slice dx of the beam.

2.2.1 Basic definitions

The reference coordinate system for a generic cross section with area A is presented in Figure 2.1. The displacement of a point in the section $\mathbf{s} = [s_x \; s_y \; s_z]^T$ is defined with respect to the cross section coordinate system x, y, z . The strain and stress, $\boldsymbol{\epsilon}$ and $\boldsymbol{\sigma}$, are given as

$$\boldsymbol{\epsilon}^T = [\epsilon_{xx} \; \epsilon_{yy} \; 2\epsilon_{xy} \; 2\epsilon_{xz} \; 2\epsilon_{yz} \; \epsilon_{zz}]$$
$$\boldsymbol{\sigma}^T = [\sigma_{xx} \; \sigma_{yy} \; \sigma_{xy} \; \sigma_{xz} \; \sigma_{yz} \; \sigma_{zz}]$$

The stress and strain relate through Hooke's law

$$\boldsymbol{\sigma} = \mathbf{Q}\boldsymbol{\epsilon} \tag{2.1}$$

where $\mathbf{Q}$ is the typical material constitutive matrix. It is assumed that the material is linear elastic, otherwise there are no restrictions regarding the level of anisotropy (see Section 3.3). The ordering of the entries in $\boldsymbol{\epsilon}$ and $\boldsymbol{\sigma}$ is such that the tractions or the components of stress acting on the cross section face, can be easily isolated in

$$\mathbf{p}^T = [\sigma_{xz} \; \sigma_{yz} \; \sigma_{zz}]$$

The tractions $\mathbf{p}$ acting upon the cross section face are statically equivalent to a force $\mathbf{T}$ and moment $\mathbf{M}$ (cf. Figure 2.2)

$$\mathbf{T} = \int_A \mathbf{p} \; \mathrm{dA} \tag{2.2}$$
$$\mathbf{M} = \int_A \mathbf{n}^T\mathbf{p} \; \mathrm{dA} \tag{2.3}$$

where the two dimensional cross product matrix $\mathbf{n}$ is

$$\mathbf{n} = \begin{bmatrix} 0 & 0 & y \\ 0 & 0 & -x \\ -y & x & 0 \end{bmatrix}$$

and thus $\tilde{\mathbf{n}} \times \mathbf{p} = \mathbf{n}^T\mathbf{p}$ where $\tilde{\mathbf{n}} = [x \; y \; z]^T$ is the vector position of a point in the cross section. The vector of section forces $\boldsymbol{\theta} = \left[\mathbf{T}^T \; \mathbf{M}^T\right]^T$ can then be written as

$$\boldsymbol{\theta} = \int_A \mathbf{Z}^T\mathbf{p} \; \mathrm{dA} \tag{2.4}$$

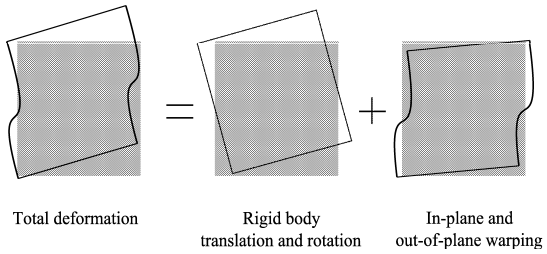

Figure 2.3: Schematic description of the different contributions for the deformation of the cross section.

where the matrix $\mathbf{Z} = \left[\mathbf{I}_3|\mathbf{n}^T\right]$, and $\mathbf{I}_i$ is the i^{th} order identity matrix,

$$\mathbf{Z} = \begin{bmatrix} 1 & 0 & 0 & 0 & 0 & -y \\ 0 & 1 & 0 & 0 & 0 & x \\ 0 & 0 & 1 & y & -x & 0 \end{bmatrix}$$

2.2.2 Kinematics

The displacement $\mathbf{s} = [s_x, s_y, s_z]^T$ at a point of the cross section is defined as

$$\mathbf{s} = \mathbf{v} + \mathbf{g}$$

where $\mathbf{v} = [v_x, v_y, v_z]^T$ is the vector of displacements associated with the rigid body translation and rotation of the cross section. The vector $\mathbf{g} = [g_x, g_y, g_z]^T$ is the vector of warping displacements associated with the cross section deformation (see Figure 2.3). Assuming small displacements and rotations, the rigid displacements $\mathbf{v}$ can be obtained as

$$\mathbf{v} = \mathbf{Z}\mathbf{r}$$

a linear combination of the the components of $\mathbf{r} = \left[\boldsymbol{\chi}^T \ \boldsymbol{\varphi}^T\right]^T$. The components of $\boldsymbol{\chi}(z) = [\chi_x, \chi_y, \chi_z]^T$ represent the translations of the cross section reference point, while $\boldsymbol{\varphi}(z) = [\varphi_x, \varphi_y, \varphi_z]^T$ are the cross section rotations. The total displacement can be rewritten as

$$\mathbf{s} = \mathbf{Z}\mathbf{r} + \mathbf{g} \tag{2.5}$$

2.2.3 Strain-displacement relation

The strain-displacement relation can be written as

$$\boldsymbol{\epsilon} = \mathbf{B}\mathbf{s} + \mathbf{S}\frac{\partial \mathbf{s}}{\partial z} \tag{2.6}$$

where $\mathbf{B}$ and $\mathbf{S}$ are defined next. The strain displacement relation can then be cast as

$$\begin{bmatrix} \epsilon_{xx} \\ \epsilon_{yy} \\ 2\epsilon_{xy} \\ 2\epsilon_{xz} \\ 2\epsilon_{yz} \\ \epsilon_{zz} \end{bmatrix} = \underbrace{\begin{bmatrix} \partial/\partial x & 0 & 0 \\ 0 & \partial/\partial y & 0 \\ \partial/\partial y & \partial/\partial x & 0 \\ 0 & 0 & \partial/\partial x \\ 0 & 0 & \partial/\partial y \\ 0 & 0 & 0 \end{bmatrix}}_{\mathbf{B}} \begin{bmatrix} s_x \\ s_y \\ s_z \end{bmatrix} + \underbrace{\begin{bmatrix} 0 & 0 & 0 \\ 0 & 0 & 0 \\ 0 & 0 & 0 \\ 1 & 0 & 0 \\ 0 & 1 & 0 \\ 0 & 0 & 1 \end{bmatrix}}_{\mathbf{S}} \begin{bmatrix} \partial s_x/\partial z \\ \partial s_y/\partial z \\ \partial s_z/\partial z \end{bmatrix} \tag{2.7}$$

Note that this the common linear three dimensional strain-displacement relation where the terms $\partial/\partial z$ have been set appart. Inserting (2.5) into (2.6) yields

$$\boldsymbol{\epsilon} = \mathbf{BZr} + \mathbf{SZ}\frac{\partial \mathbf{r}}{\partial z} + \mathbf{Bg} + \mathbf{S}\frac{\partial \mathbf{g}}{\partial z} \tag{2.8}$$

It can be shown that

$$\mathbf{BZ} = \mathbf{SZT}_r$$

where

$$\mathbf{T}_r = \begin{bmatrix} 0 & 0 & 0 & 0 & -1 & 0 \\ 0 & 0 & 0 & 1 & 0 & 0 \\ 0 & 0 & 0 & 0 & 0 & 0 \\ 0 & 0 & 0 & 0 & 0 & 0 \\ 0 & 0 & 0 & 0 & 0 & 0 \\ 0 & 0 & 0 & 0 & 0 & 0 \end{bmatrix}$$

Utilizing the relation above, Equation (2.8) can be written as

$$\boldsymbol{\epsilon} = \mathbf{SZ}\left(\mathbf{T}_r\mathbf{r} + \frac{\partial \mathbf{r}}{\partial z}\right) + \mathbf{Bg} + \mathbf{S}\frac{\partial \mathbf{g}}{\partial z}$$

It is possible at this point to define the strain parameters

$$\boxed{\boldsymbol{\psi} = \mathbf{T}_r\mathbf{r} + \frac{\partial \mathbf{r}}{\partial z}} \tag{2.9}$$

and thus rewrite the strain displacement relation in its final form

$$\boldsymbol{\epsilon} = \mathbf{SZ}\boldsymbol{\psi} + \mathbf{Bg} + \mathbf{S}\frac{\partial \mathbf{g}}{\partial z} \tag{2.10}$$

The section strain parameters $\boldsymbol{\psi} = [\tau_x,\ \tau_y,\ \tau_z,\ \kappa_x,\ \kappa_y,\ \kappa_z]^T$ are representative of the strain due to the rigid displacement of two adjacent cross sections that remain undeformed. The components $\tau_x = \frac{\partial \chi_x}{\partial z} - \varphi_y$ and $\tau_y = \frac{\partial \chi_y}{\partial z} + \varphi_x$ represent shear strains of the cross section in the x and y directions, respectively. The component $\tau_z = \frac{\partial \chi_x}{\partial z}$ is the axial elongation. Furthermore, $\kappa_x = \frac{\partial \boldsymbol{\varphi}_x}{\partial z}$ and $\kappa_y = \frac{\partial \boldsymbol{\varphi}_y}{\partial z}$ are the curvatures around x and y, respectively, and $\kappa_z = \frac{\partial \boldsymbol{\varphi}_z}{\partial z}$ is the torsion term.

Finite element discretization

The warping displacements $\mathbf{g}$ are discretized as

$$\mathbf{g}(x, y, z) = \mathbf{N}_i(x, y)\mathbf{u}(x_i, y_i, z) \tag{2.11}$$

where $\mathbf{N}$ are the typical finite element shape functions and $\mathbf{u}$ the nodal warping displacements. Note that the latter depend on the position along the beam axis although the shape functions are only defined in the plane of the section. The displacement of a point in the cross section is then given as

$$\mathbf{s} = \mathbf{Zr} + \mathbf{Nu} \tag{2.12}$$

and finally introducing (2.11) in (2.10) yields

$$\boxed{\boldsymbol{\epsilon} = \mathbf{SZ}\boldsymbol{\psi} + \mathbf{BNu} + \mathbf{SN}\frac{\partial \mathbf{u}}{\partial z}} \tag{2.13}$$

2.2.4 Virtual work principle

The total virtual work per unit length W is given as

$$W = W_e + W_i$$

The first variation of the total virtual work per unit length can be written as

$$\delta\frac{\partial W}{\partial z} = \delta\frac{\partial W_e}{\partial z} + \delta\frac{\partial W_i}{\partial z} \tag{2.14}$$

where W_i is the work done by the internal elastic forces, and W_e the work done by the external forces acting on the cross section.

External virtual work

Assuming that the surface and the body forces are zero, the axial derivative of the work produced by the section stresses is the only contribution to the external work W_e. Thus(cf. Figure 2.2)

$$\delta\frac{\partial W_e}{\partial z} = \int_A \frac{\partial\left(\delta\mathbf{s}^T\mathbf{p}\right)}{\partial z}\,\mathrm{dA}$$

The external virtual work expression can be obtained by replacing the displacement $\mathbf{s}$ as defined in (2.5) into the equation above

$$\begin{aligned}\delta\frac{\partial W_e}{\partial z} =& \int_A \frac{\partial\left(\delta\mathbf{v}^T\mathbf{p}\right)}{\partial z}\,\mathrm{dA} + \int_A \frac{\left(\delta\mathbf{g}^T\mathbf{p}\right)}{\partial z}\,\mathrm{dA}\\ =& \underbrace{\delta\frac{\partial\mathbf{r}'^T}{\partial z}\int_A \mathbf{Z}^T\mathbf{p}\,\mathrm{dA} + \delta\mathbf{r}^T\int_A \mathbf{Z}^T\frac{\partial\mathbf{p}}{\partial z}\,\mathrm{dA}}_{\text{Work from rigid displacement}}\\ &+ \underbrace{\delta\frac{\partial\mathbf{u}'^T}{\partial z}\int_A \mathbf{N}^T\mathbf{p}\,\mathrm{dA} + \delta\mathbf{u}^T\int_A \mathbf{N}^T\frac{\partial\mathbf{p}'^T}{\partial z}\,\mathrm{dA}}_{\text{Work from warping displacements}}\end{aligned}$$

Using Equation (2.4) it is possible to further simplify the previous equation

$$\begin{aligned}\delta\frac{\partial W_e}{\partial z} =& \delta\frac{\partial\mathbf{r}^T}{\partial z}\boldsymbol{\theta} + \delta\mathbf{r}^T\frac{\partial\boldsymbol{\theta}}{\partial z}\\ &+ \delta\frac{\partial\mathbf{u}^T}{\partial z}\int_A \mathbf{N}^T\mathbf{p}\,\mathrm{dA} + \delta\mathbf{u}^T\int_A \mathbf{N}^T\frac{\partial\mathbf{p}^T}{\partial z}\,\mathrm{dA}\end{aligned}$$

Note that it is possible to introduce the strain parameters in the following manner

$$\begin{aligned}\delta\frac{\partial\mathbf{r}^T}{\partial z}\boldsymbol{\theta} + \delta\mathbf{r}^T\frac{\partial\boldsymbol{\theta}}{\partial z} =& \delta\frac{\partial\mathbf{r}^T}{\partial z}\boldsymbol{\theta} + \delta\mathbf{r}^T\frac{\partial\boldsymbol{\theta}}{\partial z} + \delta\mathbf{r}^T\mathbf{T}_r^t\boldsymbol{\theta} - \delta\mathbf{r}^T\mathbf{T}_r^T\boldsymbol{\theta}\\ =& \delta\mathbf{r}^T\frac{\partial\boldsymbol{\theta}}{\partial z} - \delta\mathbf{r}^T\mathbf{T}_r^T\boldsymbol{\theta} + \delta\underbrace{\left(\mathbf{r}^T\mathbf{T}_r^t + \frac{\partial\mathbf{r}^T}{\partial z}\right)}_{\boldsymbol{\psi}^T}\boldsymbol{\theta}\\ =& \delta\mathbf{r}^T\frac{\partial\boldsymbol{\theta}}{\partial z} - \delta\mathbf{r}^T\mathbf{T}_r^t\boldsymbol{\theta} + \delta\boldsymbol{\psi}^T\boldsymbol{\theta}\end{aligned}$$

The expression for the external virtual work is then given as

$$\delta\frac{\partial W_e}{\partial z} = \delta\mathbf{r}^T\frac{\partial\boldsymbol{\theta}}{\partial z} - \delta\mathbf{r}^T\mathbf{T}_r^T\boldsymbol{\theta} + \delta\boldsymbol{\psi}^T\boldsymbol{\theta}$$

$$+\delta\frac{\partial \mathbf{u}^T}{\partial z}\int_A \mathbf{N}^T\mathbf{p}\ \mathrm{dA}+\delta\mathbf{u}^T\int_A \mathbf{N}^T\frac{\partial \mathbf{p}^T}{\partial z}\ \mathrm{dA}$$

which in matrix form read as

$$\delta\frac{\partial W_e}{\partial z}=\begin{bmatrix}\delta\frac{\partial \mathbf{u}^T}{\partial z}\\ \delta\mathbf{u}\\ \delta\boldsymbol{\psi}\end{bmatrix}^T\begin{bmatrix}\mathbf{P}\\ \frac{\partial \mathbf{P}}{\partial z}\\ \boldsymbol{\theta}\end{bmatrix}+\delta\mathbf{r}^T\left(\frac{\partial\boldsymbol{\theta}}{\partial z}-\mathbf{T}_r^T\boldsymbol{\theta}\right) \tag{2.15}$$

where

$$\mathbf{P}=\int_A \mathbf{N}^T\mathbf{p}\ \mathrm{dA}$$
$$\frac{\partial \mathbf{P}}{\partial z}=\int_A \mathbf{N}^T\frac{\partial \mathbf{p}'^T}{\partial z}\ \mathrm{dA}$$

The vector $\mathbf{P}$ can be seen as the nodal stresses in the cross section finite element discretization as it represents the discretized stresses acting on the cross section face.

Internal virtual work

The internal work or the work done by the elastic strain energy per unit length can be written as

$$\delta\frac{\partial W_i}{\partial z}=\int_A \delta\boldsymbol{\epsilon}^T\boldsymbol{\sigma}\ \mathrm{dA} \tag{2.16}$$

Observing the stress-strain relation in Equation (2.1), the internal work expression in (2.16) can be restated as

$$\delta\frac{\partial W_i}{\partial z}=\int_A \delta\boldsymbol{\epsilon}^T\mathbf{Q}\boldsymbol{\epsilon}\ \mathrm{dA}$$

Inserting the expression for the strain-displacement relation in (2.13) in the equation above yields

$$\begin{aligned}\delta\frac{\partial W_i}{\partial z}&=\int_A\left(\delta\boldsymbol{\psi}^T\mathbf{Z}^T\mathbf{S}^T+\delta\mathbf{u}^T\mathbf{N}^T\mathbf{B}^T+\delta\frac{\partial \mathbf{u}^T}{\partial z}\mathbf{N}^T\mathbf{S}^T\right)\mathbf{Q}\\ &\quad\left(\mathbf{SZ}\boldsymbol{\psi}+\mathbf{BNu}+\mathbf{SN}\frac{\partial \mathbf{u}}{\partial z}\right)\ \mathrm{dA}\\ &=\int_A \delta\boldsymbol{\psi}^T\mathbf{Z}^T\mathbf{S}^T\mathbf{QSZ}\boldsymbol{\psi}\ \mathrm{dA}\\ &\quad+\int_A \delta\boldsymbol{\psi}^T\mathbf{Z}^T\mathbf{S}^T\mathbf{QBNu}\ \mathrm{dA}\\ &\quad+\int_A \delta\boldsymbol{\psi}^T\mathbf{Z}^T\mathbf{S}^T\mathbf{QSN}\frac{\partial \mathbf{u}}{\partial z}\ \mathrm{dA}\\ &\quad+\int_A \delta\mathbf{u}^T\mathbf{N}^T\mathbf{B}^T\mathbf{QSZ}\boldsymbol{\psi}\ \mathrm{dA}\\ &\quad+\int_A \delta\mathbf{u}^T\mathbf{N}^T\mathbf{B}^T\mathbf{QBNu}\ \mathrm{dA}\\ &\quad+\int_A \delta\mathbf{u}^T\mathbf{N}^T\mathbf{B}^T\mathbf{QSN}\frac{\partial \mathbf{u}}{\partial z}\ \mathrm{dA}\\ &\quad+\int_A \delta\frac{\partial \mathbf{u}'^T}{\partial z}\mathbf{N}^T\mathbf{S}^T\mathbf{QSZ}\boldsymbol{\psi}\ \mathrm{dA}\end{aligned}$$

$$+\int_A \delta\frac{\partial \mathbf{u}^T}{\partial z}\mathbf{N}^T\mathbf{S}^T\mathbf{QBNu}\ \mathrm{dA}$$
$$+\int_A \delta\frac{\partial \mathbf{u}^T}{\partial z}\mathbf{N}^T\mathbf{S}^T\mathbf{QSN}\frac{\partial \mathbf{u}}{\partial z}\ \mathrm{dA}$$

where the following matrices can be identified

$$\begin{aligned}
\mathbf{A} &= \int_A \mathbf{Z}^T\mathbf{S}^T\mathbf{QSZ}\ \mathrm{dA}\\
\mathbf{R} &= \int_A \mathbf{N}^T\mathbf{B}^T\mathbf{QSZ}\ \mathrm{dA}\\
\mathbf{E} &= \int_A \mathbf{N}^T\mathbf{B}^T\mathbf{QBN}\ \mathrm{dA}\\
\mathbf{C} &= \int_A \mathbf{N}^T\mathbf{S}^T\mathbf{QBN}\ \mathrm{dA}\\
\mathbf{L} &= \int_A \mathbf{N}^T\mathbf{S}^T\mathbf{QSZ}\ \mathrm{dA}\\
\mathbf{M} &= \int_A \mathbf{N}^T\mathbf{S}^T\mathbf{QSN}\ \mathrm{dA}
\end{aligned} \tag{2.17}$$

Hence, rearranging the state variables it is possible to write the internal virtual work in matrix form as

$$\delta\frac{\partial W_i}{\partial z} = \begin{bmatrix} \delta\frac{\partial \mathbf{u}}{\partial z} \\ \delta\mathbf{u} \\ \delta\boldsymbol{\psi} \end{bmatrix}^T \begin{bmatrix} \mathbf{M} & \mathbf{C} & \mathbf{L} \\ \mathbf{C}^T & \mathbf{E} & \mathbf{R} \\ \mathbf{L}^T & \mathbf{R}^T & \mathbf{A} \end{bmatrix} \begin{bmatrix} \frac{\partial \mathbf{u}}{\partial z} \\ \mathbf{u} \\ \boldsymbol{\psi} \end{bmatrix} \tag{2.18}$$

Total virtual work

According to Equation (2.14) the total virtual work per unit length can be written as

$$\delta\frac{\partial W}{\partial z} = \delta\frac{\partial W_e}{\partial z} - \delta\frac{\partial W_i}{\partial z} = \int_A \frac{\partial\left(\delta\mathbf{s}'^T\mathbf{p}\right)}{\partial z}\ \mathrm{dA} - \int_A \delta\boldsymbol{\epsilon}^T\boldsymbol{\sigma}\ \mathrm{dA} \tag{2.19}$$

For a general virtual displacement $\delta\mathbf{s}$ and virtual strain $\delta\boldsymbol{\epsilon}$, a necessary and sufficient equilibrium condition is

$$\delta\frac{\partial W}{\partial z} = 0$$

Thus, inserting Equation (2.15) and (2.18) into (2.19) the following relation is obtained

$$\underbrace{\begin{bmatrix} \delta\frac{\partial \mathbf{u}}{\partial z} \\ \delta\mathbf{u} \\ \delta\boldsymbol{\psi} \end{bmatrix}^T \begin{bmatrix} \mathbf{M} & \mathbf{C} & \mathbf{L} \\ \mathbf{C}^T & \mathbf{E} & \mathbf{R} \\ \mathbf{L}^T & \mathbf{R}^T & \mathbf{A} \end{bmatrix} \begin{bmatrix} \frac{\partial \mathbf{u}}{\partial z} \\ \mathbf{u} \\ \boldsymbol{\psi} \end{bmatrix}}_{\text{Internal virtual work of the beam slice}} =$$
$$= \underbrace{\begin{bmatrix} \delta\frac{\partial \mathbf{u}}{\partial z} \\ \delta\mathbf{u} \\ \delta\boldsymbol{\psi} \end{bmatrix}^T \begin{bmatrix} \mathbf{P} \\ \frac{\partial \mathbf{P}}{\partial z} \\ \boldsymbol{\theta} \end{bmatrix}}_{\text{External virtual work of the beam slice}}$$
$$+ \underbrace{\delta\mathbf{r}^T\left(\frac{\partial \boldsymbol{\theta}}{\partial z} - \mathbf{T}_r^T\boldsymbol{\theta}\right)}_{\text{Equilibrium of the beam slice}}$$

The previous equation must be true for any admissible virtual displacement $\delta\boldsymbol{\psi}$, $\delta\mathbf{u}$, $\delta\frac{\partial\mathbf{u}^T}{\partial z}$ and $\delta\mathbf{r}$, thus leading to the following set of equations

$$\begin{aligned}\mathbf{M}\frac{\partial\mathbf{u}}{\partial z}+\mathbf{C}^T\mathbf{u}+\mathbf{L}\boldsymbol{\psi}&=\mathbf{P}\\ \mathbf{C}\frac{\partial\mathbf{u}}{\partial z}+\mathbf{E}\mathbf{u}+\mathbf{R}\boldsymbol{\psi}&=\frac{\partial\mathbf{P}}{\partial z}\\ \mathbf{L}^T\frac{\partial\mathbf{u}}{\partial z}+\mathbf{R}^T\mathbf{u}+\mathbf{A}\boldsymbol{\psi}&=\boldsymbol{\theta}\\ \frac{\partial\boldsymbol{\theta}}{\partial z}&=\mathbf{T}_r^T\boldsymbol{\theta}\end{aligned}$$

It is possible to further simplify the former by differentiating the first equation with respect to z

$$\begin{aligned}\mathbf{M}\frac{\partial^2\mathbf{u}}{\partial z^2}+\mathbf{C}^T\frac{\partial\mathbf{u}}{\partial z}+\mathbf{L}\frac{\partial\boldsymbol{\psi}}{\partial z}&=\frac{\partial\mathbf{P}}{\partial z}\\ \mathbf{C}\frac{\partial\mathbf{u}}{\partial z}+\mathbf{E}\mathbf{u}+\mathbf{R}\boldsymbol{\psi}&=\frac{\partial\mathbf{P}}{\partial z}\\ \mathbf{L}^T\frac{\partial\mathbf{u}}{\partial z}+\mathbf{R}^T\mathbf{u}+\mathbf{A}\boldsymbol{\psi}&=\boldsymbol{\theta}\\ \frac{\partial\boldsymbol{\theta}}{\partial z}&=\mathbf{T}_r^T\boldsymbol{\theta}\end{aligned}$$

and obtain the equilibrium equations for the cross section

$$\begin{aligned}\mathbf{M}\frac{\partial^2\mathbf{u}}{\partial z^2}+\left(\mathbf{C}-\mathbf{C}^T\right)\frac{\partial\mathbf{u}}{\partial z}+\mathbf{L}\frac{\partial\boldsymbol{\psi}}{\partial z}-\mathbf{E}\mathbf{u}-\mathbf{R}\boldsymbol{\psi}&=\mathbf{0}\\ \mathbf{L}^T\frac{\partial\mathbf{u}}{\partial z}+\mathbf{R}^T\mathbf{u}+\mathbf{A}\boldsymbol{\psi}&=\boldsymbol{\theta}\\ \frac{\partial\boldsymbol{\theta}}{\partial z}&=\mathbf{T}_r^T\boldsymbol{\theta}\end{aligned}\tag{2.20}$$

This concludes the derivation of the equilibrium equations of the cross section.

2.3 Solutions to equilibrium equations

The set of equations in (2.20) admits two types of solutions – a particular integral which depends on the boundary conditions, or the internal force resultants $\boldsymbol{\theta}$ in this case, and a homogeneous integral which corresponds to the eigensolutions when $\boldsymbol{\theta}=0$. The particular and homogeneous solutions will be henceforth referred to as the *extremity* and the *central* solutions (cf. Giavotto et al. [6]), respectively. A more detailed discussion on this topic is presented in Section 2.4.

2.3.1 Extremity solutions

The extremitiy solutions owe their name to the fact that they correspond to the solutions at the extremities of the beam where the loads are applied. These are the self-balanced, $\boldsymbol{\theta}=0$, eigensolutions of (2.20), that is, the solutions to the following set

$$\begin{aligned}\mathbf{M}\frac{\partial^2\mathbf{u}}{\partial z^2}+\left(\mathbf{C}-\mathbf{C}^T\right)\frac{\partial\mathbf{u}}{\partial z}+\mathbf{L}\frac{\partial\boldsymbol{\psi}}{\partial z}-\mathbf{E}\mathbf{u}-\mathbf{R}\boldsymbol{\psi}&=0\\ \mathbf{L}^T\frac{\partial\mathbf{u}}{\partial z}+\mathbf{R}^T\mathbf{u}+\mathbf{A}\boldsymbol{\psi}&=0\end{aligned}$$

or in matrix form

$$\begin{bmatrix} \mathbf{M} & 0 \\ 0 & 0 \end{bmatrix} \begin{bmatrix} \frac{\partial^2 \mathbf{u}}{\partial z^2} \\ \frac{\partial^2 \boldsymbol{\psi}}{\partial z^2} \end{bmatrix} + \begin{bmatrix} \left(\mathbf{C} - \mathbf{C}^T\right) & \mathbf{L} \\ -\mathbf{L}^T & 0 \end{bmatrix} \begin{bmatrix} \frac{\partial \mathbf{u}}{\partial z} \\ \frac{\partial \boldsymbol{\psi}}{\partial z} \end{bmatrix} - \begin{bmatrix} \mathbf{E} & \mathbf{R} \\ \mathbf{R}^T & \mathbf{A} \end{bmatrix} \begin{bmatrix} \mathbf{u} \\ \boldsymbol{\psi} \end{bmatrix} = \begin{bmatrix} \mathbf{0} \\ \mathbf{0} \end{bmatrix} \tag{2.21}$$

Assuming solutions of the type

$$\mathbf{u} = \tilde{\mathbf{u}} e^{\lambda z}$$
$$\boldsymbol{\psi} = \tilde{\boldsymbol{\psi}} e^{\lambda z}$$

and introducing the previous equation in (2.21) yields

$$\left(\lambda^2 \begin{bmatrix} \mathbf{M} & 0 \\ 0 & 0 \end{bmatrix} + \lambda \begin{bmatrix} \left(\mathbf{C} - \mathbf{C}^T\right) & \mathbf{L} \\ -\mathbf{L}^T & 0 \end{bmatrix} - \begin{bmatrix} \mathbf{E} & \mathbf{R} \\ \mathbf{R}^T & \mathbf{A} \end{bmatrix} \right) \begin{bmatrix} \tilde{\mathbf{u}} \\ \tilde{\boldsymbol{\psi}} \end{bmatrix} = \mathbf{0}$$

The solution to (2.21) can be stated in terms of a linear combination of the solutions to the eigenvalue problem

$$\lambda^2 \begin{bmatrix} \mathbf{M} & 0 \\ 0 & 0 \end{bmatrix} + \lambda \begin{bmatrix} \left(\mathbf{C} - \mathbf{C}^T\right) & \mathbf{L} \\ -\mathbf{L}^T & 0 \end{bmatrix} - \begin{bmatrix} \mathbf{E} & \mathbf{R} \\ \mathbf{R}^T & \mathbf{A} \end{bmatrix} = 0$$

where λ are the eigenvalues and $\tilde{\mathbf{u}}$ and $\tilde{\boldsymbol{\psi}}$ the corresponding eigenvectors. The eigenvectors represent the extremity modes and the corresponding eigenvalues define a diffusion length. The lowest eigenvalues are the most interesting as they propagate farther into the beam. Choosing the eigenvectors corresponding to the lowest eigenvalues it should be possible to study the effect of the loads at the extremities of the beam. Nonetheless, the solution to this eigenvalue problem may be cumbersome as the size of the matrices becomes larger.

2.3.2 Central solutions

The central solution refer to the solutions obtained at the central part of the beam corresponding to non-zero stress resultants ($\boldsymbol{\theta} \neq 0$). For convenience, let us rewrite the equilibrium equations in (2.20) so that all the terms with derivatives of the same order are grouped

$$\begin{cases} \mathbf{E}\mathbf{u} + \mathbf{R}\boldsymbol{\psi} = \left(\mathbf{C} - \mathbf{C}^T\right) \frac{\partial \mathbf{u}}{\partial z} + \mathbf{L} \frac{\partial \boldsymbol{\psi}}{\partial z} + \mathbf{M} \frac{\partial^2 \mathbf{u}}{\partial z^2} \\ \mathbf{R}^T \mathbf{u} + \mathbf{A}\boldsymbol{\psi} = -\mathbf{L}^T \frac{\partial \mathbf{u}}{\partial z} + \boldsymbol{\theta} \end{cases} \tag{2.22}$$

At this point the reader may opt to read Section 2.4 first to get an insight into the mathematical properties of the central solutions. Otherwise the necessary results to retain are that the central solutions $\mathbf{u}_c$ and $\boldsymbol{\psi}_c$ are linear combinations of polynomial functions in z with n being the highest degree of such polynomials (see Equation (2.34) in Section 2.4.2). Thus

$$\frac{\partial^n \mathbf{u}_c}{\partial z^n} = 0 \text{ and } \frac{\partial^n \boldsymbol{\psi}_c}{\partial z^n} = 0$$

Furthermore, from the equilibrium equations for a rigid cross section (see Equation (2.30) in Section 2.4.1) the following must hold

$$\frac{\partial^2 \boldsymbol{\theta}}{\partial z^2} = 0 \tag{2.23}$$

and, recall from the equilibrium equations in (2.20) that

$$\frac{\partial \boldsymbol{\theta}}{\partial z} = \mathbf{T}_r^T \boldsymbol{\theta} \tag{2.24}$$

We shall now utilize each of the results above to find an expression for the central solutions based on the set (2.22).

Let us consider the following sets which are obtained from the evaluation of the n^{th} order derivative of set (2.22)

$$
(0)\begin{cases}\mathbf{E}\mathbf{u}+\mathbf{R}\boldsymbol{\psi}=\left(\mathbf{C}-\mathbf{C}^T\right)\frac{\partial\mathbf{u}}{\partial z}+\mathbf{L}\frac{\partial\boldsymbol{\psi}}{\partial z}+\mathbf{M}\underbrace{\frac{\partial^2\mathbf{u}}{\partial z^2}}_{=0}\\ \mathbf{R}^T\mathbf{u}+\mathbf{A}\boldsymbol{\psi}=-\mathbf{L}^T\frac{\partial\mathbf{u}}{\partial z}+\boldsymbol{\theta}\end{cases}
$$

$$
\uparrow \quad \partial\mathbf{u}/\partial z\neq 0 \text{ and } \partial\boldsymbol{\psi}/\partial z\neq 0
$$

$$
(1)\begin{cases}\mathbf{E}\frac{\partial\mathbf{u}}{\partial z}+\mathbf{R}\frac{\partial\boldsymbol{\psi}}{\partial z}=\left(\mathbf{C}-\mathbf{C}^T\right)\underbrace{\frac{\partial^2\mathbf{u}}{\partial z^2}}_{=0}+\mathbf{L}\underbrace{\frac{\partial^2\boldsymbol{\psi}}{\partial z^2}}_{=0}+\mathbf{M}\underbrace{\frac{\partial^3\mathbf{u}}{\partial z^3}}_{=0}\\ \mathbf{R}^T\frac{\partial\mathbf{u}}{\partial z}+\mathbf{A}\frac{\partial\boldsymbol{\psi}}{\partial z}=-\mathbf{L}^T\underbrace{\frac{\partial^2\mathbf{u}}{\partial z^2}}_{=0}+\underbrace{\frac{\partial\boldsymbol{\theta}}{\partial z}}_{\neq 0 \text{ from (2.24)}}\end{cases}
$$

$$
\uparrow \quad \partial^2\mathbf{u}/\partial z^2=0 \text{ and } \partial^2\boldsymbol{\psi}/\partial z^2=0
$$

$$
(2)\begin{cases}\mathbf{E}\frac{\partial^2\mathbf{u}}{\partial z^2}+\mathbf{R}\frac{\partial^2\boldsymbol{\psi}}{\partial z^2}=\left(\mathbf{C}-\mathbf{C}^T\right)\underbrace{\frac{\partial^3\mathbf{u}}{\partial z^3}}_{=0}+\mathbf{L}\underbrace{\frac{\partial^3\boldsymbol{\psi}}{\partial z^3}}_{=0}+\mathbf{M}\underbrace{\frac{\partial^4\mathbf{u}}{\partial z^4}}_{0}\\ \mathbf{R}^T\frac{\partial^2\mathbf{u}}{\partial z^2}+\mathbf{A}\frac{\partial^2\boldsymbol{\psi}}{\partial z^2}=-\mathbf{L}^T\underbrace{\frac{\partial^3\mathbf{u}}{\partial z^3}}_{=0}+\underbrace{\frac{\partial^2\boldsymbol{\theta}}{\partial z^2}}_{=0 \text{ from (2.23)}}\end{cases}
$$

$$
\uparrow \quad \partial^3\mathbf{u}/\partial z^3=0 \text{ and } \partial^3\boldsymbol{\psi}/\partial z^3=0
$$

$$
\vdots
$$

$$
\uparrow \quad \partial^{(n-1)}\mathbf{u}/\partial z^{(n-1)}=0 \text{ and } \partial^{(n-1)}\boldsymbol{\psi}/\partial z^{(n-1)}=0
$$

$$
(n-1)\begin{cases}\mathbf{E}\frac{\partial^{(n-1)}\mathbf{u}}{\partial z^{(n-1)}}+\mathbf{R}\frac{\partial^{(n-1)}\boldsymbol{\psi}}{\partial z^{(n-1)}}=\left(\mathbf{C}-\mathbf{C}^T\right)\underbrace{\frac{\partial^{(n)}\mathbf{u}}{\partial z^{(n)}}}_{=0}+\mathbf{L}\underbrace{\frac{\partial^{(n)}\boldsymbol{\psi}}{\partial z^{(n)}}}_{=0}\\ \mathbf{R}^T\frac{\partial^{(n-1)}\mathbf{u}}{\partial z^{(n-1)}}+\mathbf{A}\frac{\partial^{(n-1)}\boldsymbol{\psi}}{\partial z^{(n-1)}}=-\mathbf{L}^T\underbrace{\frac{\partial^{(n)}\mathbf{u}}{\partial z^{(n)}}}_{=0}\end{cases}
$$

$$
\uparrow \quad \partial^{(n)}\mathbf{u}/\partial z^{(n)}=0 \text{ and } \partial^{(n)}\boldsymbol{\psi}/\partial z^{(n)}=0
$$

$$
(n)\begin{cases}\mathbf{E}\frac{\partial^{(n)}\mathbf{u}}{\partial z^{(n)}}+\mathbf{R}\frac{\partial^{(n)}\boldsymbol{\psi}}{\partial z^{(n)}}=0\\ \mathbf{R}^T\frac{\partial^{(n)}\mathbf{u}}{\partial z^{(n)}}+\mathbf{A}\frac{\partial^{(n)}\boldsymbol{\psi}}{\partial z^{(n)}}=0\end{cases}
$$

The analysis of the former sets will be done from bottom to top. The last set, set (n), corresponds to the n^{th} order derivative of the equilibrium equations in set (2.22). It is a linear homogeneous system of equations with unknowns $\partial^{(n)}\mathbf{u}/\partial z^{(n)}$ and $\partial^{(n)}\boldsymbol{\psi}/\partial z^{(n)}$ whose solutions are $\partial^{(n)}\mathbf{u}/\partial z^{(n)}=0$ and $\partial^{(n)}\boldsymbol{\psi}/\partial z^{(n)}=0$. These result can now be replaced in set (n-1). Hence, for set (n-1), it is possible to see that $\partial^{(n-1)}\mathbf{u}/\partial z^{(n-1)}=0$ and $\partial^{(n-1)}\boldsymbol{\psi}/\partial z^{(n-1)}=0$ also and so on up to set (1). In set (1) the derivative of the surface stresses $\partial\boldsymbol{\theta}/\partial z\neq 0$ and thus $\partial\mathbf{u}/\partial z\neq 0$ and $\partial\boldsymbol{\psi}/\partial z\neq 0$ as well. It is therefore demonstrated that the displacements $\mathbf{u}$ and strain parameters $\boldsymbol{\psi}$ are at most linear functions of z. The displacements are obtained from the solution to the following

sets

$$\boxed{\begin{array}{l} \left\{ \begin{array}{l} \mathbf{E}\frac{\partial \mathbf{u}}{\partial z} + \mathbf{R}\frac{\partial \boldsymbol{\psi}}{\partial z} = 0 \\ \mathbf{R}^T\frac{\partial \mathbf{u}}{\partial z} + \mathbf{A}\frac{\partial \boldsymbol{\psi}}{\partial z} = \frac{\partial \boldsymbol{\theta}}{\partial z} \end{array} \right. \\ \left\{ \begin{array}{l} \mathbf{E}\mathbf{u} + \mathbf{R}\boldsymbol{\psi} = \left(\mathbf{C} - \mathbf{C}^T\right)\frac{\partial \mathbf{u}}{\partial z} + \mathbf{L}\frac{\partial \boldsymbol{\psi}}{\partial z} \\ \mathbf{R}^T\mathbf{u} + \mathbf{A}\boldsymbol{\psi} = -\mathbf{L}^T\frac{\partial \mathbf{u}}{\partial z} + \boldsymbol{\theta} \end{array} \right. \end{array}} \tag{2.25}$$

where, from Equation (2.20),

$$\frac{\partial \boldsymbol{\theta}}{\partial z} = \mathbf{T}_r^T\boldsymbol{\theta}$$

The set first set in equation (2.25) is solved first to obtain $\partial\mathbf{u}/\partial z$ and $\partial\boldsymbol{\psi}/\partial z$ for a given $\boldsymbol{\theta}$. It is then possible to evaluate the right hand side of the second set and thus obtain $\mathbf{u}$ and $\boldsymbol{\psi}$. Note that the same coefficient matrix is used twice in the solution and it is therefore possible to decrease the solution time using a proper matrix factorization.

2.3.3 Constraint equations

The displacement formulation as described in (2.12) is six times redundant. Each of the redundances corresponds to a description of each of the rigid body motions and translations by the warping displacements $\mathbf{u}$. It is therefore necessary to ensure that the warping displacement $\mathbf{u}$ is uncoupled from the rigid displacements $\mathbf{r}$. The following set of constraints are therefore incorporated into the solution of the sets (2.25)

$$\left\langle \begin{bmatrix} 1 & 0 & 0 \\ 0 & 1 & 0 \\ 0 & 0 & 1 \end{bmatrix} \begin{bmatrix} u_x \\ u_y \\ u_z \end{bmatrix} \right\rangle = 0$$

$$\left\langle \begin{bmatrix} 0 & -z & y \\ z & 0 & -x \\ -y & x & 0 \end{bmatrix} \begin{bmatrix} u_x \\ u_y \\ u_z \end{bmatrix} \right\rangle = 0$$

where $\langle\cdot\rangle$ denotes integration over the reference cross section. The implication of the first equations is that warping does not contribute to the rigid-body displacement of the cross section. The remaining equations imply that the rotation variables are the average rotations of the cross section.

In practice the constraints are assembled in matrix $\mathbf{D}$

$$\mathbf{D} = \begin{bmatrix} 1 & 0 & 0 & & 1 & 0 & 0 \\ 0 & 1 & 0 & & 0 & 1 & 0 \\ 0 & 0 & 1 & \cdots & 0 & 0 & 1 \\ 0 & 0 & y_1 & & 0 & 0 & y_{n_n} \\ 0 & 0 & -x_1 & & 0 & 0 & -x_{n_n} \\ -y_1 & x_1 & 0 & & -y_{n_n} & x_{n_n} & 0 \end{bmatrix} \tag{2.26}$$

where n_n is the number of nodes in the cross section finite element mesh. Matrix $\mathbf{D}$ is appended to the set of equilibrium equations in (2.25) to ensure the existence of a solution.

2.4 On the properties of the solutions

Some results used earlier in this manuscript to justify some of the steps in the derivation of the cross section stiffness matrix of beams are described in this section. In particular, (2.30) and (2.34) are an important result in establishing the equilibrium equations for the

central solutions in Section 2.3.2. The reader may skip this section altogether if only a general overview of the method is necessary.

The section is divided in two parts. In the first part it is assumed that only the rigid body translations and rotations contribute to the displacement vector of a point in the cross section, i.e., the cross section deformation is not accounted for. The equilibrium equations are derived and it is possible to show that the force and moment resultants $\boldsymbol{\theta}$ vary linearly with respect to z or along the beam length.

In the second part the displacement of a point in the cross section is obtained through a finite element discretization of the warping displacements. The equilibrium equations are derived once again. The result is a second order homogeneous linear differential equation. The different types of solutions are identified according to Saint Venant's principle. The solutions for which the eigenvalues are different from zero will decay as z either increases or decreases. These are self-balanced ($\boldsymbol{\theta} = 0$) solutions corresponding to the modes at the extremities of the beam where the loads are applied – the *extremity* solutions. On the other hand, the solutions for which the eigenvalues are zero will not present any decay and, most importantly, it is possible to show that these will be polynomials in z. These correspond to non-zero stress resultants and account for the displacements at a section of the beam sufficiently far from the extremities so that the influence of the external forces in the stress field is negligible – the so-called *central* solutions.

2.4.1 Rigid motions

In this section we look only at the displacements $\mathbf{v}$ which do not strain the section, that is, we do not include the warping displacements. Thus

$$\mathbf{s} = \mathbf{v} = \mathbf{Z}\mathbf{r} = \boldsymbol{\chi} + \mathbf{n}\boldsymbol{\varphi} = \begin{bmatrix} \chi_x - y\varphi_z \\ \chi_y + x\varphi_z \\ \chi_z + y\varphi_x - x\varphi_y \end{bmatrix} \tag{2.27}$$

recalling that $\boldsymbol{\chi} = \boldsymbol{\chi}(z)$ and $\boldsymbol{\varphi} = \boldsymbol{\varphi}(z)$ correspond to the translation of the cross section reference point and rotations, respectively. The three dimensional strain components in this case are given by

$$\begin{aligned}
\epsilon_{xx} &= \frac{1}{2}\left(\frac{\partial v_x}{x} + \frac{\partial v_x}{x}\right) = 0 \\
\epsilon_{yy} &= \frac{1}{2}\left(\frac{\partial v_y}{y} + \frac{\partial v_y}{y}\right) = 0 \\
2\epsilon_{xy} &= \frac{1}{2}\left(\frac{\partial v_y}{x} + \frac{\partial v_x}{y}\right) = 0 \\
2\epsilon_{xz} &= \left(\frac{\partial v_z}{x} + \frac{\partial v_x}{z}\right) = -\varphi_y + \frac{\partial \chi_x}{\partial z} - y\frac{\partial \varphi_z}{\partial z} \\
2\epsilon_{yz} &= \left(\frac{\partial v_y}{z} + \frac{\partial v_z}{y}\right) = \frac{\partial \chi_y}{\partial z} + x\frac{\partial \varphi_z}{\partial z} + \varphi_x \\
\epsilon_{zz} &= \frac{1}{2}\left(\frac{\partial v_z}{z} + \frac{\partial v_z}{z}\right) = \frac{\partial \chi_z}{\partial z} + y\frac{\partial \varphi_x}{\partial z} - x\frac{\partial \varphi_y}{\partial z}
\end{aligned}$$

In matrix form the previous equations can be reduced to

$$\mathbf{p} = \mathbf{t}\boldsymbol{\varphi} + \frac{\partial \boldsymbol{\chi}}{\partial z} + \mathbf{n}\frac{\partial \boldsymbol{\varphi}}{\partial z}$$

where

$$\mathbf{t} = \begin{bmatrix} 0 & -1 & 0 \\ 1 & 0 & 0 \\ 0 & 0 & 0 \end{bmatrix}$$

It is convenient at this point to introduce the vector of strain parameters $\boldsymbol{\psi} = [\tau_x,\ \tau_y,\ \tau_z,\ \kappa_x,\ \kappa_y,\ \kappa_z]^T$ defined in (2.9) and restated here as

$$\boldsymbol{\psi} = \begin{bmatrix} \frac{\partial \boldsymbol{\chi}}{\partial z} + \mathbf{t}\boldsymbol{\varphi} \\ \frac{\partial \boldsymbol{\varphi}}{\partial z} \end{bmatrix}$$

The three dimensional strain are hence

$$\boldsymbol{\epsilon} = \mathbf{S}\mathbf{Z}\boldsymbol{\psi} \tag{2.28}$$

Recalling the expression for the total work has been defined as

$$\delta\frac{\partial W}{\partial z} = \int_A \frac{\partial\left(\mathbf{p}^T\delta\mathbf{v}\right)}{\partial z}\,\mathrm{dA} - \int_A \boldsymbol{\sigma}^T\delta\boldsymbol{\epsilon}\,\mathrm{dA} = 0 \tag{2.29}$$

where the displacement $\mathbf{s}$ in (2.19) has been simply replaced here by $\mathbf{v}$. Replacing (2.27) and (2.28) in (2.29) yields

$$\begin{aligned}
\delta\frac{\partial W}{\partial z} =& \int_A \frac{\partial\left(\mathbf{p}'^T\delta\boldsymbol{\chi} + \mathbf{p}'^T\mathbf{n}\delta\boldsymbol{\varphi}\right)}{\partial z}\,\mathrm{dA} - \int_A \boldsymbol{\sigma}^T\mathbf{S}\mathbf{Z}\delta\boldsymbol{\psi}\,\mathrm{dA} \\
=& \int_A \frac{\partial\mathbf{p}'^T\delta\boldsymbol{\chi}}{\partial z}\,\mathrm{dA} + \int_A \frac{\mathbf{p}'^T\mathbf{n}\delta\boldsymbol{\varphi}}{\partial z}\,\mathrm{dA} - \int_A \boldsymbol{\sigma}^T\mathbf{S}\mathbf{Z}\delta\boldsymbol{\psi}\,\mathrm{dA} \\
=& \int_A \frac{\partial\mathbf{p}^T}{\partial z}\delta\boldsymbol{\chi}\,\mathrm{dA} + \int_A \mathbf{p}^T\frac{\partial\delta\boldsymbol{\chi}}{\partial z}\,\mathrm{dA} + \int_A \frac{\mathbf{p}^T}{\partial z}\mathbf{n}\delta\boldsymbol{\varphi}\,\mathrm{dA} + \int_A \mathbf{p}^T\mathbf{n}\frac{\delta\boldsymbol{\varphi}}{\partial z}\,\mathrm{dA} \\
& - \int_A \boldsymbol{\sigma}^T\mathbf{S}\mathbf{Z}\delta\boldsymbol{\psi}\,\mathrm{dA} \\
=& \underbrace{\int_A \frac{\partial\mathbf{p}'^T}{\partial z}\,\mathrm{dA}}_{\partial\mathbf{T}/\partial z}\delta\boldsymbol{\chi} + \underbrace{\int_A \mathbf{p}^T\,\mathrm{dA}}_{\mathbf{T}}\frac{\partial\delta\boldsymbol{\chi}}{\partial z} + \underbrace{\int_A \frac{\mathbf{p}'^T}{\partial z}\mathbf{n}\,\mathrm{dA}}_{\partial\mathbf{M}/\partial z}\delta\boldsymbol{\varphi} + \underbrace{\int_A \mathbf{p}^T\mathbf{n}\,\mathrm{dA}}_{\mathbf{M}}\frac{\delta\boldsymbol{\varphi}}{\partial z} \\
& - \int_A \boldsymbol{\sigma}^T\mathbf{S}\mathbf{Z}\delta\boldsymbol{\psi}\,\mathrm{dA} \\
=& \frac{\partial\mathbf{T}^T}{\partial z}\delta\boldsymbol{\chi} + \mathbf{T}^T\frac{\partial\delta\boldsymbol{\chi}}{\partial z} + \frac{\partial\mathbf{M}^T}{\partial z}\delta\boldsymbol{\varphi} + \mathbf{M}^T\frac{\delta\boldsymbol{\varphi}}{\partial z} - \int_A \boldsymbol{\sigma}^T\mathbf{S}\mathbf{Z}\delta\boldsymbol{\psi}\,\mathrm{dA}
\end{aligned}$$

Noting that

$$\boldsymbol{\theta}^T\boldsymbol{\psi} = \mathbf{T}^T\frac{\partial\boldsymbol{\chi}}{\partial z} - \mathbf{T}^T\mathbf{t}\boldsymbol{\varphi} + \mathbf{M}^T\frac{\partial\boldsymbol{\varphi}}{\partial z}$$

it is possible to further simplify in the following manner

$$\begin{aligned}
\delta\frac{\partial W}{\partial z} =& \frac{\partial\mathbf{T}^T}{\partial z}\delta\boldsymbol{\chi} + \mathbf{T}^T\frac{\partial\delta\boldsymbol{\chi}}{\partial z} + \frac{\partial\mathbf{M}^T}{\partial z}\delta\boldsymbol{\varphi} + \mathbf{M}^T\frac{\delta\boldsymbol{\varphi}}{\partial z} - \int_A \boldsymbol{\sigma}^T\mathbf{S}\mathbf{Z}\delta\boldsymbol{\psi}\,\mathrm{dA} \\
=& \frac{\partial\mathbf{T}^T}{\partial z}\delta\boldsymbol{\chi} + \mathbf{T}^T\frac{\partial\delta\boldsymbol{\chi}}{\partial z} + \frac{\partial\mathbf{M}^T}{\partial z}\delta\boldsymbol{\varphi} + \mathbf{M}^T\frac{\delta\boldsymbol{\varphi}}{\partial z} \underbrace{-\mathbf{T}^T\mathbf{t}\delta\boldsymbol{\varphi} + \mathbf{T}^T\mathbf{t}\delta\boldsymbol{\varphi}}_{\text{for convenience}} - \int_A \boldsymbol{\sigma}^T\mathbf{S}\mathbf{Z}\delta\boldsymbol{\psi}\,\mathrm{dA} \\
=& \frac{\partial\mathbf{T}^T}{\partial z}\delta\boldsymbol{\chi} + \frac{\partial\mathbf{M}^T}{\partial z}\delta\boldsymbol{\varphi} + \mathbf{T}^T\mathbf{t}\delta\boldsymbol{\varphi} + \underbrace{\mathbf{T}^T\frac{\partial\delta\boldsymbol{\chi}}{\partial z} + \mathbf{M}^T\frac{\delta\boldsymbol{\varphi}}{\partial z} - \mathbf{T}^T\mathbf{t}\delta\boldsymbol{\varphi}}_{\boldsymbol{\theta}^T\delta\boldsymbol{\psi}} - \int_A \boldsymbol{\sigma}^T\mathbf{S}\mathbf{Z}\delta\boldsymbol{\psi}\,\mathrm{dA} \\
=& \frac{\partial\mathbf{T}'^T}{\partial z}\delta\boldsymbol{\chi} + \left(\frac{\partial\mathbf{M}'^T}{\partial z} + \mathbf{T}^T\mathbf{t}\right)\delta\boldsymbol{\varphi} + \left(\boldsymbol{\theta}^T - \int_A \boldsymbol{\sigma}^T\mathbf{S}\mathbf{Z}\,\mathrm{dA}\right)\delta\boldsymbol{\psi}
\end{aligned}$$

and isolate each of the variation terms in the equation. Thus, for the arbitrary variation of $\delta\boldsymbol{\psi}$ we get

$$\boldsymbol{\theta} = \int_A \mathbf{Z}\mathbf{S}\boldsymbol{\sigma} \, \mathrm{dA}$$

where $\mathbf{p} = \mathbf{S}\boldsymbol{\sigma}$. The equation above is the definition of the resultant forces acting on the cross section as stated in (2.3). Subsequently, for the arbitrary variation of $\delta\boldsymbol{\varphi}$ and $\delta\boldsymbol{\chi}$ we obtain, respectively

$$\frac{\partial \mathbf{M}^T}{\partial z} = -\mathbf{T}^T\mathbf{t} \quad , \quad \frac{\partial \mathbf{T}^T}{\partial z} = 0$$

The two expressions above are the equilibrium equations or the one dimensional beam equations when only the cross section rigid displacements are considered. These equations are typically obtained from simple statitcs and so this result shows the consistency between the one and three dimensional approaches. Furthermore, based on the results above it is possible to conclude that

$$\frac{\partial^2 \mathbf{M}^T}{\partial z^2} = 0$$

and so

$$\frac{\partial^2 \boldsymbol{\theta}}{\partial z^2} = 0 \tag{2.30}$$

The equation above states that the resulting forces acting on the section vary linearly along the beam.

2.4.2 Warping displacements

In this section we assume that

$$\mathbf{s} = \mathbf{g}$$

The displacement of a point in the cross section is given here as a function of the cross section deformation only. Note however that this definition of the displacements entails also the representation of the rigid translation $\boldsymbol{\chi}$ and rotation $\boldsymbol{\varphi}$. This is in fact the underlying motivation for the use of constraint equations as described in Section 2.3.3 to uncouple the rigid body motions and cross section deformation.

The stress-strain relation in this case is given as

$$\boldsymbol{\epsilon} = \mathbf{B}\mathbf{g} + \mathbf{S}\frac{\partial \mathbf{g}}{\partial z}$$

and the expression for the variation of the total energy is

$$\delta\frac{\partial W}{\partial z} = \int_A \frac{\partial \left(\mathbf{p}^T\delta\mathbf{s}\right)}{\partial z} \, \mathrm{dA} - \int_A \boldsymbol{\sigma}^T\delta\boldsymbol{\epsilon} \, \mathrm{dA}$$

Recalling the generalized Hooke's law $\boldsymbol{\sigma} = \mathbf{Q}\boldsymbol{\epsilon}$ and noting that $\mathbf{p} = \mathbf{S}\boldsymbol{\sigma}$,the expression for the total virtual work of the beam cross section considering only the warping

displacements is given by

$$\begin{aligned}
\delta\frac{\partial W}{\partial z} &= \int_A \frac{\partial\left(\boldsymbol{\sigma}'^T\mathbf{S}\delta\mathbf{g}\right)}{\partial z}\,\mathrm{dA} - \int_A \boldsymbol{\sigma}^T\left(\mathbf{B}\delta\mathbf{g} + \mathbf{S}\frac{\partial\delta\mathbf{g}}{\partial z}\right)\,\mathrm{dA} \\
&= \int_A \frac{\partial\boldsymbol{\sigma}^T}{\partial z}\mathbf{S}\delta\mathbf{g}\,\mathrm{dA} + \int_A \boldsymbol{\sigma}^T\mathbf{S}\frac{\partial\delta\mathbf{g}}{\partial z}\,\mathrm{dA} \\
&\quad - \int_A \boldsymbol{\sigma}^T\mathbf{B}\delta\mathbf{g}\,\mathrm{dA} - \int_A \boldsymbol{\sigma}^T\mathbf{S}\frac{\partial\delta\mathbf{g}}{\partial z}\,\mathrm{dA} \\
&= \int_A \frac{\partial\boldsymbol{\sigma}^T}{\partial z}\mathbf{S}\delta\mathbf{g}\,\mathrm{dA} - \int_A \boldsymbol{\sigma}^T\mathbf{B}\delta\mathbf{g}\,\mathrm{dA} \\
&= \int_A \frac{\partial\boldsymbol{\epsilon}'^T}{\partial z}\mathbf{Q}\mathbf{S}\delta\mathbf{g}\,\mathrm{dA} - \int_A \boldsymbol{\epsilon}^T\mathbf{Q}\mathbf{B}\delta\mathbf{g}\,\mathrm{dA} \\
&= \int_A \frac{\partial\mathbf{g}'^T}{\partial z}\mathbf{B}^T\mathbf{Q}\mathbf{S}\delta\mathbf{g}\,\mathrm{dA} + \int_A \frac{\partial^2\mathbf{g}'^T}{\partial z^2}\mathbf{S}^T\mathbf{Q}\mathbf{S}\delta\mathbf{g}\,\mathrm{dA} \\
&\quad - \int_A \mathbf{g}^T\mathbf{B}^T\mathbf{Q}\mathbf{B}\delta\mathbf{g}\,\mathrm{dA} - \int_A \frac{\partial\mathbf{g}^T}{\partial z}\mathbf{S}^T\mathbf{Q}\mathbf{B}\delta\mathbf{g}\,\mathrm{dA}
\end{aligned} \tag{2.31}$$

Expanding $\mathbf{g}$ using the typical finite element approach (cf. Equation (2.11))

$$\mathbf{g}(x,y,z) = \mathbf{N}_i(x,y)\mathbf{u}(x_i,y_i,z) \tag{2.32}$$

and replacing (2.32) in (2.31) yields

$$\begin{aligned}
\delta\frac{\partial W}{\partial z} &= \int_A \frac{\partial\mathbf{u}^T}{\partial z}\mathbf{N}^T\mathbf{B}^T\mathbf{Q}\mathbf{S}\mathbf{N}\delta\mathbf{u}\,\mathrm{dA} + \int_A \frac{\partial^2\mathbf{u}^T}{\partial z^2}\mathbf{N}^T\mathbf{S}^T\mathbf{Q}\mathbf{S}\mathbf{N}\delta\mathbf{u}\,\mathrm{dA} \\
&\quad - \int_A \mathbf{u}^T\mathbf{N}^T\mathbf{B}^T\mathbf{Q}\mathbf{B}\mathbf{N}\delta\mathbf{u}\,\mathrm{dA} - \int_A \frac{\partial\mathbf{u}^T}{\partial z}\mathbf{N}^T\mathbf{S}^T\mathbf{Q}\mathbf{B}\mathbf{N}\delta\mathbf{u}\,\mathrm{dA}
\end{aligned}$$

From the equation above it is possible then to identify the matrices

$$\begin{aligned}
\mathbf{M} &= \int_A \mathbf{N}^T\mathbf{S}^T\mathbf{Q}\mathbf{S}\mathbf{N}\,\mathrm{dA} \\
\mathbf{C} &= \int_A \mathbf{N}^T\mathbf{B}^T\mathbf{Q}\mathbf{S}\mathbf{N}\,\mathrm{dA} \\
\mathbf{E} &= \int_A \mathbf{N}^T\mathbf{B}^T\mathbf{Q}\mathbf{B}\mathbf{N}\,\mathrm{dA}
\end{aligned}$$

where $\mathbf{M}$ and $\mathbf{E}$ are symmetrical while $\mathbf{H} = \mathbf{C} - \mathbf{C}^T$ is skew-symmetrical. Rewriting the total virtual work expression

$$\delta\frac{\partial W}{\partial z} = \delta u\left(\mathbf{M}\frac{\partial^2\mathbf{u}}{\partial z^2} - \mathbf{H}\frac{\partial\mathbf{u}}{\partial z} - \mathbf{E}\mathbf{u}\right)$$

The following must hold for an arbitrary variation of δu

$$\mathbf{M}\frac{\partial^2\mathbf{u}}{\partial z^2} - \mathbf{H}\frac{\partial\mathbf{u}}{\partial z} - \mathbf{E}\mathbf{u} = 0 \tag{2.33}$$

This concludes the derivation of the equilibrium equations for the cross section considering only the warping displacements. The aim now is not to solve the equation above but rather discuss the properties of the solutions for this second order linear homogeneous differential equation.

The general solution is sought as a linear combination of

$$\mathbf{u}(z) = \mathbf{h}e^{\lambda z}$$

Inserting the above into (2.33) yields

$$\left(\lambda^2\mathbf{M} - \lambda\mathbf{H} - \mathbf{E}\right)\mathbf{h} = 0$$

where $\mathbf{h}$ are the eigenvectors associated with the eigenvalues λ resulting from the solution to

$$\lambda^2\mathbf{M} - \lambda\mathbf{H} - \mathbf{E} = 0$$

According to physical considerations and Saint-Venant's principle, we expect to have a self-balanced ($\boldsymbol{\theta} = 0$) solution associated with the exponentially decaying modes ($\lambda \neq 0$) – *extremity solutions* – and a solution presenting no decay ($\lambda = 0$) for which the stress resultants are non-zero ($\boldsymbol{\theta} \neq 0$) – *central solutions* (see [6]).

Owing to the structure of matrices $\mathbf{M}$, $\mathbf{E}$ and $\mathbf{H}$ (and mostly due to the fact that $\mathbf{H}$ is skew-symmetric), for the extremity solutions the eigenvalues will be complex and come in pairs. That is, to each eigenvalue $\lambda_j = a + ib$ corresponds a second $\lambda_j = a - ib$. The solution corresponding to the first eigenvalue decays while z increases (moving away from the first end of the beam), wheras the solution associated with the second eigenvalue in the pair is identical but decays as z decreases (moving away from the second end of the beam). This solutions can be used to study end effects and determining the diffusion length or the distance at which the effects from the external loads become negligble (e.g., see Horgan [18] and Choi and Horgan [19] for a discussion on the diffusion length in anisotropic elasticity).

The central solutions for which $\boldsymbol{\theta} \neq 0$, on the other hand, do not have any exponential decay as they correspond to eigenvalues $\lambda_j = 0$ with multiplicity p_j. These are the solutions at the central part of the beam sufficiently away from the extremities so that the effect from the external loads is negligible on the stress field. The solutions for problems where $\lambda_j = 0$ and its multiplicity $p_j \geq 2$, are given as (see [21] for a comprehensive presentation of this topic)[1]

$$\begin{aligned}
\mathbf{u}_{1j}(z) &= \mathbf{h}_{11}e^{\lambda_j z} \\
\mathbf{u}_{2j}(z) &= \mathbf{h}_{21}e^{\lambda_j z} + \mathbf{h}_{22}ze^{\lambda z} \\
&\vdots \\
\mathbf{u}_{p_j j}(z) &= \mathbf{h}_{p_j 1}e^{\lambda_j z} + \mathbf{h}_{p_j 2}ze^{\lambda_j z} + ... + z^{p_j-1}\mathbf{h}_{p_j p_j}e^{\lambda_j z}
\end{aligned}$$

where the corresponding solution in this case is

$$\begin{aligned}
\mathbf{u}_j(z) =& c_1\mathbf{h}_{11}e^{\lambda_j z} + c_2\left(\mathbf{h}_{21} + z\mathbf{h}_{22}\right)e^{\lambda_j z} + ... \\
&+ c_{p_j}\left(\mathbf{h}_{21} + z\mathbf{h}_{22} + ... + z^{p_j-1}\mathbf{h}_{p_j p_j}\right)e^{\lambda_j z}
\end{aligned}$$

In our specific case where $\lambda_j = 0$ the solutions in this case are of the polynomial type

$$\mathbf{u}_j(z) = c_1\mathbf{h}_{11} + c_2\left(\mathbf{h}_{21} + z\mathbf{h}_{22}\right) + ... + c_p\left(\mathbf{h}_{21} + z\mathbf{h}_{22} + ... + z^{p_j-1}\mathbf{h}_{p_j p_j}\right)$$

A central solution $\mathbf{u}_c$ will be any linear combination of the solutions $\mathbf{u}_j$ for which $\lambda_j = 0$. If n is the maximum of all p_j then

$$\frac{\partial^n \mathbf{u}_c}{\partial z^n} = 0 \tag{2.34}$$

Thus the central solutions are polynomial functions in z of at most degree n.

[1] The authors would like to express its gratitude to Assoc. Prof. Mads Peter Sørensen (DTU-MAT) for all the help unravelling this step of the derivation.

2.5 Cross section properties

We look first for the compliance matrix of a cross section of the beam. That is we are interested in finding an expression for the strain energy as function of the stress resultants and moments. These are in fact the central solutions derived above – a particular solution depending on the applied section forces at a given cross section subject to particular boundary conditions which guarantee that the effects of the extremity solutions are negligible. A procedure is presented in this section for the practical determination of the cross section stiffness matrix based on the result of the central solutions. Finally expressions for the determination of the shear and elastic center are derived.

2.5.1 Cross section stiffness matrix

From Equation (2.25) it is important to note that the central solutions are linear and homogeneous[2] functions of the force resultants. Thus it is possible to write

$$\begin{aligned} \mathbf{u} &= \mathbf{X}\boldsymbol{\theta}, \qquad \frac{\partial \mathbf{u}}{\partial z} = \frac{\partial \mathbf{X}}{\partial z}\boldsymbol{\theta} \\ \boldsymbol{\psi} &= \mathbf{Y}\boldsymbol{\theta}, \qquad \frac{\partial \boldsymbol{\psi}}{\partial z} = \frac{\partial \mathbf{Y}}{\partial z}\boldsymbol{\theta} \end{aligned} \tag{2.35}$$

Inserting the expressions above in (2.25) yields

$$\boxed{\begin{cases} \mathbf{EX} + \mathbf{RY} = \left(\mathbf{C} - \mathbf{C}^T\right)\frac{\partial \mathbf{X}}{\partial z} + \mathbf{L}\frac{\partial \mathbf{Y}}{\partial z} \\ \mathbf{R}^T\mathbf{X} + \mathbf{AY} = -\mathbf{L}^T\frac{\partial \mathbf{X}}{\partial z} + \mathbf{I}_6 \end{cases}} \qquad \boxed{\begin{cases} \mathbf{E}\frac{\partial \mathbf{X}}{\partial z} + \mathbf{R}\frac{\partial \mathbf{Y}}{\partial z} = 0 \\ \mathbf{R}^T\frac{\partial \mathbf{X}}{\partial z} + \mathbf{A}\frac{\partial \mathbf{Y}}{\partial z} = \mathbf{T}_r^T \end{cases}} \tag{2.36}$$

Note that the set of equations above can be obtained by replacing $\boldsymbol{\theta} = \mathbf{I}_6$ in (2.25). This corresponds to determining the central solutions for six different choices of the stress resultant $\boldsymbol{\theta}$ in an orderly way, i.e., setting one of the entries to unity and the remaining to zero. In fact, each of the six columns of $\mathbf{X}$, $\mathbf{Y}$, $\frac{\partial \mathbf{X}}{\partial z}$ and $\frac{\partial \mathbf{Y}}{\partial z}$ hold the corresponding displacement solution for each of the different stress resultants.

Restating the expression for the variation of the total energy obtained from the virtual work principle

$$\delta\frac{\partial W}{\partial z} = \int_A \frac{\partial\left(\mathbf{p}'^T\delta\mathbf{v}\right)}{\partial z}\,\mathrm{dA} - \int_A \boldsymbol{\sigma}^T\delta\boldsymbol{\epsilon}\,\mathrm{dA} = 0$$

The previous equation can be restated as

$$\delta\boldsymbol{\theta}^T\mathbf{F}\boldsymbol{\theta} = \int_A \boldsymbol{\sigma}^T\delta\boldsymbol{\epsilon}\,\mathrm{dA}$$

where $\mathbf{F}$ is the compliance matrix of the section. The strain is redefined by inserting (2.35) in (2.13)

$$\boldsymbol{\epsilon} = \mathbf{SZY}\boldsymbol{\theta} + \mathbf{BNX}\boldsymbol{\theta} + \mathbf{SN}\frac{\partial \mathbf{X}}{\partial z}\boldsymbol{\theta}$$

which then yields for the internal energy

$$\delta\frac{\partial W_i}{\partial z} = \int_A \delta\boldsymbol{\theta}\left(\mathbf{Y}^T\mathbf{Z}^T\mathbf{S}^T + \mathbf{X}^T\mathbf{N}^T\mathbf{B}^T + \frac{\partial \mathbf{X}'^T}{\partial z}\mathbf{N}^T\mathbf{S}^T\right)\mathbf{Q}$$

[2] An homogeneous function is such that $f(\alpha x) = \alpha f(x)$. In this specific case, one important inference is that homogeneous functions do not have an independent term.

$$\left(\mathbf{SZY} + \mathbf{BNX} + \mathbf{SN}\frac{\partial \mathbf{X}}{\partial z}\right)\boldsymbol{\theta}\ \mathrm{dA}$$

The former can be stated in matrix form as

$$\delta\frac{\partial W_i}{\partial z} = \begin{bmatrix} \delta\boldsymbol{\theta}\mathbf{X} \\ \delta\boldsymbol{\theta}\frac{\partial \mathbf{X}}{\partial z} \\ \delta\boldsymbol{\theta}\mathbf{Y} \end{bmatrix}^T \begin{bmatrix} \mathbf{E} & \mathbf{C} & \mathbf{R} \\ \mathbf{C}^T & \mathbf{M} & \mathbf{L} \\ \mathbf{R}^T & \mathbf{L}^T & \mathbf{A} \end{bmatrix} \begin{bmatrix} \mathbf{X}\boldsymbol{\theta} \\ \frac{\partial \mathbf{X}}{\partial z}\boldsymbol{\theta} \\ \mathbf{Y}\boldsymbol{\theta} \end{bmatrix}$$

The total virtual work expression becomes

$$\delta\boldsymbol{\theta}^T\mathbf{F}\boldsymbol{\theta} = \begin{bmatrix} \delta\boldsymbol{\theta}\mathbf{X} \\ \delta\boldsymbol{\theta}\frac{\partial \mathbf{X}}{\partial z} \\ \delta\boldsymbol{\theta}\mathbf{Y} \end{bmatrix}^T \begin{bmatrix} \mathbf{E} & \mathbf{C} & \mathbf{R} \\ \mathbf{C}^T & \mathbf{M} & \mathbf{L} \\ \mathbf{R}^T & \mathbf{L}^T & \mathbf{A} \end{bmatrix} \begin{bmatrix} \mathbf{X}\boldsymbol{\theta} \\ \frac{\partial \mathbf{X}}{\partial z}\boldsymbol{\theta} \\ \mathbf{Y}\boldsymbol{\theta} \end{bmatrix}$$

For any admissible virtual displacement $\delta\boldsymbol{\theta}\mathbf{X}$, $\delta\boldsymbol{\theta}\frac{\partial \mathbf{X}}{\partial z}$ and $\delta\boldsymbol{\theta}\mathbf{Y}$ it is possible to obtain an expression for the cross section compliance matrix dfined as

$$\boxed{\mathbf{F} = \begin{bmatrix} \mathbf{X} \\ \frac{\partial \mathbf{X}}{\partial z} \\ \mathbf{Y} \end{bmatrix}^T \begin{bmatrix} \mathbf{E} & \mathbf{C} & \mathbf{R} \\ \mathbf{C}^T & \mathbf{M} & \mathbf{L} \\ \mathbf{R}^T & \mathbf{L}^T & \mathbf{A} \end{bmatrix} \begin{bmatrix} \mathbf{X} \\ \frac{\partial \mathbf{X}}{\partial z} \\ \mathbf{Y} \end{bmatrix}} \tag{2.37}$$

The corresponding stiffness matrix $\mathbf{K}$ can be computed as

$$\boxed{\mathbf{K} = \mathbf{F}^{-1}} \tag{2.38}$$

This result can be used to generate beam finite element models for which the strains can be exactly described by the six strain parameters in $\boldsymbol{\psi}$. The material may be anisotropic, inhomogeneously distributed, and the reference coordinate system may be arbitrarily located. The stiffness matrix $\mathbf{K}$ will correctly account for any geometrical or material couplings.

2.5.2 Shear center and elastic center positions

The expressions for the positions of the shear and elastic center are presented next.

The shear center is defined as the point at which a load applied parallel to the plane of the section will produce no torsion (i.e., $\kappa_z = 0$). Hence, assume that two transverse forces, F_x and F_y are applied at a point (x_s, y_s) at a given cross section. The moments induced by the two forces are

$$M_x = -F_y(L-z) \quad , \quad M_y = F_x(L-z) \quad , \quad M_z = -F_x y_s + F_y x_s \tag{2.39}$$

The aim is to find the position (x_s, y_s) for which the curvature associated with the twist $\kappa_z = 0$. Thus, taking into account the cross section constitutive relation $\boldsymbol{\psi} = \mathbf{F}\boldsymbol{\theta}$, the following holds

$$\kappa_z = F'_{61}F'_x + F'_{62}F'_y + F'_{64}M_x + F'_{65}M_y + F'_{66}M_z = 0$$

Inserting (2.39) into the previous equation yields

$$\left[F_{61} + F_{62}(L-z) - F_{66}y_s\right]F_x + \left[F_{62} - F_{64}(L-z) + F_{66}x_s\right] = 0$$

Since the above has to be valid for any F_x and F_y,

$$x_s = -\frac{F_{62} + F_{64}(L-z)}{F_{66}}$$
$$y_s = \frac{F_{61} + F_{65}(L-z)}{F_{66}}$$

From the previous equation it can be seen that the shear center is not a property of the cross section. Instead, in the case where the entries F_{64} and F_{65} associated with the bending-twist coupling are not zero, the position of the shear center varies linearly along the beam length .

The expressions for the position of the elastic center can be determined in the same manner. The elastic center is defined as the point where a force applied normal to the cross section will produce no bending curvatures (i.e., $\kappa_x = \kappa_y = 0$). Thus, assume that a load F_z is applied at the point (x_t, y_t) in the cross section. The moments induced by this force are

$$M_x = F_z y_t \quad , \quad M_y = -F_z x_t \tag{2.40}$$

We look for the positions (x_t, y_t) for which $\kappa_x = \kappa_y = 0$. From the cross section constitutive relation,

$$\begin{aligned} \kappa_x &= F_{43} F_z + F_{44} M_x + F_{45} M_y = 0 \\ \kappa_x &= F_{53} F_z + F_{54} M_x + F_{55} M_y = 0 \end{aligned}$$

Since the previous must be valid for any force F_z, inserting (2.40) into the previous equation will result in the following set of linear equations

$$\begin{cases} F_{43} + F_{44} y_t - F_{45} x_t = 0 \\ F_{53} + F_{54} y_t - F_{55} x_t = 0 \end{cases}$$

and so

$$\begin{aligned} x_t &= -\frac{-F_{44}F_{53} + F_{45}F_{43}}{F_{44}F_{55} - F_{45}^2} \\ y_t &= -\frac{F_{43}F_{55} - F_{45}F_{53}}{F_{44}F_{55} - F_{45}^2} \end{aligned}$$

which are the expressions for the position of the elastic center.

Chapter 3

Implementation manual

The theory presented in the previous sections up to the determination of the cross section stiffness matrix and, shear and elastic centers, is implemented in the BEam Cross section Analysis Software – BECAS. This section addresses the practical implementation of the theory. The MATLAB implementation of BECAS described in Appendix A is according to the expressions described in this section.

Two different approaches have been implemented. The first approach is based on a two dimensional finite element mesh and is mostly attractive for readers which work on their own finite element code. The second approach is based on a three dimensional mesh of the cross section using eight node solid finite elements. The approach is described in detail in Ghiringhelli and Mantegazza [9] and only the most important results are presented here. The approach is implemented in BECAS for illustrative purposes only.

Although these are standard procedures, the transformation of the material constitutive matrix is a topic where, in the authors' opinion, there is often some ambiguity concerning specific definitions for specific implementations. Hence, the final section of this chapter has been dedicated to the presentation of the material constitutive matrix for orthotropic materials and the corresponding necessary transformations.

3.1 Two dimensional finite element analysis

The first step in the evaluation of the cross section properties is the generation of a two dimensional finite element mesh of the cross section. An example of a discretized profile section is presented in Figure 3.1. The material properties, fiber plane orientation and

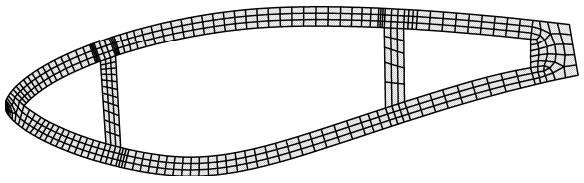

Figure 3.1: Example of the two dimensional finite element mesh of a generic wind turbine section using four node isoparametric finite elements.

fiber directions are defined at each element of the finite element mesh. Thus, a layer of a certain material is defined using a layer of elements. Having defined the cross section mesh and material properties, the subsequent step concerns the derivation of each of the matrices in Equation (2.17).

The implementation is based on a four node isoparametric elements. The node numbering and isoparametric coordinate system are presented in Figure 3.2. The shape functions

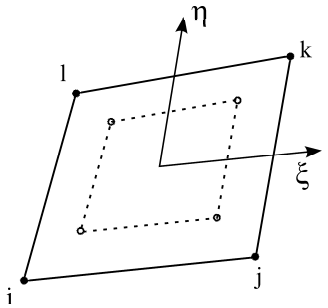

Figure 3.2: Isoparametric coordinate system, nodal positions and position of Gauss points for the four node isoparametric plane finite element.

employed in the derivation of the four node isoparametric plane finite element are

$$N_1(\xi,\eta) = \frac{1}{4}(1-\xi)(1-\eta) \quad N_2(\xi,\eta) = \frac{1}{4}(1+\xi)(1-\eta)$$
$$N_3(\xi,\eta) = \frac{1}{4}(1+\xi)(1+\eta) \quad N_4(\xi,\eta) = \frac{1}{4}(1-\xi)(1+\eta)$$

The position of a point in the element is given by interpolation of the nodal positions as

$$x = \sum_{i=1}^{n_q} N_i(\xi,\eta)\, x_i \quad y = \sum_{i=1}^{n_q} N_i(\xi,\eta)\, y_i \quad z(\xi,\eta) = \sum_{i=1}^{n_q} N_i(\xi,\eta)\, z_i$$

where n_q is the number of nodes in the element, and (x_i, y_i, z_i) are the nodal positions. In matrix form

$$\mathbf{N} = \begin{bmatrix} N_1\mathbf{I}_3 & N_2\mathbf{I}_3 & N_3\mathbf{I}_3 & N_4\mathbf{I}_3 \end{bmatrix}$$

The integration is performed with respect to the element coordinate system although the integrals in (2.17) are defined with respect to the cross section coordinate system. To account for the change of coordinates we employ the following transformation

$$\begin{bmatrix} \frac{\partial}{\partial\xi} \\ \frac{\partial}{\partial\eta} \\ \frac{\partial}{\partial\zeta} \end{bmatrix} = \mathbf{J} \begin{bmatrix} \frac{\partial}{\partial x} \\ \frac{\partial}{\partial y} \\ \frac{\partial}{\partial z} \end{bmatrix}$$

where

$$\mathbf{J} = \begin{bmatrix} \frac{\partial x}{\partial\xi} & \frac{\partial y}{\partial\xi} & \frac{\partial z}{\partial\xi} \\ \frac{\partial x}{\partial\eta} & \frac{\partial y}{\partial\eta} & \frac{\partial z}{\partial\eta} \\ \frac{\partial x}{\partial\zeta} & \frac{\partial y}{\partial\zeta} & \frac{\partial z}{\partial\zeta} \end{bmatrix} \tag{3.1}$$

is the Jacobian matrix. In this specific case

$$\mathbf{J} = \begin{bmatrix} \frac{\partial x}{\partial\xi} & \frac{\partial y}{\partial\xi} & 0 \\ \frac{\partial x}{\partial\eta} & \frac{\partial y}{\partial\eta} & 0 \\ 0 & 0 & 1 \end{bmatrix} \tag{3.2}$$

Using (2.7) and finding $\mathbf{J}^{-1}$ from (3.2) it is possible to define the strain operator $\mathbf{B}$ as

$$\mathbf{B}(\xi,\eta) = \mathbf{B}_\xi \frac{\partial}{\partial\xi} + \mathbf{B}_\eta \frac{\partial}{\partial\eta}$$

where

$$\mathbf{B}_\xi = \begin{bmatrix} J_{11}^{-1} & 0 & 0 \\ 0 & J_{21}^{-1} & 0 \\ J_{21}^{-1} & J_{11}^{-1} & 0 \\ 0 & 0 & J_{11}^{-1} \\ 0 & 0 & J_{21}^{-1} \\ 0 & 0 & 0 \end{bmatrix} \quad \mathbf{B}_\eta = \begin{bmatrix} J_{12}^{-1} & 0 & 0 \\ 0 & J_{22}^{-1} & 0 \\ J_{22}^{-1} & J_{12}^{-1} & 0 \\ 0 & 0 & J_{12}^{-1} \\ 0 & 0 & J_{22}^{-1} \\ 0 & 0 & 0 \end{bmatrix}$$

The strain operator is then applied in the derivation of the matrix product

$$\mathbf{BN} = \mathbf{B}_\xi \frac{\partial \mathbf{N}}{\partial \xi} + \mathbf{B}_\eta \frac{\partial \mathbf{N}}{\partial \eta}$$

where

$$\frac{\partial \mathbf{N}}{\partial \xi} = \begin{bmatrix} \frac{\partial N_1}{\partial \xi}\mathbf{I}_3 & \frac{\partial N_2}{\partial \xi}\mathbf{I}_3 & \frac{\partial N_3}{\partial \xi}\mathbf{I}_3 & \frac{\partial N_4}{\partial \xi}\mathbf{I}_3 \end{bmatrix}$$
$$\frac{\partial \mathbf{N}}{\partial \eta} = \begin{bmatrix} \frac{\partial N_1}{\partial \eta}\mathbf{I}_3 & \frac{\partial N_2}{\partial \eta}\mathbf{I}_3 & \frac{\partial N_3}{\partial \eta}\mathbf{I}_3 & \frac{\partial N_4}{\partial \eta}\mathbf{I}_3 \end{bmatrix}$$

The remaining matrix products **SZ** and **SN** are obtained by simple matrix multiplication. The integration is performed at the element level and hence the element matrices are evaluated as

$$\mathbf{A}_e = \int_A \mathbf{Z}^T\mathbf{S}^T\mathbf{QSZ}\ \mathrm{dxdy} = \int_A \mathbf{Z}^T\mathbf{S}^T\mathbf{QSZ}\,|J|\ \mathrm{d}\xi\ \mathrm{d}\eta$$
$$\mathbf{R}_e = \int_A \mathbf{N}^T\mathbf{B}^T\mathbf{QSZ}\ \mathrm{dxdy} = \int_A \mathbf{N}^T\mathbf{B}^T\mathbf{QSZ}\,|J|\ \mathrm{d}\xi\ \mathrm{d}\eta$$
$$\mathbf{E}_e = \int_A \mathbf{N}^T\mathbf{B}^T\mathbf{QBN}\ \mathrm{dxdy} = \int_A \mathbf{N}^T\mathbf{B}^T\mathbf{QBN}\,|J|\ \mathrm{d}\xi\ \mathrm{d}\eta$$
$$\mathbf{C}_e = \int_A \mathbf{N}^T\mathbf{B}^T\mathbf{QSN}\ \mathrm{dxdy} = \int_A \mathbf{N}^T\mathbf{B}^T\mathbf{QSN}\,|J|\ \mathrm{d}\xi\ \mathrm{d}\eta$$
$$\mathbf{L}_e = \int_A \mathbf{N}^T\mathbf{S}^T\mathbf{QSZ}\ \mathrm{dxdy} = \int_A \mathbf{N}^T\mathbf{S}^T\mathbf{QSZ}\,|J|\ \mathrm{d}\xi\ \mathrm{d}\eta$$
$$\mathbf{M}_e = \int_A \mathbf{N}^T\mathbf{S}^T\mathbf{QSN}\ \mathrm{dxdy} = \int_A \mathbf{N}^T\mathbf{S}^T\mathbf{QSN}\,|J|\ \mathrm{d}\xi\ \mathrm{d}\eta$$

where the integration is performed using a four point Gauss quadrature (cf. Figure 3.2). The global matrices are subsequently assembled following typical finite element procedures

$$\mathbf{A} = \sum_{i=1}^{n_e} \mathbf{A}_e \quad , \quad \mathbf{R} = \sum_{i=1}^{n_e} \mathbf{R}_e \quad , \quad \mathbf{E} = \sum_{i=1}^{n_e} \mathbf{E}_e$$
$$\mathbf{C} = \sum_{i=1}^{n_e} \mathbf{C}_e \quad , \quad \mathbf{L} = \sum_{i=1}^{n_e} \mathbf{L}_e \quad , \quad \mathbf{M} = \sum_{i=1}^{n_e} \mathbf{M}_e$$

where n_e is the number of finite elements in the cross section mesh.

Having obtained each of the matrices it is possible to finally solve the cross section equilibrium equations

$$\begin{bmatrix} \mathbf{E} & \mathbf{R} & \mathbf{D} \\ \mathbf{R}^T & \mathbf{A} & \mathbf{0} \\ \mathbf{D}^T & \mathbf{0} & \mathbf{0} \end{bmatrix} \begin{bmatrix} \frac{\partial \mathbf{X}}{\partial z} \\ \frac{\partial \mathbf{Y}}{\partial z} \\ \mathbf{\Lambda} \end{bmatrix} = \begin{bmatrix} \mathbf{0} \\ \mathbf{T}_r^T \\ \mathbf{0} \end{bmatrix}$$
$$\begin{bmatrix} \mathbf{E} & \mathbf{R} & \mathbf{D} \\ \mathbf{R}^T & \mathbf{A} & \mathbf{0} \\ \mathbf{D}^T & \mathbf{0} & \mathbf{0} \end{bmatrix} \begin{bmatrix} \mathbf{X} \\ \mathbf{Y} \\ \mathbf{\Lambda} \end{bmatrix} = \begin{bmatrix} \left(\mathbf{C} - \mathbf{C}^T\right) & \mathbf{L} \\ \mathbf{L}^T & \mathbf{0} \\ \mathbf{0} & \mathbf{0} \end{bmatrix} \begin{bmatrix} \frac{\partial \mathbf{X}}{\partial z} \\ \frac{\partial \mathbf{Y}}{\partial z} \end{bmatrix} + \begin{bmatrix} \mathbf{0} \\ \mathbf{I} \\ \mathbf{0} \end{bmatrix}$$

where $\mathbf{D}$ is the matrix of contraint equations defined in 2.26, and $\mathbf{\Lambda}$ are the corresponding Lagrange multipliers. The two sets above make use of the same coefficient matrix and can be solved efficiently using a proper factorization (e.g., LU factorization). The solutions are then obtained doing a forward and backward substitution.

The cross section compliance matrix is then readily obtained by inserting the solutions of the previous set into

$$\mathbf{F} = \begin{bmatrix} \mathbf{X} \\ \frac{\partial \mathbf{X}}{\partial z} \\ \mathbf{Y} \end{bmatrix}^T \begin{bmatrix} \mathbf{E} & \mathbf{C} & \mathbf{R} \\ \mathbf{C}^T & \mathbf{M} & \mathbf{L} \\ \mathbf{R}^T & \mathbf{L}^T & \mathbf{A} \end{bmatrix} \begin{bmatrix} \mathbf{X} \\ \frac{\partial \mathbf{X}}{\partial z} \\ \mathbf{Y} \end{bmatrix}$$

A MATLAB implementation of BECAS according to the theory presented above is described in Appendix A.

3.2 Implementation for commercial finite element codes

Next is a brief presentation of an implementation of the theory for commercial finite element codes. The aim is to evaluate the matrices necessary to solve the sets in (2.36) and (2.38) based on a three dimensional mesh of the cross section. For a more detailed discussion on the derivation of the expressions presented in this section the reader should refer to Ghiringhelli and Mantegazza [9].

The implementation makes use of a solid finite element representation of the cross section. It is important to note that in its present form the approach will only yield the correct results using eight node solid finite elements. Moreover, it is necessary to ensure that exactly two Gauss points are used in the length direction in the integration of the solid finite elements. Finally, an obvious requirement is that the preferred comercial finite element code allows the user to accesss and manipulate the global finite element stiffness matrix.

A possible approach consists of first generating a two-dimensional finite element mesh of the cross section in the xy plane at $z = 0$ using four node plane finite elments. A three-dimensional finite element mesh composed of eight node solid finite element is then generated by extruding the two dimensional mesh in the z direction by a distance Δz. The choice of Δx should be such that the resulting solid finite elements are not too distorted as to affect the quality of the results. Thus, a length of the order of the average side length of the two-dimensional finite elements is recommended. The finite element equilibrium equations for the three-dimensional model are

$$\mathbf{Sw} = \mathbf{f}$$

where $\mathbf{S}$ is the finit element stiffness matrix, $\mathbf{w}$ the displacement vector and $\mathbf{f}$ the external load vector. The following decomposition of the finite element stiffness matrix $\mathbf{S}$ and corresponding displacement and load vector is allowed

$$\begin{bmatrix} \mathbf{S}_{11} & \mathbf{S}_{12} \\ \mathbf{S}_{21} & \mathbf{S}_{22} \end{bmatrix} \begin{bmatrix} \mathbf{w}_1 \\ \mathbf{w}_2 \end{bmatrix} = \begin{bmatrix} \mathbf{f}_1 \\ \mathbf{f}_2 \end{bmatrix}$$

where the index 1 and 2 refer to the contributions from the nodes at $z = 0$ and $z = \Delta z$, respectively,. Based on the above submatrices Ghiringhelli and Mantegazza [9] have derived the expressions for the matrices necessary for the computation of the cross section stiffness matrix. Hence, after proper derivation the following are defined

$$\mathbf{M} = \left((\mathbf{S}_{11} + \mathbf{S}_{22}) - 2 (\mathbf{S}_{12} + \mathbf{S}_{21}) \right) \frac{\Delta z}{6}$$

$$\mathbf{C} = \frac{1}{2}\left((\mathbf{S}_{11} + \mathbf{S}_{22}) - (\mathbf{S}_{12} + \mathbf{S}_{21})\right)$$
$$\mathbf{E} = (\mathbf{S}_{11} + \mathbf{S}_{22} + \mathbf{S}_{12} + \mathbf{S}_{21})\,\frac{1}{\Delta z}$$

Note that deriving the original equations in Ghiringhelli and Mantegazza [9] yields the 1/2 factor in matrix **C**. This factor is not present in the derviation by Ghiringhelli and Mantegazza [9]. The remaining matrices can be determined as

$$\mathbf{R} = \mathbf{C}\mathbf{Z}_G, \quad \mathbf{L} = \mathbf{M}\mathbf{Z}_G, \quad \mathbf{A} = \mathbf{Z}_G^T\mathbf{M}\mathbf{Z}_G$$

where $\mathbf{Z}_G$ is defined as

$$\mathbf{Z}_G = \begin{bmatrix} 1 & 0 & 0 & 0 & 0 & -y_1 \\ 0 & 1 & 0 & 0 & 0 & x_1 \\ 0 & 0 & 1 & y_1 & -x_1 & 0 \\ & & \vdots & & & \\ 1 & 0 & 0 & 0 & 0 & -y_{n_n} \\ 0 & 1 & 0 & 0 & 0 & x_{n_n} \\ 0 & 0 & 1 & y_{n_n} & -x_{n_n} & 0 \end{bmatrix}$$

where n_n is the number of nodes in the reference cross section face (i.e., half the nodes in the whole three dimensional model). Having defined all the matrices it is possible now to solve the sets (2.36) while remembering to account for the matrix of constraint equations **D** presented in 2.3.3. Replacing the solutions of (2.36) into (2.38) it is straight forward to evaluate the cross section stiffness matrix **K**.

3.3 Material constitutive matrix

At each element of the cross section finite element mesh, the user of BECAS must specify

- Material properties
- Orientation of the laminate plane
- Orientation of the fibers laminate

Based on this input, the first step consists of assembling the material constitutive matrix in the material coordinate system based on a set of material properties.

3.3.1 Definition

In the case of orthotropic materials, the stress-strain relation or generalized Hookes' Law is stated as

$$\begin{bmatrix} \sigma_{xx} \\ \sigma_{yy} \\ \sigma_{xy} \\ \sigma_{xz} \\ \sigma_{yz} \\ \sigma_{zz} \end{bmatrix} = \underbrace{\begin{bmatrix} \frac{1}{E_x} & -\frac{\nu_{xy}}{E_x} & 0 & 0 & 0 & -\frac{\nu_{xz}}{E_z} \\ -\frac{\nu_{xy}}{E_x} & \frac{1}{E_y} & 0 & 0 & 0 & -\frac{\nu_{yz}}{E_z} \\ 0 & 0 & \frac{1}{G_{xy}} 0 & & 0 & 0 \\ 0 & 0 & 0 & \frac{1}{G_{xz}} & 0 & 0 \\ 0 & 0 & 0 & 0 & \frac{1}{G_{yz}} & 0 \\ -\frac{\nu_{xz}}{E_z} & -\frac{\nu_{yz}}{E_z} & 0 & 0 & 0 & \frac{1}{E_z} \end{bmatrix}^{-1}}_{\mathbf{Q}} \begin{bmatrix} \gamma_{xx} \\ \gamma_{yy} \\ \gamma_{xy} \\ \gamma_{xz} \\ \gamma_{yz} \\ \gamma_{zz} \end{bmatrix}$$

where the natural strains ϵ_{ij} are related to the engineering strains γ_{ij} by

$$\gamma_{xx} = \epsilon_{xx}, \quad \gamma_{yy} = \epsilon_{yy}, \quad \gamma_{zz} = \epsilon_{zz},$$
$$\gamma_{yz} = 2\epsilon_{yz}, \quad \gamma_{xz} = 2\epsilon_{xz}, \quad \gamma_{xy} = 2\epsilon_{xy}$$

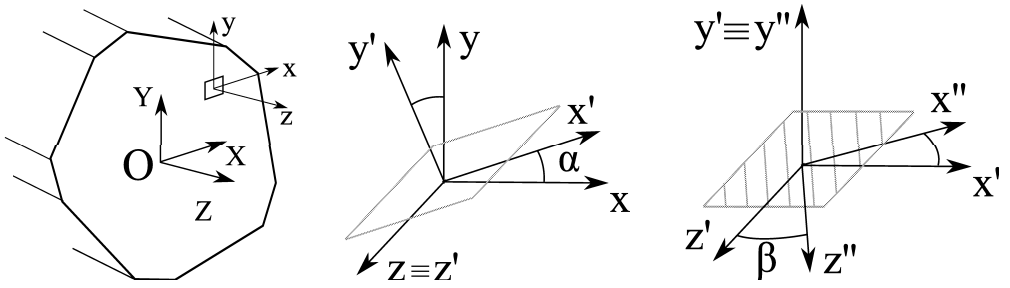

(a) (b) (c)

Figure 3.3: Determination of the material constitutive matrix at each finite element of the cross section mesh. (a) Definition of the cross section coordinate system XYZ and element coordinate system xyz. (b) Convention adopted for the rotation of the element coordinate system xyz into the fiber plane coordinate system $x'y'z'$. (c) Convention adopted for the rotation of the fiber plane coordinate system $x'y'z'$ into the fiber coordinate system $x''y''z''$.

3.3.2 Rotation

The next two steps concern the two rotations of the material constitutive matrix necessary to determine the element material constitutive matrix in the fiber coordinate system. The three element coordinate systems – element, fiber plane, and fiber – and respective conventions for each of the rotations are defined in Figure 3.3. The material constitutive matrix is rotated first into the fiber plane coordinate system and subsequently into the fiber coordinate system. Each of the rotations is performed following the procedure described next.

The following approach for the rotation of the material constitutive matrix is based on Reddy [23]. We consider the relationship between the stress components in a material (m) and a problem (p) coordinate systems. In tensor format, the stress tensor is transformed as

$$(\sigma_{ij})_m = l_{im} l_{jn} (\sigma_{mn})_p, \quad (\sigma_{mn})_p = l_{mi} l_{nj} (\sigma_{ij})_m, \tag{3.3}$$

where l_{ij} are the direction cosines defined as

$$l_{ij} = (\mathbf{e}_i)_m \cdot (\mathbf{e}_j)_p$$

The vectors $\mathbf{e}$ are unit vectors associated with the axis at each of the coordinate systems. The components of the stress in the material and problem coordinate systems are

$$\boldsymbol{\sigma}_m = \begin{bmatrix} \sigma_{xx_m} & \sigma_{yy_m} & \sigma_{xy_m} & \sigma_{xz_m} & \sigma_{yz_m} & \sigma_{zz_m} \end{bmatrix}^T$$
$$\boldsymbol{\sigma}_p = \begin{bmatrix} \sigma_{xx_p} & \sigma_{yy_p} & \sigma_{xy_p} & \sigma_{xz_p} & \sigma_{yz_p} & \sigma_{zz_p} \end{bmatrix}^T$$

The 3×3 arrays with the stress components are given by

$$\hat{\boldsymbol{\sigma}}_m = \begin{bmatrix} \sigma_{xx_m} & \sigma_{xy_m} & \sigma_{xz_m} \\ \sigma_{yx_m} & \sigma_{yy_m} & \sigma_{yz_m} \\ \sigma_{zx_m} & \sigma_{zy_m} & \sigma_{zz_m} \end{bmatrix}, \quad \hat{\boldsymbol{\sigma}}_p = \begin{bmatrix} \sigma_{xx_p} & \sigma_{xy_p} & \sigma_{xz_p} \\ \sigma_{yx_p} & \sigma_{yy_p} & \sigma_{yz_p} \\ \sigma_{zx_p} & \sigma_{zy_p} & \sigma_{zz_p} \end{bmatrix}$$

where the ($\hat{}$) refers to the array notation. Then the rotations in Equation 3.3 can be expressed as

$$\hat{\boldsymbol{\sigma}}_m = \mathbf{L} \hat{\boldsymbol{\sigma}}_p \mathbf{L}^T, \quad \hat{\boldsymbol{\sigma}}_p = \mathbf{L}^T \hat{\boldsymbol{\sigma}}_m \mathbf{L}$$

The vector of engineering strains in the material and problem coordinate systems is

$$\boldsymbol{\gamma}_m = \begin{bmatrix} \gamma_{xx_m} & \gamma_{yy_m} & \gamma_{zz_m} & \gamma_{yz_m} & \gamma_{xz_m} & \gamma_{xy_m} \end{bmatrix}^T$$
$$\boldsymbol{\gamma}_p = \begin{bmatrix} \gamma_{xx_p} & \gamma_{yy_p} & \gamma_{zz_p} & \gamma_{yz_p} & \gamma_{xz_p} & \gamma_{xy_p} \end{bmatrix}^T$$

The natural strain components may be defined in function of the engineering strains as

$$\hat{\boldsymbol{\epsilon}}_m = \begin{bmatrix} \gamma_{xx_m} & \frac{1}{2}\gamma_{xy_m} & \frac{1}{2}\gamma_{xz_m} \\ \frac{1}{2}\gamma_{yx_m} & \gamma_{yy_m} & \frac{1}{2}\gamma_{yz_m} \\ \frac{1}{2}\gamma_{zx_m} & \frac{1}{2}\gamma_{zy_m} & \gamma_{zz_m} \end{bmatrix}, \quad \hat{\boldsymbol{\epsilon}}_p = \begin{bmatrix} \gamma_{xx_p} & \frac{1}{2}\gamma_{xy_p} & \frac{1}{2}\gamma_{xz_p} \\ \frac{1}{2}\gamma_{yx_p} & \gamma_{yy_p} & \frac{1}{2}\gamma_{yz_p} \\ \frac{1}{2}\gamma_{zx_p} & \frac{1}{2}\gamma_{zy_p} & \gamma_{zz_p} \end{bmatrix}$$

where $\hat{\boldsymbol{\gamma}}$ are the engineering strains. Since the strains are also second order tensors, the relations derived for the stresses are also valid for the strains

$$\hat{\boldsymbol{\epsilon}}_m = \mathbf{L}\hat{\boldsymbol{\epsilon}}_p\mathbf{L}^T, \quad \hat{\boldsymbol{\epsilon}}_p = \mathbf{L}^T\hat{\boldsymbol{\epsilon}}_m\mathbf{L}$$

Based on the expressions presented before it is possible to establish the equations for the transformation of the material constitutive matrix. The constitutive matrix in the problem coordinate system, $\mathbf{Q}_p$, is obtained by transformation of the material constitutive matrix in the material coordinate system, $\mathbf{Q}_m$. The following steps should be followed in the rotation of the material constitutive matrix:

1. The array $\hat{\boldsymbol{\epsilon}}_p$ is assembled based on the engineering strains $\boldsymbol{\gamma}_p$ remembering to observe the 1/2 factor;
2. The strains are then rotated employing $\hat{\boldsymbol{\epsilon}}_m = \mathbf{L}\hat{\boldsymbol{\epsilon}}_p\mathbf{L}^T$;
3. Having $\hat{\boldsymbol{\epsilon}}_m$ it is possible to assemble the vector of engineering strains $\boldsymbol{\gamma}_m$ remembering to multiply by 2 the natural shear strain components;
4. The stress-strain relation $\boldsymbol{\sigma}_m = \mathbf{Q}_m\boldsymbol{\gamma}_m$ is invoked to determine $\boldsymbol{\sigma}_m$;
5. The array with the stress components $\hat{\boldsymbol{\sigma}}_m$ is then assembled to evaluate the stresses in the problem coordinate system $\hat{\boldsymbol{\sigma}}_p = \mathbf{L}^T\hat{\boldsymbol{\sigma}}_m\mathbf{L}$;
6. Assemble the vector $\boldsymbol{\sigma}_p$ based on the components of $\hat{\boldsymbol{\sigma}}_p$;
7. Finally, each of the stress components is a function of the strain components in $\boldsymbol{\gamma}_p$, the direction cosines in $\mathbf{L}$ and the entries of the constitutive matrix $\mathbf{Q}_m$. The coefficients multiplying each of the strain components in $\boldsymbol{\gamma}_p$ are the components of the constitutive matrix in the problem coordinate system $\mathbf{Q}_p$.

The procedure is used to orient the fibers in a laminate or to orient the laminate plane. When orienting the fiber plane, the rotation matrix $\mathbf{L}$ will be

$$\mathbf{L}_\alpha = \begin{bmatrix} \cos\alpha & -\sin\alpha & 0 \\ \sin\alpha & \cos\alpha & 0 \\ 0 & 0 & 1 \end{bmatrix}$$

whereas for the fiber orientation

$$\mathbf{L}_\beta = \begin{bmatrix} \cos\beta & 0 & \sin\beta \\ 0 & 1 & 0 \\ -\sin\beta & 0 & \cos\beta \end{bmatrix}$$

which are the typical two dimensional rotational matrices.

Chapter 4

Validation

In this section numerical results obtained using BECAS – the BEam Cross Section analysis Software – are presented. BECAS is the current implementation of the method presented in the previous sections. At this point the output is the cross section compliance and stiffness matrix, and the positions of the shear and elastic centers. The resulting entries of the cross section stiffness matrix $\mathbf{K}$ as well as the positions of the shear and elastic center are compared to the results from VABS – the Variational Asymptotic Beam Section analysis code (Yu et al. [13, 14]). VABS has been extensively validated against different cross section analysis tools and analytical results (see Yu et al. [13, 14], Chen et al. [15] and Volovoi et al. [17]) and it is therefore a benchmark for validation of new cross section analysis codes.

The numerical experiments presented for validation have been chosen so that different material and geometrical effects are analyzed. From a material properties standpoint, the aim is to analyze the effect of material anisotropy and its inhomogeneous distribution over the cross section. In terms of cross section geometry we look at solid, thin-walled, open and multi-cell cross sections.

This chapter is organized as follows. First, the setup for the numerical experiments is described. The material properties are defined, and the cross section coordinate systems as well as the cross section constitutive relation are restated. Moreover, the general organization of the numerical experiments and the aim of each is described. The results for the numerical experiments are presented next.

4.1 Setup

Three material types have been considered – two isotropic and one orthotropic material. Their stiffness properties are presented in Table 4.1. Furthermore, four different cross sec-

Table 4.1: Material properties for isotropic material #1 and #2, and orthotropic material (scaled values for E-glass according to Handbook of Composites [24]). The factor $\alpha = E_1/E_2$ shall be used in the study of extremely inhomogeneous sections.

Material	Isotropic #1	Isotropic #2	Orthotropic
E_{zz}	100	$100/\alpha$	480
$E_{xx} = E_{yy}$	100	$100/\alpha$	120
G_{yz}	41.667	$41.667/\alpha$	50
$G_{xz} = G_{xy}$	41.667	$41.667/\alpha$	60
ν_{yz}	0.2	$0.2/\alpha$	0.26
$\nu_{xz} = \nu_{xy}$	0.2	$0.2/\alpha$	0.19

Table 4.2: Catalogue of cross section properties analysed for validation.

Ref.	Geometry	Material
S1	Solid square	Isotropic
S2	Solid square	Isotropic #1 + Isotropic #2
S3	Solid square	Orthotropic
C1	Cylinder	Isotropic #1
C2	Half-cylinder	Isotropic #1
C3	Cylinder	Isotropic #1 + Isotropic #2
C4	Cylinder (layered)	Isotropic #1 + Isotropic #2
T1	Three-cells	Isotropic #1
T2	Three-cells	Isotropic #1 + Orthotropic

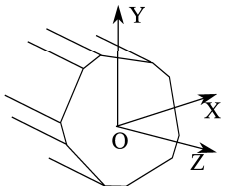

Figure 4.1: Cross section coordinate system.

tion geometries have been considered – solid square, cylinder, half cylinder and three cells. All the combinations of cross section geometry and material properties, are summarized in Table 4.2.

Recall from Section 2.2.1 the orientation of the coordinate system presented again here for convenience in Figure 4.1. The non-zero entries of the cross section stiffness matrix $\mathbf{K}$, the position of the shear and elastic center, and the warping displacements are calculated for each of the numerical experiments. The entries of $\mathbf{K}$ and the position of the shear and elastic center are compared to the results from VABS. Recall the relations between the strains and direction of forces and moments

$$\begin{bmatrix} K_{11} & K_{12} & K_{13} & K_{14} & K_{15} & K_{16} \\ K_{21} & K_{22} & K_{23} & K_{24} & K_{25} & K_{26} \\ K_{31} & K_{32} & K_{33} & K_{34} & K_{35} & K_{36} \\ K_{41} & K_{42} & K_{43} & K_{44} & K_{45} & K_{46} \\ K_{51} & K_{52} & K_{53} & K_{54} & K_{55} & K_{56} \\ K_{61} & K_{62} & K_{63} & K_{64} & K_{65} & K_{66} \end{bmatrix} \begin{bmatrix} \tau_x \\ \tau_y \\ \tau_z \\ \kappa_x \\ \kappa_y \\ \kappa_z \end{bmatrix} = \begin{bmatrix} T_x \\ T_y \\ T_z \\ M_x \\ M_y \\ M_z \end{bmatrix}$$

The warping displacements are presented only for a qualitative analysis of the solutions.

The accuracy of $\mathbf{K}$ depends on the size of the cross section finite element mesh. Just like in standard finite element analysis, a mesh convergence study should be performed in order to establish the minimum size of the cross section finite element mesh required to obtain realistic values of $\mathbf{K}$. Nonetheless, since BECAS is only being compared to VABS (which is also based on a finite element discretization of the cross section) a mesh convergence study has not been performed. Provided the same finite element mesh is used, both tools will give the same results as can be seen next.

4.2 Numerical examples

All numerical experiments conducted to validate the current implementation of BECAS are presented in this section. The first results are presented for cross section (S1). This first example illustrates the ability of BECAS to handle solid square cross section. In the second case the same solid square cross section geometry is analyzed although in this case it is made of two different materials (S2). The aim is to analyze the behaviour of BECAS when handling cross sections made of different materials with a high contrast between stiffnesses. In the third case the solid square cross section is made of orthotropic material (S3). The objective is to validate the effect of material anisotropy on the cross section stiffness properties estimated by BECAS. In particular we look at the estimated coupling terms arising from the material anisotropy. In the fourth case case the cylinder cross section made of isotropic materials is analyzed (C1). The aim is to analyze the behaviour of BECAS when dealing with thin-walled cross sections. In the fifth example only half the cylinder is modelled (C2). This experiment serves to validate the behaviour of BECAS when handling open thin-walled cross sections. The cylinder cross section is then divided in two and made of two different isotropic materials in the sixth example (C3). Much like in the case of the solid square cross section S2, the aim here is to validate the results of BECAS when studying thin-walled cross sections with extreme material inhomgeneity. A similar procedure is adopted in the seventh example where a layered type of structure is assumed through the thickness of the cylinder (C4). In the eight example, a three cell isotropic cross section is considered (T1). The aim is to validate BECAS for the analysis of multi-celled, thin-walled cross sections. The final example assumes that the three cell cross section is made of isotropic and orthotropic materials (T2). The aim in this case is to validate the results from BECAS for thin-walled, multi-celled, closed cross sections with anisotropic material properties.

4.2.1 Square

The dimensions of the solid square cross section are given in Table 4.3. The cross section is presented in Figure 4.2.

Table 4.3: Geometrical dimensions of solid square beam.

Width (W)	0.1 m
Height (H)	0.1 m

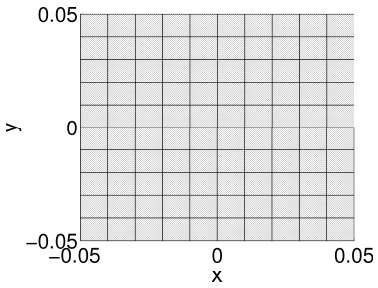

Figure 4.2: Geometry and finite element mesh of square cross section with one material.

Square cross section of isotropic material - S1

In this case the solid square cross section is made of isotropic material #1. The resulting non-zero entries of the cross section stiffness matrix are presented in Table 4.4 for both BECAS and VABS. As can be seen there is a very good agreement between the two approaches. The shear and elastic center calculated by both BECAS and VABS are exactly situated at the origo of the cross section coordinate system. Thus, $x_s = y_s = x_t = y_t = 0$ using both methods. The warping displacements are presented in Figure 4.3 for each

Table 4.4: Non-zero entries of cross section stiffness matrix for square cross section (S1). Comparison between BECAS and VABS

	BECAS	VABS	Diff. (%)
K_{11}	3.4899E-01	3.4900E-01	7.1515E-04
K_{22}	3.4899E-01	3.4900E-01	7.1515E-04
K_{33}	1.0000E+00	1.0000E+00	0.00
K_{44}	8.3384E-04	8.3384E-04	0.00
K_{55}	8.3384E-04	8.3384E-04	0.00
K_{66}	5.9084E-04	5.9084E-04	0.00

of the strain components. The shear strains, $\tau_x = 1$ and $\tau_y = 1$, induces a cross section deformation which matches the analytical results presented by Timoshenko and Goodier in [25]. The same holds for the warping displacements obtained when the torsional curvature $\kappa_z = 1$. The Poisson effect is visible in the results obtained for $\kappa_x = 1$ and $\kappa_y = 1$ with an in-plane expansion and contraction of the compression and tension sides, respectively.

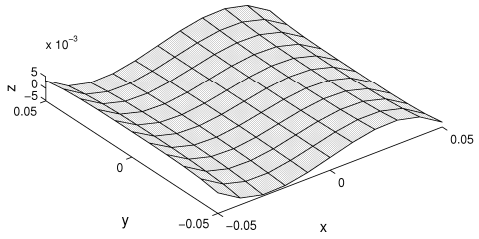

(a) $\tau_x = 1$

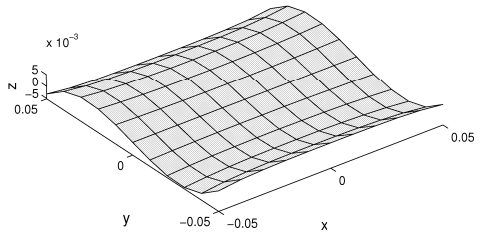

(b) $\tau_y = 1$

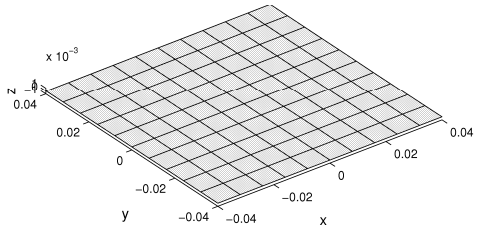

(c) $\tau_z = 1$

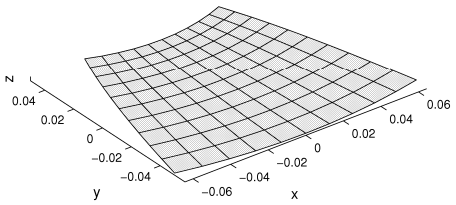

(d) $\kappa_x = 1$

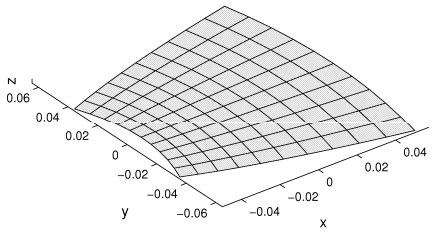

(e) $\kappa_y = 1$

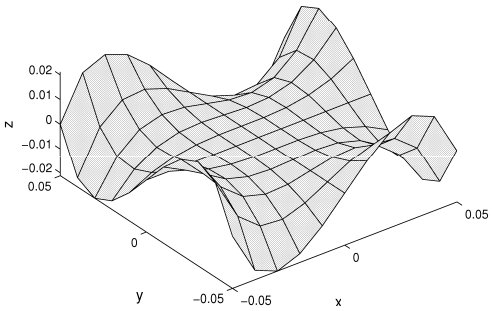

(f) $\kappa_z = 1$

Figure 4.3: Cross section warping displacements for square cross section (S1) (displacements not to scale).

Square cross section of two isotropic materials - S2

The solid square geometry is now divided in two. The section geometry and material distribution are presented in Figure 4.4. The mechanical properties of the isotropic material

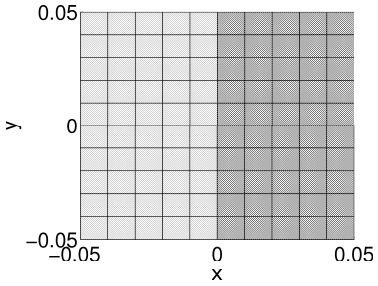

Figure 4.4: Geometry and finite element mesh of square cross section with two materials (S2) – isotropic material #1 (light) and #2 (dark).

#2 are obtained by simply dividing the mechanicals properties of the isotropic material #1 (see Table 4.1) by a factor $\alpha = E_1/E_2$. The variation of the value of the non-zero entries of the cross section stiffness matrix with respect to the stiffness ration E_1/E_2 is presented in Table 4.5. The estimated positions of the shear and elastic centers are presented in Table 4.6. Once again there is a very good agreement between the results from BECAS and VABS. As the stiffness of the material #2 vanishes, the stiffness values and positions

Table 4.5: Non-zero entries of cross section stiffness matrix for square cross section (S2) with respect to E_1/E_2 ration. Comparison between BECAS and VABS.

BECAS							
E_1/E_2	K_{11}	K_{22}	K_{33}	$K_{44} = K_{55}$	K_{66}	K_{26}	K_{35}
1E+00	1.00E+00	3.49E-01	3.49E-01	5.91E-04	8.34E-04	0.00E+00	0.00E+00
1E+01	5.50E-01	1.28E-01	1.92E-01	2.77E-04	4.59E-04	-3.93E-03	1.13E-02
1E+02	5.05E-01	1.38E-01	1.77E-01	2.35E-04	4.21E-04	-4.33E-03	1.24E-02
1E+03	5.00E-01	1.68E-01	1.75E-01	2.31E-04	4.17E-04	-4.37E-03	1.25E-02
1E+04	5.00E-01	1.73E-01	1.75E-01	2.30E-04	4.17E-04	-4.38E-03	1.25E-02
1E+05	5.00E-01	1.73E-01	1.75E-01	2.30E-04	4.17E-04	-4.38E-03	1.25E-02
VABS							
E_1/E_2	K_{11}	K_{22}	K_{33}	$K_{44} = K_{55}$	K_{66}	K_{26}	K_{35}
1E+00	1.00E+00	3.49E-01	3.49E-01	5.91E-04	8.34E-04	0.00E+00	0.00E+00
1E+01	5.50E-01	1.28E-01	1.92E-01	2.77E-04	4.59E-04	-3.93E-03	1.13E-02
1E+02	5.05E-01	1.38E-01	1.77E-01	2.35E-04	4.21E-04	-4.33E-03	1.24E-02
1E+03	5.01E-01	1.68E-01	1.75E-01	2.31E-04	4.17E-04	-4.37E-03	1.25E-02
1E+04	5.00E-01	1.73E-01	1.75E-01	2.30E-04	4.17E-04	-4.38E-03	1.25E-02
1E+05	5.00E-01	1.73E-01	1.75E-01	2.30E-04	4.17E-04	-4.38E-03	1.25E-02
Diff. (%)							
E_1/E_2	K_{11}	K_{22}	K_{33}	$K_{44} = K_{55}$	K_{66}	K_{26}	K_{35}
1E+00	0.00E+00	-7.15E-04	-7.15E-04	-7.20E-04	-1.20E-07	0.00E+00	0.00E+00
1E+01	-5.45E-13	-7.10E-04	-7.17E-04	-7.19E-04	-1.19E-07	-7.17E-04	0.00E+00
1E+02	-3.96E-13	-6.89E-04	-7.19E-04	-7.20E-04	-1.19E-07	-7.19E-04	0.00E+00
1E+03	-3.99E-13	-6.75E-04	-7.19E-04	-7.20E-04	-1.19E-07	-7.19E-04	0.00E+00
1E+04	2.00E-13	-6.73E-04	-7.19E-04	-7.20E-04	-1.19E-07	-7.19E-04	0.00E+00
1E+05	-2.00E-13	-6.72E-04	-7.19E-04	-7.20E-04	-1.19E-07	-7.19E-04	-8.05E-13

of shear and elastic centers converge to those which would be obtained if only half the cross section was considered. Note however the variation of the entry K_{11} with respect to the ration E_1/E_2 plotted in Figure 4.5. The shear stiffness as estimated by both BECAS and VABS decrease past the value obtained for half the section and have a local minima at $E_1/E_2 = 10$. Chen et al. in [15] present a similar result using a different cross section but consider only one extreme value of the stiffness ratio. To the authors' best knowledge there is no study reported in the literature where a similar study is performed.

Finally the cross section warping displacements are presented for different values of ψ in Figure 4.6 considering $E_1/E_2 = 1000$. As the stiffness of material #2 vanishes the extension-bending and shear-torsion coupling terms arise (K_{26} and K_{35} in Table 4.5).

Table 4.6: Shear and elastic center positions ((x_s, y_s) and (x_t, y_t), respectively) for square cross section (S2) with respect to the E_1/E_2 ration. Comparison between BECAS and VABS.

	BECAS		VABS	
E_1/E_2	x_s	y_s	x_s	y_s
1E+00	0.000E+00	0.000E+00	0.000E+00	0.000E+00
1E+01	2.045E-02	0.000E+00	2.045E-02	-2.306E-17
1E+02	2.450E-02	0.000E+00	2.450E-02	5.817E-17
1E+03	2.495E-02	0.000E+00	2.495E-02	-1.385E-16
1E+04	2.500E-02	0.000E+00	2.500E-02	8.010E-17
1E+05	2.500E-02	0.000E+00	2.500E-02	1.683E-16
E_1/E_2	x_t	y_t	x_t	y_t
1E+00	0.000E+00	0.000E+00	0.000E+00	0.000E+00
1E+01	2.045E-02	0.000E+00	0.000E+00	0.000E+00
1E+02	2.450E-02	0.000E+00	2.450E-02	-2.596E-19
1E+03	2.495E-02	0.000E+00	2.495E-02	1.266E-19
1E+04	2.500E-02	0.000E+00	2.500E-02	4.118E-19
1E+05	2.500E-02	0.000E+00	2.500E-02	9.174E-19

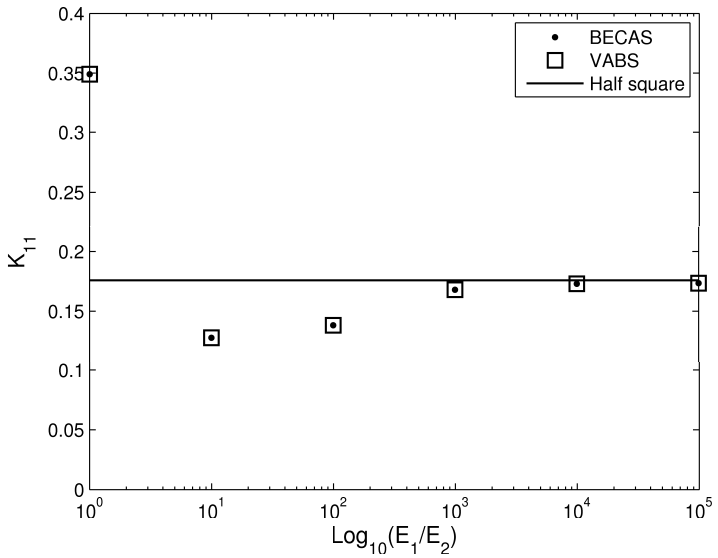

Figure 4.5: Variation of K_{11} entry of the cross section stiffness matrix with respect to the ration E_1/E_2 for the square cross section (S1). Results for BECAS and VABS compared with the solution for half the section.

These coupling effects are visible in the warping displacements. For $\tau_x = 1$ the distortion induced by the shear strain is superimposed by a torsion type of deformation pattern. When $\tau_z = 1$ the tension strain induces a bending type of in-plane deformation visible in the arched form of the cross section.

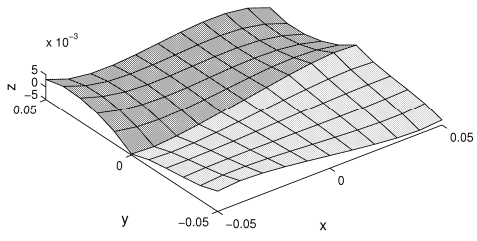

(a) $\tau_x = 1$

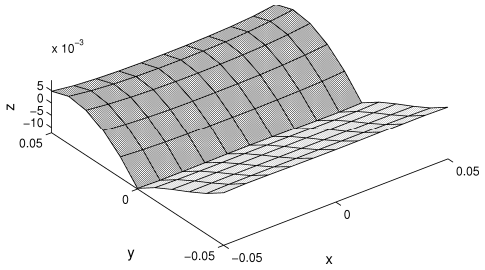

(b) $\tau_y = 1$

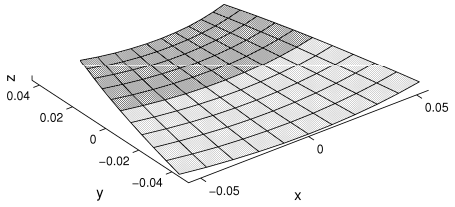

(c) $\tau_z = 1$

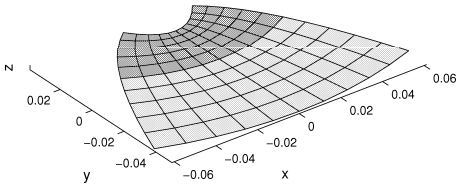

(d) $\kappa_x = 1$

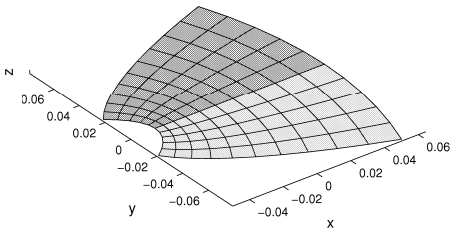

(e) $\kappa_y = 1$

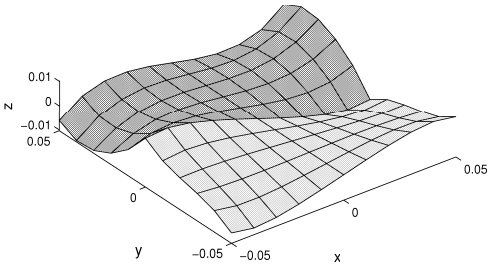

(f) $\kappa_z = 1$

Figure 4.6: Cross section warping displacements for square cross section (S2) where $E_1/E_2 = 1000$ (displacements not to scale).

Square cross section of orthotropic material - S3

In the last example, it is considered that the solid square cross section is made of layered orthotropic material. The fiber plane lies parallel to the xz plane (cf. Figure 4.1) and rotate around the y axis. The variation of the magnitude of the non-zero entries in the cross section stiffness matrix with respect to the fiber orientation are presented in Table 4.7. As

Table 4.7: Non-zero entries of cross section stiffness matrix for square cross section (S3) with respect to fiber orientation (fiber plane parallel to xz plane). Comparison between BECAS and VABS.

	BECAS	VABS	Rel. Diff. (%)	BECAS	VABS	Diff. (%)
	0 °			22.5 °		
K_{11}	5.039E-01	5.039E-01	2.129E-10	7.598E-01	7.598E-01	1.627E-10
K_{22}	4.201E-01	4.201E-01	2.123E-10	4.129E-01	4.129E-01	1.632E-10
K_{33}	4.800E+00	4.800E+00	-2.035E-13	3.435E+00	3.435E+00	7.482E-11
K_{44}	4.001E-03	4.001E-03	6.634E-10	2.489E-03	2.489E-03	7.052E-10
K_{55}	4.001E-03	4.001E-03	6.686E-10	2.274E-03	2.274E-03	9.388E-10
K_{66}	7.737E-04	7.737E-04	9.584E-10	9.499E-04	9.499E-04	9.845E-10
K_{13}	0.000E+00	0.000E+00	0.000E+00	7.387E-01	7.387E-01	2.335E-10
K_{46}	0.000E+00	0.000E+00	0.000E+00	-4.613E-04	-4.613E-04	9.910E-10
	45 °			67.5 °		
K_{11}	8.421E-01	8.421E-01	3.985E-10	6.039E-01	6.039E-01	2.663E-10
K_{22}	4.473E-01	4.473E-01	1.616E-10	4.883E-01	4.883E-01	1.954E-10
K_{33}	1.713E+00	1.713E+00	1.057E-10	1.241E+00	1.241E+00	4.043E-12
K_{44}	1.326E-03	1.326E-03	6.825E-10	1.032E-03	1.032E-03	6.659E-10
K_{55}	1.274E-03	1.274E-03	9.726E-10	1.030E-03	1.030E-03	6.778E-10
K_{66}	1.018E-03	1.018E-03	9.663E-10	9.171E-04	9.171E-04	9.804E-10
K_{13}	4.017E-01	4.017E-01	6.091E-10	6.317E-02	6.317E-02	4.366E-10
K_{46}	-2.422E-04	-2.422E-04	1.042E-09	-4.786E-05	-4.786E-05	1.023E-09
	90 °					
K_{11}	5.0202E-01	5.0202E-01	1.9581E-10			
K_{22}	5.0406E-01	5.0406E-01	2.1603E-10			
K_{33}	1.2000E+00	1.2000E+00	0.0000E+00			
K_{44}	1.0004E-03	1.0004E-03	7.2271E-10			
K_{55}	1.0002E-03	1.0002E-03	6.6684E-10			
K_{66}	8.5081E-04	8.5081E-04	9.5579E-10			
K_{13}	0.0000E+00	0.0000E+00	0.0000E+00			
K_{46}	0.0000E+00	0.0000E+00	0.0000E+00			

can be seen there is a very good agreement between the results from BECAS and VABS. For laminate orientations other than 0° and 90°, the shear-extension and bending-torsion couplings become non-zero. These effects are typical of laminated composite beams. The influence of these couplings on the cross section warping displacements can be observed in Figures 4.7 and 4.8. Comparing with the isotropic case in Section 4.2.1, the bending deformation resulting from the curvature $\tau_z = 1$ is now accompanied of an out-of-plane distortion induced by the torsion coupling. Finally, the position of shear and tension center do not depend on the orientation of fibers in the laminate (i.e., $x_s = y_s = x_t = y_t = 0$). However, note that according to the definition of the shear center (see Section 2.5.2), in this case the position of the shear center is not a property of the cross section. Instead, because the bend-twist coupling $\mathbf{K}_{46} \neq 0$, the shear center position will depend linearly on the coordinate z.

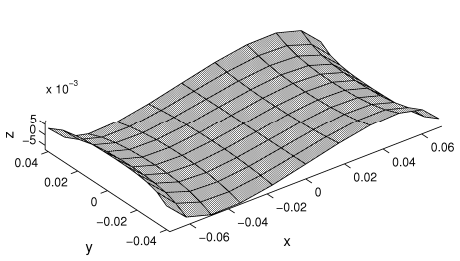

(a) $\tau_x = 1$

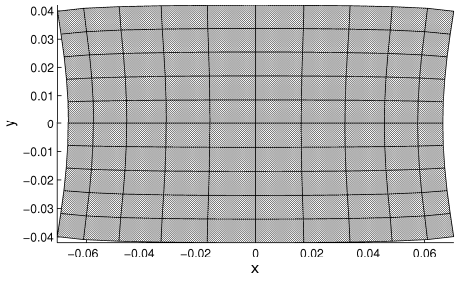

(b) $\tau_x = 1$

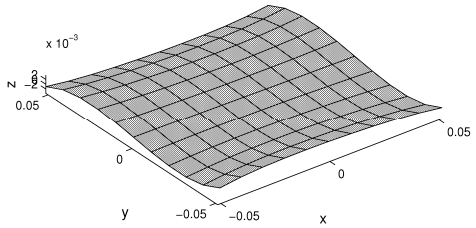

(c) $\tau_y = 1$

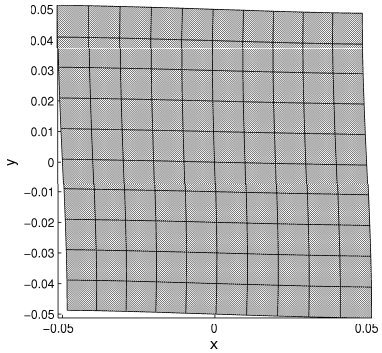

(d) $\tau_y = 1$

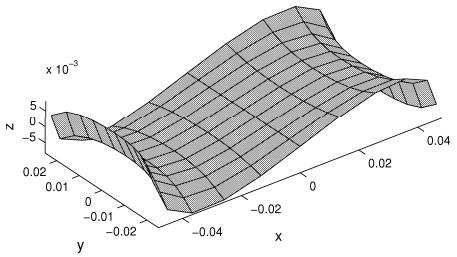

(e) $\tau_z = 1$

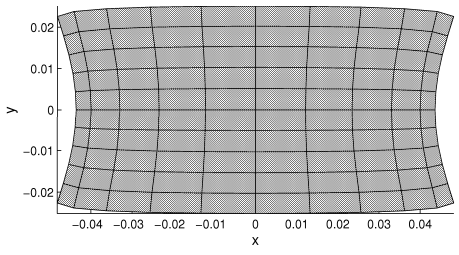

(f) $\tau_z = 1$

Figure 4.7: Cross section warping displacements for square cross section (S3) with fibers oriented at 45°. Out-of-plane (left) and in-plane (right) deformation (displacements not to scale).

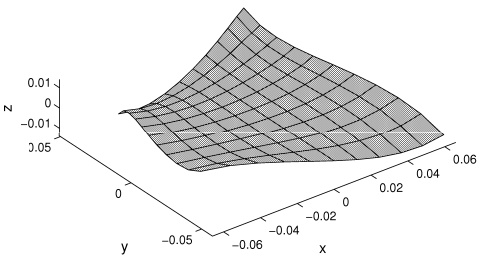

(a) $\kappa_x = 1$

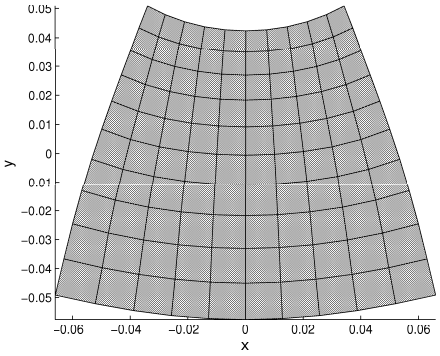

(b) $\kappa_x = 1$

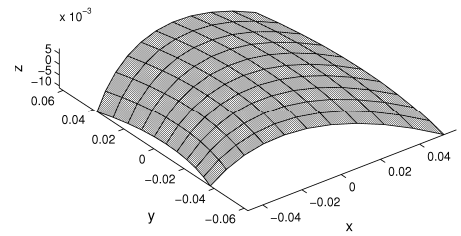

(c) $\kappa_y = 1$

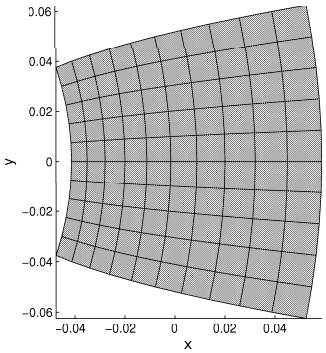

(d) $\kappa_y = 1$

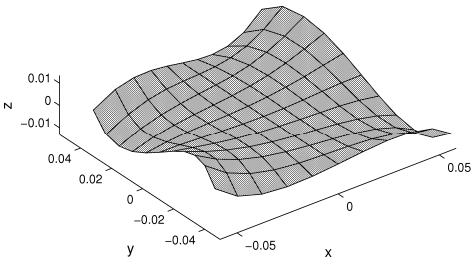

(e) $\kappa_z = 1$

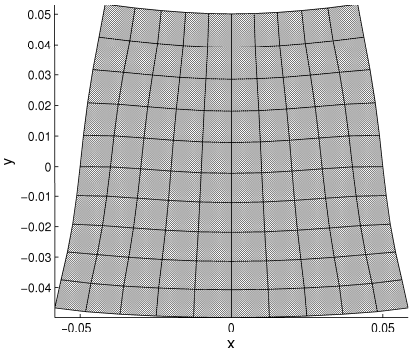

(f) $\kappa_z = 1$

Figure 4.8: (continuation) Cross section warping displacements for square cross section (S3) with fibers oriented at 45°. Out-of-plane (left) and in-plane (right) deformation (displacements not to scale).

4.2.2 Cylinder

In this section results are presented based on the cylinder cross section. The geometrical dimensions of the cylindrical cross section are presented in Table 4.8 and the geometry and finite element mesh are presented in Figure 4.8.

Table 4.8: Geometrical dimensions of cylinder section.

Outer radius (R)	0.1 m
Thickness (t)	0.01 m

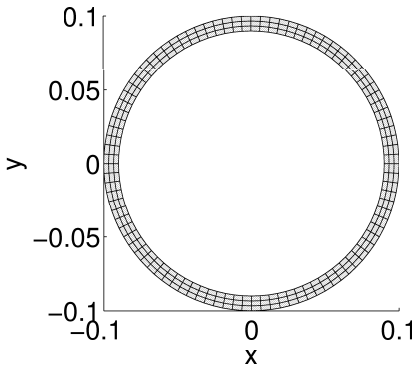

Figure 4.9: Geometry and finite element mesh of cylinder cross section with one material (C1).

Cylinder cross section of isotropic material – C1

In the first case it is assumed that the cylinder is made of isotropic material #1. The non-zero stiffness entries for both BECAS and VABS are presented in Table 4.9. As can be seen there is a very good agreement between the two approaches. The warping displacements are presented in Figure4.10. As expected the the shear strains are the only which induce out-of-plane deformation. Due to the axial symmetry the torsion strain will not induce any out-of-plane deformation. The same holds for the shear and elastic positions which coincide with the origin of the cross section coordinate system. Thus, according both BECAS and VABS $x_s = y_s = x_t = y_t = 0$.

Table 4.9: Non-zero entries of cross section stiffness matrix for cylinder cross section (C1). Comparison between BECAS and VABS.

	BECAS	VABS	Rel. Diff. (%)
K_{11}	1.249E-01	1.249E-01	7.200E-04
K_{22}	1.249E-01	1.249E-01	7.200E-04
K_{33}	5.965E-01	5.965E-01	1.675E-13
K_{44}	2.697E-03	2.697E-03	5.587E-09
K_{55}	2.697E-03	2.697E-03	5.587E-09
K_{66}	2.248E-03	2.248E-03	7.200E-04

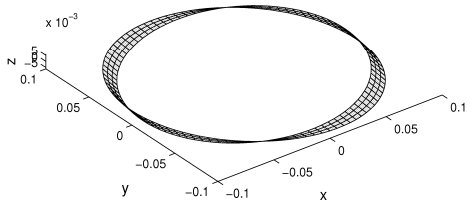

(a) $\tau_x = 1$

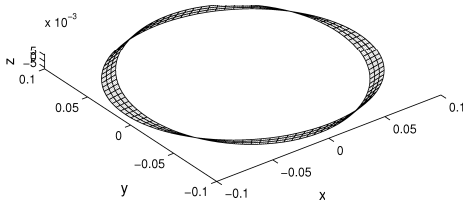

(b) $\tau_y = 1$

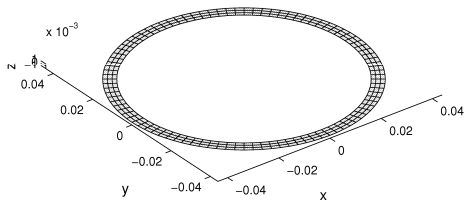

(c) $\tau_z = 1$

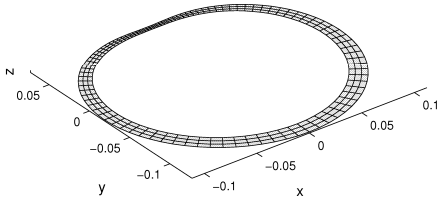

(d) $\kappa_x = 1$

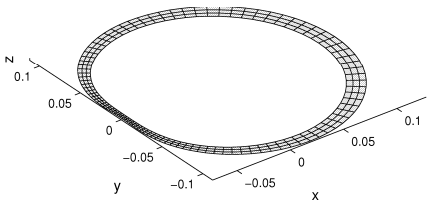

(e) $\kappa_y = 1$

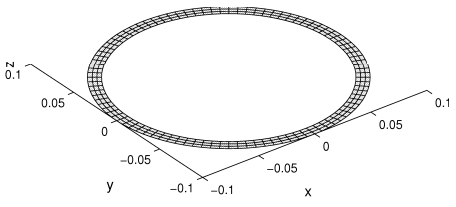

(f) $\kappa_z = 1$

Figure 4.10: Cross section warping displacements for cylinder cross section (C1) (displacements not to scale).

Half-cylinder cross section of isotropic material – C2

The cylinder cross section studied in the previous chapter is divided in two to generate the half cylinder cross section studied here. The geometry and finite element mesh are presented in Figure 4.11. This is an open cross section and the out-of-plane deformation is significant and should therefore be accounted for in the estimation of the stiffness properties. The value of the non-zero entries in the cross section stiffness matrix as estimated by

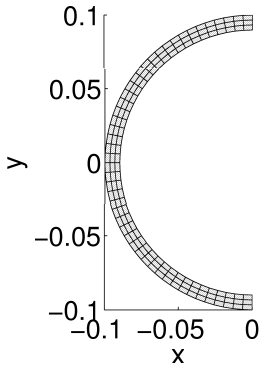

Figure 4.11: Geometry and finite element mesh of half-cylinder cross section (C2).

both BECAS and VABS are presented in Table 4.10. As can be seen there is a very good agreement between the two methods. The same is observed in the estimated positions of the elastic and shear center as presented in Table 4.11. Finally, the warping displacements for different values of the strain parameters $\boldsymbol{\psi}$ are presented in Figure 4.12. Note that the magnitude of the warping displacements for $\kappa_z = 1$, torsional curvature, are of the order of $\mathrm{O}(10^7)$. Hence it is expected that the resulting strains and stresses will also be very large also. This result serves to illustrate the fact that open cross sections are weaker in torsion then closed cross sections.

Table 4.10: Non-zero entries of cross section stiffness matrix for half-cylinder cross section (C2). Comparison between BECAS and VABS.

	BECAS	VABS	Rel. Diff. (%)
K_{11}	4.964E-02	4.964E-02	7.195E-04
K_{22}	6.244E-02	6.244E-02	7.200E-04
K_{33}	2.982E-01	2.982E-01	0.000E+00
K_{44}	1.349E-03	1.349E-03	4.672E-09
K_{55}	1.349E-03	1.349E-03	4.637E-09
K_{66}	9.120E-04	9.120E-04	7.200E-04
K_{35}	1.805E-02	1.805E-02	8.862E-12
K_{26}	-7.529E-03	-7.529E-03	7.200E-04

Table 4.11: Shear and elastic center positions ((x_s, y_s) and (x_t, y_t), respectively) for half-cylinder cross section (C2). Comparison between BECAS and VABS.

	BECAS	VABS	Diff. (%)
x_s	-1.206E-01	-1.206E-01	0
y_s	0.	0	0
x_t	-6.051E-02	-6.051E-02	0
y_t	0.	0	0

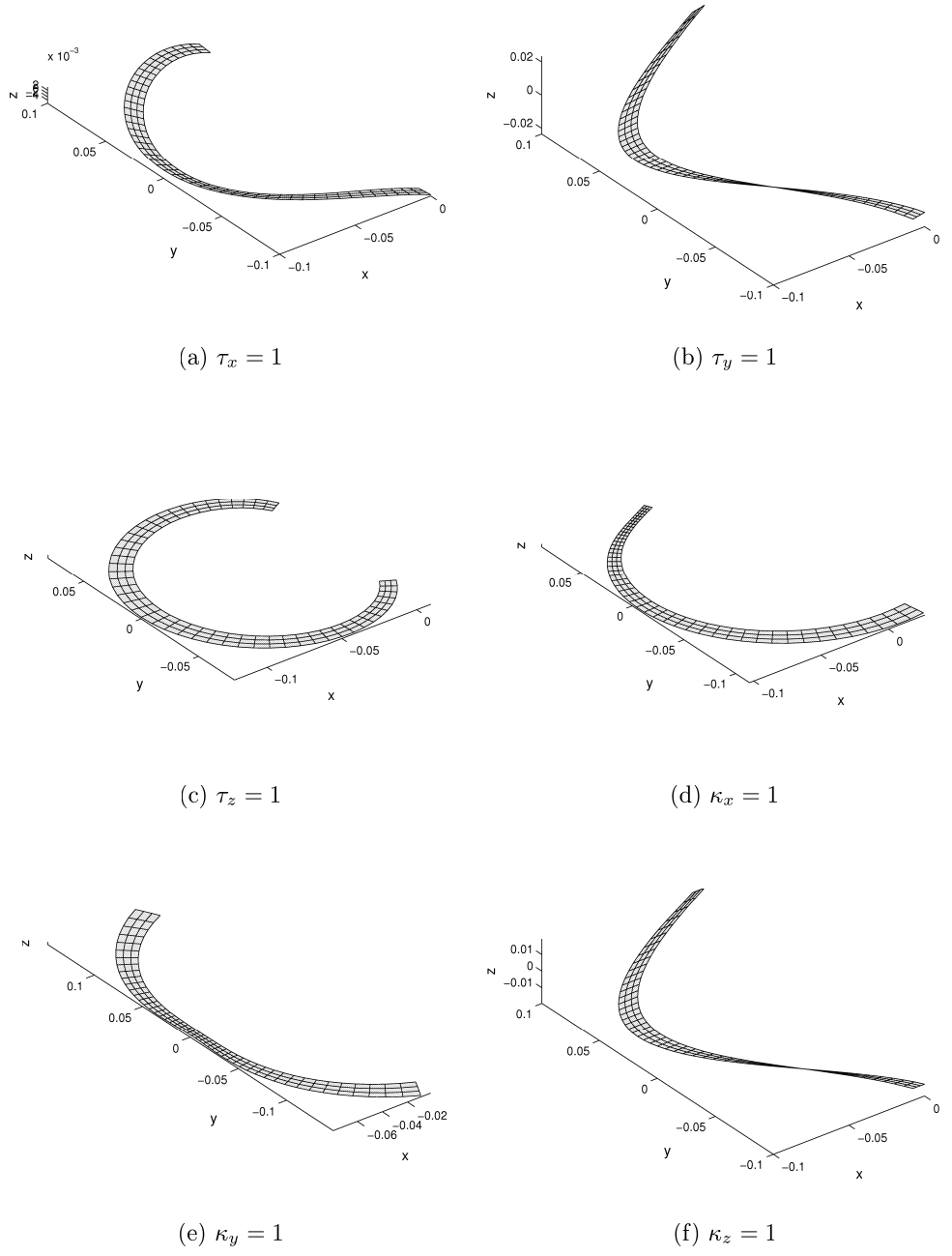

(a) $\tau_x = 1$ (b) $\tau_y = 1$

(c) $\tau_z = 1$ (d) $\kappa_x = 1$

(e) $\kappa_y = 1$ (f) $\kappa_z = 1$

Figure 4.12: Cross section warping displacements for half-cylinder cross section (C2) (displacements not to scale).

Cylinder cross section of two isotropic material (half) – C3

The effect of extreme material inhomogeneity is investigated here following the approach described in Section 4.2.1 for the solid square cross section. The cylindrical cross section is divided in two. One half is made of the isotropic material #1 while the second half of the cylinder cross section is made of the isotropic material #2. The distribution of the two materials in the cross section can be seen in Figure 4.13. The resulting non-zero entries of

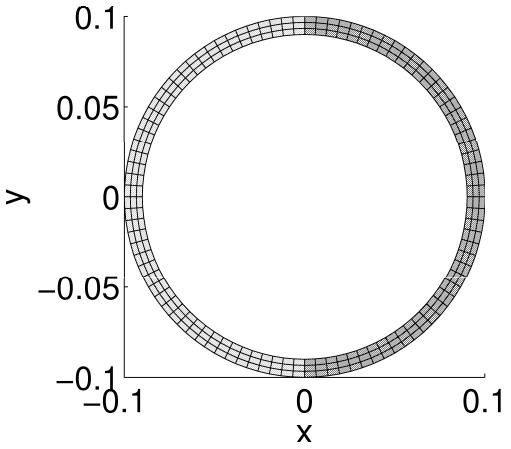

Figure 4.13: Geometry and finite element mesh of cylinder cross section with two materials (C3) – isotropic material #1 (light) and #2 (dark).

the cross section stiffness matrix are given in Table 4.12 with respect to the ration E_1/E_2. As can be seen there is a very good match between BECAS and VABS. As the stiffness of the isotropic material #2 vanishes the entries of the cross section stiffness matrix converge to those which were obtained when only half the cross section was considered (see Section 4.2.2). Note once again the behaviour of the K_{11} entry with respect to the ration E_1/E_2 plotted in Figure 4.14. Just like in the case of the solid square cross section in Section 4.2.1, the shear stiffness seems to decrease past the half-cylinder values having a minima at $E_1/E_2 = 10$. Finally the variation of the positions of the shear and elastic centers with respect to the ration E_1/E_2 are presented in Table 4.13. There is a very good agreement between BECAS and VABS. Also, note that the positions of the shear and elastic center do not explain the behavior of the K_{11} entry. The warping deformations for $E_1/E_2 = 1000$ are presented in Figure 4.15. The warping deformations in this case are also relatively large and in the same order of magnitude as the half-cylinder cross section.

Table 4.12: Non-zero entries of cross section stiffness matrix for cylinder cross section (C3) with respect to E_1/E_2. Comparison between BECAS and VABS.

BECAS							
E_1/E_2	K_{11}	K_{22}	K_{33}	$K_{44} = K_{55}$	K_{66}	K_{26}	K_{35}
1E+00	1.25E-01	1.25E-01	5.96E-01	2.70E-03	2.25E-03	-1.90E-18	0.00E+00
1E+01	3.99E-02	6.87E-02	3.28E-01	1.48E-03	1.08E-03	6.78E-03	1.62E-02
1E+02	3.75E-02	6.31E-02	3.01E-01	1.36E-03	9.29E-04	7.45E-03	1.79E-02
1E+03	4.74E-02	6.25E-02	2.99E-01	1.35E-03	9.14E-04	7.52E-03	1.80E-02
1E+04	4.94E-02	6.24E-02	2.98E-01	1.35E-03	9.12E-04	7.53E-03	1.80E-02
1E+05	4.96E-02	6.24E-02	2.98E-01	1.35E-03	9.12E-04	7.53E-03	1.80E-02
VABS							
E_1/E_2	K_{11}	K_{22}	K_{33}	K_{44}	$K_{55} = K_{55}$	K_{34}	K_{16}
1E+00	1.25E-01	1.25E-01	5.96E-01	2.70E-03	2.25E-03	-1.94E-18	0.00E+00
1E+01	3.99E-02	6.87E-02	3.28E-01	1.48E-03	1.08E-03	6.78E-03	1.62E-02
1E+02	3.75E-02	6.31E-02	3.01E-01	1.36E-03	9.29E-04	7.45E-03	1.79E-02
1E+03	4.74E-02	6.25E-02	2.99E-01	1.35E-03	9.14E-04	7.52E-03	1.80E-02
1E+04	4.94E-02	6.24E-02	2.98E-01	1.35E-03	9.12E-04	7.53E-03	1.80E-02
1E+05	4.96E-02	6.24E-02	2.98E-01	1.35E-03	9.12E-04	7.53E-03	1.80E-02
Diff (%)							
E_1/E_2	K_{11}	K_{22}	K_{33}	K_{44}	$K_{55} = K_{55}$	K_{34}	K_{16}
1E+00	-7.20E-04	-7.20E-04	-1.68E-13	-5.59E-09	-7.20E-04	-2.17E+00	0.00E+00
1E+01	-7.20E-04	-7.20E-04	-3.05E-13	-5.33E-09	-7.20E-04	-7.20E-04	-2.15E-11
1E+02	-7.20E-04	-7.20E-04	-3.32E-13	-4.82E-09	-7.20E-04	-7.20E-04	-2.13E-11
1E+03	-7.20E-04	-7.20E-04	0.00E+00	-4.67E-09	-7.20E-04	-7.20E-04	-4.45E-12
1E+04	-7.19E-04	-7.20E-04	-7.05E-12	-4.66E-09	-7.20E-04	-7.20E-04	2.21E-12
1E+05	-7.19E-04	-7.20E-04	1.27E-11	-4.68E-09	-7.20E-04	-7.20E-04	-2.23E-12

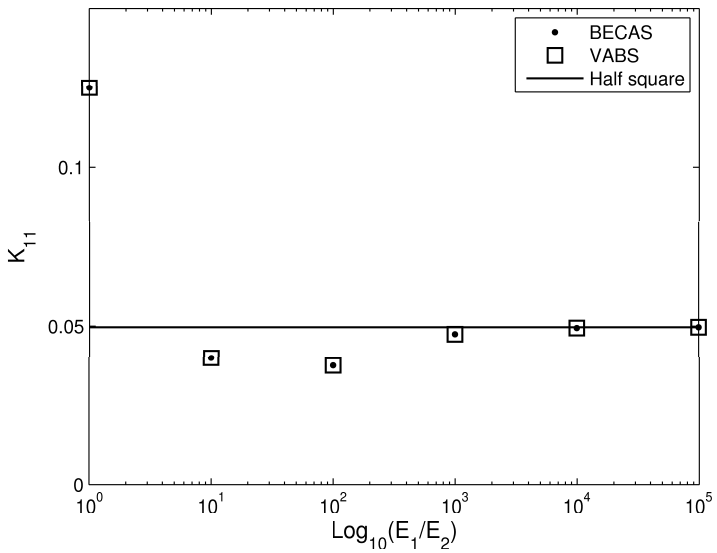

Figure 4.14: Variation of K_{11} entry of the cross section stiffness matrix with respect to the ration E_1/E_2 for the cylinder cross section (C3). Results for BECAS and VABS compared with the solution for half cylinder.

Table 4.13: Shear and elastic center positions ((x_s, y_s) and (x_t, y_t), respectively) for cylinder cross section (C3) with respect to the ration E_1/E_2. Comparison between BECAS and VABS.

	BECAS		VABS	
E_1/E_2	x_s	y_s	x_s	y_s
1E+00	0.000E+00	0.000E+00	0.000E+00	0.000E+00
1E+01	-9.866E-02	0.000E+00	-9.866E-02	-1.069E-15
1E+02	-1.182E-01	0.000E+00	-1.182E-01	-1.415E-15
1E+03	-1.203E-01	0.000E+00	-1.203E-01	-1.292E-15
1E+04	-1.206E-01	0.000E+00	-1.206E-01	3.740E-16
1E+05	-1.206E-01	0.000E+00	-1.206E-01	1.308E-15
E_1/E_2	x_t	y_t	x_t	y_t
1E+00	0.000E+00	0.000E+00	0.000E+00	0.000E+00
1E+01	-4.951E-02	0.000E+00	-4.951E-02	3.279E-17
1E+02	-5.931E-02	0.000E+00	-5.931E-02	1.920E-17
1E+03	-6.039E-02	0.000E+00	-6.039E-02	3.411E-18
1E+04	-6.050E-02	0.000E+00	-6.050E-02	4.960E-18
1E+05	-6.051E-02	0.000E+00	-6.051E-02	-1.255E-18

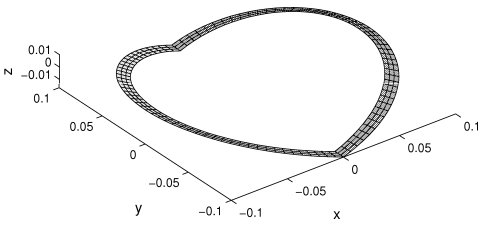

(a) $\tau_x = 1$

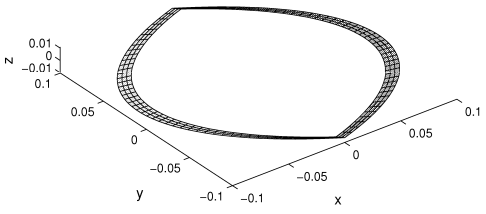

(b) $\tau_y = 1$

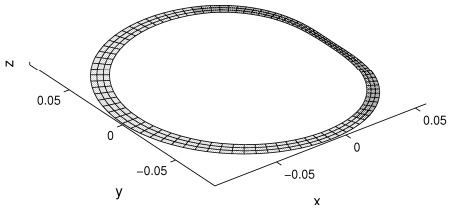

(c) $\tau_z = 1$

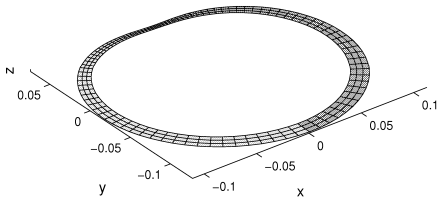

(d) $\kappa_x = 1$

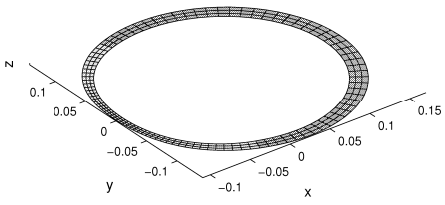

(e) $\kappa_y = 1$

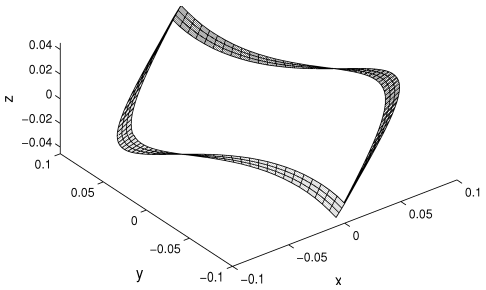

(f) $\kappa_z = 1$

Figure 4.15: Cross section warping displacements for cylinder cross section (C3) with $E_1/E_2 = 1000$ (displacements not to scale).

Cylinder cross section of two isotropic materials (layered) – C4

In the final numerical example using the cylinder cross section we assume a layered structure through the thickness. The material distribution, geometry and cross section finite element mesh are presented in Figure 4.16. It is assumedin this case that $E_1/E_2 = 1000$. The resulting non-zero entries of the cross section stiffness matrix as estimated by both

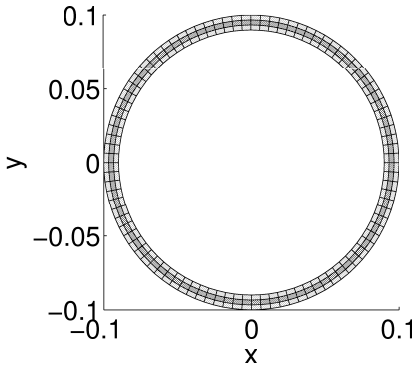

Figure 4.16: Geometry and finite element mesh of cylinder cross section with two isotropic materials (layered) (C4) – isotropic material #1 (light) and #2 (dark).

BECAS and VABS are presented in Table 4.14. As can be seen there is a very good agreement between the two cross section analysis tools. The warping displacements resulting

Table 4.14: Non-zero entries of cross section stiffness matrix for cylinder cross section with two isotropic materials (layered) (C4). Comparison between BECAS and VABS.

	BECAS	VABS	Rel. Diff. (%)
K_{11}	8.3114E-02	8.3115E-02	7.1996E-04
K_{22}	8.3114E-02	8.3115E-02	7.1996E-04
K_{33}	3.9784E-01	3.9784E-01	0.00
K_{44}	1.8012E-03	1.8012E-03	0.00
K_{55}	1.8012E-03	1.8012E-03	0.00
K_{66}	1.5010E-03	1.5010E-03	7.1996E-04

from different cross section strains are presented in Figure 4.17. The deformation patterns are very similar to those obtained in the case where only the isotropic material #1 is used. The differences can be seen in the shear deformation which shows some local perturbations due to the lower stiffness of middle layer.

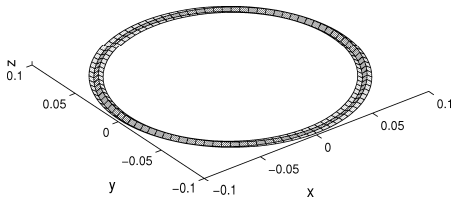

(a) $\tau_x = 1$

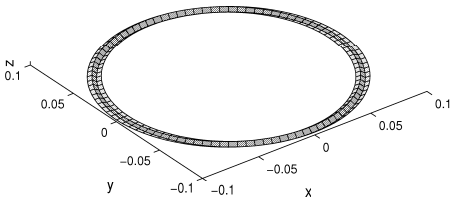

(b) $\tau_y = 1$

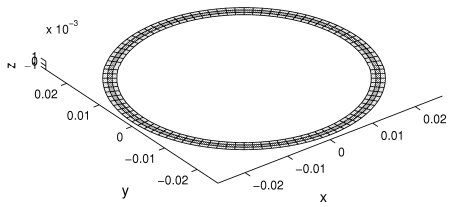

(c) $\tau_z = 1$

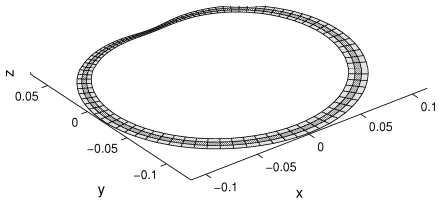

(d) $\kappa_x = 1$

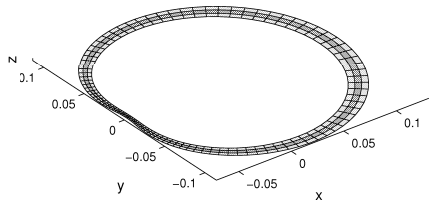

(e) $\kappa_y = 1$

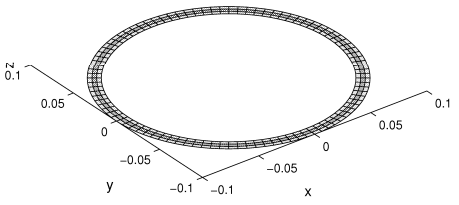

(f) $\kappa_z = 1$

Figure 4.17: Cross section warping displacements for cylinder cross section with two isotropic materials (layered) (C4) (displacements not to scale).

4.2.3 Three cells

In the final group of numerical examples a three cell sectional geometry is considered. The geometry, corresponding dimensions and finite element mesh for the three cell cross section are presented in Figure 4.18. Some cross section analysis theories rely on the integration of the shear flux over each of the closed cells. The aim of this example is to illustrate the ability of BECAS to correctly estimate the stiffness properties of cross sections regardless of the number of cells in the cross section.

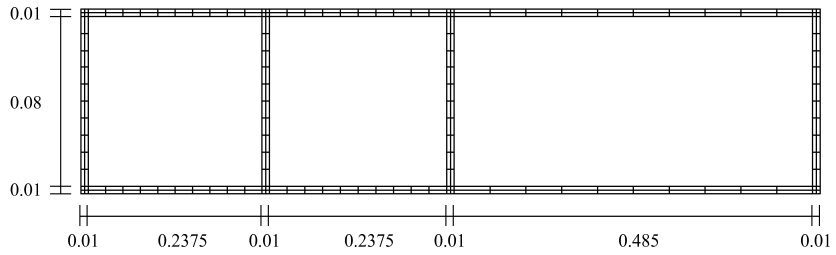

Figure 4.18: Geometry and finite element mesh of three cells cross section of one isotropic material (T1).

Three cells cross section of isotropic material – T1

In this example all faces of the three cell cross section are made of isotropic material #1. The resulting non-zero entries of the cross section stiffness matrix as determined by both BECAS and VABS, are presented in Table 4.15. The estimated positions of

Table 4.15: Non-zero entries of cross section stiffness matrix for three cells cross section (T1). Comparison between BECAS and VABS.

	BECAS	VABS	Rel. Diff. (%)
K_{11}	7.61E-01	7.61E-01	7.20E-04
K_{22}	2.93E-01	2.93E-01	6.92E-04
K_{33}	2.92E+00	2.92E+00	3.35E-13
K_{44}	3.29E-02	3.29E-02	5.88E-08
K_{55}	2.94E-01	2.94E-01	1.63E-09
K_{66}	3.95E-02	3.95E-02	7.20E-04
K_{26}	-8.26E-03	-8.26E-03	6.91E-04
K_{35}	5.75E-02	5.75E-02	-1.55E-11

the shear and elastic center are presented in Table 4.16. As can be seen there is a very

Table 4.16: Shear and elastic center positions ((x_s, y_s) and (x_t, y_t), respectively) for three cells cross section (T1). Comparison between BECAS and VABS.

	BECAS	VABS	Diff. (%)
x_s	-2.823E-02	-2.823E-02	0
y_s	0.	0	0
x_t	-1.969E-02	-1.969E-02	0
y_t	0.	0	0

good agreement between BECAS and VABS for all results. The warping displacements obtained for different values of the components of $\boldsymbol{\psi}$ are presented in Figure 4.19. As can

be seen the shear-torsion coupling term K_{26} and the extension-bending coupling K_{35} are non-zero. The effect of these couplings on the warping deformations can be seen for $\tau_y = 1$ and $\tau_z = 1$, respectively. This is due to the shift in the shear and elastic center positions due to the asymmetric geometry.

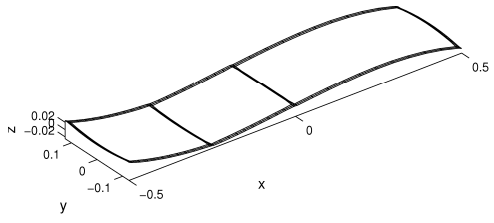

(a) $\tau_x = 1$

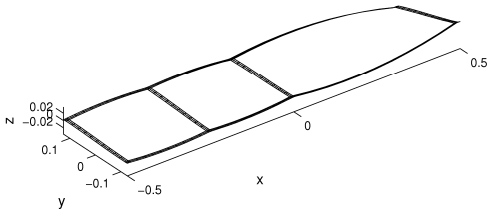

(b) $\tau_y = 1$

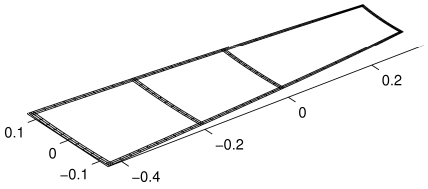

(c) $\tau_z = 1$

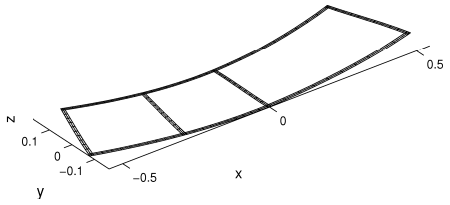

(d) $\kappa_x = 1$

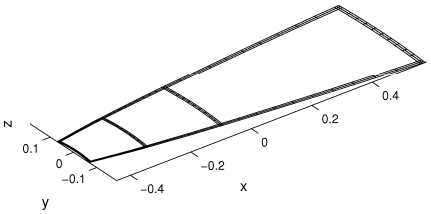

(e) $\kappa_y = 1$

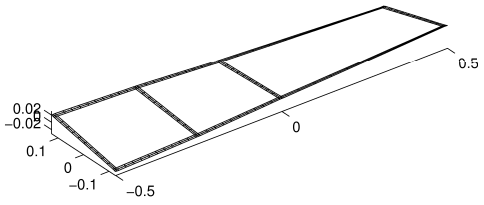

(f) $\kappa_z = 1$

Figure 4.19: Cross section warping displacements for three cells cross section (T1) (displacements not to scale).

Three cells cross section of orthotropic top faces and isostropic webs - T2

In the last numerical experiment the top faces of the three cells cross section are laminated using the orthotropic material oriented at 45°. The vertical faces are made of isotropic material. The material distribution is visible in Figure 4.20. The aim is to combine in

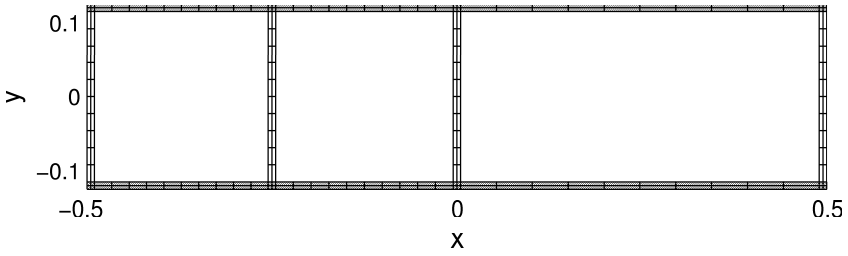

Figure 4.20: Geometry and finite element mesh of three cells cross section with orthotropic material at 45° in the top faces (dark) and isotropic material in the vertical shear webs (light) T2.

one experiment the effects of material anisotropy and inhomogeneity using a closed thin-walled multi-cell cross section. The non-zero entries of the cross section stiffness matrix as estimated by BECAS and VABS are presented in Table 4.17. As can be seen there is a very good agreement between both methods. The resulting positions of the shear and elastic center are presented in Table 4.18. Like before, both BECAS and VABS present a very good agreement in the estimation of the shear and elastic center.

Table 4.17: Non-zero entries of cross section stiffness matrix for three cells cross section with orthotropic material at 45° in the top faces and isotropic material in the vertical webs (T2).

	BECAS	VABS	Rel. Diff. (%)
K_{11}	1.79E+00	1.79E+00	1.36E-10
K_{22}	3.22E-01	3.22E-01	2.13E-09
K_{33}	4.37E+00	4.37E+00	2.98E-11
K_{44}	5.23E-02	5.23E-02	2.16E-10
K_{55}	3.81E-01	3.81E-01	1.21E-10
K_{66}	7.73E-02	7.73E-02	3.29E-10
K_{31}	-8.48E-01	-8.48E-01	1.13E-10
K_{35}	5.64E-02	5.64E-02	-3.88E-11
K_{15}	2.75E-03	2.75E-03	6.11E-09
K_{26}	-1.49E-02	-1.49E-02	2.42E-09
K_{24}	-3.13E-03	-3.13E-03	2.16E-09
K_{64}	1.83E-02	1.83E-02	5.79E-10

Table 4.18: Shear and elastic center positions ((x_s, y_s) and (x_t, y_t), respectively) for three cells cross section T2. Comparison between BECAS and VABS.

	BECAS	VABS	Diff. (%)
x_s	-4.300E-02	-4.300E-02	0
y_s	0.	0	0
x_t	-1.456E-02	-1.456E-02	0
y_t	0.	0	0

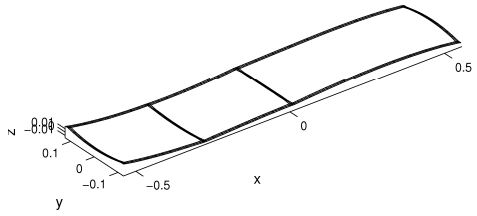

(a) $\tau_x = 1$

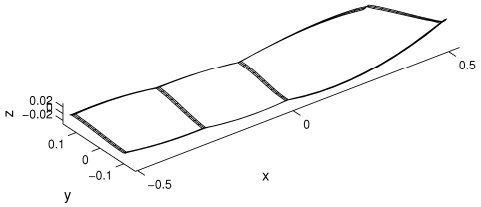

(b) $\tau_y = 1$

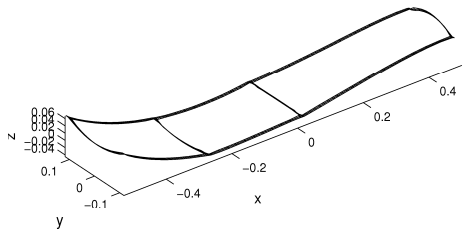

(c) $\tau_z = 1$

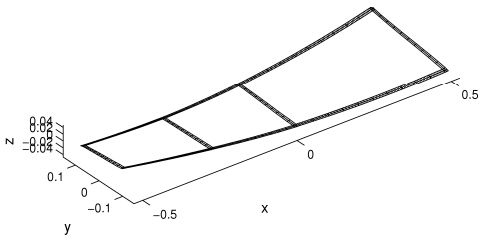

(d) $\kappa_x = 1$

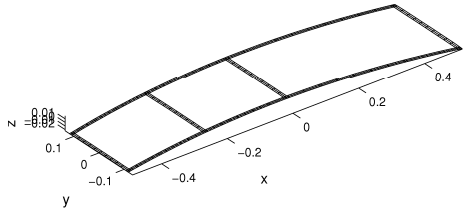

(e) $\kappa_y = 1$

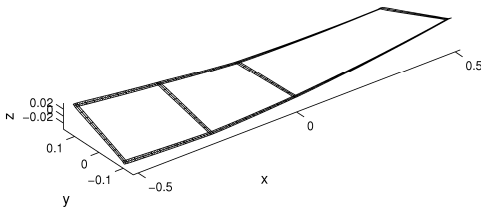

(f) $\kappa_z = 1$

Figure 4.21: Cross section warping displacements for three cells cross section with orthotropic material at 45° in the top faces and isotropic material in the vertical shear webs T2 (displacements not to scale).

Chapter 5

Conclusions

This report described the development, implementation and validation of the cross section analysis tool BECAS (BEam Cross section Analysis Software). The theory underlying the evaluation of the cross section stiffness properties has been thoroughly described. Furthermore, expressions have been derived for the development of a three dimensional linear beam finite element based on the results from BECAS. Finally, the gradients of the cross section stiffness matrix with respect to a generic design variable have been presented envisaging the application of BECAS in an optimal design context.

The numerical implementation of the theory has been subsequently addressed. Two different implementations have been considered. The first is based on a two dimensional finite element representation of the cross section and is the basis for the BECAS implementation. The second is an illustration of the implementation of the method for commercial finite element codes.

At last, the validation of BECAS was presented. The cross section stiffness properties estimated by BECAS have been compared against VABS (the Variational Asymptotic Beam Section Analysis by Yu et al. [13]). Results are presented for different combinations of solid, thin-walled and open cross sections, and isotropic and layered orthotropic materials. It is shown that the results from BECAS match exactly those of VABS for all cases. In particular, BECAS is able to correctly predict all geometrical and material induced couplings which is a typical challenge for this type of tools. These results strongly suggest that BECAS is an efficient and robust cross section analysis tool able to handle a large range of section geometries and material properties.

Bibliography

[1] Ganguli R., Chopra I., *Aeroelastic optimization of a helicopter rotor with composite coupling*, Journal of Aircraft, 32(6), 1326-1334, 1995

[2] Li L., Volovoi V. V., Hodges D. H., *Cross-sectional design of composite rotor blades*, Journal of the American Helicopter Society, 53(3), 240-251, 2008

[3] Blasques J. P., Stolpe M., *Maximum stiffness and minimum weight optimization of laminated composite beams using continuous fiber angles*, Structural and Multidisciplinary Optimization, DOI: 10.1007/s00158-010-0592-9, 2010

[4] Hansen M. O. L., Sørensen J. N., Voutsinas S., Sørensen N., Madsen H. A., *State of the art in wind turbine aerodynamics and aeroelasticity*, Progress in Aerospace Sciences, (42), 285-330, 2006

[5] Chaviaropoulos, P.K., et al., *Enhancing the damping of wind turbine rotor blades - the DAMPBLADE project*, Wind Energy, 9, 163-177, 2006.

[6] Giavotto V., Borri M., Mantegazza P., Ghiringhelli G., Carmaschi V., Maffiolu G.C., Mussi F., *Anisotropic beam theory and applications*, Composite Structures, (16)1-4, 403-413, 1983

[7] Borri M., Merlini T., *A large displacement formulation for anisotropic beam analysis*, Meccanica, (21), 30-37, 1986

[8] Borri M., Ghiringhelli G. L., Merlini T., *Linear analysis of naturally curved and twisted anisotropic beams*, Composites Engineering, (2)5-7, 433-456, 1992

[9] Ghiringhelli G. L., Mantegazza P., *Linear, straight and untwisted anisotropic beam section properties from solid finite elements*, (4)12, 1225-1239, 1994

[10] Ghiringhelli G. L., *On the thermal problem for composite beams using a finite element semi-discretization*, Composites Part B, (28B), 483-495, 1997

[11] Ghiringhelli G. L., *On the linear three dimensional behaviour of composite beams*, Composites Part B, (28B), 613-626, 1997

[12] Ghiringhelli G. L., Masarati P., Mantegazza P.,*Characterisation of Anisotropic, Non-Homogeneous Beam Sections with Embedded Piezo-Electric Materials*, Journal of Intelligent Material Systems and Structures, (8)10, 842-858, 1997

[13] Yu W., Hodges D. H., Volovoi V., Cesnik C. E. S., *On Timoshenko-like modelling of initially curved and twisted composite beams*, International Journal of Solids and Structures, (39), 5101-5121, 2002

[14] Yu W., Volovoi, V. V., Hodges D. H., Hong X., *Validation of the Variational Asymptotic Beam Sectional Analysis (VABS)*, AIAA Journal, (40)10, 2105-2113, 2002

[15] Chen H., Yu W., Capellaro M., *A critical assessment of computer tools for calculating composite wind turbine blade properties*, Wind Energy, (13)6, 497-516, 2010

[16] Jung S. N., Nagaraj V. T., Chopra I., *Assessment of composite rotor blade modeling techniques*, Journal of the American Helicopter Society, (44)3, 188-205, 1999

[17] Volovoi V. V., Hodges D. H., Cesnik C. E. S., Popescu B., *Assessment of beam modeling methods for rotor blade applications*, Mathematical and Computer Modeling, (33), 1099-1112, 2001

[18] Horgan C. O., *On Saint-Venant's principle in plane anisotropic elasticity*, Journal of Elasticity, (2)3, 169-180, 1972

[19] Choi I., Horgan C. O., *Saint-Venant's principle and end effects in anisotropic elasticity*, Transactions of the ASME, 424-430, 1977

[20] Horgan C. O., Knowles J. K., *Recent developments concerning Saint-Venant's principle*, Advances in Applied Mechanics, (23), 180-262, 1983

[21] Christensen O., *Differentialligninger of uendelige rækker*, ed. Institut for Matematik, Danmarks Tekniske Universitet, 30-32, 2009

[22] Bendsøe, M.P., Sigmund, O., *Topology Optimization: Theory, Methods and Applications*, 2nd Edition, Springer-Verlag, Berlin, 2003

[23] Reddy J. N., *Mechanics of laminated Composite plates and shells: theory and analysis*, 2nd Edition, CRC Press, 1997

[24] Peters S. T., *Handbook of composites*, 2nd Edition, Chapman & Hall, London, 1998

[25] Timoshenko S., Goodier J. N., *Theory of elasticity*, McGraw-Hill, 1951

Appendix A

BECAS

A.1 Description of code

The *BE*am *C*ross section *A*nalysis *S*oftware, BECAS, is implemented as a function in MATLAB. The function can be called issuing the following command

[Constitutive,Centers,Matrices,Solutions]=BECAS(inputdata)

In order to run the function BECAS the following files should be placed in the working path

- `BECAS.m` main file which accepts the user input and returns the results as output
- `Utils.m` used to construct and gather the working arrays.
- `Assemble.m` assembles the finite element matrices.
- `Quad4.m` returns the element stiffness matrices based on four node finite elements.
- `SolveBECAS.m` solves the two linear systems of equations and determines the cross section constitutive matrices.

The structure of `BECAS.m` is described below.

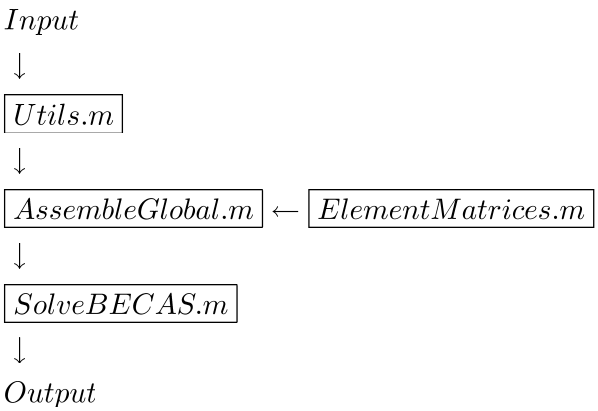

The input and output of the function BECAS is described next.

A.1.1 Input

The input to BECAS consists of the structure `inputdata`. In order to properly run BECAS, this structures should be comprised of the following items where the naming conventions have to be strictly followed

- `inputdata.nl_2d` array size $(n_n, 3)$ storing the list of nodal positions, where n_n is the number of nodes in the cross section mesh. Each of the rows should be organized as [node number, x position, y position].
- `inputdata.el_2d` array size $(n_e, 5)$ storing the element connectivity table, where n_e is the number of elements in the cross section mesh. Each of the rows should be organized as [element number, node 1, node 2, node 3, node 4]. The order of the nodes is according to Figure 3.2.
- `inputdata.emat` array size $(1, n_e)$ storing the material number at each element. The numbering convention for the materials is described next.
- `inputdata.efp` array size $(1, n_e)$ storing the orientation (in degrees) of the fiber plane at each element of the cross section mesh.
- The material properties are setup as follows:
  - `inputdata.EX(i)` the Young modulus of material i in the x direction.
  - `inputdata.EY(i)` the Young modulus of material i in the y direction.
  - `inputdata.EZ(i)` the Young modulus of material i in the z direction.
  - `inputdata.nuxz(i)` the Poisson's ratio of material i in the xz plane.
  - `inputdata.nuyz(i)` the Poisson's ratio of material i in the yz plane.
  - `inputdata.nuxy(i)` the Poisson's ratio of material i in the xy plane.
  - `inputdata.GXZ(i)` the shear modulus in of material i in the xz plane.
  - `inputdata.GYZ(i)` the shear modulus in of material i in the yz plane.
  - `inputdata.GXY(i)` the shear modulus in of material i in the xy plane.
  - `inputdata.dens(i)` the density of material i.
  - `inputdata.nangle(i)` the number of fiber angle orientations to be considered for this material.

The material numbering convention is as follows. Assume that the user inputs the following properties.

```
inputdata.EX(1)=137.6;
inputdata.EY(1)=14.448;
inputdata.EZ(1)=14.448;
inputdata.nuxy(1)=0.21;
inputdata.nuxz(1)=0.21;
inputdata.nuyz(1)=0.21;
inputdata.GXY(1)=5.848;
inputdata.GXZ(1)=5.848;
inputdata.GYZ(1)=5.848;
inputdata.nangle(1)=1;
inputdata.dens(1)=100;

inputdata.EZ(2)=480;
inputdata.EY(2)=120;
inputdata.EX(2)=120;
```

```
inputdata.nuxz(2)=0.19;
inputdata.nuyz(2)=0.26;
inputdata.nuxy(2)=0.19;
inputdata.GXZ(2)=60;
inputdata.GYZ(2)=50;
inputdata.GXY(2)=60;
inputdata.nangle(2)=4;
inputdata.dens(2)=100;
```

In this case we say there are two sets of material properties and five different materials. The first material has the properties defined in the first set above. The second, third, fourth and fifth material are obtained by rotation of the properties in the second set above by 0°, 45°, 90° and 135°, respectively. The angles are defined by the input variable `inputdata.nangle(i)` which defines the number of partitions in the interval $[0, 180]$. This numbering convention has to be considered when building the array `inputdata.emat`.

The file `InputData.m` is distributed together with BECAS to serve as an example. The file `InputData.m` relies on external files containing the list of nodal positions, element connectivity table and material properties for the generation of the input. The nodal list and element connectivity table can be created, e.g., using a finite element preprocessor.

A.1.2 Output

Having performed all the calculations, BECAS returns the following structures: `Constitutive`, `Centers`, `Matrices`, `Solutions` and `utils`. The structure `Constitutive` holds the following arrays corresponding to the cross section stiffness and compliance matrices:

- `Constitutive.Ks` a (6×6) array storing the cross section stiffness matrix $\mathbf{K}$.
- `Constitutive.Fs` a (6×6) array storing the cross section compliance matrix $\mathbf{F}$.
- `Constitutive.Kvabs` a (6×6) array storing the cross section stiffness matrix $\mathbf{K}$ but ordered according to the VABS convention for easy comparison and validation.

The structure `Centers` holds the arrays associated with the position of the cross section shear, elastic and mass centers:

- `Centers.ShearX` the x_s position of the cross section shear center.
- `Centers.ShearY` the y_s position of the cross section shear center.
- `Centers.ElasticX` the x_t position of the cross section elastic center.
- `Centers.ElasticY` the y_t position of the cross section elastic center.
- `Centers.MassX` the x_m position of the cross section mass center.
- `Centers.MassY` the y_m position of the cross section mass center.

The structure `Matrices` holds the matrixes required for the determination of the cross section stiffness properties. The arrays are stored as

- `Matrices.Ag` (6×6) matrix $\mathbf{A}$.
- `Matrices.Rg` $((n_n \times 3) \times 6)$ matrix $\mathbf{R}$.
- `Matrices.Lg` $((n_n \times 3) \times 6)$ matrix $\mathbf{L}$.

- `Matrices.Mg` $((n_n \times 3) \times (n_n \times 3))$ matrix $\mathbf{M}$.
- `Matrices.Eg` $((n_n \times 3) \times (n_n \times 3))$ matrix $\mathbf{E}$.
- `Matrices.Cg` $((n_n \times 3) \times (n_n \times 3))$ matrix $\mathbf{C}$.
- `Matrices.D` $(6 \times (n_n \times 3)$ matrix $\mathbf{D}$ with the constraint equations.

The structure `Solutions` is required for the evaluation of the warping displacements and analysis of the strains in the cross section. Hence,

- `Solutions.X1` $((n_n \times 3) \times 6)$ array $\frac{\partial \mathbf{X}}{\partial z}$.
- `Solutions.Y1` (6×6) array $\frac{\partial \mathbf{Y}}{\partial z}$.
- `Solutions.X0` $((n_n \times 3) \times 6)$ array $\mathbf{X}$.
- `Solutions.Y0` (6×6) array $\mathbf{Y}$.

The final structure `utils` gathers a number of arrays and constants which are necessary throughout the calculation procedure. This structure is output at this point for plotting purposes but is marked for removal at a later versions of BECAS.

A.1.3 Auxiliary MAPLE files

Part of the MATLAB code in BECAS is generated through MAPLE. There are four MAPLE files which follow together with the BECAS code:

- `GenerateMatricesBECAS.mw` used to generate all the element stiffness matrices which are included in the MATLAB file `Quad4.m`.
- `LayerRotationBECAS.mw` used to generate the code for the function which rotates the material constitutive matrix $\mathbf{Q}$ in the MATLAB file `Utils.m` when orienting the fibers in a layer.
- `FiberPlaneRotationBECAS.mw` used to generate the code for the function which rotates the material constitutive matrix $\mathbf{Q}$ when orienting the fiber plane in an element. The fiber plane rotation is performed in `Assemble.m` in order to avoid storing one constitutive matrix for each element.

A.1.4 Examples

All the files required for the replication of the validation examples are distributed together with BECAS. The user should specify the name of the corresponding folder in the file `Inputdata4RunMe.m`. The file `RunMe.m` which calls BECAS should then be ran to obtain the results.

Paper 5

Blasques J.P., Berggreen C., Andersen P., Hydro-elastic analysis and optimization of a composite marine propeller, Marine Structures, 23(1), 22-38, 2010.

Marine Structures 23 (2010) 22–38

Contents lists available at ScienceDirect

Marine Structures

journal homepage: www.elsevier.com/locate/marstruc

Hydro-elastic analysis and optimization of a composite marine propeller

José Pedro Blasques*, Christian Berggreen, Poul Andersen

Department of Mechanical Engineering, Technical University of Denmark, Nils Koppels Allé, Building 403, DK 2800 Kgs. Lyngby, Denmark

ARTICLE INFO

Article history:
Received 19 December 2008
Received in revised form
18 September 2009
Accepted 19 October 2009

Keywords:
Marine propellers
Composite
Hydro-elastic
Optimization
Strength analysis

ABSTRACT

The present paper addresses the design and optimization of a flexible composite marine propeller. The aim is to tailor the laminate to control the deformed shape of the blade and consequently the developed thrust. The development of a hydro-elastic model is presented, and the laminate lay-up which minimizes the fuel consumption for the cruising and maximum speed conditions is simultaneously determined. Results show a reduction of 1.25% in fuel consumption for the combined case corresponding to a decrease of 4.7% in the cruising speed condition. Finally, the strength of the optimal blade is analyzed using the Tsai-Wu strength index. After local tailoring of the laminate configuration throughout the propeller a maximum value of 0.7 is determined indicating no failure will occur under normal operation conditions. The results suggest that it is possible to design a medium-sized flexible composite marine propeller that will enable a reduction of the fuel consumption while withstanding the imposed loads

1. Introduction

Anisotropic composite materials present different levels of elastic couplings which depend on the laminate lay-up. Among these, bending- and extension-twist couplings have been identified as a possible mean for the passive control of composite structures. The aim here is to investigate the possibility of tailoring these elastic couplings to control the performance of a flexible composite

* Corresponding author. Tel.:+45 4525 1379; fax: +45 45884325.
E-mail address: jpb@mek.dtu.dk (J.P. Blasques).

0951-8339/$ – see front matter © 2009 Elsevier Ltd. All rights reserved.
doi:10.1016/j.marstruc.2009.10.002

marine propeller. The shape of the propeller blade will morph under load and thus, if optimized, it will passively adjust itself to the hydrodynamic loads of the different operational conditions. The optimal composite propeller is the one which minimizes the fuel consumption.

The use of elastic couplings to control the passive properties of different structures like wind turbine blades [1,2,3], aircraft wings [4] and helicopter rotor blades [5] has been extensively reported in the literature. The literature concerning the application of laminated composite materials in the design of marine propellers is however limited. Lee et al. [6] have optimized the laminate lay-up of a fixed pitch 0.305 m diameter composite marine propeller using genetic algorithms. The final composite design presents lower values of torque at one of the operation conditions thus outperforming its metal counterpart. An evaluation of the strength properties of a composite propeller blade with 1.4 m diameter has been presented by Lin et al. [7]. The strength is analysed using the Hashin failure criterion and the results illustrate the influence of the laminate type on the stress field and failure modes. Marsh [8] has presented an overview of the developments in the composite propeller industry. A few companies have realized the potential and claim to have designed composite marine propellers with passive properties. Nonetheless, no details of these developments have yet been published.

The work described in this paper extends the available knowledge in the field of design and optimization of composite marine propellers, with special focus on medium size marine propellers. The propeller blade considered throughout this paper is approximately four times larger than those described earlier in the literature. The results presented in this paper will indicate if the possibility and potential of using composite propeller blades in large merchant or naval vessels exists. The hydrodynamic model is based on the boundary element method instead of the lifting line method applied in earlier papers. Moreover, the optimization of the fiber orientations is combined with the strength analysis in one design process. The two analyses have earlier been treated separately.

2. Blade geometry and material properties

The original propeller blade is part of a controllable pitch propeller installed in a naval vessel. The propeller has 4 blades, a diameter, D, of 4.4 m and an expanded area ratio of 0.56. The main geometrical properties of the blade are presented in Table 1 where R is the propeller radius, r is the section radius, θ_{skew} is the sectional skew angle, *Rake* is the sectional rake, P is the sectional pitch, c is the section cord, t is the maximum section thickness and f is the section camber.

Naval vessels typically operate at two very distinct forward speed conditions – herein named cruising and maximum speed conditions – as presented in Table 2. The non-dimensional thrust and torque coefficients K_{T} and K_{Q} are defined as

$$K_T = \frac{T}{\rho n^2 D^4}, \quad K_Q = \frac{Q}{\rho n^2 D^5} \tag{1}$$

where T, Q, ρ and n are the thrust, torque, sea water density and rotational speed, respectively. The service speed, advance ratio, non-dimensional pitch at $r/R = 0.7$, the open water efficiency and the fuel consumption are identified as V_{s}, J, P/D_{07}, η_0 and FC, respectively.

Table 1
Geometrical properties of the propeller blade.

r/R	θ_{skew} [o]	Rake/R	P/D	c/D	t/c	f/c
0.300	0.000	0.0000	0.90665	0.200	0.195	0.000
0.350	−6.033	0.0006	1.02277	0.230	0.159	0.032
0.400	−10.156	−0.0018	1.13893	0.260	0.131	0.040
0.500	−16.663	−0.0250	1.30864	0.320	0.091	0.036
0.600	−16.663	−0.0309	1.42662	0.360	0.067	0.027
0.700	−6.033	−0.0787	1.46216	0.385	0.050	0.020
0.800	6.542	−0.0910	1.38514	0.380	0.037	0.015
0.900	20.141	−0.0807	1.1867	0.320	0.029	0.009
1.000	36.932	−0.0299	0.8685	0.050	0.086	0.000

Table 2
Characterization of the cruising and maximum speed operation conditions. Thrust and torque coefficients are for one blade only.

	Power [kW]	n [rps]	V_s [m/s]	J [−]	P/D_{07} [−]	K_T [−]	K_Q [−]	η_0 [−]	FC [kg/h]
Cruising Speed	1410	1.8	7	0.742	0.925	0.056	0.0091	0.59	26.83
Max. Speed	8380	2.33	11	0.901	1.465	0.176	0.0363	0.65	662.1

The composite marine propeller was designed using carbon/epoxy uni-directional reinforcements with mechanical properties presented in Table 3 (from [9]).

The laminate lay-up will be described using the notation $[(\theta_i)_j]_s$ where the subscript i indicates the design variable numbering and j refers to the number of layers oriented with the angle θ. The layers are assumed to be stacked from pressure side to suction side. Finally, the subscript s indicates symmetry with respect to the mid-thickness plane.

3. Methodology

The initial step in the analysis of the composite propeller consists of the development of the structural and hydrodynamic models. The two models are then combined into a hydro-elastic model which, for a steady incoming flow, determines the equilibrium between the structural and hydrodynamic forces. An optimization algorithm is used next to determine the laminate lay-up which will minimize the fuel consumption. Finally, the strength of the optimal blade is analyzed.

3.1. Structural model

The structural model is able to determine the deformation and stress fields induced by a given hydrodynamic pressure load on the blade. The model is generated and analyzed in the commercial finite element package ANSYS 11 [10]. The blade geometry is approximated by a surface defined by the mid-thickness lines of each section. The surface is subsequently meshed with 8 node isoparametric parabolic layered shell elements (SHELL99). The element thickness or the total laminate thickness at a given node is obtained by linear interpolation of the thickness of the blade at the corresponding position (see Fig. 1(a)). The layer fiber angles are controlled at each element independently.

The displacement degrees of freedom of all nodes at the blade root are constrained to simulate the attachment to the propeller hub. The centrifugal forces are applied as accelerations which are function of the rotational speed. The number of layers is assumed constant and fixed throughout the whole

Table 3
Mechanical properties of the High Tension Carbon/Epoxy uni-directional reinforcement. Subscripts x, y and z refer to the fiber, matrix and out-of-plane directions, respectively. The subscript t and c indicate tension and compression failure, respectively.

	Symbol	Units	
Stiffness Modulus	E_x	GPa	135
	E_y	GPa	15
	E_z	GPa	15
Shear Modulus	G_{xy}	GPa	5
	G_{xz}	GPa	5.3
	G_{yz}	GPa	2.9
Poisson's Ratio	ν_{xy}	–	0.3
	ν_{xz}	–	0.02
	ν_{yz}	–	0.02
Ult. Tensile Strength	$\sigma^f_{x_t}$	MPa	1500
	$\sigma^f_{y_t}$	MPa	50
Ult. Comp. Strength	$\sigma^f_{x_c}$	MPa	1200
	$\sigma^f_{y_c}$	MPa	250
Ult. Shear Strength	σ^f_{xy}	MPa	70
Density	ρ	kg/m^3	1600
Thickness	t	mm	0.3

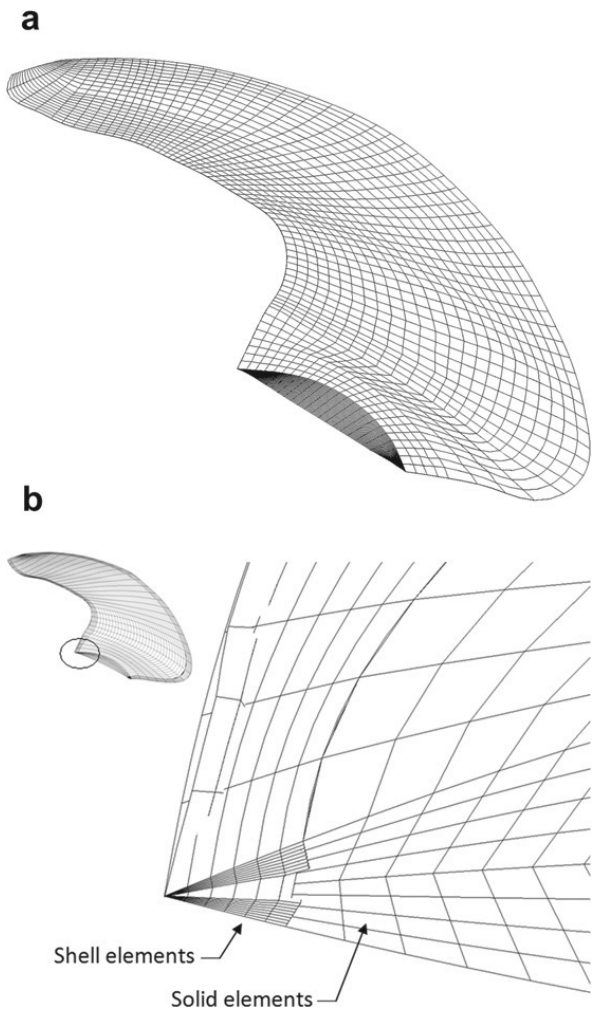

Fig. 1. (a) Aspect of the shell element model seen from the hub towards the tip. The thickness of the elements has been made visible through a graphical artifice in ANSYS. It is possible to observe the thickness variation throughout the elements and thus the shape of the blade. (b) Detail of the solid element model in the trailing edge region seen from the hub towards the tip. The layered solid elements with a total of 8 layers (2 rows of solid elements through the thickness with 8 layers each) are visible together with the shell elements with varying thickness used to mesh the trailing edge.

blade. Furthermore, all layers are assumed to have the same thickness which is a fixed portion of the total blade thickness at the corresponding point of the blade. A mesh convergence analysis aimed at displacements and stresses is conducted. The static analyses showed that a total of 1440 and 5760 shell elements are required for the convergence of the displacement and stress fields, respectively (see Fig. 2(a) and (b)). This model is henceforth named *shell element model*.

Since experimental data are not available to validate the results from the shell element model, a second numerical model is developed as well. In this second model – addressed as *solid element model* – the shape of the blade is defined by its volume. The center part of the blade excluding the leading and trailing edges are meshed using 20 node isoparametric parabolic layered solid elements (SOLID191), whereas the leading and trailing edges (covering approximately 1/16 of the chord length) are meshed with shell elements (SHELL99) (see Fig. 1(b)). An additional layer of shell elements with low stiffness is applied on the solid elements adjacent to the leading and trailing edge. By adopting this approach it is possible to ensure that the deformations contained in the rotational degrees of freedom of the shell elements are partially transferred to the solid elements containing only translational degrees of freedom. The boundary conditions are the same as used before for the shell element model.

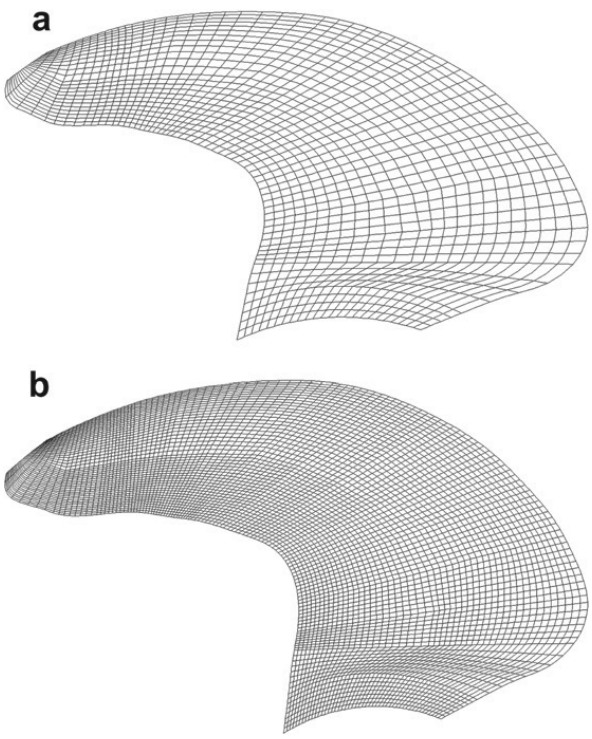

Fig. 2. Shell model mesh: (a) Mesh applied in displacement analysis. (b) Mesh applied in stress analysis. Special care has been devoted to the mesh at the tip region where the elements can suffer large distortions.

The static analyses in this case have shown that a total of 4400 elements are required for both displacement and stress convergence.

The two models are subsequently compared in terms of their ability to predict the influence of the laminate lay-up on the thrust and torque forces. The results are presented in Fig. 3 where it is assumed that the entire blade consists of the same lay-up, $[(\theta)_{32}]$, and hence all layers have the same orientation angle θ. The thrust and torque coefficients are then analyzed as a function of the angle variation, θ. By comparing the two models, it can be seen that the results are in good agreement with a maximum relative difference of 1.4%, implying that the displacement fields predicted by the two models are identical.

All results presented hereafter are obtained using the shell element model. This model is chosen because it requires a shorter computational time which is a critical aspect for the optimization procedure.

3.2. Hydrodynamic model

The hydrodynamic model is used to determine the pressure field induced by a given blade shape. It is based on the boundary element method and assumes that the inflow to the propeller is uniform and steady. Viscous forces have been neglected. A total of 480 section points define the 450 elements which are arranged in a 15×15 three-dimensional structured mesh on both faces of the blade (see Fig. 4).

The pressure is then determined at 450 nodes placed at the center of each element whose corners are defined by the section points (which define the section lines). The pressure distribution is illustrated in Fig. 5. The pressure is furthermore integrated over the hydrodynamic model mesh to determine the values of thrust and torque.

3.3. Hydro-elastic model

The displacement field, {d}, is determined using the finite element method in the structural model, and the hydrodynamic pressure field, {f}, is determined using the boundary element method in the

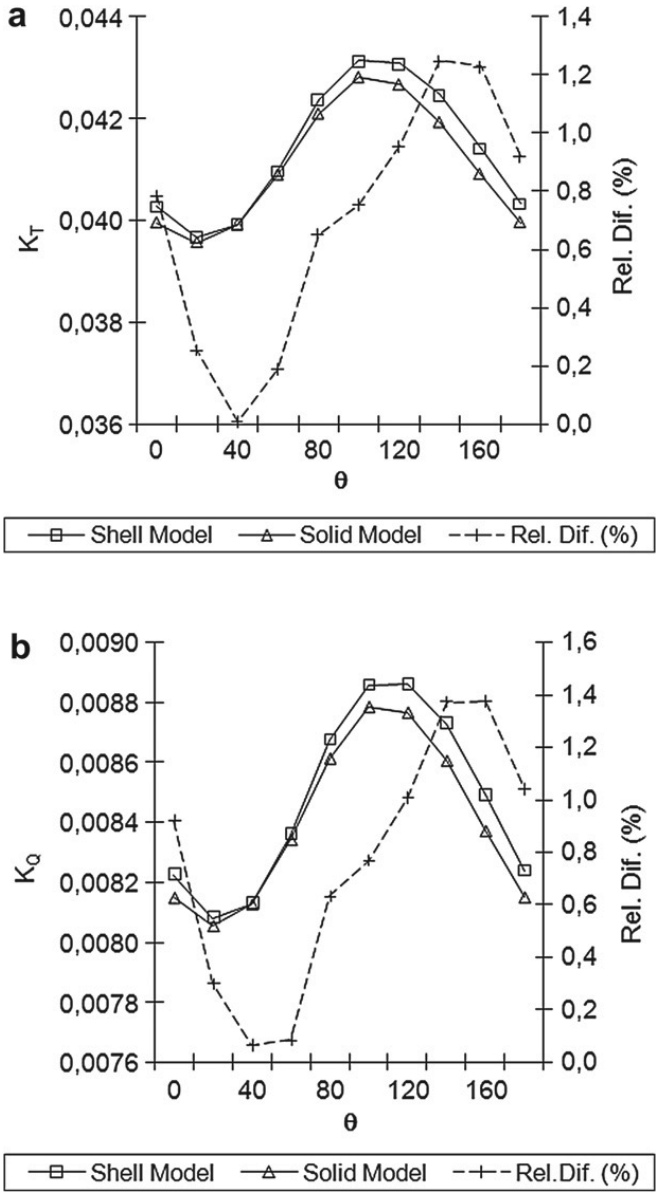

Fig. 3. Thrust (a) and torque (b) coefficients – K_T and K_Q, respectively – and relative difference as a function of the laminate angle θ for the shell and solid element models. The entire blade consists of the same uni-angle laminate lay-up. Results are for one blade only.

hydrodynamic model. The equilibrium between the hydrodynamic and structural forces is obtained by the hydro-elastic model. That is, the hydro-elastic model determines the displacement vector {d} which satisfies $[K]\{d\} = \{f\}$, where K is the structural stiffness matrix which can be tailored by optimizing the laminate lay-up sequence. Since {f} is a function of {d} the problem is nonlinear. However, {f} is only dependent on {d} which makes the problem suited for an iterative solution. The direct substitution method has been chosen.

A schematic description of the algorithm is presented in Fig. 6 where the subscript i indicates the iteration number. Each of the numbered steps is described below:

1) The displacement field is determined by the structural model for a given pressure distribution. At the first iteration the pressure distribution is that of the original blade.

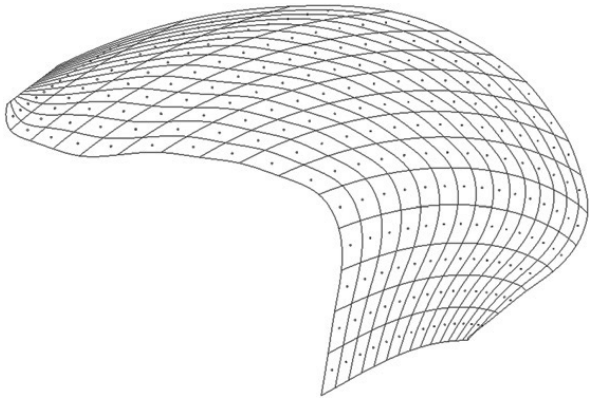

Fig. 4. Mesh of hydrodynamic sub-model (seen from the pressure side). The centroids of the elements are the control points where the pressure is evaluated. The corner points of the elements are the section points which define the geometry of the blade and are updated at each iteration step.

2) The hydrodynamic model mesh is updated based on the displacement field determined in the previous step. The updated position of the section points in the hydrodynamic model is that of the closest node in the structural model.
3) A new pressure field is determined by the hydrodynamic model based on the new shape.
4) The new pressure field given in the hydrodynamic model mesh is mapped onto the structural model. The new pressure value at each node of the structural model is determined by three-dimensional linear interpolation of the pressure calculated at the control points of the hydrodynamic model.

The process is repeated until convergence is achieved and equilibrium is found. The thrust and torque forces are calculated at each iteration. The iteration procedure has converged when the

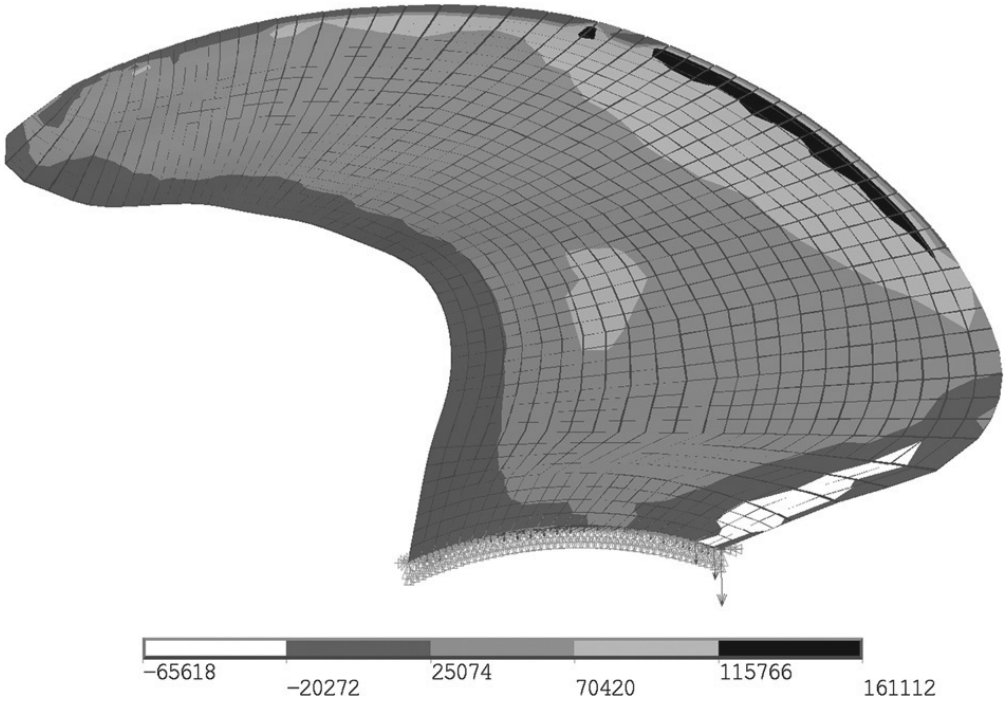

Fig. 5. Distribution of pressure difference (in Pa) over the blade surface looking in the upstream direction.

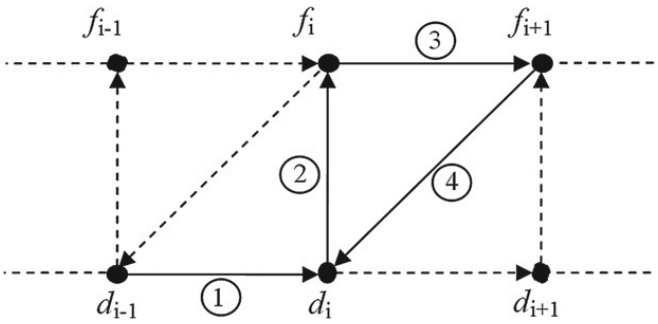

Fig. 6. Algorithm for the computation of the hydro-elastic steady state.

relative difference between the iterations of both thrust and torque is less than 1%. A typical convergence behaviour of the iteration procedure is presented in Fig. 7. According to the convergence criterion stated above, convergence is attained at the third iteration since the relative difference is below 1%. For illustrative purposes, the first 7 iterations are presented for the case where the convergence criterion has been switched off. In general the iterative procedure will converge after 3 or 4 iterations.

3.4. Optimization model

The maximum and cruising speed requirements for the ship and hence the thrust the propeller must generate are typically defined in the initial stage of the design process. Thus, the optimal propeller is the one which produces the desired thrust, the least torque, withstands the pressure forces, reduces the risk of cavitation and satisfies noise and vibration constraints. In this investigation the cavitation, noise and vibration constraints have been neglected. The strength constraints have not been included in the optimization model, but have instead been studied separately in parallel. The optimization problem is therefore posed as a torque minimization problem and formally stated as:

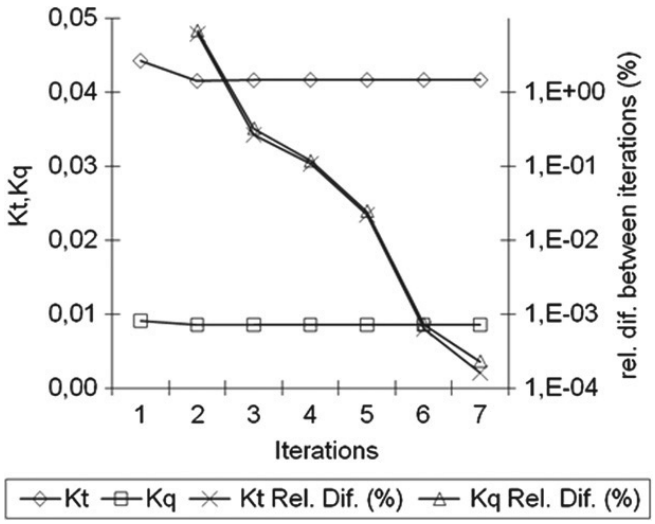

Fig. 7. Convergence behavior of the hydro-elastic model.

$$\min_{\theta_n\in\Re,\ \varphi_C\in\Re,\ \varphi_M\in\Re} CFOC(Q_C(\theta,\varphi_C),Q_M(\theta,\varphi_M)) \tag{2}$$

$$\begin{aligned} subject\ to: & \frac{T_C^o(\theta,\varphi_C)}{T_C(\theta,\varphi_C)}-1\le 0\\ & \frac{T_M^o(\theta,\varphi_M)}{T_M(\theta,\varphi_C)}-1\le 0\\ & 0\le\theta_n<180\\ & \varphi_{C,min}\le\varphi_C<\varphi_{C,max} \end{aligned}$$

where the combined fuel oil consumption, CFOC, is function of the torque at both conditions and is given by

$$CFOC(Q_C(\theta,\varphi_C),Q_M(\theta,\varphi_M)) = \Delta t_C\cdot SFOC_C\cdot 2\cdot\pi\cdot n_C\cdot Q_C(\theta,\varphi_C)+\Delta t_M\cdot SFOC_M\cdot 2\cdot\pi\cdot n_M\cdot Q_M(\theta,\varphi_M) \tag{3}$$

In the expressions above, the subscript *C*, *M* and *O* indicate *cruising*, *maximum* and *original* (or required), respectively. The CFOC is the weighted average of the fuel consumptions at the two operational conditions where the torque correspond to Q_C and Q_M, Δt is the percentage of time the ship operates at each of the forward speed conditions, *SFOC* is the specific fuel oil consumption and n is the propeller rotational speed. In this case it is assumed that the ship operates 90% of the time at cruising speed and 10% at maximum speed, i.e., $\Delta t_C = 0.9$ and $\Delta t_M = 0.1$. The specific fuel consumptions for each of the operation conditions are estimated to be $SFOC_C = 0.190$ kg/kWh and $SFOC_M = 0.540$ kg/kWh.

The design variables are the ply angles, θ, and the blade pitch angles φ_C and φ_M, all of which are assumed to vary continuously. The ply angles have been defined using two different approaches. In a first approach – *straight fiber path* approach – the ply angles are used directly as the design variables. A second approach – *curved fiber path* approach – uses a parameterization of θ inspired by the results of Parnas et al. [11]. The curved fiber paths represent a simple way to vary the properties of the laminate throughout the structure without increasing the number of design variables significantly. Thus the ply angles are defined as a function of a curved fiber path and the design variables become the parameters defining this path. The determination of the angle is as illustrated in Fig. 8. The ply angle at an element in position A or at any position with the same z coordinate is equal to the angle θ_e. This angle is determined by the tangent to the curve of a second degree polynomial defined by the points $c_0(y_0,z_0)$, $c_1(y_1,z_1)$ and $c_2(y_2,z_2)$. The design variables then become the parameters y_1 and y_2. The point c_0 and the coordinates z_1 and z_2 are assumed fixed.

The blade pitch angles, φ_C and φ_M, of the controllable pitch propeller are also included as design variables and can be adjusted independently for each operational condition. A change in the blade pitch angle corresponds to a rotation of the blade around the hub and consequently to a variation in the

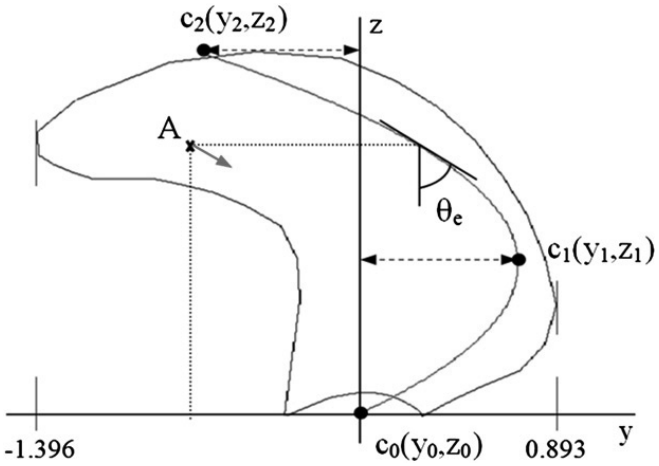

Fig. 8. Definition of the second degree curved fiber path.

angle of attack of all sections of the blade. In general, an increase in the blade pitch angle will correspond to an increase in the angle of attack of all sections and therefore to a variation in the lift and drag forces, and finally to an increase in the thrust and torque.

The constraints on the thrust, T_C and T_M, are included to assure that the optimal composite propeller will produce the same thrust as the original propeller. Note that the thrust is constrained from below indicating that the thrust may not be lower than the target thrust values. The inequality constraints are used (instead of equality constraints) due to the fact that the torque and thrust are coupled in their variations. That is, a decrease (or increase) in the torque will be accompanied by a decrease (or increase) in the thrust. Thus, the optimization model is limited by the thrust values as it tries to minimize the torque.

The choice of the optimization method depends heavily on the characteristics of the problem at hand. In this case the decision to opt for a gradient free method (as opposed to a gradient based method) is motivated by the low accuracy of the iterative method implemented for the determination of the hydro-elastic response. The gradient of the objective function and constraints cannot be defined analytically and therefore the alternative would be to resort to finite differences. The effect of the perturbations in the design variables is however not possible to measure as it cannot be distinguished from the oscillations resulting from the equilibrium iterations. The determination of the gradients is consequently compromised. The optimization model NOMADm [12] is therefore chosen. This is a type of derivative free, pattern-search algorithm specially suited for the analysis of nonlinear optimization problems where the gradients of the objective function and constraints are not available. Furthermore, NOMADm is combined with DACE [13] to form a surrogate model using spline interpolation which approximates the objective function and constraints. This procedure allows for a considerable reduction in the solution time of the optimization model.

4. Failure criteria

The strength of the blade is analyzed using a two dimensional version of the Tsai-Wu strength index (TWSI) [14] as given in Eq. (4),

$$TWSI = A + B \tag{4}$$

$$A = -\frac{\sigma_x^2}{\sigma_{x_t}^f \sigma_{x_c}^f} - \frac{\sigma_y^2}{\sigma_{y_t}^f \sigma_{y_c}^f} - \frac{\sigma_{xy}^f}{\left(\sigma_{xy}^f\right)^2} \frac{C_{xy}\sigma_x\sigma_y}{\sqrt{\sigma_{x_t}^f \sigma_{x_c}^f \sigma_{y_t}^f \sigma_{y_c}^f}}$$

$$B = \left(\frac{1}{\sigma_{x_t}^f} + \frac{1}{\sigma_{x_c}^f}\right)\sigma_x + \left(\frac{1}{\sigma_{y_t}^f} + \frac{1}{\sigma_{y_c}^f}\right)\sigma_y$$

where C_{xy} is an empirical parameter typically assumed as 0.5. The remaining terms are described together with Table 3. The TWSI is a quadratic multiaxial failure criterion specially developed for orthotropic materials where an index above one indicates material failure.

$$\begin{aligned}
&\textit{fiber tension} : \frac{\sigma_x}{\sigma_{x_t}^f} \quad \textit{if} \quad \sigma_x > 0\\
&\textit{Matrix tension} : \frac{\sigma_y}{\sigma_{y_t}^f} \quad \textit{if} \quad \sigma_y > 0\\
&\textit{Matrix tension} : \frac{\sigma_y}{\sigma_{y_t}^f} \quad \textit{if} \quad \sigma_y > 0\\
&\textit{Fiber compression} : \frac{\sigma_x}{\sigma_{x_c}^f} \quad \textit{if} \quad \sigma_x > 0\\
&\textit{Matrix compression} : \frac{\sigma_y}{\sigma_{y_c}^f} \quad \textit{if} \quad \sigma_y > 0\\
&\textit{In-plane shear} : \frac{\sigma_{xy}}{\sigma_{xy}^f}
\end{aligned} \tag{5}$$

The main disadvantage of the TWSI is that it is not possible to distinguish between the contributions of the different failure modes. In order to overcome this limitation, the Maximum Stress Failure Criterion (MSFC) is used in parallel with the TWSI. The stress ratios in Eq. (5) have been determined at

each layer of all elements. The critical failure mode will then be the mode with largest associated ratio over all layers. It is possible in this way to determine the dominating failure mode at each element in the blade.

5. Results

In the following, notice that the optimization and strength analysis steps are performed in parallel. The laminate properties are optimized first. The strength of the blade is subsequently analyzed and the necessary reinforcements are included on a trial and error basis. The laminate properties are then once again optimized but this time the properties of the laminate in the critically stressed regions are kept fixed. All results are obtained using the shell element model. The ply angle reference axes as well as the blade coordinate system are presented in Fig. 9. The *x* axis points in the upstream direction (direction of forward motion of the ship). The propeller rotates in the clockwise direction when looking upstream.

5.1. Effect of fiber orientation on blade properties

Before proceeding with the optimization of the laminate lay-up, several simple tests were conducted to investigate the influence of the fiber orientation on the propulsive and geometrical properties of the blade. Initially the analysis is conducted assuming that the blade consists of one laminate with one single lamina angle, i.e., $[(\theta)_{32}]$ over the entire blade. The variations in the fuel consumption, thrust and torque are then calculated as functions of the ply angle, θ, for both cruising and maximum speed operation conditions. The results are presented in Fig. 10 and are defined as ratios between the calculated values from the composite blade and those of the original blade. The case where the thrust

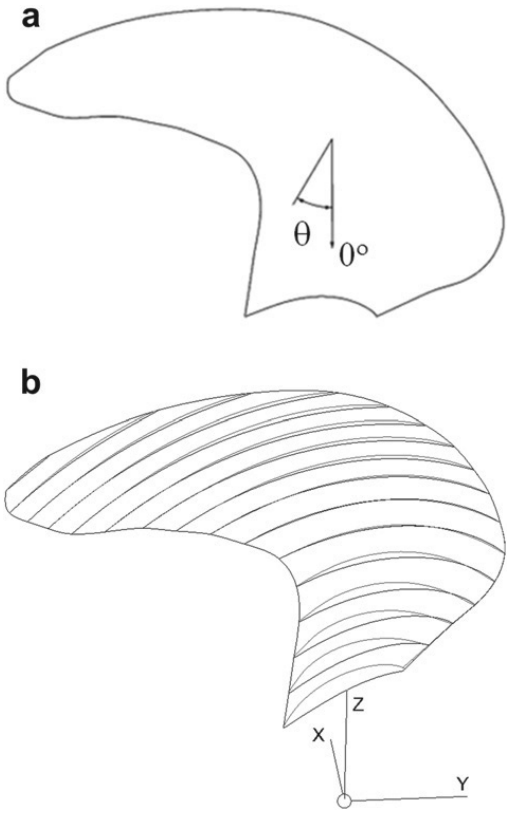

Fig. 9. (a) Ply angle orientation reference axis. (b) Blade coordinate system: *x*-direction corresponds to the forward speed direction, *y*-direction points in the starboard direction of the ship and the *z*-direction is the vertical direction of the blade. The *yz*-plane coincides with the plane of rotation of the propeller.

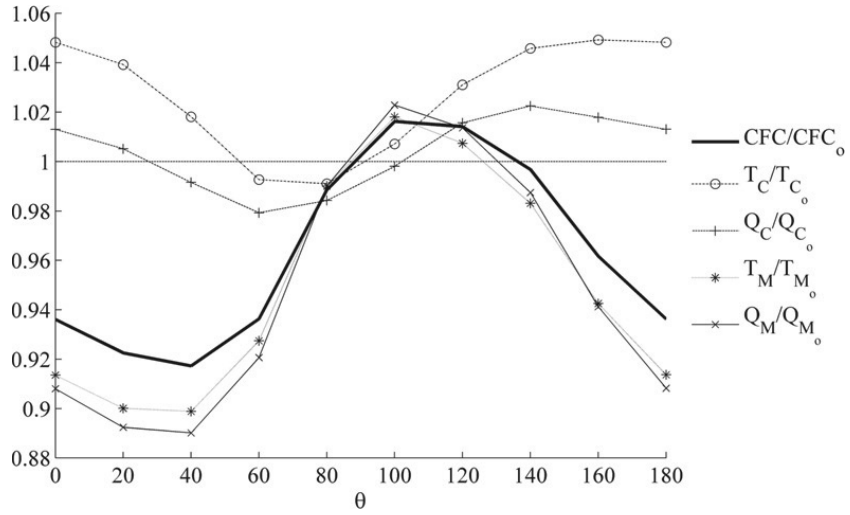

Fig. 10. Combined fuel consumption (CFOC), thrust (T) and torque (Q) ratios between the composite and original blade for varying lamina angle, given for both the cruising and maximum speed conditions.

or torque ratio is above one indicates fiber angles for which the composite propeller generates more thrust or torque than the original one. The same holds for the fuel consumption. Furthermore, if the thrust ratio is larger than the torque ratio then the efficiency of the composite propeller is higher than the original. Thus, in the cruising speed condition the efficiency of the composite blade is higher than the original for any fiber orientation since the thrust ratio is always higher than the torque ratio. The thrust generated by the composite propeller only matches that of the original blade when the fiber angle is around 50° and 90°. In the maximum speed condition the efficiency of the composite propeller is lower than the original for ply angles between 80° and 150°, and higher otherwise. Concerning the generated thrust, in this case it only matches the target values for fiber angles close to 80° and 130°.

As mentioned before, the optimal composite propeller minimizes the fuel consumption or torque while generating the same thrust force as the original. Hence, the aim is to find one fiber orientation for which the thrust ratio is equal to one (i.e., equal to the required) and the torque ratio is lower than unity (or lower than the original) for both operating conditions simultaneously. This case is not verified for any of the fiber angles presented in Fig. 10. The inclusion of the blade pitch angles as design variables in the optimization model is consequently justified. By varying the blade pitch angles for each operation condition independently it is possible to compensate for any necessary variations of the thrust and torque.

All the parameters describing the blade geometry presented in Table 1 were analyzed for the two ply angles where thrust and torque reach their maximum and minimum values. From Fig. 10 it is possible to see that the respective ply angles are 80° (minimum value) and 160° (maximum value) for the cruising speed condition and 40° (minimum value) and 100° (maximum value) for the maximum speed condition. The largest variations were observed in the radial distributions of pitch, camber and mid-chord positions (see Fig. 11). The radial distribution of pitch tends to be equal or lower than the original rigid blade (see Fig. 11(a,b)), whereas the camber tends to be larger in sections close to the hub and lower close to the tip (see Fig. 11(c,d)). The only exception being the maximum speed case for $[(100^\circ)_{32}]$ where the camber of most sections is larger than for the original blade. As expected for both cases the blade has deformed in the upstream direction (see Fig. 11(e,h)). At maximum speed the effect of the fiber direction on the local stiffness of the tip region is visible (see Fig. 11(f)). A laminate lay-up of $[(100^\circ)_{32}]$ will reinforce the tip whereas a laminate $[(40^\circ)_{32}]$ will result in more local flexibility.

Generally an increase in pitch and camber will correspond to an increase in the lift force (assuming there is no flow separation) and consequently also in the thrust and torque. Based on the results from Fig. 11 it is however difficult to establish the relation between the variation of the propulsive forces and the geometrical characteristics of the composite blade.

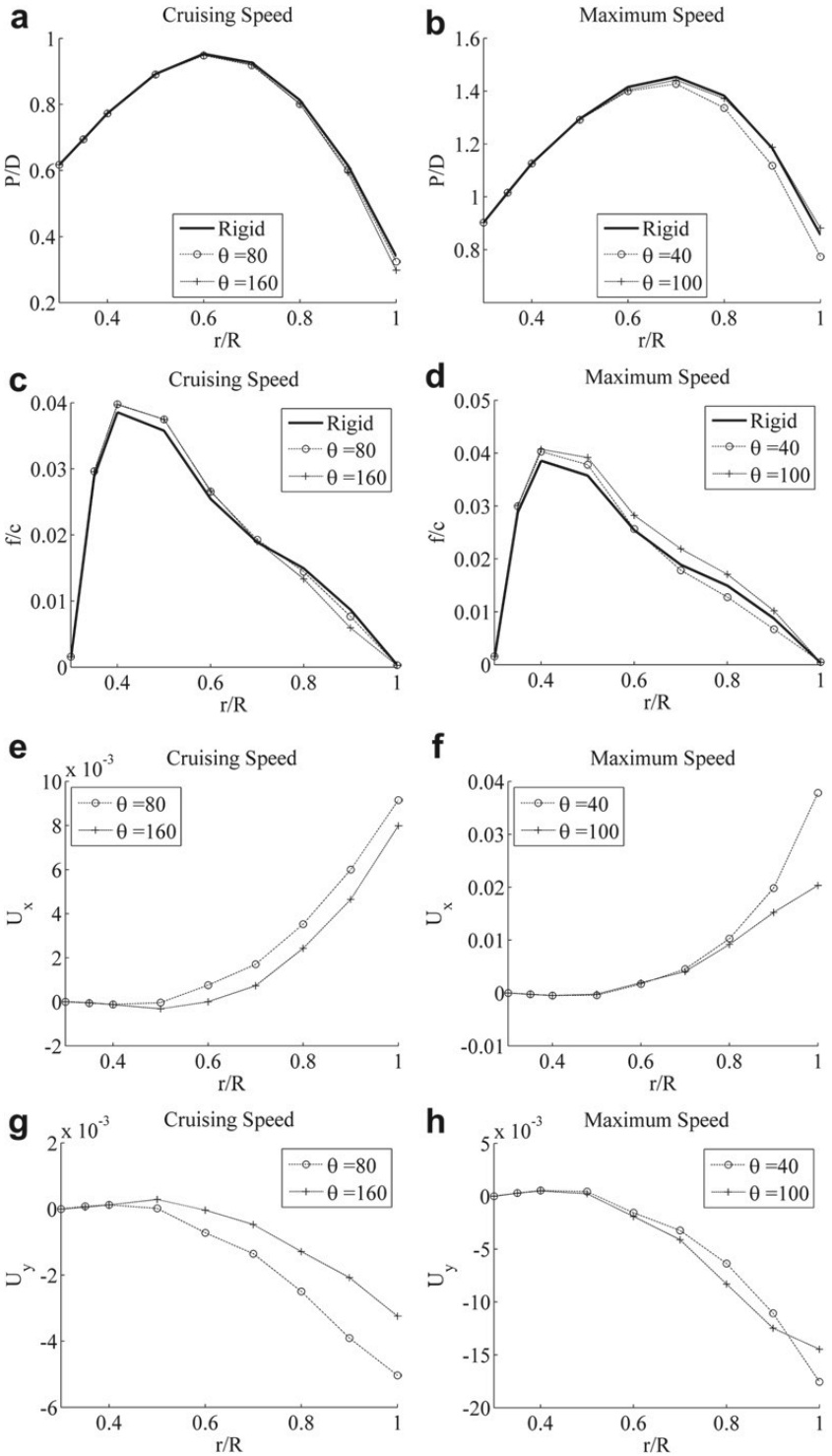

Fig. 11. Radial distributions of pitch (a,b), camber (c,d), displacement in *x*-direction (cf. Fig. 9(b)) of mid-chord point (e,f) and displacement in *y*-direction (cf. Fig. 9(b)) of mid-chord point (g,h). Results for the cruising speed condition are for laminate lay-ups $[(80^\circ)_{32}]$ and $[(160^\circ)_{32}]$, and $[(40^\circ)_{32}]$ and $[(100^\circ)_{32}]$ for the maximum speed condition.

5.2. Optimization of laminate lay-up

The first optimization results are obtained using the straight fiber path approach where the following three laminate configurations are tested: $[(\theta_1)_{32}]$, $[(\theta_1)_8, (\theta_2)_8, (\theta_3)_8, (\theta_4)_8]$ and $[(\theta_1)_8, (\theta_2)_8]_s$. The optimal fiber angles, resulting fuel consumption reduction and optimal blade pitch angles for all three laminate configurations are presented in Table 4. All laminate configurations converge to approximately the same lay-up – $[(40^\circ)_{32}]$ – and the one layer case is that which holds the largest reduction in fuel consumption. The fiber angles for this case are presented in Fig. 12 (a).

At maximum speed the thrust and torque are exactly equal to that of the original blade. Nonetheless, a reduction of 4.2% in the fuel consumption was found at the cruising speed condition corresponding to 1.12% in the combined case. The latter results suggest that the variation of the ply angles through the thickness has little influence on the blade response. This is in agreement with the presumption that the coupling effects are maximized for a laminate whose layers are mostly oriented in the same direction. This is also a direct consequence of the fact that the optimization model searches only for the optimal stiffness distribution and neglects other effects like stress constraints.

In the next step, the laminate angles are defined using the curved fiber path approach described earlier. The following laminate configurations are used in the analysis: $[(\theta_1(y_1,y_2))_{32}]$, $[(\theta_1(y_1^1,y_2^1))_{16}, (\theta_2(y_1^2,y_2^2))_{16}]$ and $[(\theta_1(y_1^1,y_2^1))_8, (\theta_2(y_1^2,y_2^2))_8, (\theta_3(y_1^3,y_2^3))_8, (\theta_4(y_1^4,y_2^4))_8]$. The results of the optimization analysis showed once again that the blade performance is not sensitive to the variations of the angles through the thickness. The optimal laminate lay-up $[(\theta_1(0.756,0.677))_{32}]$ is therefore chosen as illustrated in Fig. 12(b). The resulting decrease in the fuel consumption amounted to 4.7% at cruising speed corresponding to a reduction of 1.25% in the combined case (see Table 4). This corresponds to a further decrease of 0.13% in the combined fuel consumption when compared to the straight fiber path approach.

Finally, it should be noted that all optimal laminate configurations promote a flexible tip (cf. Fig. 11(f)). In the curved fiber path case, the maximum displacement occurs at the tip and is approximately 50 mm. Furthermore, the weight of the composite blade is approximately 230 kg, or around 1/4 of the weight of the original metal blade which is 1087 kg (assuming $\rho_{\text{metal}} \approx 7800\ \text{kg/m}^3$).

5.3. Strength analysis

All results presented hereafter are obtained for the maximum speed condition since this was identified as the most critical load condition of the two considered in this investigation. However, the backing and crash-stop conditions have been neglected in this investigation. The maximum TWSI over all layers at each element is plotted in Fig. 13(a). The maximum TWSI targeted during the design process is 0.7 since this is considered to be a reasonable level of safety in a practical design situation. The strength analysis is performed in parallel with the optimization of the fiber angles. The optimal

Table 4
Optimal laminate configurations and blade pitch angles (P/D_{07}). The thrust ration for the cruising and maximum speed conditions are given by (T_C/T_{C0}) and (T_M/T_{M0}), respectively. The percentage reduction in fuel consumption is given by ($\%FC_S$).

Laminate		Cruising Speed			Maximum Speed			Combined
		P/D_{07}	T_C/T_{C0}	$\%FC_S$	P/D_{07}	T_M/T_{M0}	$\%FC_S$	$\%FC_S$
$[(\theta_1)_{32}]$	$[(40^\circ)_{32}]$	0.544	1.00	4.2	2.412	1.00	0.0	1.12
$[(\theta_1)_8, (\theta_2)_8, (\theta_3)_8, (\theta_4)_8]$	$[(40.2^\circ)_8, (40.2^\circ)_8, (30.7^\circ)_8, (39.3^\circ)_8]$	0.611	1.00	3.5	2.391	1.00	0.0	0.94
$[(\theta_1)_8, (\theta_2)_8]_s$	$[(41.8^\circ)_8, (42.4^\circ)_8]_s$	0.635	1.00	3.3	2.372	1.00	0.0	0.89
$[(\theta_1(y_1^1,y_2^1))_{32}]$	$[(\theta_1(0.756,0.677))_{32}]$	0.512	1.00	4.7	2.550	1.00	0.0	1.25
$[(\theta_1(y_1^1,y_2^1))_{16}, (\theta_2(y_1^2,y_2^2))_{16}]$	$[(\theta_1(0.767,0.694))_{16}, (\theta_2(0.764,0.689))_{16}]$	0.514	1.00	4.7	2.467	1.00	0.0	1.25
$[(\theta_1(y_1^1,y_2^1))_8, (\theta_2(y_1^2,y_2^2))_8, (\theta_3(y_1^3,y_2^3))_8, (\theta_4(y_1^4,y_2^4))_8]$	$[(\theta_1(0.765,0.694))_8, (\theta_2(0.757,0.678))_8, (\theta_3(0.759,0.680))_8, (\theta_4(0.767,0.693))_8]$	0.514	1.00	4.7	2.464	1.00	0.0	1.25

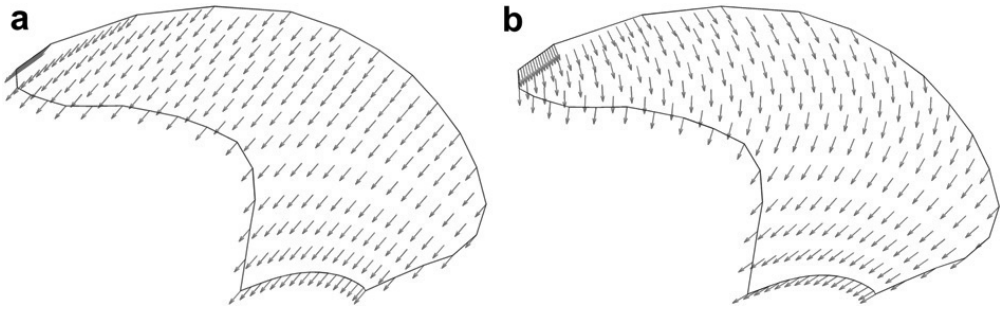

Fig. 12. (a) Resulting fiber angles obtained using straight fiber paths. (b) Resulting fiber angles obtained using curved fiber paths.

fiber angles are defined first and the strength of the resulting lay-up is examined next. The critical regions where the TWSI reaches the highest value are identified as the trailing edge and hub regions. The lay-up at these regions is then modified on a trial and error basis in order to reduce the maximum TWSI. The following lay-up sequences were consequently found: regions 1, 2, 3 and 4 (cf. Fig. 13(a)) are respectively changed to $[(-45^\circ)_{32}]$, $[(0^\circ)_{32}]$, $[(0^\circ)_{32}]$ and $[(90^\circ)_{32}]$.Finally, the lay-up of the critical regions is fixed while the optimal fiber angles in the remaining parts of the blade is optimized once again. Notice that the results from Table 4 refer to this final case where the laminate of the critical regions has been fixed and the remaining laminate over the entire blade has been optimized a second time.

Finally, the failure modes which according to the MSFC (Eq. (5)) show the largest ratios at each element are presented in Fig. 13(b). The results indicate that the laminates in the leading and trailing edge regions close to the hub, and in the central part of the blade close to the tip, may fail due to in-plane shear and matrix compression. The effect of the reinforcements is particularly visible in the trailing edge region. Before the re-orientation of the fibers in those regions was adopted, matrix failure was the failure mode with the largest ration whereas after the re-orientation of the fibers, in-plane shear is the failure mode holding the largest ration.

6. Discussion

Overall the results indicate that it is possible to tailor the orthotropic properties of laminated composite materials to design a flexible composite propeller whose shape passively adapts to the different working conditions while resisting the imposed loads. Optimal fiber orientations have been identified which result in a decrease of the fuel consumption. It is important to note though that the hydrodynamic model does not account for flow separation or cavitation. Consequently the resulting

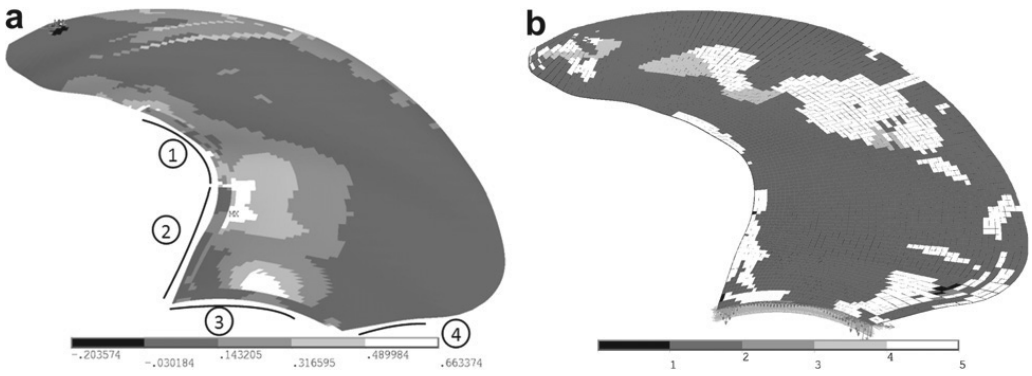

Fig. 13. (a) Maximum TWSI over all layers for the optimal propeller blade with curved fiber path. The regions 1, 2, 3 and 4 indicate regions with the lay-up configurations: $[(-45^\circ)_{32}]$, $[(0^\circ)_{32}]$, $[(0^\circ)_{32}]$ and $[(90^\circ)_{32}]$. (b) Failure modes for layer with highest stress ratios (see Eq. (5)) for each element. Legend: (1) – Fiber tension; (2) – Matrix tension; (3) – Fiber compression; (4) – Matrix compression; (5) – In-plane shear stress.

optimal blade pitch angles may be too large. Furthermore, the results indicate a possibility for reducing the fuel consumption further by varying the laminate orientation across the length and width of the blade, e.g., using curved fiber paths. However, these variations in the fiber alignment may be difficult to achieve in practice in which case the straight fiber path results should be used as reference.

From a strength point of view, the TWSI has been used to identify overly stressed blade areas while the MSFC provided information as to the failure modes with the highest possibility of failure. The laminate in the critical regions was consequently redesigned and the TWSI was decreased. The proposed laminate orientations however disregard once again production constraints and would need to be revised in a subsequent iteration of the design process. In this sense, the analysis model used in this investigation assumes that all layers have the same thickness. An analysis model incorporating ply drop-off to account for changes in thickness should also be considered at a later stage for a more accurate evaluation of the strength properties. Besides, the full reverse and crash-stop conditions should be considered as well since these are usually critical load cases. Finally, propeller blades are subjected to cyclic loads and the analysis of the effects due to fatigue is therefore strongly recommended.

7. Conclusions

A framework for the design and optimization of composite marine propellers has been presented. The laminate lay-up configuration and blade pitch angles of a large naval type controllable pitch composite propeller blade with high skew was optimized for two different load conditions – cruising and maximum speed. Two parameterizations of the fiber angles have been considered in the optimization model. Namely, the straight fiber path approach which assumes constant fiber angles throughout the blade and the curved fiber path approach which assumes that the orientation of the fibers throughout the blade follows a polynomial curve. The largest reduction in fuel consumption was obtained using the curved fiber path approach. The optimal fiber and blade pitch angles have been determined and a reduction of the combined fuel consumption of 1.25%, corresponding to a decrease of 4.7% for the cruising speed and no reduction for the maximum speed condition, was observed.

Concerning the geometrical properties of the blade, the largest variations were observed in the radial distributions of pitch, camber and mid-chord positions. The optimal configurations promoted a flexible tip and a stiff body closer to the hub.

The strength of the blade was analysed in terms of the Tsai-Wu strength index and performed in parallel with the optimization of the fiber and blade pitch angles. The leading edge and hub regions were identified as the critical areas. The blade was therefore reinforced and the lay-up configuration in these regions was modified. It was shown that after reinforcement of the critical areas, the maximum Tsai-Wu failure index was lowered from 1.6 to around 0.7 suggesting that no failure occurs. The most significant failure modes were identified as matrix failure in tension and in-plane shear.

The results are encouraging and suggest that it should be possible to build a large flexible composite marine propeller which outperforms its metal counterpart.

Acknowledgements

This work has been performed within the Network of Excellence on Marine Structures (MARSTRUCT) and has been partially funded by the European Union through the Growth Programme under contract TNE3-CT-2003-506141.

The invaluable support given by Associate Professor Mathias Stolpe, Department of Mathematics, Technical University of Denmark is gratefully acknowledged.

References

[1] Berring P, Branner K, Berggreen C, Knudsen HW, "Torsional performance of wind turbine blades – Part I: Experimental investigation", 16th International Conference on Composite Materials (ICCM-16), Kyoto, Japan, July 8–13, 2007.

[2] Branner K, Berring P, Berggreen C, Knudsen HW, "Torsional performance of wind turbine blades – Part II: Numerical verification", 16th International Conference on Composite Materials (ICCM-16), Kyoto, Japan, July 8–13, 2007.

[3] Lobitz DW, Veers PS, Eisler GR, Laino DJ, Migliore PG, Bir G. The use of twist coupled blades to enhance the performance of horizontal axis wind turbines. SANDIA Report SAND2001–1303.
[4] Livne E, Weisshaar TA. Aeroelasticity of non-conventional airplane configurations-past and future. Journal of Aircraft 2003;40(6):1047–65.
[5] Ganguli R, Chopra I. Aeroelastic optimization of a helicopter rotor with composite coupling. Journal of Aircraft 1995;32(6): 1326–34.
[6] Lee YJ, Lin CC. Optimized design of composite propellers. Mechanics of Advanced Materials and Structures 2004;11:17–30.
[7] Lin HJ, Lin JJ, Chuang TJ. Strength evaluation of a composite marine propeller blade. Journal of Reinforced Plastics and Composites 2004;24(17):1791–807.
[8] Marsh G. A new start for marine propellers? Reinforced Plastics, December, 2004.
[9] Zenkert D, Battley M. Foundations of fiber composites. Royal Institute of Technology, Paper 96–10.
[10] www.ansys.com.
[11] Parnas L, Oral S, Ceyhan Ü. Optimum design of composite structures with curved fiber paths. Composites Science and Technology 2003;63:1071–82.
[12] Booker AJ, Dennis JE, Frank PD, Serafini DB, Torczon V, Trosset MW. A rigorous framework for the optimization of expensive functions by surrogates. Technical Report CRPC-TR98739-S, Center for Research on Parallel Computation, Rice University; 1998.
[13] Lophaven SN, Nielsen HB, Søndergaard J. DACE – A MATLAB Kriging Toolbox. Technical Report IMM-TR-2002–12.
[14] Tsai SW, Wu EM. A general theory of strength for anisotropic materials. Journal of Composite Materials 1971;5:58–80.

DTU Mechanical Engineering
Section of Coastal, Maritime and Structural Engineering
Technical University of Denmark

Nils Koppels Allé, Bld. 403
DK- 2800 Kgs. Lyngby
Denmark
Phone (+45) 45 25 13 60
Fax (+45) 45 88 43 25
www.mek.dtu.dk
ISBN: 978-87-90416-62-1

DCAMM
Danish Center for Applied Mathematics and Mechanics

Nils Koppels Allé, Bld. 404
DK-2800 Kgs. Lyngby
Denmark
Phone (+45) 4525 4250
Fax (+45) 4593 1475
www.dcamm.dk
ISSN: 0903-1685